Improvement of the axial buckling capability of elliptical cylindrical shells

Maurizio Paschero

Dissertation submitted to the Faculty of the
Virginia Polytechnic Institute and State University
in partial fulfillment of the requirements for the degree of

Doctor of Philosophy
in
Engineering Mechanics

Prof. Michael W. Hyer, Chair
Prof. Romesh C. Batra
Prof. Aloysius A. Beex
Prof. Mayuresh Patil
Prof. Surot Thangjitham

March 25, 2008
Blacksburg, Virginia

Keywords: Elliptical cylinders,Variable thickness cylinder
Material tailoring, Stability, Anisogrid cylinder

Improvement of the axial buckling capability of elliptical cylindrical shells

Maurizio Paschero

ABSTRACT

A rather thorough and novel buckling analysis of an axially-loaded orthotropic circular cylindrical shell is formulated. The analysis assumes prebuckling rotations are negligible and uses a unique re-defining of the orthotropic material properties in terms of a so-called geometric mean isotropic (GMI) material. Closed-form expressions for the buckling stress in terms of cylinder geometry and orthotropic material properties are presented, the particular closed form depending on the specific character of the orthotropic material relative to the GMI material. With the formulation, the specific character of the buckling deformations - e.g., axisymmetric or nonaxisymmetric, the number of axial and circumferential waves - can be established. By using the maximum radius of curvature of an elliptical cross section in this formulation, the analysis is used to demonstrate the detrimental effects of an elliptical cross section on axial buckling capacity when compared to a circular cross section with the same circumference. Using the circumferentially-varying radius of curvature of an elliptical cross section, the analysis is then further used as the basis for developing two methods for improving the axial buckling capacity of elliptical cylinders. The first approach involves varying the wall thickness of an isotropic elliptical cylinder with circumferential position. Uniformly stable elliptical cross sections which preserve the same critical stress, critical load, or volume of an axially loaded circular cylinder of the same circumference are designed with the formulation. The second approach involves maintaining a uniform wall thickness but varying the orthotropic material properties with circumferential position. This approach is applied to a cylindrical lattice structure where it is assumed that the ribs are dense enough to be able to describe the lattice structure by means of an equivalent homogenized material. The orthotropic properties of the homogenized material are varied by varying the lattice rib angle with circumferential position. Considerable recovery of the axial buckling capacity of the variable-rib-angle design elliptical cylinder compared to the same cylinder constructed in isogrid fashion is demonstrated. In fact, recovery relative to an isogrid circular cylinder of the

same circumference is demonstrated. For both approaches confirming finite element models are used to verify the findings. The two different approaches are compared, and finally the two approaches are recognized as special cases of a more general design philosophy.

Acknowledgments

I wish to first and foremost acknowledge my advisor Dr. Michael W. Hyer for his guidance, advice, and encouragement through the years. Working with him is interesting, fruitful and, at the same time, extremely pleasant. He is one of the few persons I met in my academic life who is able to be rigorous without being unsmiling. I will always pleasantly remember our conversations made of jokes and equations research and everyday life. I really hope to be in touch with him for the rest of my life. Next, I would like to thank my other committee members, Dr. R. C. Batra, Dr. A. A. Beex, Dr. M. Patil, and Dr. S. Thangjitham, and the entire Department of Engineering Science and Mechanics that gave me the chance to improve my knowledge by offering me a valuable education. Moreover, I would like to thank all the friends I met during the years in Blacksburg. Among them a special thanks goes to the people I like to call the "Italian gang of Blacksburg" for their liking and friendship. Thanks to them, my time out of the office has never been boring. Finally, I wish to thank my family who always supported me, especially my father, who left us too early. He taught me tolerance and humility and I will always carry him in my heart. My mother, who encouraged me to come here just a few months after the unexpected death of my father, showing uncommon altruism.

Contents

List of Figures

List of Tables

Chapter 1

Literature review and overview of the dissertation

1.1 Introduction

Among the many aspects of interest in the study of structures, stability plays a fundamental role. Thin-walled shells are particularly susceptible to a loss of stability. In some cases this loss of stability causes the structure to collapse. Consequently, it is of unquestionable importance to have a full understanding of the stability behavior of shells in order to produce suitable designs for practical purposes. A thin-walled cylinder is a prime example of a structure for which stability is an important consideration. Most cylindrical structures are constructed with a circular cross section because of the efficiency of the circular shape in reacting, for example, to internal and external pressure, and to torsional, bending, and axial loads. Therefore, much has been written regarding the stability of cylinders subjected to a variety of loads. A glance at the recent book by Jones [1] illustrates this point by way of the long list of references on the topic.

Cylinders with noncircular cross sections, on the other hand, are not so common. Accordingly, there is considerably less written about their stability, or for that matter, any other aspect of their structural response. Yet, there are applications where a noncircular cross section may be required because it provides a measurable advantage relative to a circu-

lar cross section. For example, blended-wing-body aircraft design could take advantage of a noncircular fuselage cross section to provide a flatter underbody and a smoother shape that could enhance aerodynamic performance. Likewise, submersible vehicles with noncircular cross sections may prove to have an advantage. From a different perspective, it may be that geometric constraints would dictate a noncircular design for tankage. Unfortunately, for a given circumference, length, and thickness, and therefore weight, relative to a cylinder with a circular cross section a cylinder with a noncircular cross section cannot support the same level of load, for a variety of loading types. The primary objective of this dissertation is to investigate two specific concepts designed to overcome this disadvantage. An axial loading is considered, but the concepts have broad implications.

To follow is a brief review of studies concerning the stability of shells. Particular attention will be devoted to cylindrical shells having a noncircular cross-section. Both isotropic and anisotropic composite materials will be considered. A section will be devoted to the literature on stiffened and lattice structures, as one of the concepts investigated in this dissertation to improve the load capacity of noncircular cylinders will address noncircular lattice cylinders. Finally, more specific details of the objectives of the work discussed in this dissertation will be given, and an overview of this document will be presented.

1.2 Classical theory of elastic stability of shells

The unstable behavior of shell-like structures has been experimentally observed since the XIX^{th} century in tubes under external pressure [2]. Even though a rough theoretical background was given in that century [3], a more general and complete theory for the stability of shells was developed only in the XX^{th} century. The first studies on stability of shells assumed a membrane state and no kind of imperfection. Based on those hypotheses it was determined that instability resulted in small, often localized, superposed bending [4, 5, 6, 7] deformation. Experimental works, that were carried out in the 1920s in order to validate those theories, resulted in much lower values for the critical load than the one theoretically predicted. Consequently, new approaches were proposed in order to find better agreement with the experimental results. Nonlinear equations, which were able to describe the pre- and

postbucking state of a shell, were derived by Donnell [8], Marguerre [9], and Mushtari [10]. Karman and Tsien applied those equations to the study of cylindrical shells subjected to compressive load in the axial direction [11]. They found unstable behavior up to a certain minimum load, followed by a stable region. This lower bound for the load was called the lower critical load. The lower critical load was considered for a while a good estimation of the instability of shells suitable to be used for design purposes [12]. The classical critical load was further investigated, attributing to the imperfections of the material the drop of the experimentally-found critical load with respect to the theoretical one. General consideration on the effect of imperfections on the estimation of the critical load were performed by Koiter [13] and Budiansky [14]. The set of nonlinear equations taking into account imperfections were derived in [8], even though effective solutions were given some years later in [15, 16]. Those studies seem to highlight that the classical critical load becomes meaningful in the limit for vanishing imperfections. More precisely, it seemed to be proven that any imperfection results in a drop of the critical load. A set of experiments conducted mainly by Tennyson using the photoelasticity phenomenon and high speed cameras [17, 18, 19] found reasonable agreement with the theory. More precisely, the critical buckling loads were found to agree within $10 - 14\%$ of the classical value, or within a few percent of the reduced buckling load when taking into account the clamped end constraint.

1.3 Stability of noncircular cylindrical shells

In this section a brief review of the literature on the noncircular cylindrical shells will be given. Isotropic and fiber-reinforced composite materials will be treated in two different subsections. The main difference between a circular cylinder and a noncircular one is that while the curvature of the first one is constant in the circumferential direction, the curvature of the second one generally changes point by point in the circumferential direction. Usually the curvature is described by means of the radius of curvature R that for a noncircular cylinder becomes a function of a parameter which describes the variation of the cross-sectional geometry. A common choice is to use as a parameter the curvilinear abscissa s, which has the geometrical meaning of the length of the arc spanned moving around the the circumference from a reference point to another point. Other parameter choices can be made. A common

technique to represent a variable curvature is to expand it in a Fourier series of the form

$$\frac{1}{R(s)} = \frac{1}{R_0}\left(1 + \sum_{k=1}^{\infty} a_k \cos\left(\frac{4k\pi s}{C}\right)\right) \tag{1.1}$$

where C is the circumference of the cyinder. It should be noted that the factor R_0 in (1.1) can be interpreted as the radius of curvature of a circular cylinder having an equivalent circumference, while the coefficients a_k take into account the correction needed to produce the actual noncircular shape. Equation (1.1) was initially introduced by Marguerre to describe an elliptical cross section [20], but it can be used for any section having two orthogonal axes of symmetry. The convergence of (1.1) for an elliptical cross section was investigated in [21, 22]. In [23, 24] and [25] only two terms in the expansion (1.1) were used in order to describe a closed oval cylindrical shell. The nonlinear governing equations needed to investigate the stability behavior of isotropic and anisotropic noncircular cylindrical shells were derived in [21, 22, 26, 27, 28]. A model taking into account the effect of the transverse shear deformation was derived in [28, 29], while a theory that accounts for both transverse normal and transverse shear deformations was proposed in [30, 31]. Finally, three-dimensional elasticity models were developed in [32].

1.3.1 Stability of isotropic noncircular cylindrical shells

The majority of the earlier works on the stability of noncircular cylindrical shells were concerned with isotropic materials due to the simplicity of their constitutive equations relative to those for anisotropic materials. The necessity to deal with simpler equations also motivated the first investigators to assume in most of those works a membrane prebuckling deformation state. Moreover, in order to avoid the influence of the boundary conditions on the stability of the structure, they assumed infinitely-long cylinders. As a result of the latter assumption, the prebuckling rotations of boundary conditions were not included, thus avoiding the complications of localized bending effects at the ends of the cylinder. The first work that investigated the stability of a noncircular cylinder seems to be [33], where pure overall bending was considered. As mentioned in the previous section, after a long debate most of the researchers agreed that the large discrepancy between the classical critical load and the

one experimentally-found could be attributed to the imperfections of the shells. This observation was historically one of the main reasons that brought researchers to study noncircular cross section cylindrical shells; they were in fact used to model geometric imperfections on circular shells. As mentioned before, Marguerre was the first one to express the curvature of a noncircular section having biaxial symmetry as a trigonometric series [20]. This approach implements the idea of considering a noncircular cross-section as a perturbation of a circular one, another interpretation of (1.1). Kempner and Chen [26, 34] used the Marguerre's technique to develop a geometrically nonlinear analysis of an oval cylinder under axial load based on a variational approach. They consider an infinitely-long cylinder and modeled the variable curvature with a two-term Fourier series using (1.1). Numerical results were derived through the Ritz method. The main results of their work can be summarized by saying that the bucking phenomenon on a noncircular shell starts from the region having minimum curvature, i.e., the location where the shell is flatter. This result can be expressed in a neater way by saying that the critical load of a thin shell having a noncircular section approaches that of a circular section having a radius equal to the maximum radius of curvature found spanning the whole noncircular circumference. A direct consequence of this behavior is that the more the eccentricity of a section increases, the more the critical load decreases relative to the circular case. Another interesting result found by Kempner and Chen is that although the critical load of a noncircular cylindrical shell decreases with respect to that of a circular section having the same circumferential length, the postbuckling stiffness of an oval section is larger than the stiffness of a circular one. This increased stiffness is due to the regions of high curvature at the ends of the major radius not participating in the buckling deformations and thus able to continue to support load. Further theoretical studies on the postbuckling of noncircular cylindrical shells [35, 36] highlight that the more the eccentricity of the section increases, the more the snap-though phenomenon, which occurs when the axial load exceeds the critical value, is moderated. Experimental results found good agreement with the theoretical predictions. More accurate analysis, including more nonlinear terms in the strain-displacement relations, was performed in [37], where the buckling behavior of axially compressed elliptical cones and cylinders, for both the perfect and imperfect cases, were studied. In [38] the effect of the introduction of clamped boundary conditions on the stability of isotropic noncircular cylinders was studied in order to account for nonmembrane

prebuckling deformations. The correction due to the effects of the clamped boundaries on the critical load predicted by theories based on infinite-length cylinders has been found to be moderate for low eccentricity cross sections. Theoretical predictions were confirmed by experimental results [39].

1.3.2 Stability of noncircular composite cylindrical shells

The studies of the stability of noncircular composite shells are much more recent than the studies of isotropic shells. An early contribution in this direction is found in [40], where the instability under axial compression of oval symmetric and antisymmetric cross-ply laminated cylinders was studied using the Donnell-Mustari-Vlasov (so-called DMV) shallow-shell theory, which will be briefly discussed in Chapter 2. The results of this study provided evidence that for the antisymmetric laminates they considered the bending-extension coupling decreased quite rapidly as the number of layers increased. A similar approach was used in [27] in order to show that the stability performance of symmetric cross-ply noncircular infinite-length cylinders are quite insensitive to imperfections for a wide range of eccentricities. An analysis taking into account the most general boundary conditions was performed in [41, 42] using a Galerkin approach based on a Marguerre-like series expansion of the radius of curvature. In this work it was shown that the coupling between axial and circumferential modes becomes more relevant as the eccentricity increases. It was also shown that noncircular laminated composite shells are less sensitive to imperfection relative to circular ones. This behavior becomes more evident as the eccentricity increases. In [28, 29] a Love-type parabolic shear deformation shell theory was applied to a noncircular laminated shell. The buckling load of a cross-ply laminated cylinder under axial compression was derived through the Galerkin method. The results of this work showed that taking into account shear deformations produces a more conservative estimation of the buckling load. It was also observed that the effect of transverse shear deformations decreases as the eccentricity increases. In more recent years a formulation taking into account transverse normal and transverse shear deformations was proposed in [30, 31]. In this work a trigonometric series expansions of the displacements, including higher order terms, was assumed. Generalized variables associated with zig-zag functions were included in the model. The solutions obtained through a finite el-

ement approach showed that the coupling between axial and circumferential modes increased as the eccentricity increased, as was found in [41, 42]. Recently Sun [43] investigated the effects of the fiber orientation on the stability of an elliptical $[\pm\theta, 0, 0]_S$ composite cylinder. A procedure to vary the angle θ around the circumference was proposed and numerically validated. An improvement of the axial load capability up to 30% relative to an elliptical cylinder with quasi-isotropic laminate was obtained.

1.4 Stability of cylindrical stiffened shells

The introduction of properly spaced stiffeners can be used to increase the stability performance of a cylindrical shell and lower its weight. In a cylindrical shell the longitudinal stiffeners are usually referred to as stringers, while the circumferential ones are referred to as ribs. The usefulness of stiffeners can be understood by realizing that the global bending stiffness of the shell is significantly increased. The danger of local buckling, typical of thin shells, is avoided by the use of properly spaced reinforcements. The first contributions to the optimal design of stiffened cylindrical shells go back to the late 1940s. Pure bending of a cylindrical shell was discussed in [44, 45]. The so-called optimum design was achieved by equating the global and the local buckling loads, a so-called simultaneous mode design. Modal interaction was not considered. The literature on the stability of stiffened cylindrical shells is quite large. Here the most relevant contributions investigating the stability of reinforced shells under compressive axial load will be discussed. In [46] an analysis of perfect shells with rectangular cross section stiffeners under axial compressive load was reported. In [47] the effect of the eccentricity on longitudinal and circumferential stiffeners was considered. In [48] the use of different material combinations was investigated. In [49] the optimal shape of stiffeners was discussed. In [50] experimental investigations of stiffened cylinders under axial compression was discussed. In [51, 52] the influence of imperfections on the stability of stiffened cylindrical shells under compressive load was discussed. The influence of the shape of the cross section of the stiffeners was considered in [53]. In [54] the influence of boundary conditions on the buckling of stiffened cylindrical shells was investigated. The stiffener eccentricity effect on the initial postbuckling behavior of stringer- or ring-stiffened laminated composite circular cylindrical shells subjected to axial compression was investigated in [55]

using the general Koiter's theory. It was found that, in every case studied, external stiffening was more efficient than internal stiffening. Moreover, it was highlighted that the buckling and initial postbuckling behavior of stiffened laminated cylinders were significantly influenced by the laminate configuration. In [56] the nonaxisymmetric buckling of stiffened shells was investigated through both static and dynamic analyses. Recently, there has been an interest in stiffening of shell structures using a so-called lattice approach, also referred to as isogrid stiffening. With this approach, as illustrated in Fig. 1.1, a network of beam-like elements

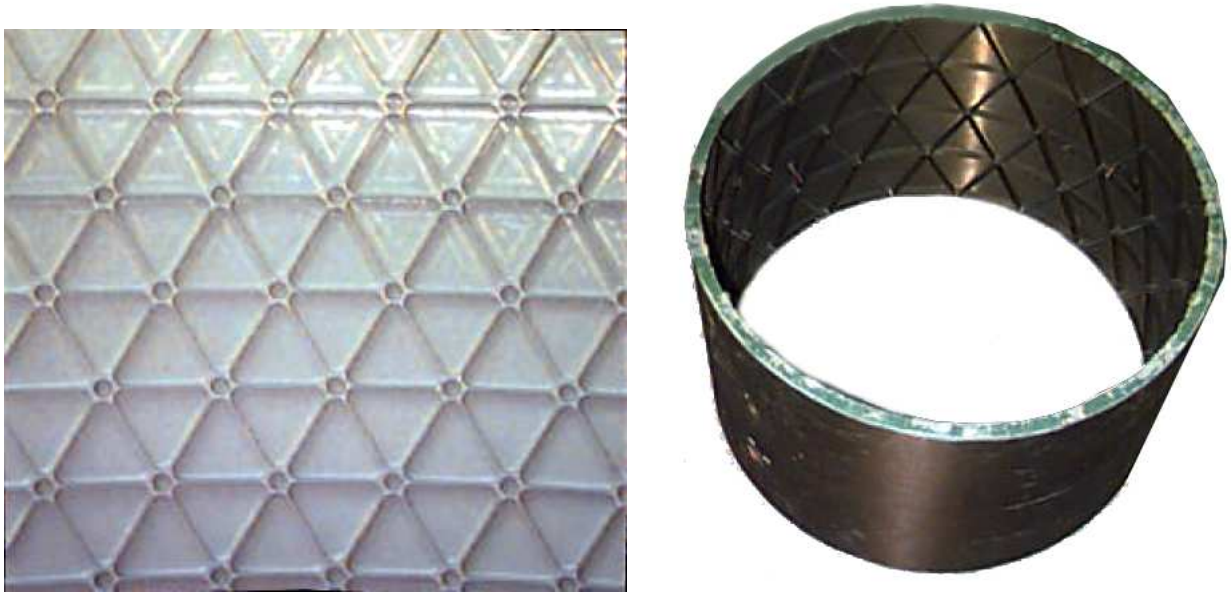

Figure 1.1: Examples of isogrid lattice structure

are joined to form a lattice with a triangle as the basis. The isogrid concept is based on the included angle between the ribs of each triangle being 60°. With this rib angle the inplane elastic behavior of the lattice is the same in all directions, hence the prefix "iso". The cross-sectional dimensions and elastic properties of the ribs, as well as the overall dimension of the basic triangle, control the properties of the lattice structure. The lattice structure can actually be sandwiched between two thin layers of material to form a sandwich structure with the lattice as a core. Lattice-based cylinders have been shown to be quite efficient in resisting axial buckling. A generalization of isogrid structure can be obtained by allowing the included angle between the ribs to assume values different from 60°. This relaxation of geometry produces a structure which does not exhibit isotropic behavior. For this reason these structures are usually referred to as anisogrid lattice structures. An example of an

anisogrid lattice is shown in Fig. 1.2. In [57] a combined analytical and experimental study

Figure 1.2: Example of anisogrid lattice structure

on buckling and postbuckling of an isogrid stiffened shell is reported. In [58] the basic design concepts and industrial design fabrication methods of anisogrid lattice structures are presented, together with experimental testing and serial development methodologies in the former Soviet Union. Analogous progress in the fabrication, analysis, and design methods of anisogrid stiffened structures achieved mostly in the United states is reported in [59, 60]. There are disadvantages to lattice structures that have slowed their development, not the least of which is the difficulty in fabricating such structures, particularly the verticies of the triangles. Repair of a lattice structure is also an issue, though it can be argued that a lattice-stiffened structure is more damage tolerant than a conventionally-stiffened structure.

1.5 Overview of the dissertation

As has been discussed, after considerable debate most researchers agreed that classical critical load becomes meaningful in the limit of vanishing imperfections. Moreover, classical results of thin shell theory showed how the load capability of a circular cylinder under axial compression decreases as soon as any eccentricity is assigned to the cross section. As Sun [43] has shown, it is possible to improve the axial load capability of fiber-reinforced composite cylinders with elliptical cross-section by varying the fiber orientation with the circumferential position. But, what can be done for an elliptical cylinder made using an isotropic material? About the only possible solution is to vary wall thickness with circumferential position. But how should the thickness be varied with circumferential position? And considering a lattice

structure in the form of an elliptical cylinder, it may be that rib angles other than 60° lead to improved axial load capability. This is potentially true if the rib angle is allowed to vary with circumferential position, much like Sun [43] allowed the fiber angle to vary with circumferential position. Again, there is the question of determining the rule by which the rib angle varies with circumferential position. The purpose of this dissertation is to investigate both concepts, and develop the rules. However, these two problems are not investigated as unrelated problems. Rather they are investigated as variations of the same concept, specifically, the same design philosophy.

This dissertation actually presents three important and new developments. Specifically, as a tool for improving the axial buckling capacity of elliptical isotropic and lattice cylinders, and as a prelude to those two studies, a buckling analysis of circular orthotropic cylinders is developed using a rather unique viewpoint. The viewpoint, which is based on the definition of a so-called Geometric Mean Isotropic (GMI) material, results in simple expressions for the axial buckling capacity of circular orthotropic cylinders, the expression being valid depending on the character of the orthtropic material relative to the GMI material. The approach also presents several methods to determine the character of the buckling deformations as a function of material orthotropy, including the case of multiple buckling deformation patterns for the same buckling load. Therefore, the objectives of the proposed research are to

1. Develop a buckling analysis for circular orthotropic cylinders
2. Develop an approach for improving the axial buckling capacity of an isotropic elliptical cylinder by varying the thickness of the cylinder wall with circumferential location
3. Develop a lattice geometry that varies with circumferential position so as to improve the axial load capability of an elliptical lattice cylinder

For the third objective only the lattice network is addressed. No attached thin layers are considered. As the geometry of the lattice structure is to be varied with circumferential location, it is important to understand the behavior of the lattice network itself. Considering a variable geometry lattice with attached thin layers, say, composite layers, within which the fiber angles could also vary with position is considered a very complex problem, one beyond the scope of the present study.

A brief overview of the present dissertation in given below:

- In Chapter 2 is presented the theory of surfaces as it applies to cylindrical shells, the kinematic relations, and assumed constitutive behavior for Donnell-Mustari-Vlasov (DMV) shell theory as it is used here. The governing equilibrium equations and boundary conditions, as well as the stability equations and accompanying boundary conditions are presented.

- In Chapter 3 the buckling analysis of orthotropic cylinders subjected to an axial load is developed. This is the first objective of this study. The Geometic Mean Isotropic material is defined, the polynomial expressions which determine the buckling load are closely examined, simple expressions for the buckling load are derived, and the buckling deformation pattern is analysed.

- In Chapter 4 the representation of a lattice structure as an equivalent orthotropic material is used with the analysis developed in Ch. 3. The axial buckling behavior of a circular lattice cylinder is expressed in terms of the rib angle, which in this Chapter is assumed constant with circumferential position. It is shown that there is a rib angle for which the buckling load is a maximum, and over a range of rib angles the buckling deformations are axisymmetric.

- In Chapter 5 is defined the geometry and nomenclature of elliptical cylinders. The loss of axial load capacity of an isotropic elliptical cylinder relative to a circular cylinder of the same circumference, length, and wall thickness is quantified. The theoretical analysis is numerically validated for aluminum and isogrid cylinder. A philosophical view of the approaches proposed to improve the axial load capacity of an isotropic cylinder and a lattice cylinder is presented.

- In Chapter 6 is proposed the variation of wall thickness with circumferential position of an isotropic cylinder to mitigate the loss of capacity relative to a circular cylinder. This is the second objective of this study. An analytical treatment of the problem is used to quantify the results for three different designs of wall thickness variation, all of which show improved capacity. The improvements are verified by way of a finite-element analysis of the same designs.

- In Chapter 7 is investigated the use of a variable geometry lattice, by virtue of varying the rib angle, to improve the axial buckling behavior of an elliptical lattice cylinder having the same circunference of a constant geometry circular lattice cylinder. A semi-analytical treatment of the problem is used to quantify the results for one design of rib angle variation. The improvement is verified by way of a finite-element analysis of the same design. The design is performed assuming the lattice structure is dense enough to be smeared. Once the variation of the rib angle with circumferetnial position is determined, a procedure to obtain the variable geometry grid is studied.

- In Chapter 8 are summarized the key findings and conclusions of the study and a comparison between the two complementary approaches proposed in Chapters 6 and 7 is given. Recommendations for future work are presented.

Chapter 2

Fundamental equations of quasi-shallow shells

2.1 Introduction

In this Chapter the basic principles, relations, and equations for developing a shell theory in the context of the assumptions of the Donnell-Mushtari-Vlasov shell theory are presented to serve as a reference. The material in this Chapter is not new, but it is included for completeness.

2.2 Geometry of surfaces

Consider a Cartesian reference coordinate system $X_i \quad i = 1, 2, 3$ and a smooth surface embedded in the three-dimensional space, as shown in Fig. 2.1. The coordinates of each point P belonging to the surface are given by the following vector equation

$$\mathbf{r}(x_1, x_2) = X_1(x_1, x_2)\hat{\mathbf{i}} + X_2(x_1, x_2)\hat{\mathbf{j}} + X_3(x_1, x_2)\hat{\mathbf{k}} \tag{2.1}$$

where $\hat{\mathbf{i}}$, $\hat{\mathbf{j}}$ and $\hat{\mathbf{k}}$ are the unit vectors of the Cartesian reference, while x_1, x_2 are two generic parameters used to describe the geometry of the surface. The parameters x_1 and x_2 can

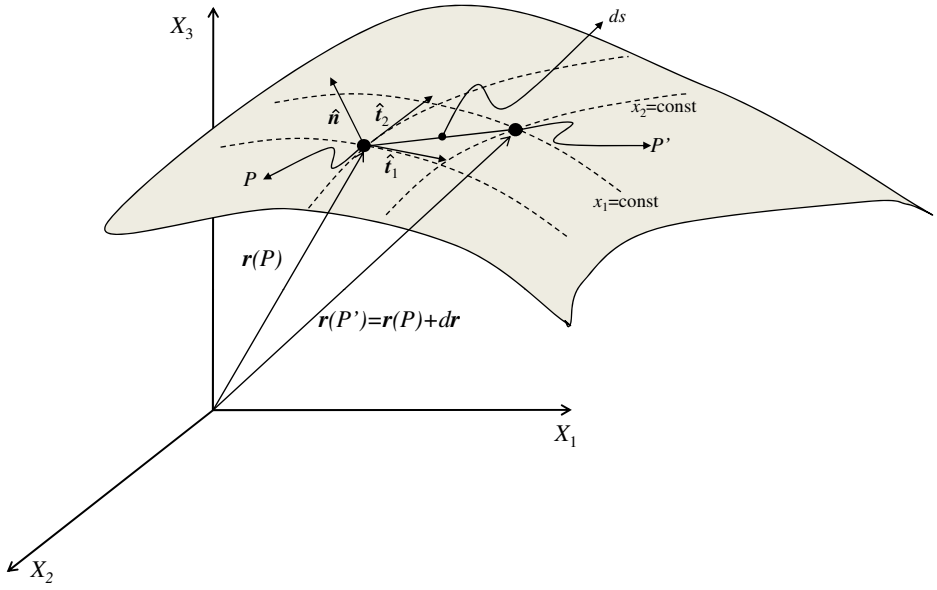

Figure 2.1: Geometry of the reference surface

be interpreted as a two-dimensional system of curvilinear coordinates lying on the surface. When each coordinate line, obtained by setting $x_1 = const$, is perpendicular point by point to the other coordinate line, obtained by setting $x_2 = const$, the curvilinear coordinates x_1 and x_2 will be referred to as orthogonal curvilinear coordinates. In the following only orthogonal coordinate system will be taken under consideration. Consider now a second point P' in the immediate vicinity of the point P. The increment of the radius vector $\mathbf{r}(x_1, x_2)$ from the point P to the generic point P' can be expressed as

$$d\mathbf{r}(x_1, x_2) = \frac{\partial \mathbf{r}(x_1, x_2)}{\partial x_1} dx_1 + \frac{\partial \mathbf{r}(x_1, x_2)}{\partial x_2} dx_2 \tag{2.2}$$

For convenience of notation special symbols will be use to indicate the partial derivative of the vector $\mathbf{r}(x_1, x_2)$ with respect to the curvilinear coordinates x_1 and x_2. The following notation will be adopted

$$\frac{\partial \mathbf{r}(x_1, x_2)}{\partial x_1} = A_1(x_1, x_2)\hat{\mathbf{t}}_1(x_1, x_2) \qquad \frac{\partial \mathbf{r}(x_1, x_2)}{\partial x_2} = A_2(x_1, x_2)\hat{\mathbf{t}}_2(x_1, x_2) \tag{2.3}$$

where $A_1(x_1, x_2)$ and $A_2(x_1, x_2)$ are scalar quantities equal to the modulus of the increment $d\mathbf{r}(x_1, x_2)$ along the x_1 and x_2 direction, while $\hat{\mathbf{t}}_1(x_1, x_2)$ and $\hat{\mathbf{t}}_2(x_1, x_2)$ are vectorial quantities representing the the unit vector tangent to the x_1 and x_2 coordinate axes, respectively. The scalar quantities $A_1(x_1, x_2)$ and $A_2(x_1, x_2)$ are usually referred to as Lamé's parameters. It should be noted that, due to the orthogonality of the curvilinear coordinates x_1 and x_2, the scalar product between $\hat{\mathbf{t}}_1(x_1, x_2)$ and $\hat{\mathbf{t}}_2(x_1, x_2)$ vanishes. Symbolically,

$$\hat{\mathbf{t}}_1(x_1, x_2) \cdot \hat{\mathbf{t}}_2(x_1, x_2) = 0 \tag{2.4}$$

It is useful to introduce a third unit vector forming an orthogonal triad with the two tangent vectors $\hat{\mathbf{t}}_1(x_1, x_2)$ and $\hat{\mathbf{t}}_2(x_1, x_2)$. This unit vector, representing the outward normal to the surface, can be defined through the cross product between $\hat{\mathbf{t}}_1(x_1, x_2)$ and $\hat{\mathbf{t}}_2(x_1, x_2)$. Symbolically,

$$\hat{\mathbf{n}}(x_1, x_2) = \hat{\mathbf{t}}_1(x_1, x_2) \wedge \hat{\mathbf{t}}_2(x_1, x_2) \tag{2.5}$$

Based on (2.5) the two following relations are verified

$$\hat{\mathbf{n}}(x_1, x_2) \cdot \hat{\mathbf{t}}_1(x_1, x_2) = 0 \qquad \hat{\mathbf{n}}(x_1, x_2) \cdot \hat{\mathbf{t}}_2(x_1, x_2) = 0 \tag{2.6}$$

For convenience of notation the explicit dependence on x_1 and x_2 of all the quantities of interest will be omitted in what follows. The infinitesimal arc length ds joining the points P and P' will be equal to the modulus of the increment $d\mathbf{r}$. For convenience of notation the quantity ds^2 will be taken into consideration. Using (2.4)

$$ds^2 = |d\mathbf{r}|^2 = d\mathbf{r} \cdot d\mathbf{r} = A_1^2 dx_1^2 + A_2^2 dx_2^2 \tag{2.7}$$

Equation (2.7) is usually referred to as the first fundamental quadratic form of a surface. The two principal curvatures of the surface will be referred to as κ_1 and κ_2. They can be defined as the inverse of the radius of curvature R_1 and R_2 along the two orthogonal coordinate directions x_1 and x_2. It can be proven that it is always possible to describe a smooth surface by means of a set of orthogonal coordinates by choosing those coordinates to coincide with the direction of the principal curvatures, or conversely, the curvatures along a set of orthogonal coordinates are the principal curvatures. Based on the Frenet's formulas

it can be seen that the curvature of the surface, along the x_1 direction, coincides with the modulus of the vector defined as the partial derivative of the unit vector $\hat{\mathbf{t}}_1$ with respect to s_1, where s_1 is the arc length along the x_1 direction. This vector has the same direction as the unit normal to the surface $\hat{\mathbf{n}}$, even if it has opposite orientation. Consequently the sign of its modulus must be changed. By setting $dx_2 = 0$ in (2.7) the relation becomes

$$ds_1 = A_1 dx_1 \tag{2.8}$$

Based on these arguments, the curvature κ_1 along the coordinate line x_1 can be obtained by taking the scalar product between the partial derivative of the unit vector $\hat{\mathbf{t}}_1$ with respect to infinitesimal arc length ds_1 and the normal unit vector with the sign changed. In symbols

$$\kappa_1 = \frac{1}{R_1} = -\hat{\mathbf{n}} \cdot \frac{\partial \hat{\mathbf{t}}_1}{\partial s_1} = -\frac{1}{A_1^2}\left(\hat{\mathbf{n}} \cdot \frac{\partial^2 \mathbf{r}}{\partial x_1^2}\right) \tag{2.9}$$

Similarly the curvature κ_2 along the x_2 coordinate line can be defined as

$$\kappa_2 = \frac{1}{R_2} = -\hat{\mathbf{n}} \cdot \frac{\partial \hat{\mathbf{t}}_2}{\partial s_2} = -\frac{1}{A_2^2}\left(\hat{\mathbf{n}} \cdot \frac{\partial^2 \mathbf{r}}{\partial x_2^2}\right) \tag{2.10}$$

Before closing this section it should be noted that the Lamé coefficients A_1 and A_2 and the principal radii of curvature R_1 and R_2 can not be chosen arbitrarily. In fact they are related by the so called Gauss-Codazzi equations. The compatibility equations are

$$\frac{\partial}{\partial x_2}\left[\frac{A_1}{R_1}\right] = \frac{1}{R_2}\frac{\partial A_1}{\partial x_2} \qquad \frac{\partial}{\partial x_1}\left[\frac{A_2}{R_2}\right] = \frac{1}{R_1}\frac{\partial A_2}{\partial x_1} \tag{2.11}$$

$$\frac{\partial}{\partial x_2}\left[\frac{1}{R_2}\frac{\partial A_1}{\partial x_2}\right] + \frac{\partial}{\partial x_1}\left[\frac{1}{R_1}\frac{\partial A_2}{\partial x_1}\right] = -\frac{A_1 A_2}{R_1 R_2} \tag{2.12}$$

2.3 Nomenclature and basic assumptions

The following nomenclature will be adopted.

ϵ_{11} ► *elongation strain along the x_1-direction*

ϵ_{22} ► *elongation strain along the x_2-direction*

ϵ_{33} ▶ *elongation strain along the x_3-direction*

ϵ_{12} ▶ *shear strain in the x_1-x_2 plane*

ϵ_{13} ▶ *shear strain in the x_1-x_3 plane*

ϵ_{23} ▶ *shear strain in the x_2-x_3 plane*

ϵ^0_{11} ▶ *elongation strain on the reference surface along the x_1-direction*

ϵ^0_{22} ▶ *elongation strain on the reference surface along the x_2-direction*

ϵ^0_{12} ▶ *shear strain on the reference surface*

κ^0_{11} ▶ *change in curvature on the reference surface along the x_1-direction*

κ^0_{22} ▶ *change in curvature on the reference surface along the x_2-direction*

κ^0_{12} ▶ *change in twist curvature on the reference surface*

u_1 ▶ *tangential displacement along the x_1-direction*

u_2 ▶ *tangential displacement along the x_2-direction*

u_3 ▶ *normal displacement*

u^0_1 ▶ *tangential displacement of the reference surface along the x_1-direction*

u^0_2 ▶ *tangential displacement of the reference surface along the x_2-direction*

u^0_3 ▶ *normal displacement of the reference surface*

τ_{11} ▶ *normal stress on the x_1-plane in the x_1-direction*

τ_{22} ▶ *normal stress on the x_2-plane in the x_2-direction*

τ_{33} ▶ *normal stress on the x_3-plane in the x_3-direction*

τ_{12} ▶ *normal stress on the x_1-plane in the x_2-direction*

τ_{13} ▶ *normal stress on the x_1-plane in the x_3-direction*

τ_{23} ▶ *normal stress on the x_2-plane in the x_3-direction*

N^0_{11} ▶ *force resultant on the reference surface along the x_1-direction*

N^0_{22} ▶ *force resultant on the reference surface along the x_2-direction*

N_{12}^0 ► *force resultant on the reference surface in the x_1-x_2 plane*

M_{11}^0 ► *moment resultant on the reference surface along the x_1-direction*

M_{22}^0 ► *moment resultant on the reference surface along the x_2-direction*

M_{12}^0 ► *moment resultant on the reference surface in the x_1-x_2 plane*

The theory of quasi-shallow shells can be derived when appropriate assumptions are postulated. Consequently, it can be successfully applicable only when these fundamental hypotheses are verified. The fundamental assumptions of this theory are listed below:

1. The maximum ratio between the thickness and the radius of curvature is negligible compared with unity.

2. Straight lines perpendicular to the reference surface in the undeformed configuration remain straight and perpendicular to the reference surface in the deformed configuration. Moreover their length is unchanged.

3. The magnitudes of the tangential displacement fields u_1^0 and u_2^0 are much smaller than the thickness of the shell, while the magnitude of the transverse displacement field u_3^0 is comparable with the thickness of the shell.

4. The transverse normal stress τ_{33} is small enough to be negligible.

2.4 Kinematic relations

Under the hypotheses stated in section 2.3 the inplane strains can be expressed as a function of the inplane displacements as follows

$$\epsilon_{11}^0 = \frac{1}{A_1}\frac{\partial u_1^0}{\partial x_1} + \frac{1}{A_1 A_2}\frac{\partial A_1}{\partial x_2}u_2^0 + \frac{u_3^0}{R_1} + \frac{1}{2}\left(\frac{1}{A_1}\frac{\partial u_3^0}{\partial x_1}\right)^2 \tag{2.13a}$$

$$\epsilon_{22}^0 = \frac{1}{A_2}\frac{\partial u_2^0}{\partial x_2} + \frac{1}{A_1 A_2}\frac{\partial A_2}{\partial x_1}u_1^0 + \frac{u_3^0}{R_2} + \frac{1}{2}\left(\frac{1}{A_2}\frac{\partial u_3^0}{\partial x_2}\right)^2 \tag{2.13b}$$

$$\epsilon_{12}^0 = \frac{A_1}{A_2}\frac{\partial}{\partial x_2}\left[\frac{u_1^0}{A_1}\right] + \frac{A_2}{A_1}\frac{\partial}{\partial x_1}\left[\frac{u_2^0}{A_2}\right] + \left(\frac{1}{A_1}\frac{\partial u_3^0}{\partial x_1}\right)\left(\frac{1}{A_2}\frac{\partial u_3^0}{\partial x_2}\right) \tag{2.13c}$$

By virtue of the assumption 2 in the previous subsection, the displacements of a point at a distance x_3 from the reference surface can be expressed as

$$u_1 = u_1^0 - x_3 \left(\frac{1}{A_1} \frac{\partial u_3^0}{\partial x_1} \right) \tag{2.14a}$$

$$u_2 = u_2^0 - x_3 \left(\frac{1}{A_2} \frac{\partial u_3^0}{\partial x_2} \right) \tag{2.14b}$$

$$u_3 = u_3^0 \tag{2.14c}$$

Replacing the quantities u_1^0, u_2^0 and u_3^0 of (2.13) with the quantities u_1, u_2 and u_3 given in (2.14), the relations between the strains at a distance x_3 from the reference surface to the displacements of the reference surface can be found. They are

$$\epsilon_{11} = \epsilon_{11}^0 + x_3 \kappa_{11}^0 \tag{2.15a}$$

$$\epsilon_{22} = \epsilon_{22}^0 + x_3 \kappa_{22}^0 \tag{2.15b}$$

$$\epsilon_{12} = \epsilon_{12}^0 + x_3 \kappa_{12}^0 \tag{2.15c}$$

where

$$\kappa_{11}^0 = - \frac{1}{A_1} \frac{\partial}{\partial x_1} \left[\frac{1}{A_1} \frac{\partial u_3^0}{\partial x_1} \right] - \frac{1}{A_1 A_2} \frac{\partial A_1}{\partial x_2} \left(\frac{1}{A_2} \frac{\partial u_3^0}{\partial x_2} \right) \tag{2.16a}$$

$$\kappa_{22}^0 = - \frac{1}{A_2} \frac{\partial}{\partial x_2} \left[\frac{1}{A_2} \frac{\partial u_3^0}{\partial x_2} \right] - \frac{1}{A_1 A_2} \frac{\partial A_2}{\partial x_1} \left(\frac{1}{A_1} \frac{\partial u_3^0}{\partial x_1} \right) \tag{2.16b}$$

$$\kappa_{12}^0 = - \frac{2}{A_1 A_2} \frac{\partial^2 u_3^0}{\partial x_1 \partial x_2} + \frac{1}{A_1^2 A_2} \frac{\partial A_1}{\partial x_2} \frac{\partial u_3^0}{\partial x_1} + \frac{1}{A_1 A_2^2} \frac{\partial A_2}{\partial x_1} \frac{\partial u_3^0}{\partial x_2} \tag{2.16c}$$

It should be noted that in this derivation the changes in the geometry along the normal direction to the reference surfaces are completely neglected, i.e., the Lamé coefficient and the radii of curvature are assumed to be independent of the x_3-coordinate. This assumption is a consequence of the hypothesis (1) stated in the previous subsection.

2.5 Constitutive equations

It will be assumed a linear constitutive behavior as stated by the Hooke's law is applicable. By virtue of hypothesis (4), the point-wise constitutive equation of an anisotropic material can be expressed as follows

$$\begin{pmatrix} \tau_{11} \\ \tau_{22} \\ \tau_{12} \end{pmatrix} = \begin{pmatrix} Q_{11} & Q_{12} & Q_{13} \\ Q_{21} & Q_{22} & Q_{23} \\ Q_{31} & Q_{32} & Q_{33} \end{pmatrix} \begin{pmatrix} \epsilon_{11} \\ \epsilon_{22} \\ \epsilon_{12} \end{pmatrix} \tag{2.17}$$

where the Qs are referred to as the reduced stiffnesses. It is often convenient to give an alternative form of the constitutive equation that involves only quantities related to the midsurface. This can be done by defining the system of force and moment resultants of the stresses integrated through the thickness h. These forces and moments are defined as follows

$$\begin{pmatrix} N_{11}^0 \\ N_{22}^0 \\ N_{12}^0 \end{pmatrix} = \int_{-\frac{h}{2}}^{\frac{h}{2}} \begin{pmatrix} \tau_{11} \\ \tau_{22} \\ \tau_{12} \end{pmatrix} dx_3 \qquad \begin{pmatrix} M_{11}^0 \\ M_{22}^0 \\ M_{12}^0 \end{pmatrix} = \int_{-\frac{h}{2}}^{\frac{h}{2}} \begin{pmatrix} \tau_{11} \\ \tau_{22} \\ \tau_{12} \end{pmatrix} x_3 dx_3 \tag{2.18}$$

Substituting (2.15) in (2.17), the result in (2.18), and performing integration through the thickness the alternative form of the constitutive equation can be obtained. The alternative form is given in (2.19).

$$\left(\begin{array}{c} N_{11}^0 \\ N_{22}^0 \\ N_{12}^0 \\ \hline M_{11}^0 \\ M_{22}^0 \\ M_{12}^0 \end{array}\right) = \left(\begin{array}{ccc|ccc} A_{11} & A_{12} & A_{13} & B_{11} & B_{12} & B_{13} \\ A_{21} & A_{22} & A_{23} & B_{21} & B_{22} & B_{23} \\ A_{31} & A_{32} & A_{33} & B_{31} & B_{32} & B_{33} \\ \hline B_{11} & B_{12} & B_{13} & D_{11} & D_{12} & D_{13} \\ B_{21} & B_{22} & B_{23} & D_{21} & D_{22} & D_{23} \\ B_{31} & B_{32} & B_{33} & D_{31} & D_{32} & D_{33} \end{array}\right) \left(\begin{array}{c} \epsilon_{11}^0 \\ \epsilon_{22}^0 \\ \epsilon_{12}^0 \\ \hline \kappa_{11}^0 \\ \kappa_{22}^0 \\ \kappa_{12}^0 \end{array}\right) \tag{2.19}$$

where

$$A_{ij} = \int_{-\frac{h}{2}}^{\frac{h}{2}} Q_{ij} dx_3 \quad B_{ij} = \int_{-\frac{h}{2}}^{\frac{h}{2}} Q_{ij} x_3 dx_3 \quad D_{ij} = \int_{-\frac{h}{2}}^{\frac{h}{2}} Q_{ij} x_3^2 dx_3 \quad i,j = 1,2,3 \tag{2.20}$$

The matrix relating the inplane force and moment resultants to the inplane strains and curvatures is usually referred to as the classical laminate matrix, or the ABD matrix. The latter name highlights the internal structure of the constitutive matrix. In fact, it can be thought of as a block matrix having three fundamental blocks representing three different kinds of constitutive behavior. The A matrix takes into account pure extensional behavior, the D matrix takes into account pure bending behavior, while the B matrix takes into account the coupling between extensional and bending behavior. In general all the entries of the matrix are nontrivial. There exist special cases for which some of the entries in each of the A, B, and D matrices vanish. For example, if the shell has material properties that are symmetric with respect to the reference surface, all entries in the B matrix vanish. Other possible simplifications of the constitutive relation can be obtained considering materials having particular symmetries. Very important cases of materials having special symmetries are the orthotropic and the isotropic materials. The form assumed by the general plane-stress costitutive equations (2.17) for these two classes of material will be given in the two following subsections.

2.5.1 Orthotropic materials

A material is said to be orthotropic when it has different properties in orthogonal directions. When the principal directions of the material are chosen to be coincident with the principal directions of the shell, constitutive equations (2.17) simplify. In fact, in this situation both the reduced stiffnesses Q_{13} and Q_{23} vanish, reducing the number of independent constants of the material from six to four. Sometimes, in order to model an orthotropic material in state of plane-stress, it is convenient to introduce the five alternative constitutive constants E_1, E_2, ν_{12}, ν_{21}, and G_{12}, usually referred to as engineering properties. Only four of these constants are independent because $\nu_{21}E_1 = \nu_{12}E_2$. The reduced stiffnesses and the engineering properties are related by the following equations:

$$Q_{11} = \frac{E_1}{1 - \nu_{12}\nu_{21}} \tag{2.21a}$$

$$Q_{22} = \frac{E_2}{1 - \nu_{12}\nu_{21}} \tag{2.21b}$$

$$Q_{12} = \frac{\nu_{21} E_1}{1 - \nu_{12}\nu_{21}} \tag{2.21c}$$

$$Q_{33} = G_{12} \tag{2.21d}$$

2.5.2 Isotropic materials

A material is said to be isotropic when it has the same properties in all directions. In this situation the constitutive equations (2.17) simplify even more. In fact, in this situation both the reduced stiffnesses Q_{13} and Q_{23} also vanish. Moreover, $Q_{11} = Q_{22}$ and $Q_{33} = (Q_{11} - Q_{12})/2$, reducing the number of independent constants of the material from six to two. Sometimes, in order to model an isotropic material in a state of plane-stress it is convenient to introduce the two alternative constitutive constants E and ν, usully referred to as engineering properties. The reduced stiffnesses and the engineering properties are related by the following equations:

$$Q_{11} = Q_{22} = \frac{E}{1 - \nu^2} \tag{2.22a}$$

$$Q_{12} = \frac{\nu E}{1 - \nu^2} \tag{2.22b}$$

$$Q_{33} = \frac{1}{2}(Q_{11} - Q_{12}) = \frac{E}{2(1 + \nu)} \tag{2.22c}$$

2.6 Governing equilibrium and stability equations

Once the kinematic and the constitutive equations are specified, a convenient way to derive the governing equations is to postulate the total potential energy of the system and then use a variational approach. This technique has the invaluable advantage to automatically produce a set of boundary conditions consistent with the specified assumptions. Due to the basic assumption 2, the shear strains through the thickness ϵ_{13} and ϵ_{23} are zero and consequently, the corresponding stresses τ_{13} and τ_{23} can not be determined by means of the

constitutive relations. By the way, when considering a Newtonian rather then an energy approach, those stresses can not be ignored because they are needed for the static equilibrium. From the energy perspective, another way to express this concept is to say that the shear stresses τ_{13} and τ_{23} contribute nothing to the total potential energy of the shell. Based on these arguments, it should be clear that the derivation of the boundary conditions consistent with the theory of shallow shells is not trivial at all. As said before, the use of a variational method automatically solves this problem. In the following all the kinematic and the static quantities will be referred to the reference surface, so the superscript "0" will be omitted for brevity of notation.

Assuming that the whole reference surface is spanned when $x_1 \in [x_1^-, x_1^+]$ and $x_2 \in [x_2^-, x_2^+]$,the strain energy U of the shell can be expressed as follows

$$U = \frac{1}{2}\int_{x_1^-}^{x_1^+}\int_{x_2^-}^{x_2^+}(N_{11}\epsilon_{11} + N_{22}\epsilon_{22} + N_{12}\epsilon_{12} + M_{11}\kappa_{11} + M_{22}\kappa_{22} + M_{12}\kappa_{12})A_1A_2dx_1dx_2 \quad (2.23)$$

Consider two opposite compressive forces acting on the boundary in the x_1 direction. More precisely, a force N_{11}^+ is applied at $x_2 = x_2^+$ and a force N_{11}^- is applied at $x_2 = x_2^-$. Under these circumstances the work W done by external forces can be expressed as follows

$$W = \int_{x_2^-}^{x_2^+}\left(-N_{11}^+u_1\Big|_{x_2=x_2^+} + N_{11}^-u_1\Big|_{x_2=x_2^-}\right)A_1dx_2 \quad (2.24)$$

The total potential energy Π of the shell can be expressed as follows

$$\Pi = U - W \quad (2.25)$$

Substituting (2.13), (2.16), and (2.19) in (2.23), and (2.23) and (2.24) in (2.25), and taking the first variation of Π, the Euler-Lagrange equations in terms of the force and moment resultants and the displacements can be derived together with the consistent boundary conditions. The Euler-Lagrange equations, which constitute equilibrium equations for the shell, in their most fundamental form are given by

$$\frac{\partial}{\partial x_1}[A_2N_{11}] + \frac{\partial}{\partial x_2}[A_1N_{12}] - \frac{\partial A_2}{\partial x_1}N_{22} + \frac{\partial A_1}{\partial x_2}N_{12} = 0 \quad (2.26a)$$

$$\frac{\partial}{\partial x_2}[A_1 N_{22}] + \frac{\partial}{\partial x_1}[A_2 N_{12}] - \frac{\partial A_1}{\partial x_2} N_{11} + \frac{\partial A_2}{\partial x_1} N_{12} = 0 \tag{2.26b}$$

$$\frac{\partial}{\partial x_1}\left[\frac{1}{A_1}\frac{\partial}{\partial x_1}[A_2 M_{11}]\right] + \frac{\partial}{\partial x_2}\left[\frac{1}{A_2}\frac{\partial}{\partial x_2}[A_1 M_{22}]\right] - \frac{\partial}{\partial x_2}\left[\frac{1}{A_2}\frac{\partial A_1}{\partial x_2} M_{11}\right] - \tag{2.26c}$$
$$\frac{\partial}{\partial x_1}\left[\frac{1}{A_1}\frac{\partial A_2}{\partial x_1} M_{22}\right] + 2\left(\frac{\partial^2 M_{12}}{\partial x_1 \partial x_2} + \frac{\partial}{\partial x_1}\left[\frac{1}{A_1}\frac{\partial A_1}{\partial x_2} M_{12}\right] + \frac{\partial}{\partial x_2}\left[\frac{1}{A_2}\frac{\partial A_2}{\partial x_1} M_{12}\right]\right) +$$
$$\frac{\partial}{\partial x_1}\left[N_{11}\frac{A_2}{A_1}\frac{\partial u_3}{\partial x_1} + N_{12}\frac{\partial u_3}{\partial x_2}\right] + \frac{\partial}{\partial x_2}\left[N_{22}\frac{\partial u_3}{\partial x_2} + N_{12}\frac{A_1}{A_2}\frac{\partial u_3}{\partial x_1}\right] - A_1 A_2\left(\frac{N_{11}}{R_1} + \frac{N_{22}}{R_2}\right) = 0$$

The consistent boundary conditions are different for each edge of the shell. Specifically, the boundary conditions to be prescribed at $x_1 = x_1^+$ are

$$\begin{array}{llll} \text{either} & N_{11} = -N_{11}^+ & \text{or} & \delta u_1 \quad \text{specified} \\ \text{either} & N_{12} = 0 & \text{or} & \delta u_2 \quad \text{specified} \\ \text{either} & N_{13} = 0 & \text{or} & \delta u_3 \quad \text{specified} \\ \text{either} & M_{11} = 0 & \text{or} & \delta\left(\frac{\partial u_3}{\partial x_1}\right) \quad \text{specified} \end{array} \tag{2.27}$$

The boundary conditions to be prescribed at $x_1 = x_1^-$ are

$$\begin{array}{llll} \text{either} & N_{11} = -N_{11}^- & \text{or} & \delta u_2 \quad \text{specified} \\ \text{either} & N_{12} = 0 & \text{or} & \delta u_1 \quad \text{specified} \\ \text{either} & N_{13} = 0 & \text{or} & \delta u_3 \quad \text{specified} \\ \text{either} & M_{11} = 0 & \text{or} & \delta\left(\frac{\partial u_3}{\partial x_1}\right) \quad \text{specified} \end{array} \tag{2.28}$$

The boundary conditions to be prescribed at $x_2 = x_2^-$ and $x_2 = x_2^+$ are

$$\begin{array}{llll} \text{either} & N_{22} = 0 & \text{or} & \delta u_1 \quad \text{specified} \\ \text{either} & N_{12} = 0 & \text{or} & \delta u_2 \quad \text{specified} \\ \text{either} & N_{23} = 0 & \text{or} & \delta u_3 \quad \text{specified} \\ \text{either} & M_{22} = 0 & \text{or} & \delta\left(\frac{\partial u_3}{\partial x_2}\right) \quad \text{specified} \end{array} \tag{2.29}$$

where

$$N_{13} = \frac{1}{A_1 A_2}\left(\frac{\partial A_2}{\partial x_1} M_{11} + \frac{\partial A_1}{\partial x_2} M_{12}\right) + \frac{1}{A_1}\left(\frac{\partial M_{11}}{\partial x_1} + N_{11}\frac{\partial u_3}{\partial x_1}\right) + \frac{1}{A_2}\left(2\frac{\partial M_{12}}{\partial x_2} + N_{12}\frac{\partial u_3}{\partial x_2}\right) \tag{2.30a}$$

$$N_{23} = \frac{1}{A_1 A_2}\left(\frac{\partial A_1}{\partial x_2}M_{22} + \frac{\partial A_2}{\partial x_1}M_{12}\right) + \frac{1}{A_2}\left(\frac{\partial M_{22}}{\partial x_2} + N_{22}\frac{\partial u_3}{\partial x_2}\right) + \frac{1}{A_1}\left(2\frac{\partial M_{12}}{\partial x_1} + N_{12}\frac{\partial u_3}{\partial x_1}\right) \tag{2.30b}$$

Finally, the boundary condition to be prescribed at each corner is

$$\text{either} \quad M_{12} = 0 \quad \text{or} \quad \delta u_3 \quad \text{specified} \tag{2.31}$$

The boundary conditions given above are valid for a shell open with respect to both directions x_1 and x_2. If a shell closed in the x_2 direction is considered, the set of boundary conditions (2.29) must be replaced with a set of conditions stating the continuity of kinematic fields. It should be remarked once again that while the force quantities doing work on the transversal displacement u_3 are not determinable through the constitutive relation, these quantities, indicated above with N_{13} and N_{23}, are related to the resultant force and moment resultants through the the nontrivial expressions (2.30). Equation (2.26) represents the geometrically nonlinear equilibrium equations of Donnell-Mushtari-Vlasov shell theory applied to cylinders. The buckling equations for the Donnell-Mushtari-Vlasov theory can be derived by means of the Trefftz criterion, i.e., by imposing the stationarity of the second variation of the total potential energy Π. The following buckling equations are obtained:

$$\frac{\partial}{\partial x_1}[A_2\delta N_{11}] + \frac{\partial}{\partial x_2}[A_1\delta N_{12}] - \frac{\partial A_2}{\partial x_1}\delta N_{22} + \frac{\partial A_1}{\partial x_2}\delta N_{12} = 0 \tag{2.32a}$$

$$\frac{\partial}{\partial x_2}[A_1\delta N_{22}] + \frac{\partial}{\partial x_1}[A_2\delta N_{12}] - \frac{\partial A_1}{\partial x_2}\delta N_{11} + \frac{\partial A_2}{\partial x_1}\delta N_{12} = 0 \tag{2.32b}$$

$$\begin{aligned}
&\frac{\partial}{\partial x_1}\left[\frac{1}{A_1}\frac{\partial}{\partial x_1}[A_2\delta M_{11}]\right] + \frac{\partial}{\partial x_2}\left[\frac{1}{A_2}\frac{\partial}{\partial x_2}[A_1\delta M_{22}]\right] - \frac{\partial}{\partial x_2}\left[\frac{1}{A_2}\frac{\partial A_1}{\partial x_2}\delta M_{11}\right] - \\
&\frac{\partial}{\partial x_1}\left[\frac{1}{A_1}\frac{\partial A_2}{\partial x_1}\delta M_{22}\right] + 2\left(\frac{\partial^2 \delta M_{12}}{\partial x_1 \partial x_2} + \frac{\partial}{\partial x_1}\left[\frac{1}{A_1}\frac{\partial A_1}{\partial x_2}\delta M_{12}\right] + \frac{\partial}{\partial x_2}\left[\frac{1}{A_2}\frac{\partial A_2}{\partial x_1}\delta M_{12}\right]\right) + \\
&\frac{\partial}{\partial x_1}\left[\delta N_{11}\frac{A_2}{A_1}\frac{\partial u_3}{\partial x_1} + \delta N_{12}\frac{\partial u_3}{\partial x_2} + N_{11}\frac{A_2}{A_1}\frac{\partial}{\partial x_1}[\delta u_3] + N_{12}\frac{\partial}{\partial x_2}[\delta u_3]\right] + \\
&\frac{\partial}{\partial x_2}\left[\delta N_{22}\frac{\partial u_3}{\partial x_2} + \delta N_{12}\frac{A_1}{A_2}\frac{\partial u_3}{\partial x_1} + N_{22}\frac{\partial}{\partial x_2}[\delta u_3] + N_{12}\frac{A_1}{A_2}\frac{\partial}{\partial x_1}[\delta u_3]\right] - \\
&A_1 A_2\left(\frac{\delta N_{11}}{R_1} + \frac{\delta N_{22}}{R_2}\right) = 0
\end{aligned} \tag{2.32c}$$

where the buckling variables are denoted with a δ. In (2.32) the buckling variables and

the prebuckling variables are coupled. More precisely, it can be seen that the prebuckling rotations are involved in the stability equation. The boundary conditions to be prescribed at $x_1 = x_1^-$ and $x_1 = x_1^+$ are

$$\begin{array}{llll} \text{either} & \delta N_{11} = 0 & \text{or} & \delta^2 u_2 \quad \text{specified} \\ \text{either} & \delta N_{12} = 0 & \text{or} & \delta^2 u_1 \quad \text{specified} \\ \text{either} & \delta N_{13} = 0 & \text{or} & \delta^2 u_3 \quad \text{specified} \\ \text{either} & \delta M_{11} = 0 & \text{or} & \delta^2 \left(\frac{\partial u_3}{\partial x_2} \right) \quad \text{specified} \end{array} \tag{2.33}$$

The boundary conditions to be prescribed at $x_2 = x_2^-$ and $x_2 = x_2^+$ are

$$\begin{array}{llll} \text{either} & \delta N_{22} = 0 & \text{or} & \delta^2 u_1 \quad \text{specified} \\ \text{either} & \delta N_{12} = 0 & \text{or} & \delta^2 u_2 \quad \text{specified} \\ \text{either} & \delta N_{23} = 0 & \text{or} & \delta^2 u_3 \quad \text{specified} \\ \text{either} & \delta M_{22} = 0 & \text{or} & \delta^2 \left(\frac{\partial u_3}{\partial x_2} \right) \quad \text{specified} \end{array} \tag{2.34}$$

Finally, the boundary condition to be prescribed at each corner is

$$\text{either} \quad \delta M_{12} = 0 \quad \text{or} \quad \delta^2 u_3 \quad \text{specified} \tag{2.35}$$

These basic relations and equations will be used in the subsequent chapters dealing with bucklin of cylindrical shells. The next chapter addresses orthotropic circular cylinders.

Chapter 3

Axial buckling behavior of orthotropic circular cylinders

3.1 Introduction

In this Chapter the exact solution of the classical axial buckling stress equation for a circular orthotropic cylinder will be given and an expression for the critical axial stress resultant will be derived as a function of the ABD matrix coefficients and the axial and circumferential wave numbers m and n. Then, assuming the orthotropic material to be homogeneous through the thickness, an expression for the critical axial stress as a function of the Q matrix coefficients and the axial and circumferential wave numbers m and n will be derived. Starting from this expression, the axial and the circumferential wave numbers will be treated as real variables and, using calculus, the analytical minimum of the function will be evaluated. Following this approach a closed form for a lower bound for the axial buckling stress will be derived. A similar procedure has been used in [61] for an orthotropic cylinder and in [62] for an isotropic cylinder. Both those authors partially obtained the same results. The main advantage of the derivation presented in this Chapter must be found in the notation used that allows a general formulation of the problem and gives a simple procedure to determine the pattern of deformation based only on the knowledge of the constitutive properties of the orthotropic material, allowing a more complete understanding of the buckling behaviour

of an orthotropic circular cylinder based on a novel useful mechanical interpretation of the found results. Moreover, the proposed approach furnishes a mathematical explanation of the high density of close eigenvalues associated with different buckled shapes for the case of isotropic circular cylinder.

3.2 Exact solution of the classical buckling equations for a circular cylindrical shell

In this section an analytical solution of the buckling equation (2.32) will be evaluated under several specific assumptions. More precisely, it will be assumed that the applied axial prebuckling load is distributed uniformly axially and circumferentially, and prebuckling rotations can be ignored. The stability equations obtained under these assumptions are usually referred to as classical buckling equations. The exact solution of the classical buckling equations will be presented for an axially-loaded simply-supported circular cylindrical shell made of an orthotropic material. The geometry of a circular cylindrical shell of radius R and length L is specified by the following relations based on the definitions of the previous Chapter:

$$x_1 = x \quad x_2 = \theta \qquad A_1 = 1 \quad A_2 = R \qquad \frac{1}{R_1} = 0 \quad \frac{1}{R_2} = \frac{1}{R} \tag{3.1}$$

Substituting (3.1) in (2.26) and assuming N_{xx}^{+} to be the prebuckling axial stress resultant, resulting from the axial prebuckling load, the classical buckling equations become

$$\frac{\partial}{\partial x}[\delta N_{xx}] + \frac{1}{R}\frac{\partial}{\partial \theta}[\delta N_{x\theta}] = 0 \tag{3.2a}$$

$$\frac{\partial}{\partial x}[\delta N_{x\theta}] + \frac{1}{R}\frac{\partial}{\partial \theta}[\delta N_{\theta\theta}] = 0 \tag{3.2b}$$

$$\frac{\partial^2}{\partial x^2}[\delta M_{xx}] + \frac{2}{R}\frac{\partial^2}{\partial x \partial \theta}[\delta M_{x\theta}] + \frac{1}{R^2}\frac{\partial^2}{\partial \theta^2}[\delta M_{\theta\theta}] - \frac{\delta N_{\theta\theta}}{R} + N_{xx}^{+}\frac{\partial^2}{\partial x^2}[\delta u_3^0] = 0 \tag{3.2c}$$

In order to enforce the simply supported boundary conditions, the following relation must be fulfilled at both $x = 0$ and $x = L$

$$\delta N_{xx} = 0 \qquad \delta u_2^0 = 0 \qquad \delta M_{xx} = 0 \qquad \delta u_3^0 = 0 \tag{3.3}$$

The material will be assumed to be orthotropic and symmetric with respect to the mid-surface, consequently, the only nontrivial elements of its ABD matrix are A_{11}, A_{22}, A_{12}, A_{33}, D_{11}, D_{22}, D_{12} and D_{33}. In virtue of the fact that $A_{13} = A_{23} = B_{13} = B_{23} = D_{13} = D_{23} = 0$ it is possible to evaluate the exact solution of the differential eigenvalue problem stated by (3.2) and (3.3) by assuming the displacement fields u_1^0, u_2^0 and u_3^0 in the following form:

$$u_1^0 = U_1 \cos\left(\frac{\pi m}{L}x\right)\cos(n\theta) \tag{3.4a}$$

$$u_2^0 = U_2 \sin\left(\frac{\pi m}{L}x\right)\sin(n\theta) \tag{3.4b}$$

$$u_3^0 = U_3 \sin\left(\frac{\pi m}{L}x\right)\cos(n\theta) \tag{3.4c}$$

where U_1, U_2, and U_3 are amplitude coefficients to be determined. It should be noted that as usual in eigenvalue problems only the ratio between these coefficients can be determined. Equations (3.2) can be expressed as functions of the displacement amplitudes U_1, U_2, and U_3 by chain substitution of the constitutive equations through the thickness (2.19), the strain-displacement relations (2.13), and the assumed displacements (3.4). The results of the substitutions lead to a linear system of three homogeneous equations in the three unknowns U_1, U_2, and U_3. In order to obtain a nontrivial solution the coefficient matrix must be singular, i.e., its determinant must vanish. It should be noted that the coefficient matrix depends on the axial load N_{xx}^+, so the critical load can be defined as the lowest value of N_{xx}^+ that renders the coefficient matrix singular. Performing the needed calculation, the critical load can be found to be

$$N_{cr} = \left(N_{xx}^+\right)_{cr} = \min_{m,n}\left\{\left(\frac{L}{\pi m}\right)^2\left(T_{33} + \frac{2T_{12}T_{13}T_{23} - T_{11}T_{23}^2 - T_{22}T_{13}^2}{T_{11}T_{22} - T_{12}^2}\right)\right\} \tag{3.5}$$

where T_{ij} $i, j = 1, 2, 3$ are the elements of the coefficient matrix of the linear system. They are defined as

$$T_{11} = A_{11}\left(\frac{\pi m}{L}\right)^2 + A_{33}\left(\frac{n}{R}\right)^2 \tag{3.6a}$$

$$T_{12} = (A_{12} + A_{33})\left(\frac{\pi m}{L}\right)\left(\frac{n}{R}\right) \tag{3.6b}$$

$$T_{13} = \frac{A_{12}}{R}\left(\frac{\pi m}{L}\right) \tag{3.6c}$$

$$T_{22} = A_{33}\left(\frac{\pi m}{L}\right)^2 + A_{22}\left(\frac{n}{R}\right)^2 \tag{3.6d}$$

$$T_{23} = \frac{A_{22}}{R}\left(\frac{n}{R}\right) \tag{3.6e}$$

$$T_{33} = D_{11}\left(\frac{\pi m}{L}\right)^4 + (2D_{12} + 4D_{33})\left(\frac{\pi m}{L}\right)^2\left(\frac{n}{R}\right)^2 + D_{22}\left(\frac{n}{R}\right)^4 + A_{22}\left(\frac{1}{R}\right)^2 \tag{3.6f}$$

3.3 Nondimensionalization and notation

In this section the wave numbers m and n will be assumed to be real in order to perform analytical minimization of (3.5). First of all, a suitable notation will be introduced in order to make (3.5) and (3.6) more convenient for analytical manipulation. To that end, the following nondimensional parameters will be introduced:

$$\eta = \frac{h}{R} \qquad \lambda = \frac{\pi R}{L} \tag{3.7}$$

The parameter η measures the thinness of the shell, while the parameter λ measures the aspect ratio of the cylinder, i.e., the ratio between the half-circumference and the length. Of course η and λ must be both positive. When the orthotropic material is homogeneous through the thickness h, the A and the D coefficients in (3.5) can be expressed in terms of the reduced stiffnesses by means of the following simple equations

$$A_{ij} = hQ_{ij} \qquad D_{ij} = \frac{h^3}{12}Q_{ij} \qquad i,j = 1,2,3 \tag{3.8}$$

Moreover, in this case the critical stress can be exactly found by dividing the critical axial stress resultant by the shell thickness (i.e., $\sigma_{cr} = N_{cr}/h$). Substituting (3.8) in (3.5) and dividing by h the following expression is found

$$\sigma_{cr} = \frac{N_{cr}}{h} = \min_{m,n}\left\{\frac{1}{m^2\lambda^2}\left(t_{33} + \frac{2t_{12}t_{13}t_{23} - t_{11}t_{23}^2 - t_{22}t_{13}^2}{t_{11}t_{22} - t_{12}^2}\right)\right\} \tag{3.9}$$

where

$$t_{11} = T_{11}R^2 = Q_{11}\lambda^2 m^2 + Q_{33}n^2 \tag{3.10a}$$

$$t_{12} = t_{21} = T_{12}R^2 = (Q_{12} + Q_{33})\,\lambda mn \tag{3.10b}$$

$$t_{13} = t_{31} = T_{13}R^2 = Q_{12}\lambda m \tag{3.10c}$$

$$t_{22} = T_{22}R^2 = Q_{33}\lambda^2 m^2 + Q_{22}n^2 \tag{3.10d}$$

$$t_{23} = t_{32} = T_{23}R^2 = Q_{22}n \tag{3.10e}$$

$$t_{33} = T_{33}R^2 = \frac{\eta^2}{12}\left(Q_{11}\lambda^4 m^4 + 2\,(Q_{12} + 2Q_{33})\,\lambda^2 m^2 n^2 + Q_{22}n^4\right) + Q_{22} \tag{3.10f}$$

For convenience, an isotropic material having constitutive constants equal to the geometric mean of the constitutive constants of the given orthotropic material will be introduced as follows:

$$E = \sqrt{E_1 E_2} \qquad \nu = \sqrt{\nu_{12}\nu_{21}} \qquad G = \frac{E}{2(1+\nu)} = \frac{\sqrt{E_1 E_2}}{2(1+\sqrt{\nu_{12}\nu_{21}})} \tag{3.11}$$

An isotropic material defined through the constitutive constants (3.11) will be referred to in the following as the geometric mean isotropic (GMI) material associated with the given orthotropic material. The essential requirement for the stiffness matrix to be positive definite produces the following constraint equation for the constitutive constant of the GMI material:

$$E > 0 \qquad \nu^2 - 1 < 0 \qquad G > 0 \tag{3.12}$$

Moreover, two nondimensional parameters will be introduced:

$$e_{12} = \frac{E_1}{E_2} \qquad g_{12} = \frac{G_{12}}{G} \tag{3.13}$$

The parameter e_{12} measures the level of orthotropy between the two principal directions, whereas the parameter g_{12} measures how much the actual shear modulus G_{12} differs from the shear modulus G of the associated GMI material defined in (3.11). The requirement for the stiffness matrix to be positive definite produces the condition that both e_{12} and g_{12} must be positive. In the following, orthotropic materials having $0 < g_{12} < 1$, $g_{12} = 1$, and $g_{12} > 1$ will be referred to as under shear-GMI, shear-GMI, and over shear-GMI, respectively. Also, instead of the usual constants E_1, E_2, ν_{12} and G_{12}, the orthotropic material will be described through the four parameters E, ν, e_{12}, and g_{12}. The relations among the standard and actual

parameters are

$$E_1 = \sqrt{e_{12}}E \qquad E_2 = \frac{E}{\sqrt{e_{12}}} \qquad \nu_{12} = \sqrt{e_{12}}\nu \qquad \nu_{21} = \frac{\nu}{\sqrt{e_{12}}} \qquad G_{12} = \frac{g_{12}E}{2(1+\nu)} \tag{3.14}$$

Based on (3.14) it should be noted that when both e_{12} and g_{12} are equal to unity, the orthotropic material becomes isotropic and coincident with the associated GMI material.

Substituting (3.14) in (2.21) and the results in (3.10), the exact solution of the classical buckling equation for an orthotropic axially-loaded simply-supported circular cylinder homogeneous through the thickness can be written as

$$\sigma_{cr} = \min_{m,n} \left\{ E \left(\frac{p_{08}n^8 + p_{26}m^2n^6 + p_{40}m^4 + p_{44}m^4n^4 + p_{62}m^6n^2 + p_{80}m^8}{q_{24}m^2n^4 + q_{42}m^4n^2 + q_{60}m^6} \right) \right\} \tag{3.15}$$

where the p and q coefficients are functions of the previously-introduced dimensionless parameters η, ν, g_{12} and the nondimensional parameter γ defined as

$$\gamma = \lambda \sqrt[4]{e_{12}} \tag{3.16}$$

It is useful to remark that E and ν are purely constitutive parameters, η is a pure geometric parameter, while γ is a mixed parameter in the general case of an orthotropic material and becomes purely geometric (i.e., λ) in the case of an isotropic material. The p and q coefficients are given by

$$p_{08} = g_{12}\eta^2 \tag{3.17a}$$

$$p_{26} = 2\gamma^2\eta^2 \left((1+g_{12}^2) + \nu(1-g_{12}^2) \right) \tag{3.17b}$$

$$p_{40} = 12 g_{12}\gamma^4(1-\nu^2) \tag{3.17c}$$

$$p_{44} = 2\gamma^4\eta^2 \left(3g_{12} + 2\nu(1-g_{12}^2) + 2\nu^2(1-g_{12}^2)^2 \right) \tag{3.17d}$$

$$p_{62} = 2\gamma^6\eta^2 \left((1+g_{12}^2) + \nu(1-g_{12}^2) \right) \tag{3.17e}$$

$$p_{80} = \gamma^8\eta^2 g_{12} \tag{3.17f}$$

$$q_{24} = 12\gamma^2 g_{12}(1-\nu^2) \tag{3.17g}$$

$$q_{42} = 24\gamma^4(1-\nu^2)\left(1+\nu(1-g_{12})\right) \tag{3.17h}$$

$$q_{60} = 12\gamma^6 g_{12}(1-\nu^2) \tag{3.17i}$$

It should be noted that the constant E appears only as a factor in the critical stress expression (3.15) and does not appear in the coefficients p and q. In order to find the critical stress and the eigenmode associated with that stress, (3.15) must be evaluated for a considerably large number of values of the integers m and n. It should be noted that this operation is time consuming and does not guarantee that the needed minimum belongs to the set of spanned values of m and n, even if this set is large. In this work it will be shown how it is possible to find a closed-form expression for a lower bound of the critical axial stress of an orthotropic circular cylinder. Moreover, it will be shown how a qualitative prediction of the buckling shape (i.e., axisymmetric or not) can be made based only on the value of the parameter g_{12} defined in 3.13. In the following, the integer values m and n will be considered as real variables, and consequently the stress will be considered a real function of the two real variables m and n defined as

$$\sigma(m,n) = E\left(\frac{p_{08}n^8 + p_{26}m^2n^6 + p_{40}m^4 + p_{44}m^4n^4 + p_{62}m^6n^2 + p_{80}m^8}{q_{24}m^2n^4 + q_{42}m^4n^2 + q_{60}m^6}\right) \tag{3.18}$$

where the p and q coefficients are given again by (3.17). The classical problem of finding the pair of integer values (m,n) such that (3.15) is minimum is replaced here by the problem of finding the minimum of the real function (3.18) in $\mathcal{D}$, defined as follows

$$\mathcal{D} := \{(m,n) \in \mathbb{R}^2 : m > 0, n \geq 0\} \tag{3.19}$$

The definition of the set $\mathcal{D}$ is based on few arguments. First, it should be noted that the origin is a singular point for (3.18) and consequently must be excluded by $\mathcal{D}$. Second, as mentioned previously, the variables m and n are associated with the number of half and full waves in the axial and circumferential directions, respectively, and can not assume negative values. Finally, $m = 0$ must be discarded because it is associated with the trivial solution, while $n = 0$ can be included as it is associated with axisymmetric deformations.

3.4 Stationary points

In order to establish if (3.18) admits a minimum in $\mathcal{D}$, its stationary points must be evaluated. The stationary condition can be expressed as

$$\begin{cases} \dfrac{\partial \sigma(m,n)}{\partial m} = 0 \\ \dfrac{\partial \sigma(m,n)}{\partial n} = 0 \end{cases} \tag{3.20}$$

Performing the needed calculation, (3.20) can be rearranged to give

$$\begin{cases} P_{m1}(m,n) P_{m2}(m,n) = 0 \\ P_{n1}(m,n) P_{n2}(m,n) = 0 \end{cases} \tag{3.21}$$

where $P_{m1}(m,n)$, $P_{m2}(m,n)$, $P_{n1}(m,n)$, and $P_{n2}(m,n)$ are polynomial functions of the two real variables m and n. More precisely, $P_{m1}(m,n)$ and $P_{n1}(m,n)$ are quite simple and are given by

$$P_{m1}(m,n) = n^2 - \gamma^2 m^2 \tag{3.22a}$$

$$P_{n1}(m,n) = n \tag{3.22b}$$

It should be noted that the equation $P_{m1}(m,n) = 0$ corresponds in the Cartesian plane m, n to a pair of specular lines through the origin having slope $\pm\gamma$, while the equation $P_{n1}(m,n) = 0$ simply represents the m axis. By contrast, the polynomials $P_{m2}(m,n)$ and $P_{n2}(m,n)$ are more complicated. They are tenth-degree polynomials having the form

$$\alpha_{010} n^{10} + \alpha_{28} m^2 n^8 + \alpha_{46} m^4 n^6 + \alpha_{42} m^4 n^2 + \alpha_{60} m^6 + \alpha_{64} m^6 n^4 + \alpha_{82} m^8 n^2 + \alpha_{100} m^{10} \tag{3.23}$$

The α coefficients of the $P_{m2}(m,n)$ and $P_{n2}(m,n)$ polynomials will be indicated with the superscript m and n, respectively. They are

$$\alpha^m_{010} = g_{12}^2 \eta^2 \tag{3.24a}$$

$$\alpha^m_{28} = g_{12} \gamma^2 \eta^2 \left((4 + g_{12}) + 4\nu(1 - g_{12}) \right) \tag{3.24b}$$

$$\alpha^m_{46} = 2\gamma^4 \eta^2 \left((2 + 2g_{12} + g_{12}^2) + 2\nu(1 - g_{12})(2 + g_{12}) + 2\nu^2 (1 - g_{12}^2)^2 \right) \tag{3.24c}$$

$$\alpha^m_{42} = -12g^2_{12}\gamma^4(1-\nu^2) \tag{3.24d}$$

$$\alpha^m_{60} = -12g^2_{12}\gamma^6(1-\nu^2) \tag{3.24e}$$

$$\alpha^m_{64} = 2\gamma^6\eta^2\left((2+2g_{12}+g^2_{12})+2\nu(1-g_{12})(2+g_{12})+2\nu^2(1-g^2_{12})^2\right) \tag{3.24f}$$

$$\alpha^m_{82} = g_{12}\gamma^8\eta^2\left((4+g_{12})+4\nu(1-g_{12})\right) \tag{3.24g}$$

$$\alpha^m_{100} = g^2_{12}\gamma^{10}\eta^2 \tag{3.24h}$$

$$\alpha^n_{010} = g^2_{12}\eta^2 \tag{3.24i}$$

$$\alpha^n_{28} = g_{12}\gamma^2\eta^2\left((4+g^2_{12})+\nu(1-g_{12})(4+g_{12})\right) \tag{3.24j}$$

$$\alpha^n_{46} = 2\gamma^4\eta^2\left((2+3g^2_{12})+2\nu(1-g_{12})(2+g_{12}+g^2_{12})+2\nu^2(1-g_{12})^2(1+g_{12})\right) \tag{3.24k}$$

$$\alpha^n_{42} = -12g^2_{12}\gamma^4(1-\nu^2) \tag{3.24l}$$

$$\alpha^n_{60} = -12g_{12}\gamma^6(1-\nu^2)(1-\nu(1-g_{12})) \tag{3.24m}$$

$$\alpha^n_{64} = 2\gamma^6\eta^2\left(g_{12}(4+g^2_{12})+\nu(1-g_{12})(2+6g_{12}+g^2_{12})+2\nu^2(1-g_{12})^2(2+g_{12})+\right. \tag{3.24n}$$
$$\left.+2\nu^3(1-g_{12})^3\right)$$

$$\alpha^n_{82} = g_{12}\gamma^8\eta^2\left(5g_{12}+4\nu(1-g^2_{12})+4\nu^2(1-g_{12})^2\right) \tag{3.24o}$$

$$\alpha^n_{100} = g^2_{12}\gamma^{10}\eta^2(g_{12}+\nu(1-g_{12})) \tag{3.24p}$$

Looking at (3.23) it can be noted that all powers of the variables m and n appearing in the polynomials $P_{m2}(m,n)$ and $P_{n2}(m,n)$ are even. This guarantees that the associated curves will be symmetric with respect to both the m and n axes. Moreover the absence of a constant term guarantees the relations $P_{m2}=0$ and $P_{n2}=0$ to pass through the origin $(m,n)=(0,0)$. That said, despite the domain definition of (3.19), because of several symmetry arguments that are useful for illustrating specific points, m and n will be allowed to assume positive and negative values. The domain defined in (3.19) will be enforced after these points are made.

Based on (3.21), it can be noted that the problem under study admits four different types of stationary points. The four types are defined in Tab. 3.1. The stationary points of type-1, -2, and -3 involve at least one of the polynomials P_{m1} and P_{n1} defined in (3.22). These polynomials are of low degree, consequently the equations $P_{m1}=0$ and $P_{n1}=0$ can be easily solved for the variable n. By substituting the solutions for n into the remaining

Type	$P_{m1}=0$	$P_{n1}=0$	$P_{m2}=0$	$P_{n2}=0$
1	$True$	$True$	$False$	$False$
2	$True$	$False$	$False$	$True$
3	$False$	$True$	$True$	$False$
4	$False$	$False$	$True$	$True$

Table 3.1: Definition of four different types of stationary points

equation, identified as *True* in the definition of the stationary point given in Tab. 3.1, the intersection of the two curves can be obtained. The coordinates of the stationary points associated with type-1, -2, and -3 are listed in Tab. 3.2. Looking at Tab. 3.2 it can be

Type	m	n
1	0	0
2	$\pm\frac{1}{\gamma}\sqrt{\frac{\sqrt{3g_{12}(1-\nu^2)}}{\eta((1+g_{12})+\nu(1-g_{12}))}}$	$\pm\sqrt{\frac{\sqrt{3g_{12}(1-\nu^2)}}{\eta((1+g_{12})+\nu(1-g_{12}))}}$
3	$\pm\frac{1}{\gamma}\sqrt{\frac{2\sqrt{3(1-\nu^2)}}{\eta}}$	0

Table 3.2: Value of m and n for three types of stationary points

noted that there exists a single solution for a type-1 stationary point, four solutions for a type-2 stationary point symmetrical with respect to both the m and the n axes, and two solutions for a type-3 stationary point symmetrical with respect to the n axis, for a total of seven stationary points. The position of the stationary point of type-1, -2, and -3 in the plane (m,n) is shown in Fig. 3.1. The two straight lines $n=\pm\gamma m$ are even shown in the figure to highlight the fact that the stationary point of type-2 moves on these lines when g_{12} is varied from zero to infinity. More precisely, all four stationary points of type-2 coincide with the origin when $g_{12}=0$. As soon as g_{12} is increased they move away from the origin following the two lines $n=\pm\gamma m$ until they reach the maximum value of their coordinates, namely $(\pm\sqrt[4]{3}/(\gamma\sqrt{2\eta}),\pm\sqrt[4]{3}/(\sqrt{2\eta}))$, for $g_{12}=(1+\nu)/(1-\nu)$. When $g_{12}>(1+\nu)/(1-\nu)$ they reverse their direction and move back towards the origin on the same lines. Conversely, the coordinates of the stationary points of type-1 and -3 are independent of g_{12}.

Type-4 stationary points are much more complicated to study. As previously remarked, both polynomial equations $P_{m2}=0$ and $P_{n2}=0$ are symmetric with respect to both the m

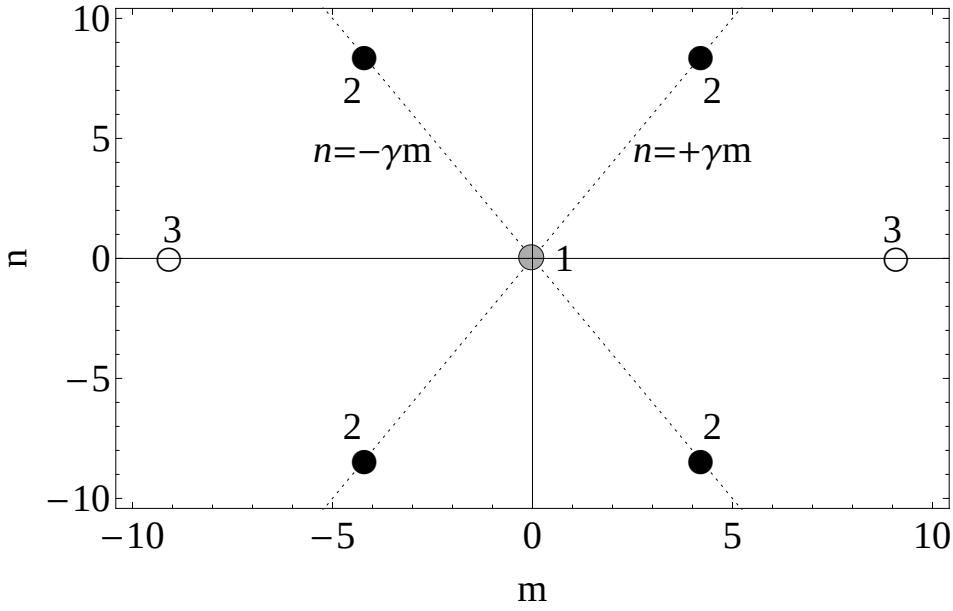

Figure 3.1: Stationary points of type-1 (grey), -2 (black), and-3 (white)

and n axes. Moreover, they pass through the origin, which means the origin is always an intersection point. In order to detect any potential nontrivial intersection points between the two equations $P_{m2} = 0$ and $P_{n2} = 0$, the intersections between each of them and a generic straight line through the origin will be compared. More precisely, each potential nontrivial intersection between a straight line through the origin with slope k, i.e., $n = km$, where k will be allowed to vary from zero to infinity, and the equations $P_{m2} = 0$ and $P_{n2} = 0$ can be defined as

$$Q_m(k) := \left\{(m,n) \in \mathbb{R}^2 \setminus \{(0,0)\} : P_{m2} = 0, n = km\right\} \tag{3.25a}$$

$$Q_n(k) := \left\{(m,n) \in \mathbb{R}^2 \setminus \{(0,0)\} : P_{n2} = 0, n = km\right\} \tag{3.25b}$$

The quantities $Q_m(k)$ and $Q_n(k)$ define the set of nontrivial pairs (m,n) in common with the straight line through the origin and the polynomial equations $P_{m2} = 0$ and $P_{n2} = 0$, respectively, as the slope k of the line changes. If $P_{m2} = 0$ and $P_{n2} = 0$ have a nontrivial intersection, then there must exist a value of slope k_0 such that $Q_m(k_0) \cap Q_n(k_0) \neq \varnothing$. If such a value of k_0 occurs, a type-4 stationary point exists. Performing the needed calculations, i.e., substituting $n = km$ into the equations $P_{m2} = 0$ and $P_{n2} = 0$ and solving for m, the

following expression for $Q_m(k)$ and $Q_n(k)$ can be found

$$Q_m(k) = (m,n) = (m,km) = m(1,k) = \pm g(k)(1,k) \tag{3.26a}$$

$$Q_n(k) = (m,n) = (m,km) = m(1,k) = \pm g(k)f(k)(1,k) \tag{3.26b}$$

where

$$g(k) = \gamma \sqrt{\frac{2g_{12}\sqrt{3(1-\nu^2)}}{\eta(g_{12}k^4 + 2\gamma^2(1+\nu(1-g_{12}))k^2 + g_{12}\gamma^2)}} \tag{3.27a}$$

$$f(k) = \sqrt[4]{\frac{g_{12}k^2 + \gamma^2(1+\nu(1-g_{12}))}{g_{12}(k^2 + \gamma^2(g_{12}+\nu(1-g_{12})))}} \tag{3.27b}$$

With the above notation it is seen that $g(k)$ is actually the value of the m-coordinate of the generic point belonging to the set $Q_m(k)$ for a given slope k. Similarly, $g(k)f(k)$ is actually the value of the m-coordinate of the generic point belonging to the set $Q_n(k)$ for a given slope k. Looking at (3.26) it can be seen that, due to their plus-minus nature, for each value of the slope k there exist only two intersections symmetric with respect to the origin. The plus-minus nature is a consequence of the symmetry of the two equations $P_{m2} = 0$ and $P_{n2} = 0$ with respect to both the m and n axes. Taking the limit of $g(k)$ and $f(k)$ for k approaching infinity (i.e., the n axis) it can be seen that the intersections of the straight line with both the equations $P_{m2} = 0$ and $P_{n2} = 0$ approach the origin, as stated by the following equations

$$\lim_{k\to\infty} g(k) = 0 \qquad \lim_{k\to\infty} f(k) = 1 \tag{3.28}$$

The relations in (3.28) mean that both the loci $P_{m2} = 0$ and $P_{n2} = 0$ are tangent to the n axis at the origin. Similarly, it can be seen that when the slope of the straight line equals zero (i.e., $k = 0$, the m axis) the following relations are obtained:

$$g(0) = \sqrt{\frac{2}{\eta}\sqrt{3(1-\nu^2)}} \qquad f(0) = \sqrt[4]{\frac{1+\nu(1-g_{12})}{g_{12}(g_{12}+\nu(1-g_{12}))}} \tag{3.29}$$

Looking at (3.29) it can be seen that $g(0)$, representing the nontrivial intersection between $P_{m2} = 0$ and the m axis, is always a positive quantity when the parameters η and ν are varied

in their range of definition (i.e., $\eta > 0$ and $\nu^2 < 1$), meaning that this intersection with the m axis always exists. Moreover, it can be proven that $g(k)$ is limited for each $k > 0$, and according to (3.29) tends to zero as $k \to \infty$. Similarly, it can be proven that the quantity $kg(k)$ representing the n coordinate of the intersection point is equal to zero for $k = 0$, is limited for each $k > 0$, and tends to zero as $k \to \infty$. Based on the these arguments, it can be stated that $P_{m2} = 0$ forms two closed loops, symmetric with respect to the n axis, where they are tangent at the origin, one loop to the other loop and each one with the n axis (See Fig. 3.2). Moreover, each loop is symmetric with respect to the m axis and intersects it only at the origin and at a second location that is independent of the parameter g_{12}. These loops are plotted as black lines in Figs. 3.2 (a), (b), and (c) for various ranges of the parameter g_{12}, the measure of the shear deviation of the orthotropic material from the GMI material (see (3.14)). To provide some insight into the findings at this point, it should be remarked that an intersection of the loop with the m axis ($n = 0$), other than the trivial intersection, could represent axisymetric buckling deformations (see (3.4)). By contrast, it can be seen that $g(0)f(0)$, representing the nontrivial intersection between $P_{n2} = 0$ and the m axis, is defined only when the function $f(k)$ assumes real values (i.e., only when the argument of the root in (3.29) is positive). It can be seen that when $0 < g_{12} < (1+\nu)/\nu$, $f(k)$ is defined and $P_{n2} = 0$ forms two closed loops symmetric with respect to both the m and n axes, and tangent to the n axis at the the origin (see gray line of Fig. 3.2 (a)), when $g_{12} = (1 + \nu)/\nu$, $f(0) = 0$ and $P_{n2} = 0$ splits into two petals, both of them tangent to the m axis at the origin (see grey line Fig. 3.2 (b)), when $g_{12} > (1 + \nu)/\nu$, $f(k)$ is not defined for $k^2 < (-\gamma^2(1 + \nu(1 - g_{12}))/g_{12}$, meaning there is no intersection between $P_{n2} = 0$ and the straight line through the origin when its slope is in the range $k^2 < (-\gamma^2(1 + \nu(1 - g_{12}))/g_{12}$ (see grey line of Fig. 3.2 (c) where the limit straight lines $k = \pm\sqrt{(-\gamma^2(1 + \nu(1 - g_{12}))/g_{12}}$ are shown dashed).

The previous arguments furnish a qualitative description of the two equations $P_{m2} = 0$ and $P_{n2} = 0$, but do not give any information about the existence of stationarity points of type-4 defined as the potential intersections between the two equations $P_{m2} = 0$ and $P_{n2} = 0$. In order to detect any possible intersection between $P_{m2} = 0$ and $P_{n2} = 0$, the coordinates of the intersection between the straight line and $P_{m2} = 0$ and $P_{n2} = 0$, respectively, must be compared. Looking at (3.25) it can be seen that the nontrivial intersection between the equations $P_{m2} = 0$ and $P_{n2} = 0$ and the straight line through the origin are proportional to

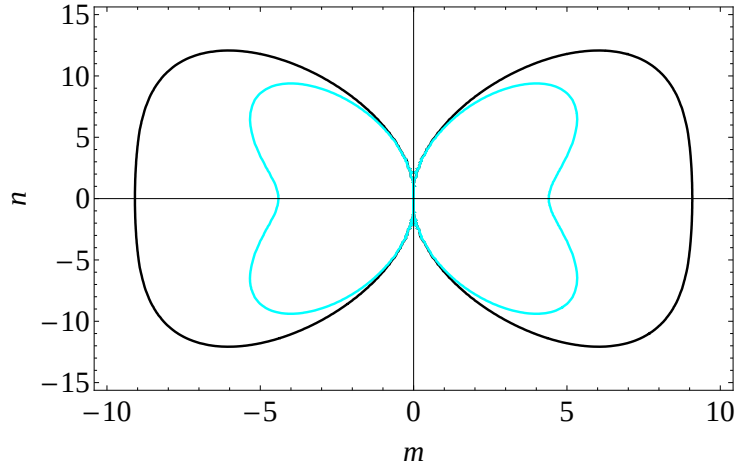

(a) $0 < g_{12} < (1+\nu)/\nu$

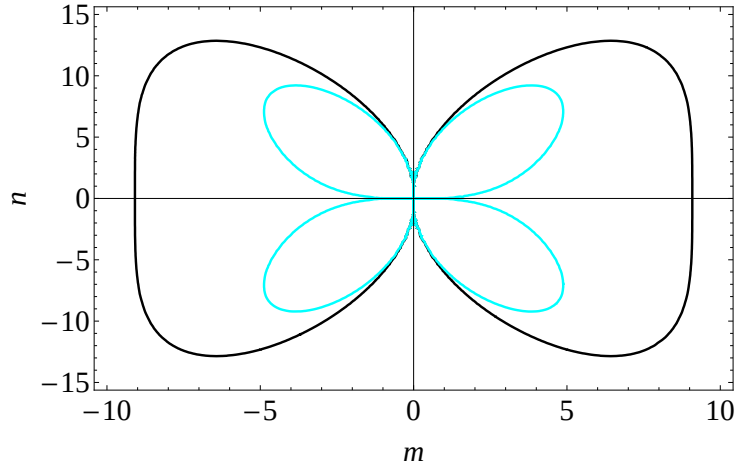

(b) $g_{12} = (1+\nu)/\nu$

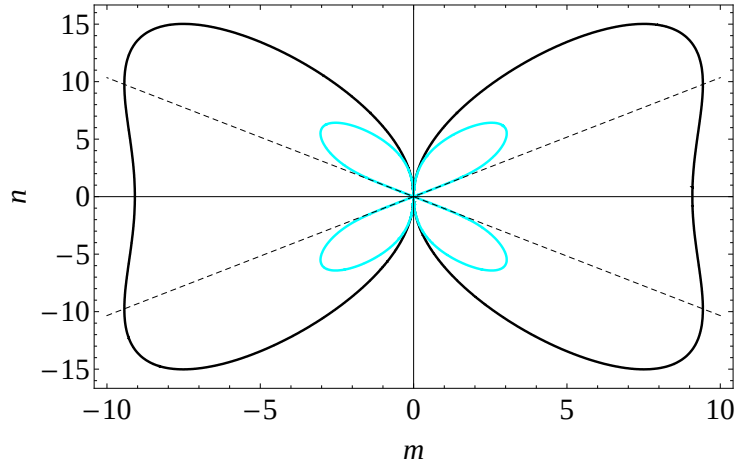

(c) $g_{12} > (1+\nu)/\nu$

Figure 3.2: Curves associated with the polynomial $P_{m2} = 0$ (black line) and $P_{n2} = 0$ (gray line), limit lines $k = \pm\sqrt{(-\gamma^2(1+\nu(1-g_{12}))/g_{12}}$, dashed in (c): $\gamma = 2$, $\eta = 0.01$

each other through the function $f(k)$. Consequently $Q_m(k)$ and $Q_n(k)$ can be equal for a given $k = k_0$ if and only if $f(k_0) = 1$. It easy to see from (3.27) that the equation $f(k) = 1$ is independent of k. This means that there does not exist any value of the slope k_0 such that the polynomials equations $P_{m2} = 0$ and $P_{n2} = 0$ have a single point in common, or equivalently, the function $f(k)$ doesn't intersect the unit value in a single point for any value k_0, but approaches the unit value only when k approaches infinity (see (3.28)), producing the trivial intersection. For convenience, a new function $\phi(g_{12}, \nu)$ will be defined as the numerator of $(f(k)^4 - 1)/\gamma^2)$, i.e.,

$$\Phi(g_{12}, \nu) = -g_{12}^2(1 - \nu) - 2\nu g_{12} + (\nu + 1) \tag{3.30}$$

It can be proved that (3.30) satisfies the following implications

$$\Phi(g_{12}, \nu) < 0 \Rightarrow f(k) < 1 \tag{3.31a}$$

$$\Phi(g_{12}, \nu) = 0 \Rightarrow f(k) = 1 \tag{3.31b}$$

$$\Phi(g_{12}, \nu) > 0 \Rightarrow f(k) > 1 \tag{3.31c}$$

Based on (3.31) it can be understood that the sign of the function $\Phi(g_{12}, \nu)$ controls the behavior of the two relations $P_{m2} = 0$ and $P_{n2} = 0$. More precisely when $\Phi(g_{12}, \nu) < 0$ each of the two loops of $P_{n2} = 0$ is completely inside the corresponding loop of $P_{m2} = 0$, having in common only the origin where all loops are tangent to the n axis (see Fig. 3.3 (c), $P_{m2} = 0$ in black, $P_{n2} = 0$ in gray). Conversely, when $\Phi(g_{12}, \nu) > 0$ each of the two loops of $P_{m2} = 0$ is completely inside the corresponding loop of $P_{n2} = 0$, having in common the origin only where all loops are tangent to the n axis (see Fig. 3.3 (a), $P_{m2} = 0$ in black $P_{n2} = 0$ in gray). The roots of the function $\phi(g_{12}, \nu)$ have an important meaning. Although according to the characteristics illustrated in Figs. 3.3 (a) and (c) the functions $P_{m2} = 0$ and $P_{n2} = 0$ can never intersect each other at just a single nontrivial point, they can intersect at an infinite number of points, i.e., the two polynomials P_{m2} and P_{n2} can be coincident. This situation occurs when the two constitutive parameter ν and g_{12} are related by

$$\Phi(g_{12}, \nu) = 0 \quad \Rightarrow \quad g_{12} = \frac{\nu \pm 1}{\nu - 1} \quad \Rightarrow \quad (g_{12})_1 = 1 \quad , \quad (g_{12})_2 = \frac{\nu + 1}{\nu - 1} \tag{3.32}$$

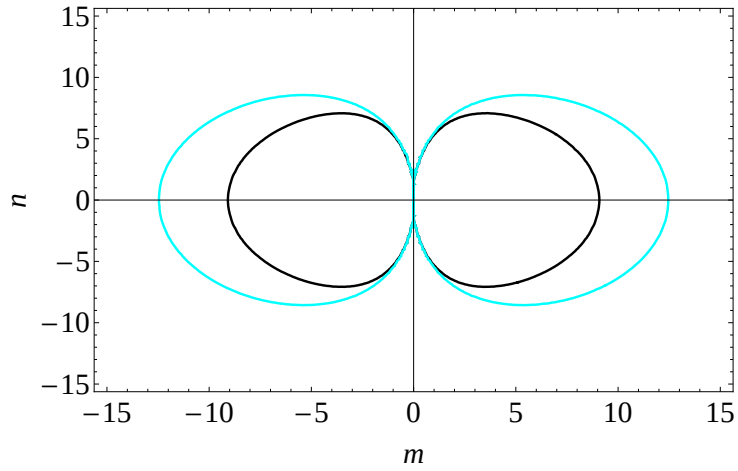

(a) $0 < g_{12} < 1$

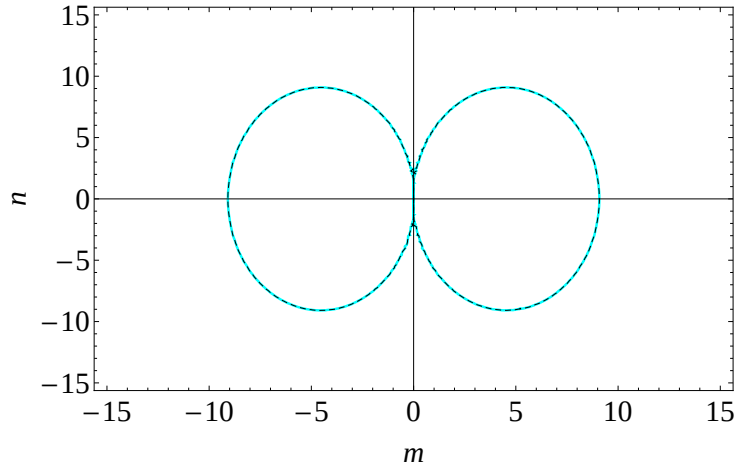

(b) $g_{12} = 1$

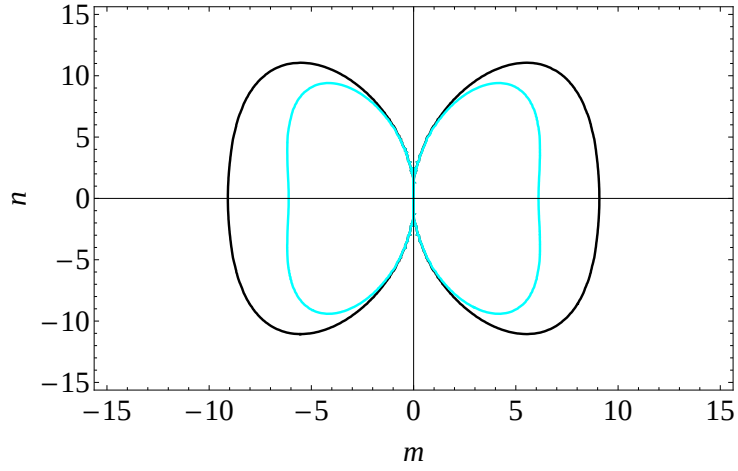

(c) $g_{12} > 1$

Figure 3.3: Curves associated with the polynomial $P_{m2} = 0$ (black line) and $P_{n2} = 0$ (gray line): $\gamma = 2$, $\eta = 0.01$

Looking at (3.13) it can be seen that the root $(g_{12})_1$ is associated with a shear-GMI material. The root $(g_{12})_2$ must be discarded because it violates the requirement that the stiffness matrix be positive definite (see (3.12)). The relations $P_{m2} = 0$ and $P_{n2} = 0$ corresponding to the root $(g_{12})_1$ are illustrated in Fig. 3.3(b). Substituting the admissible root $g_{12} = (g_{12})_1 = 1$ in (3.24) and the results in (3.23), the two polynomials P_{m2} and P_{n2} become coincident, or equivalently they intersect each other at an infinite number of points. These degenerate intersections result in degenerate stationarity points of type-4. The condition necessary to have type-4 stationarity points can be rewritten in the following form:

$$\begin{aligned} P_{m2} = P_{n2} = (n^2 + \gamma^2 m^2) \left(\eta n^4 + 2\gamma^2 \eta m^2 n^2 + \gamma^4 \eta m^4 + 2\gamma^2 \sqrt{3(1-\nu^2)} m^2 \right) \\ \left(\sqrt{\eta} n^2 + \gamma^2 \sqrt{\eta} m^2 + \sqrt{2}\gamma \sqrt[4]{3(1-\nu^2)} m \right) \left(\sqrt{\eta} n^2 + \gamma^2 \sqrt{\eta} m^2 - \sqrt{2}\gamma \sqrt[4]{3(1-\nu^2)} m \right) = 0 \end{aligned} \tag{3.33}$$

Looking at (3.33) it can be noted that the first two factors of P_{m2} and P_{n2} are always positive quantities and can never vanish, while both the third and the fourth factors can be zero. These two factors represent the equations of two identical ellipses tangent to the n axis at the origin as shown in Fig. 3.3 (b). The minor radius a, the major radius b and the ratio b/a for these identical ellipses are given by

$$a = \frac{1}{\gamma} \frac{\sqrt[4]{3(1-\nu^2)}}{\sqrt{2\eta}}, \qquad b = \frac{\sqrt[4]{3(1-\nu^2)}}{\sqrt{2\eta}}, \qquad \frac{b}{a} = \gamma \tag{3.34}$$

All the previous arguments can be summarized by saying that there does not exist a nontrivial stationary point of type-4 except when the orthotropic material is shear-GMI (i.e., $G_{12} = G$ or $g_{12} = 1$). When this happens, there are an infinite number of stationary points that lie on two coincident ellipses that are tangent to the n axis at the origin.

According with the statement of the problem, given at the end of the previous section, which requires the stationary points to belong to the set $\mathcal{D}$ (see (3.19)), any stationary points that do not belong to $\mathcal{D}$ must be discarded. It can be seen that among all the stationary points of type-1, -2, and -3 of Tab. 3.2, only two of them belong to $\mathcal{D}$. More precisely, the stationary point of type-2 having both positive coordinates, which will be referred to in the following as $P_2 = (m_2, n_2)$, and the stationary points of type-3 having positive m coordinates, which will be referred to in the following as $P_3 = (m_3, 0)$ are in $\mathcal{D}$. Regarding

tyype-4 stationary points: it should be noted that only the points belonging to the upper branch of the right ellipse of Fig. 3.3(b) (without the origin) lie in the domain $\mathcal{D}$ and consequently can be accepted as stationary points for the problem under study. All the stationary points of interest can be taken into consideration by defining the following set

$$P_4(t) := (m_4(t), n_4(t)) = \{(m, n) : m = a(1 + \cos(t)), n = b\sin(t), 0 \leq t < \pi\} \tag{3.35}$$

where the equation of an ellipse in terms of the parameter t can be recognized. It should be noted that when $g_{12} = 1$ both the stationary points of type-2 and -3 belong to $P_4(t)$. More precisely, when $g_{12} = 1$ it can be seen that $P_2 = P_4(\pi/2)$ and $P_2 = P_4(0)$. This result can be expressed by saying that when $g_{12} = 1$ all possible stationary points lie on the branch of the ellipse defined by (3.35). It should be further remarked that while the stationary points of types -2 and -3 are defined for each positive value of g_{12}, the degenerate nontrivial stationary points of type-4 exist only for $g_{12} = 1$. The stationary points in $\mathcal{D}$ for $g_{12} = 1$ are shown in Fig. 3.4. Before closing this section, a few comments can be made on the stationary

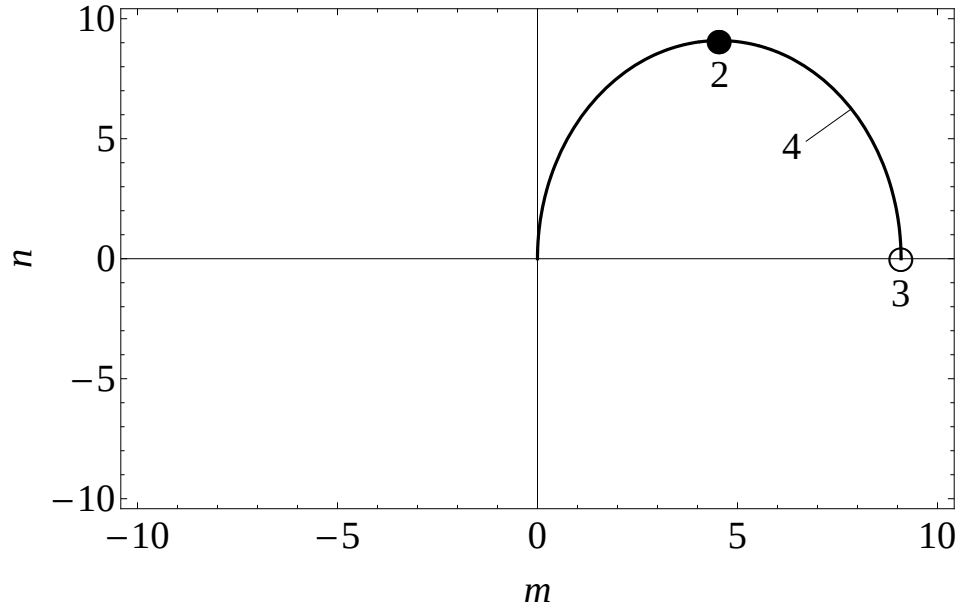

Figure 3.4: Stationary points in $\mathcal{D}$ for $g_{12} = 1$, with type indicated

point of type-1. According with the assumed displacement (3.4), the pair $(m, n) = (0, 0)$ is associated with the deformation state $u_1^0 = U_1$, $u_2^0 = 0$, and $u_3^0 = 0$, which corresponds to a compression of the membrane prebuckling state, i.e., the configuration from which adjacent

equilibrium states are sought. This configuration is equipotential to each buckled shape and and consequently is always a solution.

3.5 Classification of the stationary points

In the previous section three different types of nontrivial stationary points have been highlighted. In this section Hesse's matrix associated with the stress function (3.18) will be evaluated for each of these nontrivial stationary points in order to classify them as minima, maxima, or saddles. As known from real analysis, a given function admits a maximum at a stationary point when Hesse's matrix, evaluated in this point, is negative definite. Conversely, a given function admits a minimum at a stationary point when Hesse's matrix evaluated at the stationary point is positive definite. Finally, if Hesse's matrix is neither positive nor negative definite when it is evaluated at a stationary point, it admits both negative and positive eigenvalues, resulting in a saddle point. Hesse's matrix associated with (3.18) is given by

$$H(m,n) = \begin{pmatrix} \dfrac{\partial^2\sigma(m,n)}{\partial m^2} & \dfrac{\partial^2\sigma(m,n)}{\partial m \partial n} \\ \dfrac{\partial^2\sigma(m,n)}{\partial n \partial m} & \dfrac{\partial^2\sigma(m,n)}{\partial n^2} \end{pmatrix} \tag{3.36}$$

Evaluating (3.36) for the stationary point of type-2 (see Tab. 3.2) the following matrix is obtained

$$H_2 = H(m_2,n_2) = \frac{2E\eta^2}{3(1-\nu^2)} \begin{pmatrix} \gamma^2(1-g_{12}) & -\gamma(1-g_{12}) \\ -\gamma(1-g_{12}) & (3+2\nu)+g_{12}(1-2\nu) \end{pmatrix} \tag{3.37}$$

According with the Sylvester criterion (3.37) is positive definite when

$$\begin{cases} (H_2)_{11} > 0 \\ \det(H_2) > 0 \end{cases} \Rightarrow \begin{cases} (1-g_{12}) > 0 \\ \Phi(g_{12},\nu) > 0 \end{cases} \Rightarrow \quad 0 < g_{12} < 1 \tag{3.38}$$

Similarly, (3.37) is negative definite when

$$\begin{cases} (H_2)_{11} < 0 \\ \det(H_2) > 0 \end{cases} \Rightarrow \begin{cases} (1 - g_{12}) < 0 \\ \Phi(g_{12}, \nu) > 0 \end{cases} \Rightarrow \quad never \tag{3.39}$$

Equation (3.38) states that stationary point of type-2 is the local minimum when $0 < g_{12} < 1$. Similarly, (3.39) states that stationary point of type-2 can never be a local maximum. Consequently, it is a saddle point when $g_{12} > 1$. It is interesting to note that the sign of $\det(H_2)$ (i.e., the sign of the product of the two eigenvalues of (3.37)) is coincident with the sign of $\Phi(g_{12}, \nu)$ defined by (3.30). This means that the nature of the stationary point of type-2 is intimately related with the behavior of the two polynomials P_{m2} and P_{n2}. When $g_{12} = 1$, $\det(H_2) = 0$ meaning that one of the two eigenvalues of H_2 is zero. The second eigenvalue is positive, resulting in H_2 being positive semi-definite. This characteristic is associated with a function that is flat in one direction. That coincides with the fact that with $g_{12} = 1$ the stationary point of type-2 is on the ellipse defined by (3.35), as noted in the previous section.

Evaluating (3.36) for the stationary point of type-3 (see Tab. 3.2), the following matrix is obtained

$$H_3 = H(m_3, 0) = \frac{2E\eta^2}{3(1-\nu^2)} \begin{pmatrix} \gamma^2 & 0 \\ 0 & -\dfrac{\Phi(g_{12}, \nu)}{2g_{12}} \end{pmatrix} \tag{3.40}$$

Since (3.40) is diagonal, it is positive definite when

$$\begin{cases} (H_3)_{11} > 0 \\ (H_3)_{22} > 0 \end{cases} \Rightarrow \begin{cases} always \\ -\Phi(g_{12}, \nu) > 0 \end{cases} \Rightarrow \quad g_{12} > 1 \tag{3.41}$$

Since $(H_3)_{11} > 0$ for each $g_{12} > 0$, (3.40) can never be negative definite, and consequently the stationary point of type-3 can never be a maximum. Consequently, when $\Phi(g_{12}, \nu) > 0$, i.e., when $0 < g_{12} < 1$, the second eigenvalue of (3.40) becomes negative and the stationary point of type-3 becomes a saddle point. Again the sign of $(H_3)_{22}$ (i.e., the sign of one eigenvalue of (3.40)) is related to the sign of $\Phi(g_{12}, \nu)$ defined by (3.30). The stationarity point of type-3 is a minimum when H_3 is positive definite. This happens when $\Phi(g_{12}, \nu) < 0$, i.e., when the loops of the equation $P_{n2} = 0$ are inside of the loops of the equation $P_{m2} = 0$. Similarly,

the stationarity point of type-3 is a saddle point when $\Phi(g_{12}, \nu) > 0$, i.e., when the loops of the equation $P_{m2} = 0$ are inside of the loops of the equation $P_{n2} = 0$. When $g_{12} = 1$, $\det(H_3) = 0$, meaning that one of the two eigenvalues of H_3 is zero. The second eigenvalue is positive, resulting in H_3 being positive semi-definite. This can be again interpreted as the function being flat in one direction for $g_{12} = 1$. That is true because the stationary point of type-3 is on the ellipse defined by (3.35), as mentioned in the previous section.

Finally, evaluating (3.36) for the stationary points of type-4 (see (3.35)), the following matrix is obtained

$$H_4(t) = H(m_4(t), n_4(t)) = \frac{2E\eta^2}{3(1-\nu^2)} \begin{pmatrix} \gamma^2 \cos^2(t) \sec^4(t/2) & 2\gamma \cos(t) \sec^2(t/2) \tan(t/2) \\ 2\gamma \cos(t) \sec^2(t/2) \tan(t/2) & 4 \tan^2(t/2) \end{pmatrix} \tag{3.42}$$

Looking at (3.42) it is easy to realize that $\det(H_4(t)) \equiv 0$. This means that one of the two eigenvalues of (3.42) is always zero. Therefore, the stationary point is a curve instead of a point. The second eigenvalue is given by

$$\kappa_{\perp}(t) = \frac{2E\eta^2}{3(1-\nu^2)} \left(\gamma^2 \cos^2(t) \sec^4\left(\frac{t}{2}\right) + 4 \tan^2\left(\frac{t}{2}\right) \right) \tag{3.43}$$

where the subscript $\perp$ denotes the fact that the nonzero eigenvalue is associated with a direction perpendicular to the zero eigenvalue, i.e., perpendicular to the flat direction. It can be noted that (3.43) is positive for each $0 \leq t < \pi$, meaning that (3.42) is positive semi-definite on each point of the set $P_4(t)$ defined in (3.35), and consequently, the critical ellipse is a degenerate minimum.

All the results previously obtained are summarized in Tab. 3.3. Looking at Tab. 3.3 it

Type	$0 < g_{12} < 1$	$g_{12} = 1$	$g_{12} > 1$
2	*Minimum*	*DegMin*	*Saddle*
3	*Saddle*	*DegMin*	*Minimum*
4	*Not exist*	*DegMin*	*Not exist*

Table 3.3: Classification of the stationary points versus g_{12}

can be easy realized that for each value of the parameter g_{12} there is only a local minimum for (3.18). This guarantees that the local minimum is the global minimum of the function (3.18). Moreover three different behaviors can be found when the dimensionless parameter

g_{12} is varied between zero and infinity.

1. For $0 < g_{12} < 1$ the global minimum of the function is at the stationary point of type-2 (see Fig. 3.5 part (a)). The orthotropic material is associated with an under shear-GMI material. The deformations associated with stationary point of type-2 are nonaxisymmetric.

2. For $g_{12} = 1$ the global minimum of the function is at the degenerate stationarity points of type-4 (see Fig. 3.5 part (b)). The orthotropic material is associated with a shear-GMI material. The deformations associated with stationary point of type-2 are in general nonaxisymmetric, but can be occasionally axisymmetric.

3. For $g_{12} > 1$ the global minimum of the function is at the stationary points of type-3 (see Fig. 3.5 part (c)). The orthotropic material is associated with an over shear-GMI material. The deformations associated with stationary point of type-3 are axisymmetric.

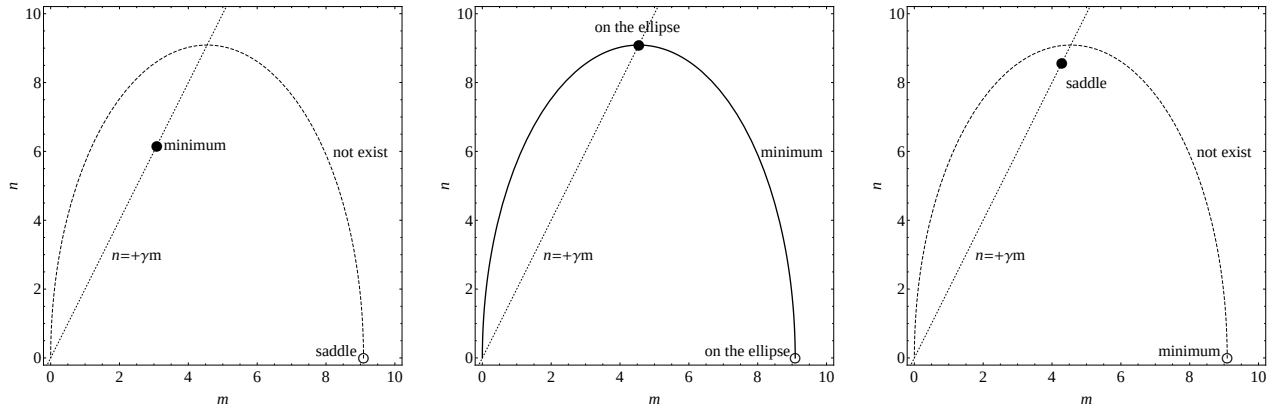

(a) $0 < g_{12} < 1$ (b) $g_{12} = 1$ (c) $g_{12} > 1$

Figure 3.5: Classification of stationary points in $\mathcal{D}$

3.6 Closed-forms for the buckling load of an orthotropic circular cylinder

In this section closed-forms for the buckling load of an orthotropic simply-supported circular cylinder homogeneous through the thickness will be obtained by evaluating the stress

relation (3.18) at the stationary point where the function assumes the global minimum. As remarked at the end of the previous section, all the three types of non-trivial stationary points can result in the global minimum of the function (3.18), depending on the value of the parameter g_{12}. Based on these arguments, the minimum of the stress relation (3.18) becomes a function of the parameter g_{12} and can be defined as follows

$$\sigma_{min}(g_{12}) = \begin{cases} \dfrac{\eta E\sqrt{g_{12}}}{\sqrt{3(1-\nu^2)}} & for \quad 0 < g_{12} < 1 \\ \dfrac{\eta E}{\sqrt{3(1-\nu^2)}} & for \quad g_{12} \geq 1 \end{cases} \tag{3.44}$$

Looking at (3.44), a few comments can be made. First, it should be noted that stationary points of type-3 and -4 ($g_{12} \geq 1$) admit as a minimum the same value. Moreover, it is interesting to note that this value coincides exactly with the expression for the classical buckling load of a homogeneous isotropic circular cylinder where the Young's modulus and the Poisson's ratio of the isotropic material are replaced with the corresponding constitutive constants of the GMI material associated with the given orthotropic material (see (3.11)). This value is independent of the shear modulus. Conversely, the value of the minimum associated with stationary point of type-2 ($0 < g_{12} < 1$) is scaled by the quantity $\sqrt{g_{12}}$, meaning that the minimum stress for a under shear-GMI orthotropic material becomes dependent on the shear modulus, and approaches zero as the shear modulus approaches zero. It is also interesting to note that approaching the origin from the point belonging to the stationarity point of type-4 produces the following results

$$\lim_{t \to \pi} \quad \sigma(m_4(t), n_4(t))) = \frac{\eta E}{\sqrt{3(1-\nu^2)}} \tag{3.45}$$

Based on (3.45) it can be seen that its limit value is independent from g_{12} and coincident with the value that the function assumes in P_3, namely the second equation of (3.44). This means that even if (3.18) cannot be evaluated at the origin (because it is a singular point), there exist points in the immediate neighborhood of the origin having a stress very close to the minimum value that (3.18) can assume for $g_{12} > 1$. This fact does not affect the previous arguments on the minimum of the function, but it can be important when an estimation of the deformed shape associated with the minimum stress is needed. In fact, it should be

noted that (3.44) is the exact solution of the original problem (3.15) only if the coordinates of the stationary points listed in Tab. 3.2 assume integer values. When the values of m and n are not integers, the solution of (3.15) will be slightly bigger than the values estimated by (3.44), which is a lower bound for the critical stress.

3.7 Prediction of the deformed buckling shape

The deformed shape of the circular cylinder, associated with the lower critical stress, is well defined when the integer pair $(m,n)_{min}$ corresponding to the solution of (3.15) is known. When the coordinates of the minimum of (3.18) belong to $\mathbb{N}^2$ for $g_{12} \neq 1$, or there exists at least one value t_0 of the parameter t such that $P_4(t_0) \in \mathbb{N}^2$ for $g_{12} = 1$, then the pair (m,n) associated with P_2, $P_4(t_0)$, and P_3 is the pair $(m,n)_{min}$ minimizing (3.15) for $0 < g_{12} < 1$, $g_{12} = 1$, and $g_{12} > 1$, respectively. When the coordinates of the stationary points are not integer values it is impossible to make a certain prediction of the deformed shape. However a few considerations can be made:

For $0 < g_{12} < 1$ the minimum of (3.18) is located by P_2. As discussed in the previous section, in this case there do not exist any other locations where the function (3.18) assumes values close to the minimum, so it is reasonable to expect the pair of integers $(m,n)_{min}$ minimizing (3.15) to be in the immediate neighborhood of P_2. Consequently, the four points in the immediate neighborhood of P_2, i.e., the four pairs of integers (m,n) closest to P_2, should be checked as candidates for the solution of (3.15). For a generic real pair (m,n) the set of the four integer pairs closest to the real pair can be defined as follows

$$P(m,n) := (\lceil m \rceil, \lceil n \rceil) \cup (\lceil m \rceil, \lfloor n \rfloor) \cup (\lfloor m \rfloor, \lceil n \rceil) \cup (\lfloor m \rfloor, \lfloor n \rfloor) \tag{3.46}$$

Based on (3.46) the rule of thumb for predicting the integer pair $(m,n)_{min}$ minimizing (3.15) can be expressed as follows

$$(m,n)_{min} = (m,n) \in P(m_2,n_2) : \min_{m,n}\{\sigma(m,n)\} \tag{3.47}$$

A simpler, but less accurate, prediction of the buckled shape can be based exclusively on the

estimation of the closer integer value to the real stationary point (i.e., ignoring the curvature of $\sigma(m,n)$). This approach brings the following equation

$$(m,n)_{min} = (\lceil m_2 - 1/2 \rceil, \lceil n_2 - 1/2 \rceil) \tag{3.48}$$

For $g_{12} > 1$ the minimum of (3.18) is located by P_3. As discussed in the previous section, in this case the function (3.18) evaluated at the points on the critical ellipse defined by $P_4(t)$ for $t \to \pi$ assumes values close to the minimum. So, in general, it is not reasonable to expect the pair of integers $(m,n)_{min}$ minimizing (3.15) to be in the immediate neighborhood of P_3. In this regard, (3.43), which represents the nontrivial eigenvalue of (3.42), can be used to make a few comments. Since (3.42) is symmetric, it admits two orthogonal eigenvectors. Moreover, the eigenvector associated with the trivial eigenvalue must be tangent to the ellipse defined by $P_4(t)$ in each location. Consequently (3.43) represents the curvature of (3.18) on $P_4(t)$ in the direction orthogonal to the ellipse, for $g_{12} = 1$. This quantity can be used to estimate the tendency of the stress relation (3.18) to increase in value in the direction normal to the ellipse as the parameter t varies. Taking the limit

$$\lim_{t \to \pi} \quad \kappa_{\perp}(t) = \infty \tag{3.49}$$

It is seen that when the ellipse approaches the origin, i.e., when $t \to \pi$, the curvature in the direction orthogonal to the ellipse defined by $P_4(t)$ tends to infinity. This means that even if for the point on the ellipse in the immediate neighborhood of the origin the value of the stress given by (3.18) is very close to the minimum value assumed in P_3, the evaluation of (3.18) on the points close to the ellipse results in large increments in the stress with respect to the minimum values assumed in P_3. These arguments, of course, don't guarantee that it is impossible to find the pair of integers $(m,n)_{min}$ minimizing (3.15) in the immediate neighborhood of the origin, but they make this circumstance very improbable. Consequently, it is reasonable to check as a potential candidate for $(m,n)_{min}$ the two integer points in the neighborhood of P_3.

$$(m,n)_{min} = (m,n) \in P(m_3, 0) : \min_{m,n}\{\sigma(m,n)\} \tag{3.50}$$

A simpler, but less accurate, prediction of the buckled shape can be based exclusively on the estimation of the closer integer value to the real stationary point (i.e. ignoring the curvature of $\sigma(m,n)$). This approach brings the following equation

$$(m,n)_{min} = (\lceil m_3 - 1/2 \rceil, 0) \tag{3.51}$$

When $g_{12} = 1$, i.e., when the orthotropic material is shear-GMI, the minimum is no loger a single point, but rather the minimum is the branch of an ellipse defined by $P_4(t)$ (see (3.35)) and locating the closest integer values becomes a hard task. The relevant branch of the ellipse is shown in Fig. 3.6 together with the grid of integer values for $\gamma = 2$, $\eta = 0.01$, and $\nu = 0.3$. Looking at this figure, it is easily realized that there are many integer pairs (m,n) quite close to the real minimum lying on the ellipse. This sophisticated behavior is not a purely theoretical issue. In fact, it is the case for isotropic materials. The understanding of Fig. 3.6 makes clear why a slight variation in the geometry of the shear-GMI cylinder may result in a completely different buckled shape, even if the variation in the buckling load is only slight. In fact, based on (3.34), it is seen that the geometry of the critical ellipse is controlled by the geometry and material properties of the cylinder through the parameters η and γ. Even a small variation of these parameters may result in completely different intersection between the ellipse and the grid of integers. In order to find the pair $(m,n)_{min}$ minimizing (3.15), a few considerations can be made looking again at the orthogonal curvature of (3.18) all around the elliptical minimum. It seems reasonable that there is a higher probability finding the pair $(m,n)_{min}$ minimizing (3.15) close to the region of the ellipse where $\kappa_\perp$ is small. Equation (3.43) depends on γ (i.e., the aspect ratio of the critical ellipse, (3.34)), consequently, the value of the parameter $t = t_{min}$ for which the orthogonal curvature is a minimum is also dependent on γ. Performing the needed calculation, the following expression is found for t_{min}

$$t_{min} = \begin{cases} 0 & for \quad 0 < \gamma < \sqrt{2} \\ 2\arcsin\left(\dfrac{\sqrt{2(\gamma^2-1)}}{\gamma}\right) & for \quad \gamma > \sqrt{2} \end{cases} \tag{3.52}$$

The value of $t = t_{min}$ from (3.52) is plotted in Fig. 3.7. Looking at Fig. 3.7 it can be noted

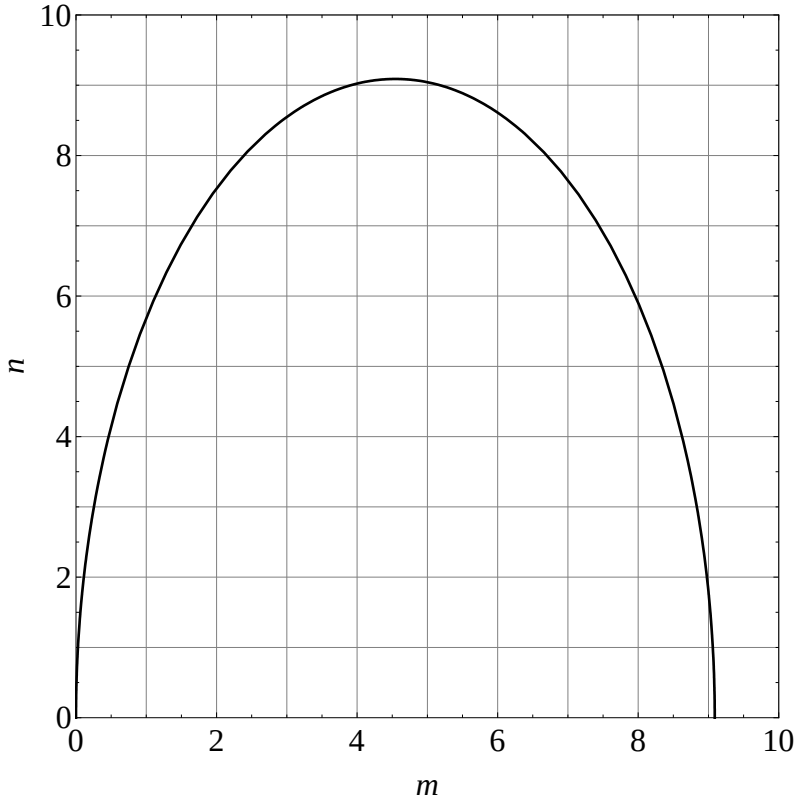

Figure 3.6: Critical ellipse for $\gamma = 2$, $\eta = 0.01$, and $\nu = 0.3$

that when $0 < \gamma < \sqrt{2}$ the region of the ellipse with the smallest orthogonal curvature is located at $t_{min} = 0$ (i.e., at the nontrivial intersection with the m axis). As noted before, this location coincides with P_3 when $g_{12} = 1$. Similarly when $\gamma > 5$, the region of the ellipse with the smallest orthogonal curvature is located very close to $t_{min} = \pi/2$, approaching P_2 when $\gamma \to \infty$. Finally, when $\sqrt{2} < \gamma < 5$ (see gray band in Fig. 3.7) the value of t_{min} increases rapidly from zero to $\pi/2$. More precisely, for $\gamma = \sqrt{2}$, t_{min} jumps almost instantaneously from zero to about $\pi/4$. This translates into the fact that for $\gamma = \sqrt{2}$ the orthogonal curvature to the ellipse is almost constant for $0 < t < \pi/4$, while the transition between $\pi/4$ and $\pi/2$ is less rapid. It should be noted that based on practical values of λ due to cylinder geometry and material properties (see (3.16)), the previous arguments simply state that the pair $(m, n)_{min}$ minimizing (3.15) has a high probability of being in the neighborhood of the quarter of ellipse spanned by $0 < t < \pi/2$. This fact explains why homogeneous isotropic circular cylinders tend to buckle with a high wave number in the axial direction. By the way, as can be seen from Fig. 3.6, most likely the elliptical minimum passes through or

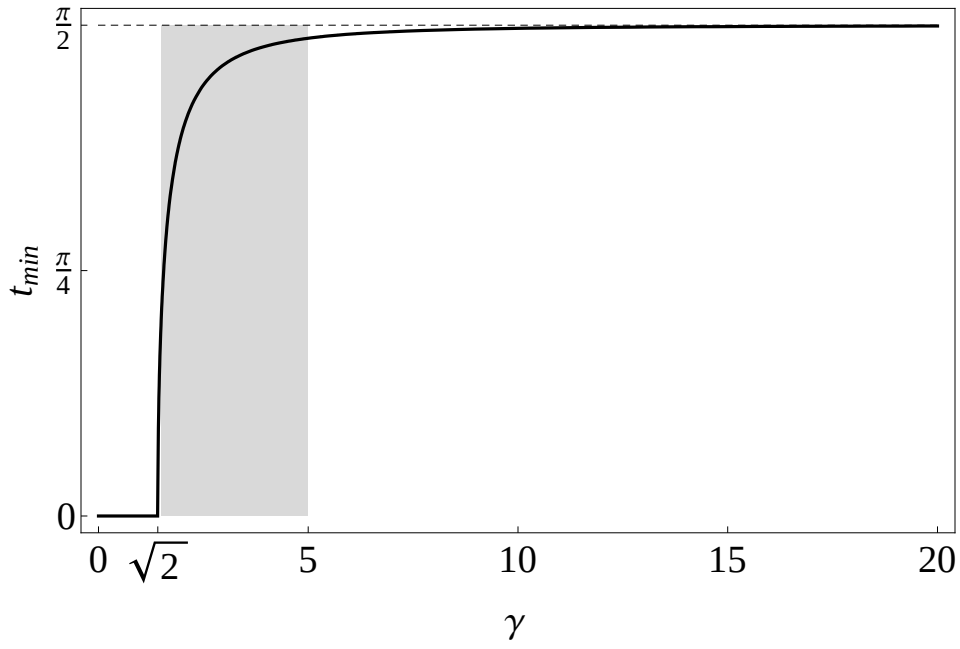

Figure 3.7: Location of minimum curvature vs γ: $\gamma = 2$, $\eta = 0.01$, $\nu = 0.3$

very close to some integer pair. Consequently, even if in the neighborhood of that pair the orthogonal curvature is not minimum, the pair $(m, n)_{min}$ has a high probability of being located there. Based on the previous arguments, it is necessary to check all the integer pairs in the vicinity of the critical ellipse as potential candidates for the pair $(m, n)_{min}$ minimizing (3.15). The use of the critical ellipse concept dramatically reduces the integer pairs to check and consequently the computational time needed, and most importantly, guarantees finding the right pair in the spanned set. In fact, the pair $(m, n)_{min}$ minimizing (3.15) must satisfy the following relation

$$(m, n)_{min} \in \{(m, n) \in \mathbb{N}^2 : m \leq \lceil 2a \rceil, n \leq \lceil b \rceil\} \tag{3.53}$$

Using more sophisticated arguments for the case $g_{12} = 1$, an analytical technique to determine the pair $(m, n)_{min}$ as a function of the parameter γ and η can be derived. As shown previously the critical ellipse must be tangent in the origin to the n axis, so there are only two degrees of freedom left for defining the ellipse. One of these degrees of freedom can be used to require that the ellipse pass through a given integer pair (m_0, n_0), for example, if it is desirable to have a particular buckling deformation pattern. This procedure allows for

establishment of a relation between the parameters γ and η that produce this deformation pattern given by

$$\hat{\eta}(\gamma, m_0, n_0) = \frac{\eta}{\sqrt{12(1-\nu^2)}} = \frac{m_0^2\gamma^2}{(n_0^2 + m_0^2\gamma^2)^2} \tag{3.54}$$

In Fig. 3.8 are plotted the curves (3.54) for $m_0 = 1, 2, ..., 10$ and $n_0 = 0, 1, ..., 10$. Each curve is associated with an integer pair (m_0, n_0), shown in a few cases as a label. Looking at these labels it is easy to realize that the relations (3.54) become closer to the $\hat{\eta}$ axis as m increases, and become closer to the γ axis as n increases. Consequently, all the curves are located between the $\hat{\eta}$ axis, the γ axis, and the curve associated with the pair $(1, 0)$. Based

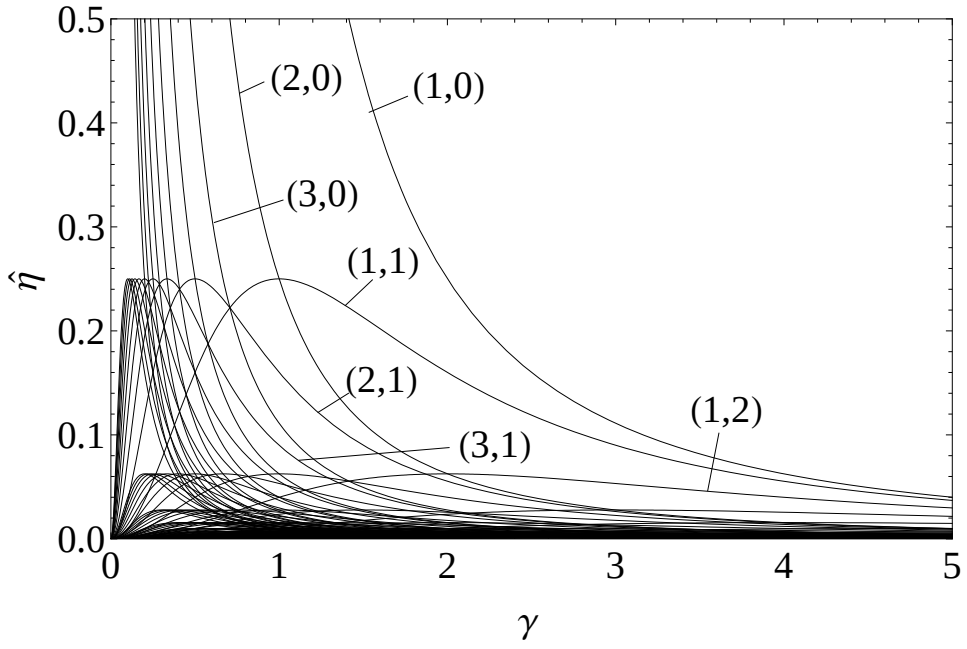

Figure 3.8: $\hat{\eta}(\gamma, m_0, n_0)$ versus γ for different pairs (m_0, n_0)

on Fig. 3.8 a few more considerations can be made. First, it should be noted that the curve $\hat{\eta}(\gamma, m_0, n_0)$ represents all points of the plane γ, $\hat{\eta}$ such that (3.44) is the exact solution of (3.15) for the given pair (m_0, n_0). Second, it should be noted that the values of $\hat{\eta}$ and λ defined by the intersection of two relations given by (3.54) for two different values of m_0 and n_0 correspond to special geometry having two different eigenfunctions associated with a single eigenvalue. The pair $(\gamma, \hat{\eta})$ forcing the ellipse to pass through the two integer pairs

(m_1, n_1) and (m_2, n_2) is given by

$$\gamma = \sqrt{\frac{m_2 n_1^2 - m_1 n_2^2}{m_1 m_2^2 - m_2 m_1^2}} \qquad \hat{\eta} = m_1 m_2 (m_1 - m_2) \frac{m_1 n_2^2 - m_2 n_1^2}{m_2^2 n_1^2 - m_1^2 n_2^2} \tag{3.55}$$

Similarly it can be proven that the critical ellipse can be forced to pass by three integer pairs when they are chosen using the following rule

$$m_1 = m_2 + m_3, \quad n_1 = 0, \quad n_2 = n_3 \tag{3.56}$$

Using (3.56), the pair $(\gamma, \hat{\eta})$ needed to force the critical ellipse to pass through the three integer pairs (m_1, n_1), (m_2, n_2), and (m_3, n_3) (constrained by the relations (3.56)) can be evaluated. The pair is given by

$$\gamma = \frac{n_2}{\sqrt{m_2 m_3}} \qquad \hat{\eta} = \frac{m_2 m_3}{m_1^2 n_2^2} \tag{3.57}$$

If the cylinder is designed using (3.57) it admits three buckled shapes associated with the same eigenvalue. More precisely, two shapes are nonaxisymmetric and have an equal number of waves in the circumferential direction. The other shape is axisymmetric with the number of waves in the axial direction equal to the sum of the waves in the axial direction of the two nonaxisymmetric shapes.

It is interesting to show how the dependence of the integer pair $(m, n)_{min}$, minimizing (3.15), on the parameters γ and $\hat{\eta}$ can be predicted using Fig. 3.8. More precisely, the (γ, $\hat{\eta}$) plane can be partitioned in tiles associated with all the possible deformation patterns of the cylinder. In the following, an algorithm using Fig. 3.8 as a starting point will be proposed in order to produce the needed partition. Before starting to describe the proposed algorithm it is useful to introduce some notation. Each closed region of the plane $(\gamma, \hat{\eta})$ will be referred to as a tile. Each tile is defined by portions of relations $\hat{\eta}(\gamma, m_0, n_0)$ referred to in the following as sides of the tile. The points where two (or three) different relations $\hat{\eta}(\gamma, m_0, n_0)$ intersect will be referred to as corners. At each corner four (or six) different tiles meet. Among those four (or six) tiles, one tile will be referred to as the opposite of an another tile if it is possible to move from one tile to the other moving on a straight line through the corner. Moreover

if this line through the corner joining the two opposite tiles can be vertical, they will be referred to as vertically-opposite. The algorithm needed to obtain the partition is described below:

1. Find all the corners.
2. For each corner select the two closest relations $\hat{\eta}(\gamma, m_0, n_0)$ met moving vertically up and down, respectively. Then for each corner find the two middle points between it and the top and bottom relation, respectively.
3. For each corner join the two midpoints closest to the corner of the two vertically-opposite tiles with a vertical segment.
4. For each corner join the two midpoints closest to the corner of each remaining pair of opposite tiles with the mean of the two relation $\hat{\eta}(\gamma, m_0, n_0)$ defining the corner (i.e., $1/2(\hat{\eta}(\gamma, m_1, n_1) + \hat{\eta}(\gamma, m_2, n_2))$).
5. For each midpoint of each tile that is not already joined with three other midpoints, join it with the closest similar midpoints of the same tile with the mean of the two relations $\hat{\eta}(\gamma, m_0, n_0)$ defining the opposite side of the tile in the between the two midpoints.
6. Remove all relations $\hat{\eta}(\gamma, m_0, n_0)$.

The procedure described above is shown in Fig. 3.9 step-by-step for a small region of the plane $(\gamma, \hat{\eta})$. The construction points and lines added at each step are drawn in different colors to highlight the constructive procedure. At the end of step 5 each portion of the dashed lines, representing the relations $\hat{\eta}(\gamma, m_0, n_0)$, are trapped in a single tile. This means that all the region of the $(\gamma, \hat{\eta})$ plane inside the tile is associated with the same deformation pattern, defined by the trapped relations. As seen, there exist more tiles associated with the same integer pair $(m, n)_{min}$. All those tiles have a corner in common. In order to validate the found results, the partition obtained in Fig. 3.9 will be compared with the solution of (3.15) evaluated on the same region of the $(\gamma, \hat{\eta})$ plane. The results obtained are shown in Fig. 3.10. More precisely, in Fig. 3.10 part (a) is repeated the partition constructed in Fig. 3.9 with the addition of labels indicating the deformation pattern associated with each tile. In Fig. 3.10 part (b) is shown the results of the solution of equation (3.15) in a grid of 300 x 300 points. Each color corresponds to a deformation pattern, so that tiles having same color

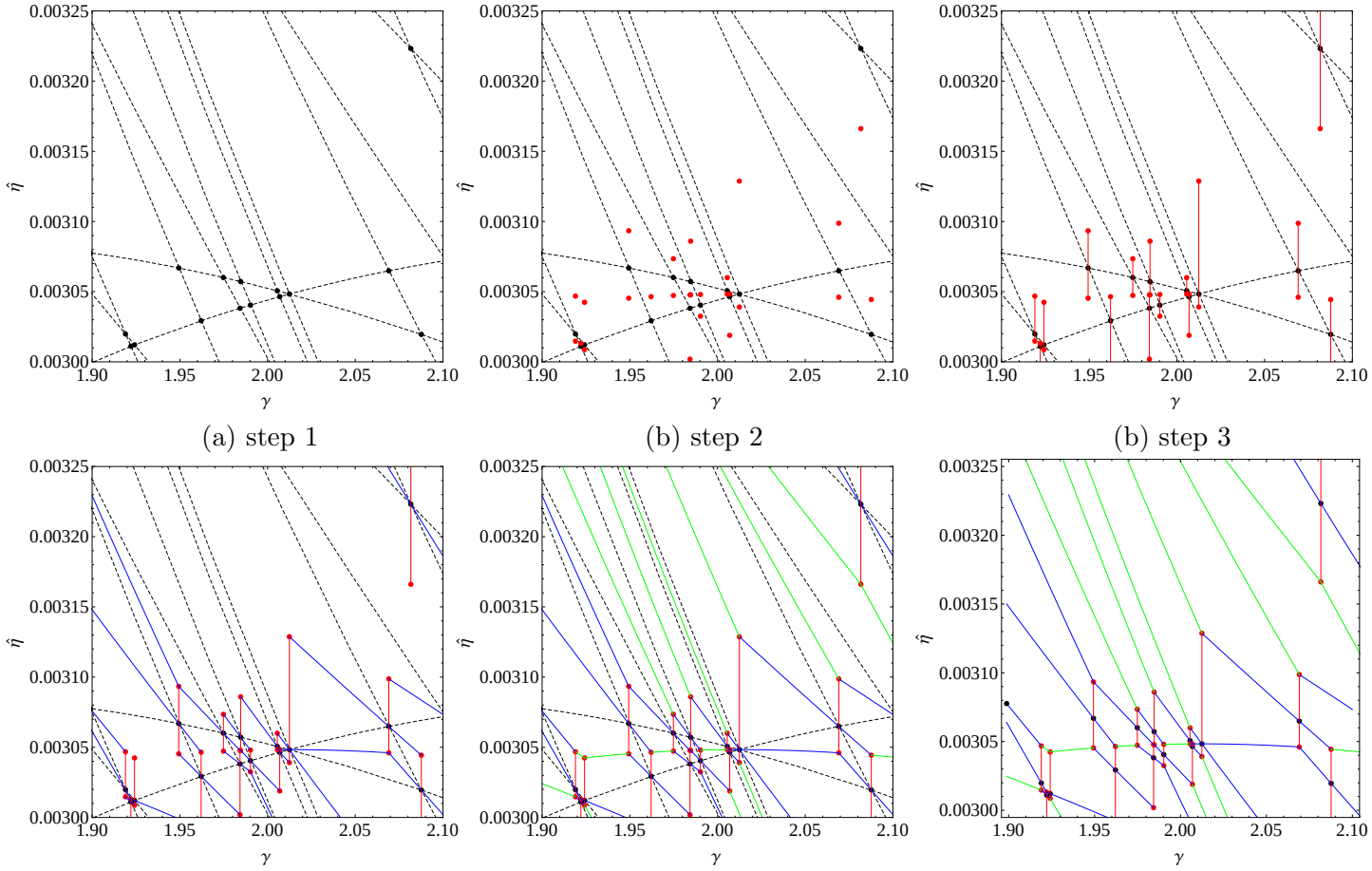

(a) step 1 (b) step 2 (b) step 3

(d) step 4 (e) step 5 (f) step 6

Figure 3.9: Steps needed for the partition of the $(\gamma, \hat{\eta})$ plane

are associated with the same pair $(m, n)_{min}$. Comparing the two parts of Fig. 3.10, it is seen that the constructive procedure proposed accurately predicts the pair $(m, n)_{min}$ minimizing (3.15) in the whole region. Although the proposed theory is quite complicated, it furnishes a quantitative explanation of the apparently random way in which an axially loaded circular cylinder buckles, allowing for the design of a cylindrical shell that will buckle following a deformation pattern specified *a priori*. Moreover, it should be noted that the deformation chart, shown in Fig. 3.10 for a subregion of the $(\gamma, \hat{\eta})$ plane, must be evaluated only once because it is valid in general. Of course the previous statements are true with respect to the classical buckling equation used to derive the present theory.

The discussion in the next chapter will focus on a specific application of the analysis developed in this chapter.

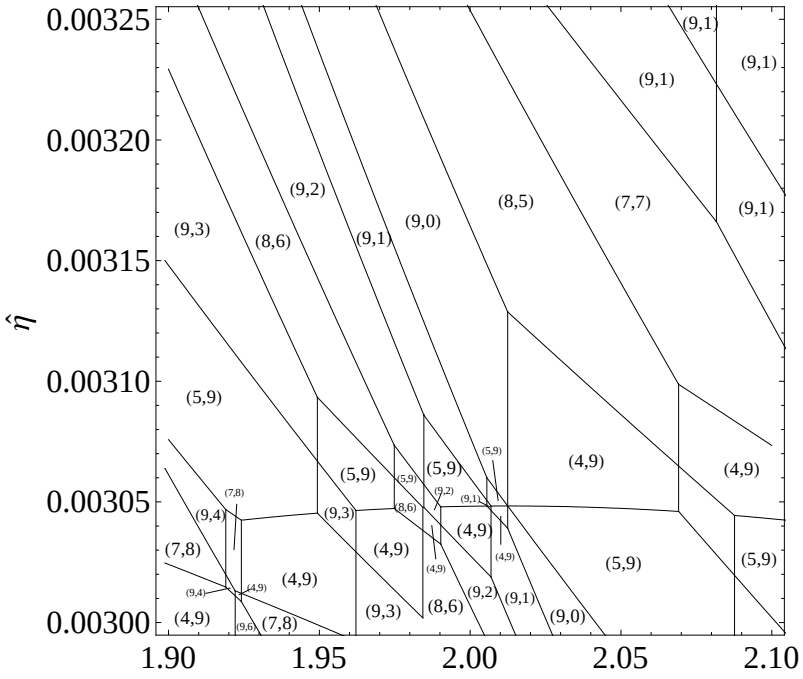

(a) partition obtained using the described step-by-step procedure

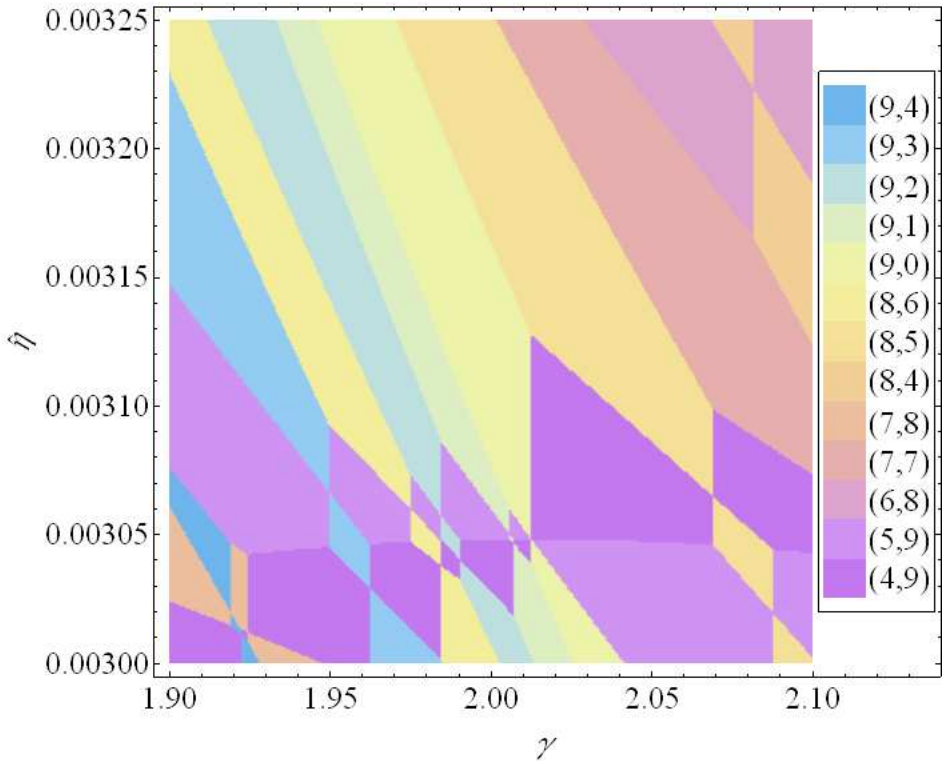

(b) partition obtained solving (3.15) on a grid of 300 x 300 points

Figure 3.10: Comparison between obtained partition and solution of (3.15)

Chapter 4

Axial buckling behavior of anisogrid circular cylinders

4.1 Introduction

In this Chapter the general results found in the previous Chapter will be applied to the study of a circular lattice cylinder. The lattice structure is assumed to be constituted from a system of helical ribs, the included angle not necessarly being 30°. As mentioned in Chapter 1, those kind of structures are usually referred to as anisogrid structures. When the ribs are dense enough, the lattice can be described through a set of homogenized equivalent constitutive equations. Those homogenized constitutive equations will be derived in the next section for an anisogrid lattice made of a single layer of helical and circumferential ribs. Under these specifications the lattice can be modeled as an orthotropic material having engineering properties depending on the rib angle. The expressions for the engineering properties as a function of the rib angle will be derived. Those expressions will be used in Sec. 4.3, together with the theory developed in the previous Chapter, to study the axial buckling behaviour of an anisogrid circular cylinder.

4.2 Homogenized constitutive equations for an anisogrid structure

In this section the homogenized constitutive constants of an equivalent orthoropic material, used to model an anisogrid structure, i.e., a regular system of densely arranged ribs, will be derived as a function of the geometry and the constitutive properties of the ribs. A representative anisogrid contruction is illustrated in Fig. 4.1, where relevant quantities are labeled. More precisely, the thickness of the lattice layer is referred to with the usual symbol h, the widths of helical and circumferential ribs are referred to with the symbols, d_h and d_c, respectively, and the spacings between two adjacent helical and circumferential ribs are referred to with the symbols, a_h and a_c, respectively. Finally the angle between the helical ribs and the axial x_1-direction is referred to with the symbol ϕ. When the cross section

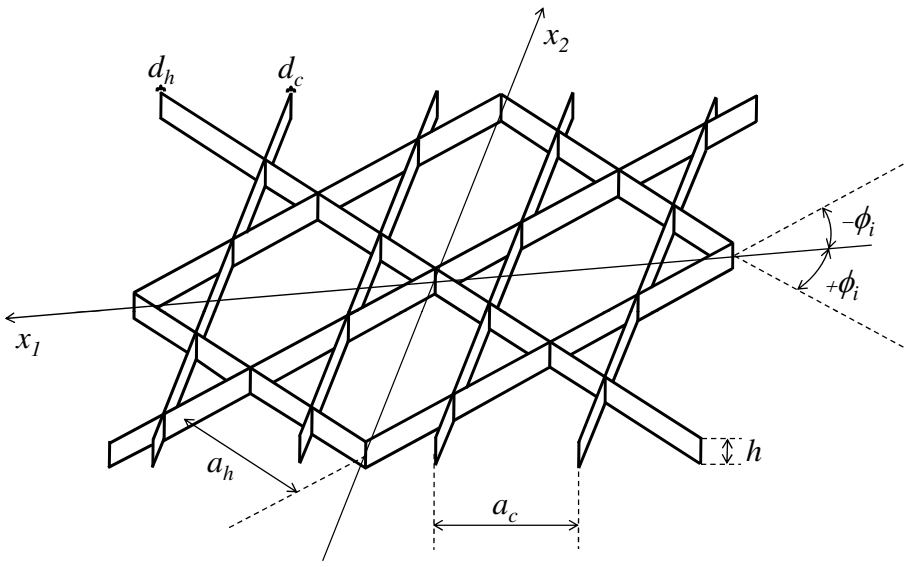

Figure 4.1: Lattice structure

of a rib is not rectangular, its cross-sectional area will be indicated with the symbol S. In this circumstace the equivalent width of the rib can be expressed as S/h. Only a specular system of helical ribs will be taken into consideration, which means that for each set of ribs having orientation $+\phi$, there exists a complementary set of ribs having orientation $-\phi$, except for circumferential or axial ribs (i.e., $\phi = \pi/2$ or $\phi = 0$ in Fig. 4.1). The anisogrid construction shown in Fig. 4.1 is a portion of a lattice structure with a specular set of ribs having orientation ϕ and a set of ribs aligned with the circumferential x_2-direction. It should

be noted that for a lattice structure all the ribs lie in the same layer. This circumstance causes the reduced stiffnesses coupling extensional and shear deformations to vanish (i.e., $Q_{13} = Q_{23} = Q_{31} = Q_{32} = 0$, (2.17)). This means that a lattice construction can be considered as a single layer which behaves as an orthotropic material. According to [61], a lattice layer of specular ribs having arbitrary cross section and forming an angle ϕ with the coordinate line x_1 (see Fig. 4.1) can be considered as a continuum layer having the equivalent reduced stiffness given by

$$Q_{11} = \frac{E_r S}{a_h h} \cos^4(\phi) \tag{4.1a}$$

$$Q_{22} = \frac{E_r S}{a_h h} \sin^4(\phi) \tag{4.1b}$$

$$Q_{12} = Q_{21} = \frac{ES}{a_h h} \cos^2(\phi) \sin^2(\phi) \tag{4.1c}$$

$$Q_{33} = \frac{E_r S}{a_h h} \cos^2(\phi) \sin^2(\phi) \tag{4.1d}$$

where E_r is the Young's modulus in the principal direction of a single rib, that is modeled locally as a beam. The cross-section area of a system of helical ribs must be doubled to take into account both the $+\phi$ and the $-\phi$ ribs. If more then one system of specular ribs is present in the lattice layer, it can be considered as an homogeneous layer having the following equivalent properties

$$Q_{11} = \frac{1}{h} \sum_{i=1}^{m} \frac{(E_r)_i S_i}{(a_h)_i} \cos^4(\phi_i) \tag{4.2a}$$

$$Q_{22} = \frac{1}{h} \sum_{i=1}^{m} \frac{(E_r)_i S_i}{(a_h)_i} \sin^4(\phi_i) \tag{4.2b}$$

$$Q_{12} = Q_{21} = \frac{1}{h} \sum_{i=1}^{m} \frac{(E_r)_i S_i}{(a_h)_i} \cos^2(\phi_i) \sin^2(\phi_i) \tag{4.2c}$$

$$Q_{33} = \frac{1}{h} \sum_{i=1}^{m} \frac{(E_r)_i S_i}{(a_h)_i} \cos^2(\phi_i) \sin^2(\phi_i) \tag{4.2d}$$

where m is the number of systems of specular ribs, $(E_r)_i$ is the Young's modulus in the principal direction of the i^{th} system of specular ribs, S_i is the cross-section area of the i^{th} system of specular ribs, $(a_h)_i$ is the spacing between two adjacent ribs of the i^{th} system of specular ribs, and h is the thickness of the layer. The equivalent reduced stiffnesss of a lattice

layer including a system of specular rectangular cross section ribs forming an angle ϕ with the x_1-direction and a system of rectangular cross section ribs in the x_2-direction (see Fig. 4.1) are given below

$$Q_{11} = 2\frac{E_r d_h}{a_h}\cos^4(\phi) \tag{4.3a}$$

$$Q_{22} = 2\frac{E_r d_h}{a_h}\sin^4(\phi) + \frac{E_r d_c}{a_c} \tag{4.3b}$$

$$Q_{12} = Q_{21} = 2\frac{E_r d_h}{a_h}\cos^2(\phi)\sin^2(\phi) \tag{4.3c}$$

$$Q_{33} = 2\frac{E_r d_h}{a_h}\cos^2(\phi)\sin^2(\phi) \tag{4.3d}$$

In order to improve the local buckling capabilities, the length of each unsupported segment of a rib in the grid must be made as short as possible. One approach to achieve this condition is obtained by attaching the circumferential ribs at the middle point between two adjacent joints of helical ribs, as shown in Fig. 4.1. It should be noted that this special geometry of the grid produces the following constraint equation between the distances a_h and a_c

$$a_h = 2a_c\sin(\phi) \tag{4.4}$$

Assuming all the ribs to have the same width (i.e., $d_h = d_c$), a dimensionless parameter taking into account the rib density can be defined as follow

$$\delta = d_c/a_c \tag{4.5}$$

Substituting (4.4) and (4.5) in (4.3) results in equivalent reduced stiffness which can be written as

$$Q_{11} = E_r\delta\frac{\cos^4(\phi)}{\sin(\phi)} \tag{4.6a}$$

$$Q_{22} = E_r\delta(\sin^3(\phi) + 1) \tag{4.6b}$$

$$Q_{12} = Q_{21} = E_r\delta\cos^2(\phi)\sin(\phi) \tag{4.6c}$$

$$Q_{33} = E_r\delta\cos^2(\phi)\sin(\phi) \tag{4.6d}$$

Using (4.6), the equivalent engineering properties of the homogenized orthotropic material can be obtained as

$$E_1 = Q_{11} - \frac{Q_{12}^2}{Q_{22}} = E_r\delta\left(\frac{\cos^3(\phi)\cot(\phi)}{1+\sin^3(\phi)}\right) \tag{4.7a}$$

$$E_2 = Q_{22} - \frac{Q_{12}^2}{Q_{11}} = E_r\delta \tag{4.7b}$$

$$\nu_{12} = \frac{Q_{12}}{Q_{22}} = \frac{\cos^2(\phi)\sin(\phi)}{1+\sin^3(\phi)} \tag{4.7c}$$

$$\nu_{21} = \frac{Q_{12}}{Q_{22}} = \tan^2(\phi) \tag{4.7d}$$

$$G_{12} = Q_{33} = E_r\delta\cos^2(\phi)\sin(\phi) \tag{4.7e}$$

4.3 Axial buckling behavior of an anisogrid circular cylinder

In this section the equivalent engineering properties for an anisogrid lattice, derived in the previous section, will be substituted into the general theory developed in Chapter 3 in order to predict the axial buckling behavior of an anisogrid circular cylinder as a function of the angle of the helical ribs, ϕ. First, using (3.11) and (4.7) it is possible to define the constitutive properties of the associated GMI material as a function of the rib angle ϕ as

$$E = \sqrt{E_1 E_2} = E_r\delta\sqrt{\frac{\cos^3(\phi)\cot(\phi)}{1+\sin^3(\phi)}} \tag{4.8a}$$

$$\nu = \sqrt{\nu_1\nu_2} = \sqrt{\frac{\sin^3(\phi)}{1+\sin^3(\phi)}} \tag{4.8b}$$

$$G = \frac{E}{2(1+\nu)} = E_r\delta\frac{\cos^2(\phi)}{2\left(\sin^2(\phi)+\sqrt{1+\sin^4(\phi)}\right)} \tag{4.8c}$$

Similarly, the dimensionless parameters e_{12} and g_{12}, defined in (3.13), can be specialized for an anisogrid structure as

$$e_{12} = \frac{E_1}{E_2} = \frac{\cos^3(\phi)\cot(\phi)}{1+\sin^3(\phi)} \tag{4.9a}$$

$$g_{12} = \frac{G_{12}}{G} = 2\sin(\phi)\left(\sin^2(\phi)+\sqrt{\sin(\phi)+\sin^4(\phi)}\right) \tag{4.9b}$$

As shown in (3.44), the axial buckling stress of an orthotropic cylinder can assume two different values, depending on the value of the parameter g_{12}. More precisely, when $0 <$

$g_{12} < 1$, the cylinder deforms in a nonaxisymmetric fashion and the buckling stress becomes dependent on the shear modulus, while when $g_{12} > 1$ the cylinder deforms in an axisymmetric fashion and the axial buckling stress does not depend on the shear modulus. The range of validity of each solution can be expressed as a function of the rib anlge ϕ as

$$0 \leq g_{12} < 1 \Rightarrow 0 \leq \phi < \pi/6 \qquad g_{12} > 1 \Rightarrow \pi/6 < \phi < \pi/2 \tag{4.10}$$

Consequently, using (3.44), (4.8), (4.9), and (4.10), the axial buckling stress of an anisogrid circular cylinder can be expressed as a function of the rib angle ϕ as follows

$$\sigma_{min}(\phi) = \begin{cases} E_r \delta \eta \cos^2(\phi) \sqrt{\frac{2}{3}\left(\sin^2(\phi) + \sqrt{\sin(\phi) + \sin^4(\phi)}\right)} & for \quad 0 < \phi < \frac{\pi}{6} \\ E_r \delta \eta \dfrac{\cos^2(\phi)}{\sqrt{3\sin(\phi)}} & for \quad \frac{\pi}{6} < \phi < \frac{\pi}{2} \end{cases} \tag{4.11}$$

When $\phi = \pi/6$ the anisogrid medium becomes isotropic (usually referred to as isogrid) with Young's modulus $E_r\delta$ and Poisson's ratio 1/3 (see (4.7)) and (4.11) assumes the following value.

$$\sigma_{min}(\pi/6) = \frac{1}{2}\sqrt{\frac{3}{2}} E_r \delta \eta = \frac{(E_r\delta)\eta}{\sqrt{3\left(1 - (1/3)^2\right)}} \tag{4.12}$$

A few comments can be made regarding (4.11). First, it is seen that the value of the critical stress depends on the rib width, spacing, and constitutive property only through a multiplicative factor $E_r\delta$, coinciding with the Young's modulus of the homogenized structure in the isogrid case. Consequently, the rib angle is the main parameter controlling the stability properties of the structure. Second, it can be easily verified using (4.11) that $\sigma_{min}(0) = \sigma_{min}(\pi/2) = 0$. This behaviour is due to the loss of accuracy of the homogenized model in the vicinity of the boundaries of the range of variation of the angle ϕ. In fact, according with (4.7), it is seen that $G_{12} = 0$ at $\phi = 0$ and $E_1 = 0$ at $\phi = \pi/2$. These singular values result in the axial buckling stress vanishing.

It is useful to define a dimensionless version of the axial buckling stress (4.11). A convenient choice is to normalize (4.11) by the isogrid value defined in (4.12). Performing

the needed calculation results in

$$\Sigma_{min}(\phi) = \frac{\sigma_{min}(\phi)}{\sigma_{min}(\pi/6)} = \begin{cases} \frac{4}{3}\cos^2(\phi)\sqrt{\sin^2(\phi) + \sqrt{\sin(\phi) + \sin^4(\phi)}} & for \quad 0 < \phi < \frac{\pi}{6} \\ \frac{2}{3}\sqrt{2}\frac{\cos^2(\phi)}{\sqrt{\sin(\phi)}} & for \quad \frac{\pi}{6} < \phi < \frac{\pi}{2} \end{cases} \tag{4.13}$$

It is important to note that (4.13) depends only on the rib angle ϕ. Equation (4.13) is plotted in in Fig. 4.2 in solid bold line. The extensions of the two functions defining (4.13)

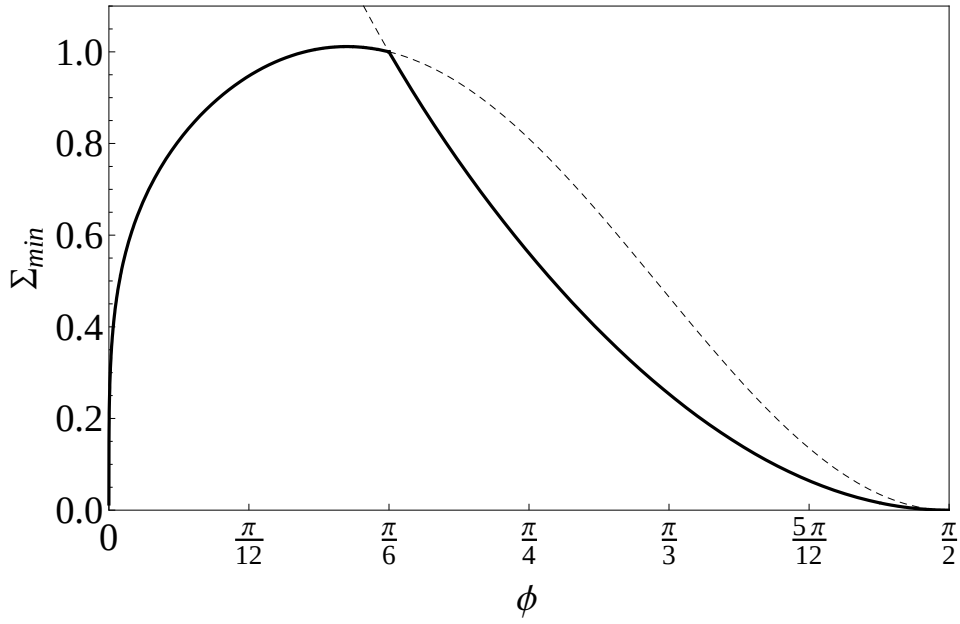

Figure 4.2: Normalized axial buckling stress versus rib angle ϕ: solid line, (4.13) within range of ϕ; dashed line, (4.13) outside range of ϕ

out of their respective ranges of validity are plotted as dashed lines to highlight the fact that the solution switches from the nonaxisymmetric branch, associated with the under shear-GMI material ($0 < \phi < \pi/6$), to the axisymmetric branch, associated with the over shear-GMI($\pi/6 < \phi < \pi/2$), at $\phi = \pi/6$, where the lattice becomes shear-GMI. Looking at Fig. 4.2 it is seen that (4.13) admits a maximum in the under shear-GMI region, where the anisogrid cylinder deforms in a nonaxisymmetric pattern. This maximum can be found to be at $\phi_{best} = 25.46°$. It is useful to remark that this value of ϕ is independent of the geometry (i.e., δ) and the elastic modulus (i.e., E_r) of the ribs.

In order to validate the derived closed-forms, results obtained using them will be compared with the exact solution obtained by spanning (3.15) for $m = 1, 2, ..., 200$ and

$n = 1, 2, ..., 50$. The calculation will be performed using the geometric and constitutive properties given in Tab. 4.1.

η	γ	δ	$E_r\,[Pa]$
0.01	2	0.1	130×10^9

Table 4.1: Geometric and constitutive properties of the anisogrid cylinder used for calculations

In order to compare (4.13) with (3.15), the value of (3.15) at $\phi = \pi/6$ must be evaluated. This value is given in Tab. 4.2 together with the value from (4.12). As seen from Tab. 4.2 the value predicted by (4.12) is in good agreement with the exact solution of (3.15). Moreover, as expected, the value predicted by (4.12) is slightly less than the exact one (3.15). Using

ϕ	Eq. (4.12)	Eq. (3.15)		
	$\sigma_{min}\,[Pa]$	m	n	$\sigma_{cr}\,[Pa]$
$\pi/6$	7.96084×10^7	9	1	7.96085×10^7

Table 4.2: Comparison between (4.12) and (3.15) solved for $\phi = \pi/6$

the value given in Tab. 4.2, a qualitative comparison between (3.15) and (4.13) is shown in Fig. 4.3, where the solid line represents (4.13) and the dots represent the solution of (3.15) at different values of the rib angle ϕ normalized with respect to the isogrid value given previously (i.e., $\sigma_{cr}(\pi/6) = 7.96085 \times 10^7$ Pa). Each dot is labeled with the pair of integers minimizing (3.15) for the corresponding values of ϕ. A few comments can be made based on Fig. 4.3. First, it is seen that (4.13) predicts accurately the solution of (3.15) over the whole range of the rib angle ϕ. Second, looking at the (m, n) labels it can be seen that the three different behaviours associated with the under shear-GMI, shear-GMI, and over shear-GMI material are confirmed. In fact, as predicted, the deformations associated with the under shear-GMI region are nonaxisymmetric (i.e., $n \neq 0$), the deformation associated with the over shear-GMI region are axisymmetric (i.e., $n = 0$), while the deformations associated with the shear-GMI case are, in general, independent from other regions. A quantitative comparison between the critical axial stress, estimated by (3.15) and normalized with respect to the isogrid critical stress, and the minimum stress estimated by (4.13) is given in Tab. 4.3 for the same values of ϕ given in Fig. 4.3 belonging to the under shear-GMI region. Looking at Tab. 4.3 it is seen that, as expected, (4.13) always gives an under-prediction of the true axial buckling stress given by (3.15), according with (4.13) to be a lower bound for (3.15).

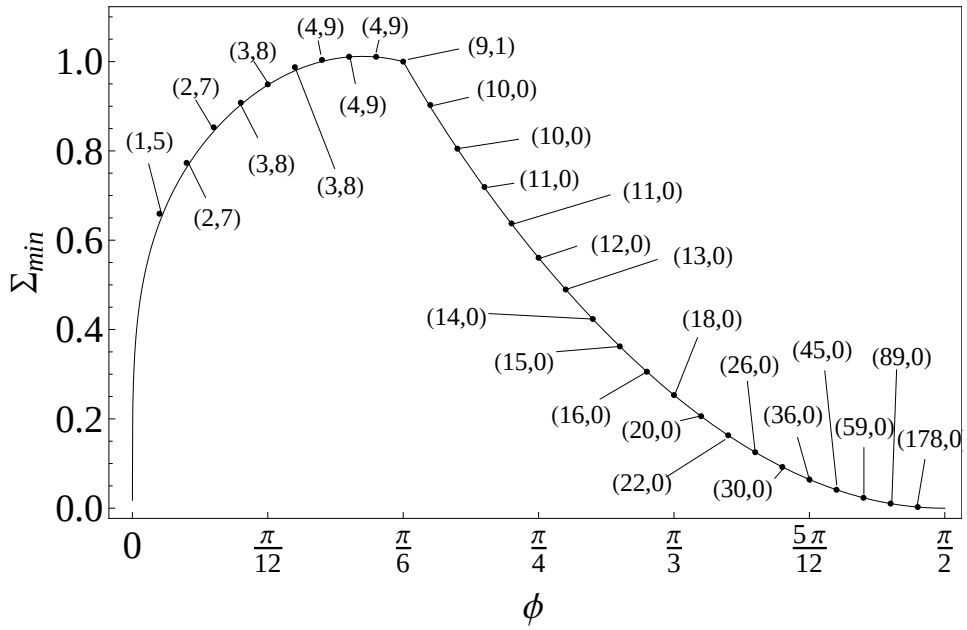

Figure 4.3: Normalized axial buckling stress versus rib angle ϕ: solid line (4.13); dots (3.15) with (m, n) producing minimum

ϕ	$\pi/60$	$\pi/30$	$\pi/20$	$\pi/15$	$\pi/12$	$\pi/10$	$7\pi/60$	$2\pi/15$	$3\pi/20$
Eq. (3.15)	0.6593	0.7730	0.8529	0.9078	0.9490	0.9874	1.0036	1.0109	1.0106
Eq. (4.13)	0.6398	0.7626	0.8437	0.9032	0.9475	0.9794	1.0001	1.0103	1.0102

Table 4.3: Comparison between (3.15) and (4.13) in the under shear-GMI region

Similarly in Tab. 4.4, a comparison between (3.15) and (4.13) is given for a few samples belonging to the over shear-GMI region (see Fig. 4.3). All the comments made for Tab. 4.3

ϕ	$\pi/5$	$7\pi/30$	$4\pi/15$	$3\pi/10$	$\pi/3$	$11\pi/30$	$2\pi/5$	$13\pi/30$	$7\pi/15$
Eq. (3.15)	0.8049	0.6376	0.4897	0.3621	0.2533	0.1633	0.0923	0.0412	0.0103
Eq. (4.13)	0.8049	0.6365	0.4897	0.3621	0.2533	0.1632	0.0923	0.0412	0.0103

Table 4.4: Comparison between (3.15) and (4.13) in the over shear-GMI region

apply to Tab. 4.4 even if the prediction given by (4.13) seems to be more accurate in the over shear-GMI region.

The shear-GMI case (i.e., $\phi = \pi/6$) needs some extra comments. In fact, as seen in the previous Chapter, for this value the minimum of (4.13) lies on an ellipse in the (m, n) plane. The two radii of the critical ellipse can be evaluated by substituting (4.8) and (4.9) in (3.34).

Performing the needed calculation, the following expressions are found

$$a = \frac{1}{\gamma\sqrt{\eta}}\sqrt[4]{\frac{2}{3}} = 4.518 \qquad b = \frac{1}{\sqrt{\eta}}\sqrt[4]{\frac{2}{3}} = 9.036 \tag{4.14}$$

The ellipse obtained using (4.14) is shown in Fig. 4.4. The critical ellipse does not pass

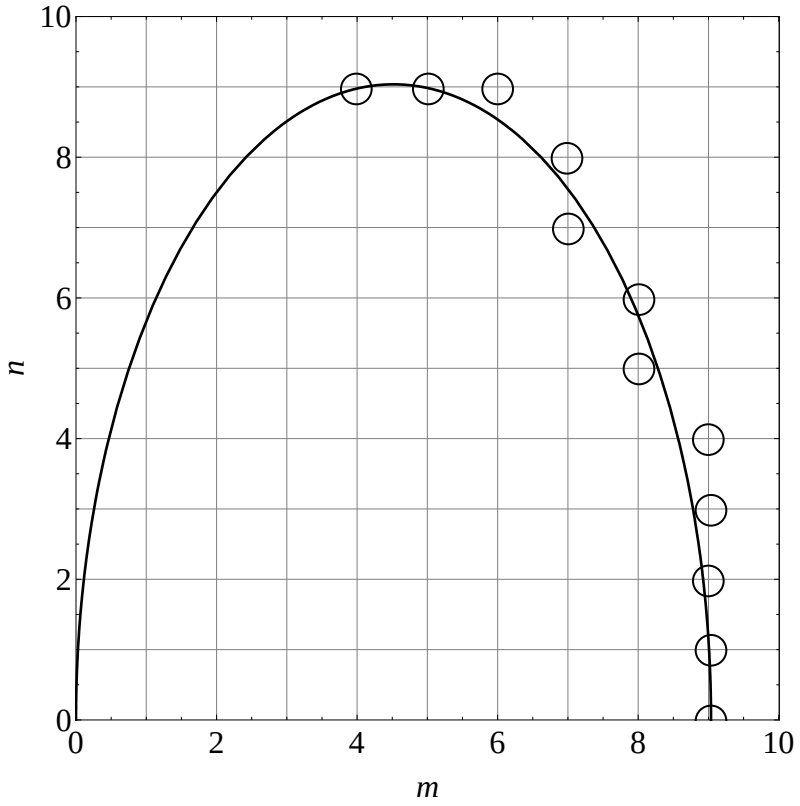

Figure 4.4: Critical ellipse associated with the isogrid case. Closest integer pairs encircled

through any integer pair, so (4.13) is not the exact solution for the problem under examination. By the way, looking at Fig. 4.4 it is seen that the pair $(9, 1)$ minimizing (3.15) for $\phi = \pi/6$ (see Tab. 4.2) corresponds to one of the integer pairs that are close to the critical ellipse (encircled in Fig. 4.4), in line with the theoretical prediction. From Fig. 4.4 it is seen that a slight variation of the ellipse geometry can cause the curve to pass exactly through some integer pairs, and consequently force (4.12) to be the exact solution of (3.15). The geometry of the ellipse can be controlled through the parameters η and γ. As seen previously (see (3.44) and (4.11)), the critical stress depends on the parameter η, but it is independent of the parameter γ that appears in the derived theory only as the aspect ratio of the critical ellipse. Consequently, the geometry of the critical ellipse in Fig. 4.4 can be modified by

varying the parameter γ without changing the critical stress of the cylinder. The proper value of γ_0 needed to force the critical ellipse to pass through the pair of integers (m_0, n_0) is given by the following expression

$$\gamma_0 = \frac{b \pm \sqrt{b^2 - n_0^2}}{m_0} \tag{4.15}$$

where b is given by (4.14). As seen from Tab. 4.5 the critical ellipse can be forced to pass through nine of the integer pairs encircled in Fig. 4.4 by varying the parameter γ within $\pm 5\%$ from its nominal value (i.e., $\gamma = 2$ in Tab. 4.1). Needless to say, for totality of the

m_0	n_0	γ_0	$\Delta\gamma\%$	Eq. (3.15)		
				m	n	$\sigma_{cr}\,[Pa]$
9	4	1.90427	-4.7865%	9	4	$7.96084\,10^7$
9	3	1.95106	-2.4470%	9	3	$7.96084\,10^7$
5	9	1.96841	-1.5795%	5	9	$7.96084\,10^7$
8	6	1.97406	-1.2970%	8	6	$7.96084\,10^7$
9	2	1.98310	-0.8450%	9	2	$7.96084\,10^7$
9	1	2.00184	$+0.0920\%$	9	1	$7.96084\,10^7$
9	0	2.00800	$+0.4000\%$	9	0	$7.96084\,10^7$
4	9	2.05750	$+2.8750\%$	4	9	$7.96084\,10^7$
8	5	2.07033	$+3.5165\%$	8	5	$7.96084\,10^7$

Table 4.5: Solution of (3.15) for nine variations of λ

cases shown in Tab. 4.5 the axial buckling stress estimated using (3.15) exactly coincides with the one obtained using the close form (4.12). The results of Tab. 4.5 are visualized in Fig. 4.5, where the $\hat{\eta}(\gamma, m_0, n_0)$ relations for the the nine integer pairs listed in Tab. 4.5 are shown as solid lines and $\hat{\eta}_0 = \eta/(\sqrt{12(1-\nu^2)}) = 0.00306186$ is shown as a dashed line. The intersection points having coordinates $(\hat{\eta}_0, \gamma_0)$, which represents the intersection between the $\hat{\eta}(\gamma, m_0, n_0)$ relations and $\hat{\eta}_0$, are shown as dots. As expected, the abscissa of each intersection coincides with one of the two roots of (4.15), as can be easily realized comparing Fig. 4.5 with Tab.4.5. The second root of (4.15) is still a valid solution but does not belong to the range shown in Fig. 4.5, i.e., $\pm 5\%$ with respect to the nominal value $\gamma = 2$.

If the requirement of having (4.12) be the exact solution of (3.15) is relaxed, a few more considerations can be made using the partition of the $(\gamma, \hat{\eta})$ plane derived in the previous Chapter. In Fig. 4.6 the partition is shown together with the line $\hat{\eta} = \hat{\eta}_0$ and a dot repre-

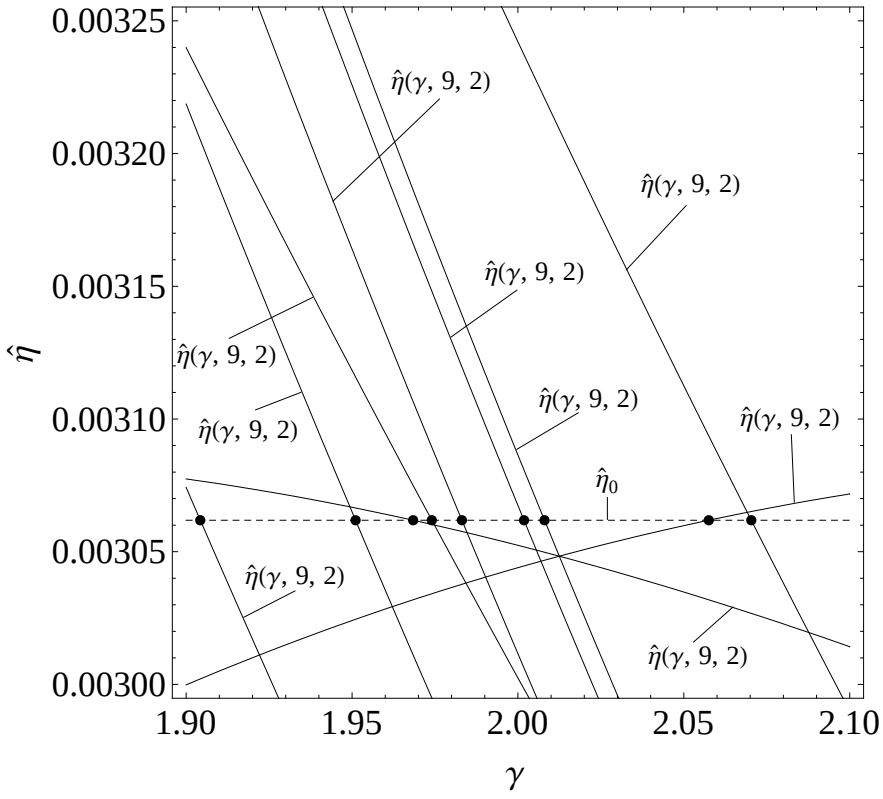

Figure 4.5: Visualization of the γ values needed to force the critical ellipse to pass through nine integer pairs

senting the nominal geometry of the cylinder (see Tab. 4.1). As seen, the partition correctly predicts the cylinder will buckle following the deformation pattern $(9, 1)$, and highlights the fact that a very slight decrease in the parameter γ (less than 0.06%) results in a cylinder that buckles with a deformation pattern of $(5, 9)$ instead of $(9, 1)$. Moving continuously on the line $\hat{\eta} = \hat{\eta}_0$, in the $\pm 5\%$ range of variation thirteen different tiles of the partition are crossed. It is interesting to note that four of these tiles are associated with the integer pair $(5, 9)$ and two with the pair $(4, 9)$, so the different integer pairs intercepted in the range of variation of $\pm 5\%$ are still nine, as shown in Tab. 4.5. The presence of multiple tiles associated with the same integer pair produces the cylinder that buckles with the same deformation pattern in multiple disjoint ranges of the parameter γ, alternated with different ranges within which the buckled shapes are different. More precisely, from Fig. 4.6 it is seen that continuously varying the parameter γ from 1.9 to 2.1 the following deformation pattern are produced $(9, 4) \leftrightarrow (5, 9) \leftrightarrow (9, 3) \leftrightarrow (5, 9) \leftrightarrow (8, 6) \leftrightarrow (5, 9) \leftrightarrow (9, 2) \leftrightarrow (5, 9) \leftrightarrow (9, 1) \leftrightarrow (9, 0) \leftrightarrow (4, 9) \leftrightarrow (8, 5) \leftrightarrow (4, 9)$. As seen from Fig. 4.6 the length of each

range is different and could be even very small. For example, the range associated with the deformation pattern $(8, 6)$ is $1.97345 < \gamma < 1.97484$ and a really small positive or negative variation of the cylinder geometry produces the cylinder that buckles following the pattern $(5, 9)$. An alternative way to highlight the sophisticated behaviour of an axially loaded

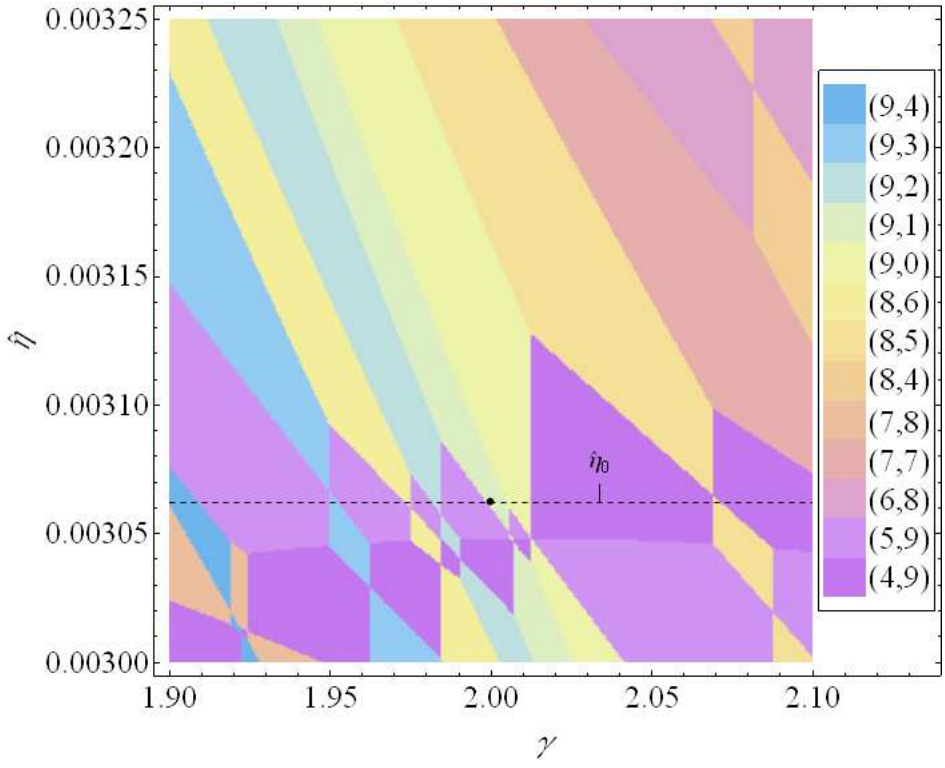

Figure 4.6: Tiles intercepted varying γ of $\pm 5\%$ and keeping $\hat{\eta}$ constant

shear-GMI circular cylinder is to plot σ_{cr} versus γ. When the parameter γ is thought as a variable, σ_{cr} can be interpreted as the minimum among a set of functions of γ obtained by spanning the wave numbers m and n among integers (see (3.15)). In Fig. 4.7 the nine functions associated with the nine integer pairs of interest, normalized with respect to σ_{min} (see (4.12)), are plotted together. The minimum profile, which represents σ_{cr} versus γ is highlighted with a bold line. Moreover, a dashed line is plotted at unity to represent the normalized value of $\sigma_{min}(\pi/6)$. Looking at Fig. 4.7, it is understood why in the partition of the $(\gamma, \hat{\eta})$ plane there appear multiple tiles associated with the pairs $(5, 9)$ and $(4, 9)$ alternating with the remaining ones. In fact, as seen from Fig. 4.7, different portions of the curves associated with these two integer pairs serve as minimum in different ranges of γ.

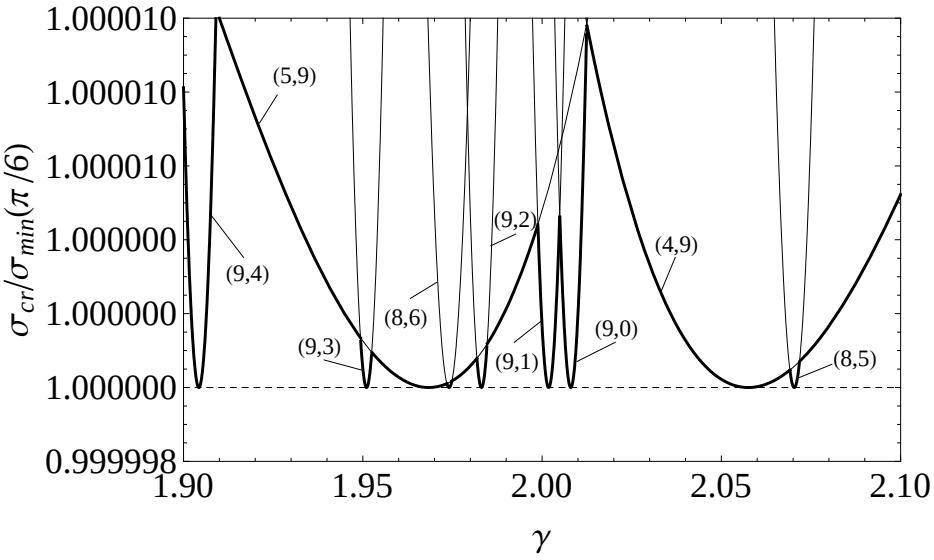

Figure 4.7: Normalized σ_{cr} versus γ

Moreover, from the figure it is seen that the nine values of γ listed in Tab. 4.5 and visualized in Fig. 4.5 correspond to those values (of γ) for which each of the nine functions associated with each of the nine pairs assumes its minimum. These minima, in the totality of the case of interest, are equal to the lower bound $\sigma_{min}(\pi/6)$. As seen previously, these points are the values of γ for which the critical ellipse passes through the corresponding integer pair and consequently (4.12) is the exact solution of (3.15). Similarly the range of γ for which each of the nine functions serves as a minimum corresponds to the ranges of the different crossed tiles in Fig. 4.6, as can be easily verified comparing the two figures.

This example shows how, for a shear-GMI medium, a slight change in the cylinder geometry can produce completely different buckled shapes without producing any change in the axial buckling stress. Moreover both axisymmetric and nonaxisymmetric deformations can be produced. It should be finally noted that, due to the plus-minus nature of (4.15), for each integer pair there exist two different geometries having the same buckled shape and the same axial buckling stress. For the axisymmetric solution (i.e., $n = 0$) the second possible geometry is given by $\lambda = 0$, i.e., an infinitely long cylinder.

In order to predict how the buckled shape of the anisogrid cylinder depends on the rib angle ϕ in the under and over shear-GMI regions, the coordinates of the stationary points as a function of ϕ must be determined. As shown in Chapter 3, for the over shear-GMI region the

global minimum is located at the stationary point of type-2 having coordinates (m_2, n_2), and for the over shear-GMI region at the stationary point of type-3 having coordinates $(m_3, 0)$. Substituting (4.8) and (4.9) in the general equation of the stationary point of type-2 and -3 given in Tab. 3.2 results in the following expressions

$$m_2(\phi) = \frac{1}{\gamma\sqrt{\eta}} \frac{\sqrt[4]{\sin(\phi)+\sin^4(\phi)}}{\cos(\phi)} \frac{\sqrt[4]{6\sin(\phi)\left(\sin^2(\phi)+\sqrt{\sin(\phi)+\sin^4(\phi)}\right)}}{\sqrt{\sqrt{1+\sin^3(\phi)}+3\sqrt{\sin^3(\phi)}}} \tag{4.16a}$$

$$n_2(\phi) = \frac{1}{\sqrt{\eta}} \frac{\sqrt[4]{6\sin(\phi)\left(\sin^2(\phi)+\sqrt{\sin(\phi)+\sin^4(\phi)}\right)}}{\sqrt{\sqrt{1+\sin^3(\phi)}+3\sqrt{\sin^3(\phi)}}} \tag{4.16b}$$

$$m_3(\phi) = \frac{1}{\gamma\sqrt{\eta}} \frac{\sqrt[4]{12\sin(\phi)}}{\cos(\phi)} \tag{4.16c}$$

The results obtained using (3.48) in order to predict the integers pair m and n minimizing (3.15) in the under shear-GMI region are shown in Figs. 4.8 (a) and (b), respectively. More precisely: $m_2(\phi)$ and $n_2(\phi)$ (see (4.16)) are shown in dashed line; (3.48), i.e., $\lceil m_2(\phi) - 1/2 \rceil$ and $\lceil n_2(\phi) - 1/2 \rceil$, are shown in solid line; and the exact solution of (3.15) is shown as dots for the same values of ϕ shown in Tab. 4.3. Looking at Fig. 4.8 it is seen that (3.48)

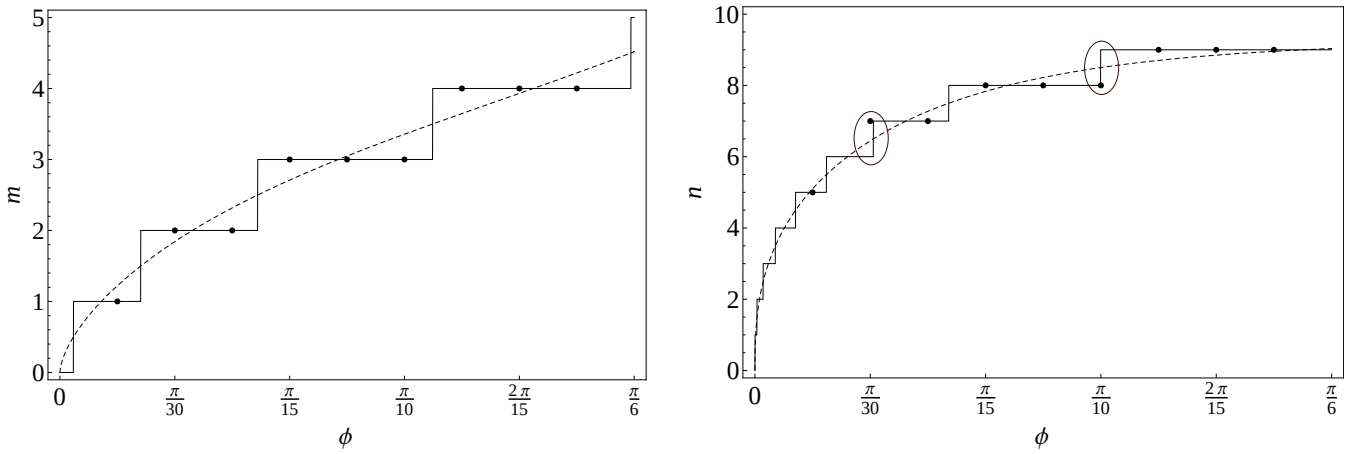

Figure 4.8: Comparison among (3.48), solid line; continuous solution (4.16), dashed line; and (3.15), dots, in the under shear-GMI region

correctly predicts the m value in the totality of the cases. Conversely, the value of n is not predicted correctly in two cases, namely $\phi = \pi/30$ and $\phi = \pi/10$, encircled in Fig. 4.8 (b).

It is easy to realize that the incorrect prediction is due to the proximity of $\phi = \pi/30$ and $\phi = \pi/10$ to the discontinuities of $\lceil n_2(\phi) - 1/2 \rceil$. Performing the needed calculation it can be shown that using (3.47) instead of (3.48) to predict the pair (m, n) the incorrect predictions are avoided. Similarly, the results obtained using (3.51) in order to predict the integer pair $(m, 0)$ minimizing (3.15) in the over shear-GMI region are shown in Fig. 4.9. More precisely:

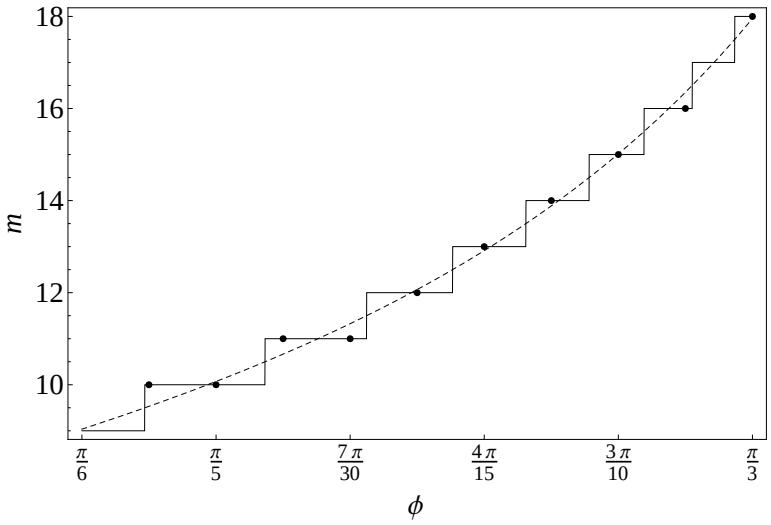

Figure 4.9: Comparison among (3.51), solid line; continuous solution (4.16), dashed line; and (3.15), dots, in a portion of the over shear-GMI region

$m_3(\phi)$ (see (4.16)) is shown in dashed line; (3.51), i.e., $\lceil m_3(\phi) - 1/2 \rceil$, is shown in solid line; and the exact solution of (3.15) is shown as dots. Due to the very large range of variability of $m_3(\phi)$ (see labels in Fig. 4.3), only a portion of the over shear-GMI region is shown in Fig. 4.9. Looking at Fig. 4.9 it is seen that (3.51) correctly predicts the m value in the totality of the cases shown in the figure. Performing the needed calculation, it can be shown that (3.51) correctly predicts the m value in the whole over shear-GMI range.

This chapter has presented a comprehensive analysis of the buckling behavior of anisogrid circular cylinders, assuming the lattice structure can be homogenized as an equivalent orthotropic material. Chapter 7 will make use of the findings in this chapter as applied to elliptical anisogrid cylinders. The next chapter provides an introduction to elliptical cylinders.

Chapter 5

Introduction to elliptical cylindrical shells

5.1 Introduction

In the previous chapters the stability of a cylindrical shell having a circular cross section has been investigated, resulting in a general theory describing the buckling behavior of an axially loaded orthotropic circular cylinder. As seen, the simple geometry of a circular cross section allows for the solution of the stability equation and the derivation of useful closed-form expressions. Furthermore, as reported in Chapter 1, the studies on noncircular cylinders have shown that the introduction of even a small imperfection in the circular cross section results in a deterioration of the stability performances. Both of those aspects contribute to the historical orientation to design cylindrical structures with circular cross sections. A few examples of structures containing circular cylindrical shells are shown in Fig. 5.1 However, noncircular cross section shells can introduce valuable advantages in the design of certain structures. An interesting example of this concept can be found in the most recent studies on aerodynamics. Those studies show how a noncircular fuselage blended with the wings will result in the entire aircraft which generates lift and minimizes drag, thereby increasing fuel economy. A comparison between the traditional tube-and-wings design and this futuristic design, usually referred to as blended wing body (BWB), is shown in Fig. 5.2.

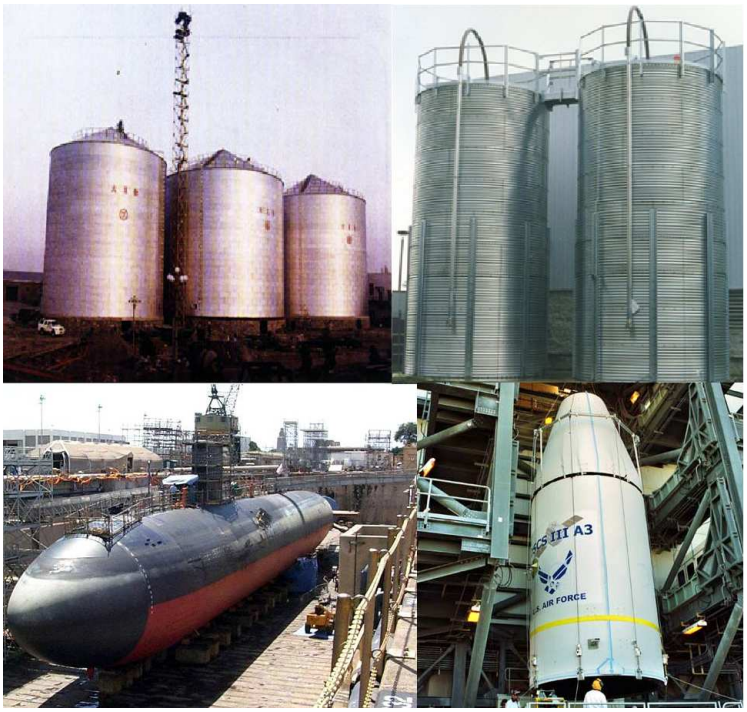

Figure 5.1: Examples of structures constructed of circular cylindrical shells

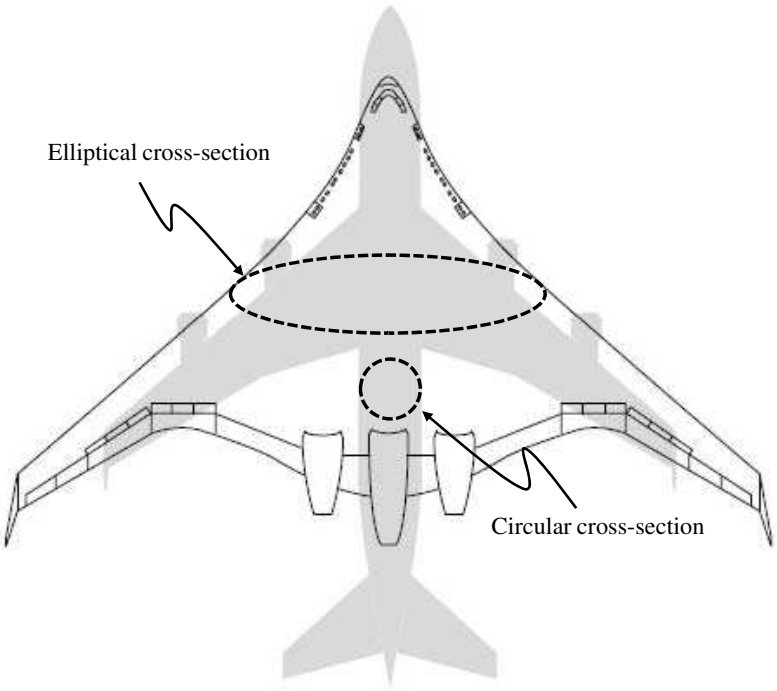

Figure 5.2: Comparison between traditional aircraft and BWB design

Another obvious advantage related to the use of an elliptical fuselage must be found in the unprecedent space availability within the center body of the structure that can be fruitfully earmarked to the efficient accommodation of large numbers of passengers and payload. On the other hand, the use of an elliptical fuselage comes with important structural inefficiencies. In fact, while for a traditional fuselage with a circular cross section a thin skin layer is able to carry internal pressure efficiently via hoop tension, for a noncircular fuselage cross section internal pressure loads also induce large bending stresses. Moreover, the structure is also loaded with further bending and compression loads due to aerodynamic and gravitational forces.

The BWB example highlights how the study of the improvement of the structural performance of an elliptical cylindrical shell is not only an interesting theoretical problem, but could even be of practical and economical interest.

5.2 Buckling behaviour of an elliptical cylinder

In this section a more detailed explanation of the deterioration of the stability performances of a noncircular section will be given. Initially, a circular cylinder will be considered. Then, keeping the circumference constant, an eccentricity e_0 will be assigned to the cross section. Finally the stability performances of the two shells will be compared in order to establish the dependence of the degeneration of structural properties with the assigned eccentricity.

Consider a circular cylindrical shell with radius R_c, constant thickness h_c, and length L_c. Suppose the given circular cross section is made elliptical by assigning to it an eccentricity e_0, but the circumference is kept the same as the original circular cylinder, namely $2\pi R_c$. An elliptical cross section can be described parametrically using the parameter t by the radius vector $\mathbf{v}(t)$ defined by

$$\mathbf{v}(t) = (a\cos(t), b\sin(t)) \qquad t \in [0, 2\pi) \tag{5.1}$$

where, as illustrated in Fig. 5.3, a and b are the major and the minor radii of the cross section of the midsurface and, as shown, $\mathbf{n}(t)$, $R(t)$, and $h(t)$ are the unit normal, the radius

of curvature, and the thickness of the cross section, which, for generality and later use in subsequent sections and chapters, is assumed to vary with circumferential position. The arc length in the circumferential direction is measured by the parameter s.

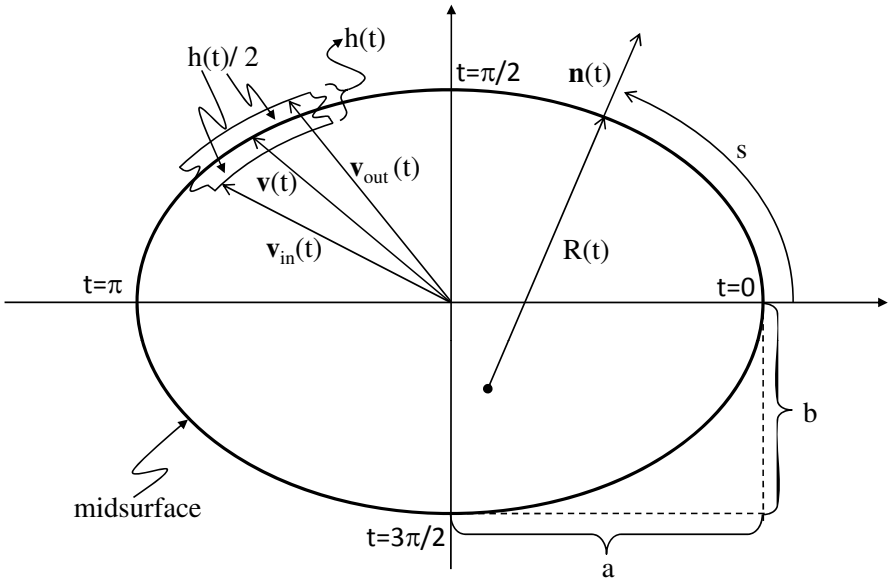

Figure 5.3: Cross section of midsurface of elliptical cylinder

The eccentricity of an ellipse e is defined as

$$e = \sqrt{1 - \frac{b^2}{a^2}} \tag{5.2}$$

It should be noted that $e = 0$ when $a = b$, the ellipse degenerating to a circle. Similarly, $e = 1$ when $b = 0$, the ellipse degenerating to a flat panel. Based on these arguments, it should be clear that in order to have an ellipse the following relation must be fulfilled: $0 \leq e < 1$. All the expressions involving the eccentricity derived in the following are meaningful only for this range of values. Using the parametrization (5.1), the unit normal can be expressed as

$$\mathbf{n}(t) = \left(\frac{b\cos(t)}{\sqrt{a^2\sin^2(t) + b^2\cos^2(t)}}, \frac{a\sin(t)}{\sqrt{a^2\sin^2(t) + b^2\cos^2(t)}} \right) \qquad t \in [0, 2\pi) \tag{5.3}$$

Using (5.3), an analytical expression for the outer and the inner surface of a variable thickness

ellipse can be obtained by adding and subtracting, respectively, a quantity $h(t)/2$ along the normal direction from the midsurface, as shown in Fig. 5.3. The radius vectors describing the cross sections of those surfaces can be written as follows:

$$\mathbf{v}_{out}(t) = \mathbf{v}(t) + \frac{h(t)}{2}\mathbf{n}(t) \qquad \mathbf{v}_{in}(t) = \mathbf{v}(t) - \frac{h(t)}{2}\mathbf{n}(t) \tag{5.4}$$

The radius of curvature of the elliptical cross section can be expressed as a function of the parameter t as

$$R(t) = \frac{(b^2\cos^2(t) + a^2\sin^2(t))^{\frac{3}{2}}}{ab} \qquad t \in [0, 2\pi) \tag{5.5}$$

The major radius a and the minor radius b of an ellipse having an assigned eccentricity e_0 and the same circumference as the original circular cylinder are given by

$$a = \frac{R_c}{\mathcal{E}(e_0^2)} \qquad\qquad b = \frac{R_c}{\mathcal{E}(e_0^2)}\sqrt{1 - e_0^2} \tag{5.6}$$

where $\mathcal{E}(.)$ is the normalized complete elliptical function of second kind defined by

$$\mathcal{E}(k) = \frac{2}{\pi}\int_0^{\frac{\pi}{2}} \sqrt{1 - k\sin^2(\theta)}\, d\theta \tag{5.7}$$

It should be noted that when the assigned eccentricity $e_0 = 0$ (i.e., the circular case), (5.6) gives correctly $a = R_c$ and $b = R_c$, while when $e_0 = 1$ (i.e., the flat plate case), (5.6) gives correctly $a = \pi R_c/2$ and $b = 0$.

The radius of curvature $R(t)$ of an ellipse having the same circumference as the original circle and an assigned eccentricity e_0 can be obtained by substituting (5.6) in (5.5), that is,

$$R(t, e_0) = \frac{R_c}{\mathcal{E}(e_0^2)}\sqrt{\frac{(1 - e_0^2\cos^2(t))^3}{1 - e_0^2}} \qquad t \in [0, 2\pi) \tag{5.8}$$

The minimum and the maximum radii of curvature are given by the following relations:

$$R_{min} = R(0) = \frac{R_c}{\mathcal{E}(e_0^2)}(1 - e_0^2) \qquad\qquad R_{max} = R(\pi/2) = \frac{R_c}{\mathcal{E}(e_0^2)}\frac{1}{\sqrt{1 - e_0^2}} \tag{5.9}$$

The prebuckling deformed shape of a circular cylinder at the buckling load level, simply supported at both its ends and of constant wall thickness, is shown in Fig. 5.4 (a). The

results in Fig. 5.4 (a) were computed using the commercially-available finite element code $ABAQUS^{®}$ [63], considering a linear elastic analysis, and including geometrically nonlinear stress-displacement relations. Details of finite-element analysis will be presented shortly. Looking at the picture it is quite evident that the deformations of this shell are axially symmetric and all circumferential locations of the cylinder equally contribute to the stability of the structure Similarly, the prebuckling deformed shapes of the elliptical cylinders with

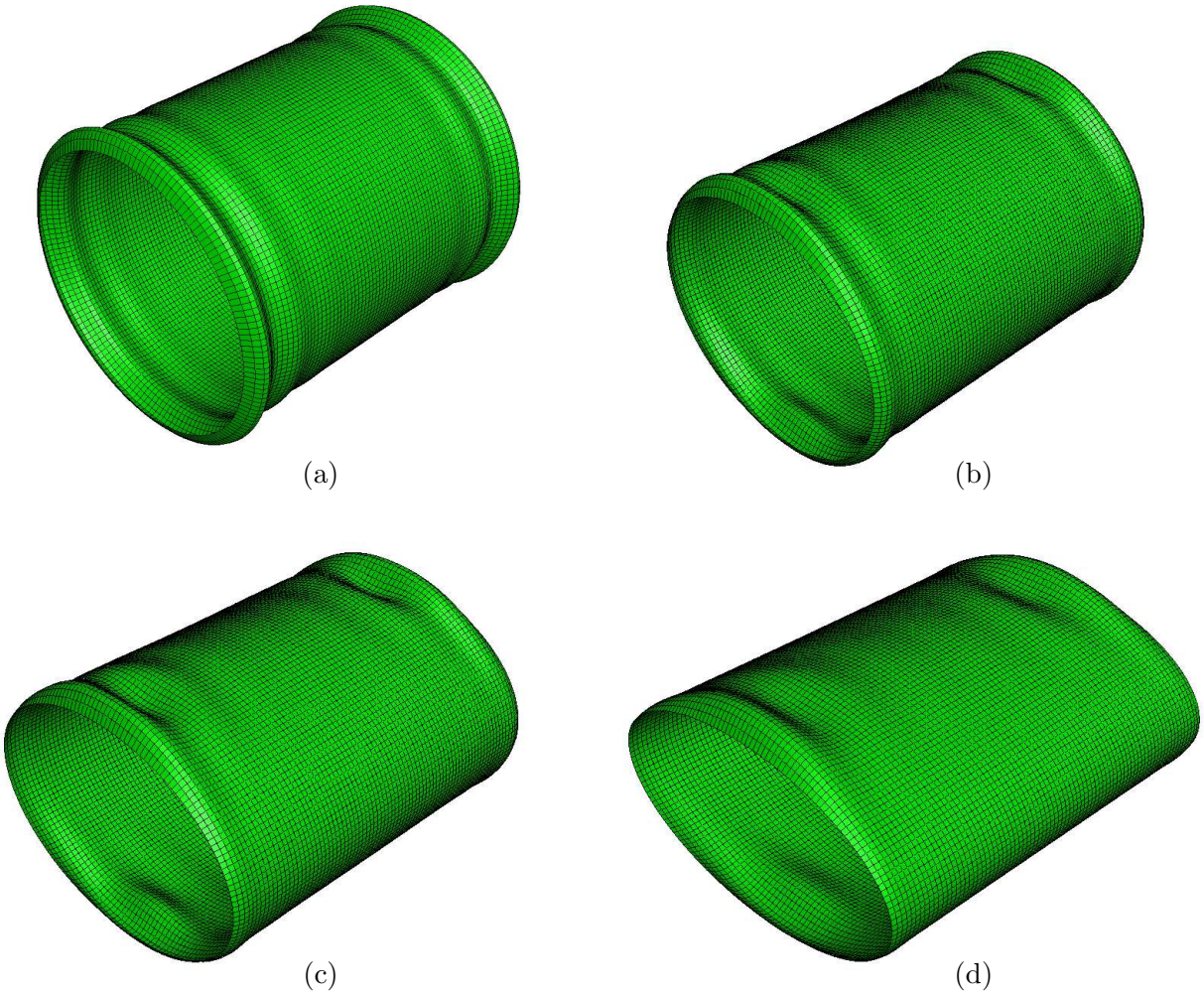

Figure 5.4: Deformed shape of an axially-loaded simply-supported cylindrical shell with constant wall thickness: (a) circular cross section (b) elliptical cross section, $e_0 = 0.50$ (c) elliptical cross section, $e_0 = 0.70$ (d) elliptical cross section, $e_0 = 0.85$.

the same constant wall thickness as the circular cylinder and obtained by assigning the eccentricities $e_0 = 0.50$, $e_0 = 0.70$, and $e_0 = 0.85$ to the original circular cross section are illustrated in parts (b), (c), and (d) of Fig. 5.4, respectively. From this figure is evident that

the deformations occur mainly at the flatter locations of the elliptical cross section, while the more curved portions are practically undeformed. The flatter portions correspond to the locations of the cross-section having maximum radius of curvature. This behaviour can be interpreted keeping in mind that, as seen in Chapter 3, the axial buckling load of a circular cylinder depends on the inverse of the radius of curvature that, for a circular cylinder, is the same at all circumferential locations. Conversely, for an elliptical cross section the radius of curvature becomes a function of circumferential location, being maximum at the flatter regions, and consequently, even the critical stress becomes different for each circumferential location, being minimum in the flatter regions. Based on these arguments it can be seen that the axial buckling load of an elliptical cylindrical shell can still be predicted using (3.44) if the parameter η is defined as h/R_{max}. This statement is equivalent to asserting that the axial buckling behaviour of an elliptical cylinder is coincident with the one of a circular cylinder having radius equal to the maximum radius of curvature that the ellipse assumes all around its circumference. This circle is usually referred to as the maximum osculating circle. In Fig. 5.5 an ellipse having eccentricity $e = 0.7$ is shown in solid line together with its maximum osculating circle, shown in dashed line.

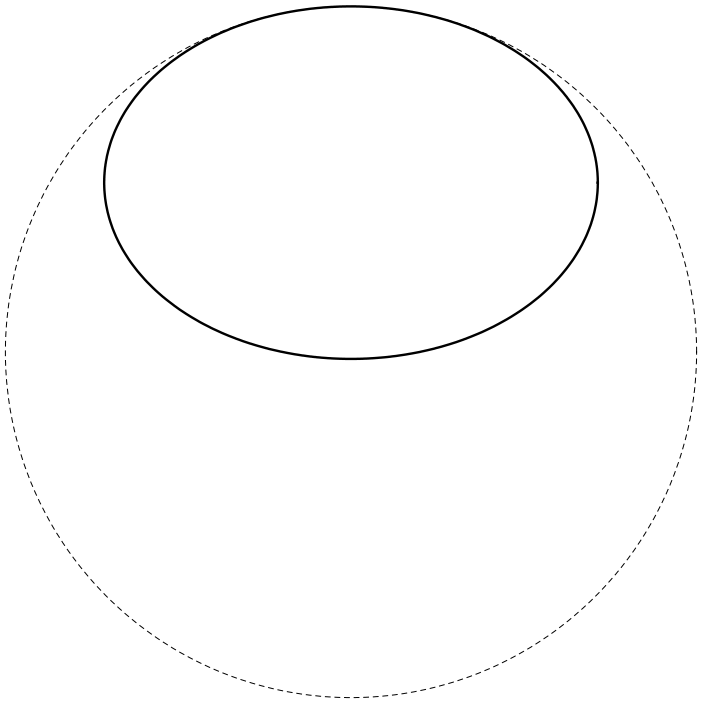

Figure 5.5: Maximum osculating circle of an ellipse having $e = 0.7$.

Based on this idea, using (5.9), the ratio between the buckling stress of a constant thickness elliptical (CTE) cylinder, obtained by assigning an eccentricity e_0 to the original constant thickness circular (CTC) cylinder, and the original CTC cylinder is predicted to be

$$\frac{\sigma_{CTE}}{\sigma_{CTC}} = \frac{R_c}{R_{max}} = \mathcal{E}(e_0^2)\sqrt{1-e_0^2} \tag{5.10}$$

It should be noted that the ratio of the buckling stresses between the two cylinders depends only on the assigned eccentricity e_0. In Fig. 5.6 the ratio in (5.10) is plotted vs. the assigned

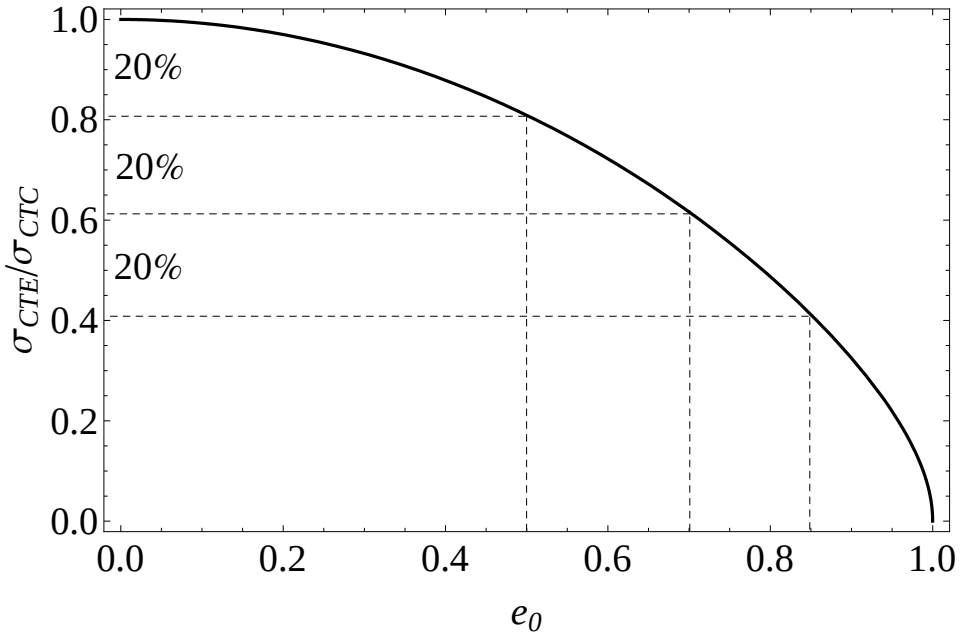

Figure 5.6: Comparison between the buckling stress of elliptical and original circular cylinders.

eccentricity e_0. As seen, the buckling stress of a CTE cylinder decreases considerably with increasing eccentricity. For example, about 20% of the stress level is lost when an eccentricity of 0.50 is assigned to the original CTC cylinder. Similarly about 40% of the stress level is lost for $e_0 = 0.70$ and about 60% for $e_0 = 0.85$.

5.3 Numerical validation of the developed analysis

Since the developed analysis was based on a rather simple premise (i.e., the elliptical cross section is treated as its maximum osculating circle and prebuckling rotations are ne-

glected) (5.10) will be compared with a finite-element analysis performed using *ABAQUS*. The finite-element mesh employs 81 equispaced nodes in the axial direction and 168 equispaced nodes in the circumferential direction, for a total of 13,440 elements. A S4R four-node shell element from the *ABAQUS* library is used. This element uses thick-shell theory as the shell thickness increases and becomes a Kirchhoff thin-shell element as the thickness decreases. Geometrically nonlinear prebuckling analysis will be employed, and the results for simply-supported boundary conditions will be considered. The buckling condition will be identified by applying to one end of each cylinder the smallest axial compressive displacement that causes the tangent stiffness matrix of the numerical analysis to become singular. The stress state for this condition, in particular, the axial stress level, will be considered the buckling stress. The quantities of interest at this level of displacement will be compared with the respective analytical predictions for three values of assigned eccentricities, $e_0 = 0.50$, 0.70, and 0.85, as discussed in Fig. 5.6, and two cylinder sizes in order to check the generality of (5.10). So-called small and large circular cylinders with the geometrical dimensions listed in Tab. 5.1 will be considered as the original CTC cylinders for the two sizes. In addition to the increased overall size of the large cylinder, the large cylinder is more

	R_c	L_c	h_c
small	0.1 m	0.32 m	1.12 mm
large	0.5 m	1.60 m	2.24 mm

Table 5.1: Geometrical properties used in the calculations

flexible than the small cylinder in terms of wall thickness to radius ratio, i.e., the wall of the large cylinder is thinner relative to the radius. The mesh described above was used for both cylinder sizes. Moreover, two different isotropic materials will be taken into consideration, namely aluminum and an isogrid lattice structure. The constitutive properties of these material are listed in Tab. 5.2. For reasons that will be clear in the following two chapters, the

	E [GPa]	ν
Aluminum	70	0.3
Isogrid	13	1/3

Table 5.2: Constitutive properties used in the calculations

circular and elliptical aluminum cylinders will be referred to in the following as the CTC and CTE cylinders, respectively. The circular isogrid cylinder and the elliptical isogrid cylinder

will be referred to in the following as the CGC and CGE cylinders, respectively. The G in the notation stands for Geometry, meaning the rib angle of the lattice [1].

Using (5.6), the major and the minor radii a and b for the three different values of the eccentricity e_0 can be evaluated for both small and large cylinders. These values are listed in Tab. 5.3, along with the ratios of the minor to major radii.

e_0	small		large		b/a
	a	b	a	b	
0.50	0.1070	0.0927	0.5350	0.4635	0.87
0.70	0.1159	0.0827	0.5795	0.4135	0.71
0.85	0.1279	0.0674	0.6395	0.3370	0.53

Table 5.3: Tabulation of relevant quantities for three values of eccentricity

In Fig. 5.7 (a) and (b) the axial stress at the buckling condition as computed by *ABAQUS* for the CTC and CTE cylinders for all the eccentricity values under consideration for the small and the large cylinders, and normalized by the critical stress of the CTC, are plotted versus the normalized circumferential location $s/2\pi R_c$ (see Fig. 5.3) for simply-supported boundary conditions. Looking at this figure, it is first observed that the finite-

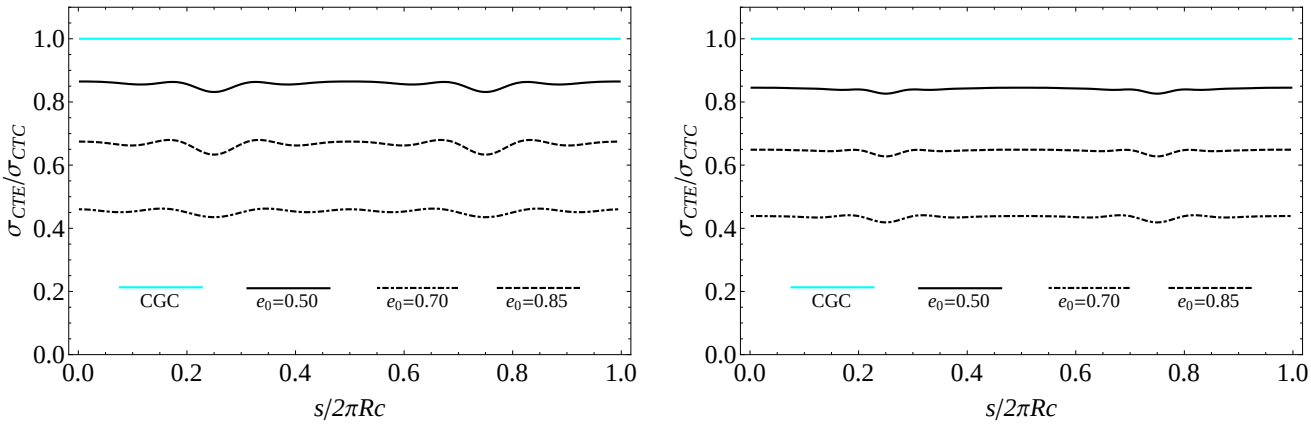

(a) small (b) large

Figure 5.7: Circumferential variation of axial stress at the buckling condition for small and large CTC and CTE cylinders and three values of eccentricity

element analysis predicts that axial stress for CTE cylinders varies with circumferential position. The degree of the variation depends on the assigned eccentricity e_0 and the size

[1] In Chapter 7 the rib angle (i.e., the Geometry) of an elliptical lattice cylinder will be allowed to vary with circumferential position, and the notation VGE will be used. Hence the notation CGE for the case being discussed presently, where the rib angle is fixed for all circumferential locations at $\phi = \pi/6$.

of the cylinder. The variation is less for the large cylinder, due to lower value of the ratio h/R. For the CTE cylinder, most of the variation occurs in the flatter portions of the cross section, $s/(2\pi R_c) = 0.25, 0.75$, where the stress level is equal to the buckling stress. In Tab. 5.4 both the circumferentially-averaged magnitude and the circumferentially-averaged normalized magnitude of the axial stress of the CTE cylinders at the buckling condition as computed from the finite element results of Fig. 5.7 are reported for all the eccentricity values of interest for both small and large cylinders. In the same table the ratio of buckling stress for the CTE cylinder relative to the CTC cylinder, $\sigma_{CTE}/\sigma_{CTC}$, predicted in the developed analysis by (5.10) and Fig. 5.6 is reported. Although the finite-element calculations show the axial stress in the CTE cylinders to vary somewhat with circumferential position, considering the average axial buckling stress from the finite-element calculations for the CTE cylinders in that ratio, i.e., $\overline{\sigma}_{CTE}/\sigma_{CTC}$, it is seen from the table that the analytic predictions of (5.10) are no more than 6% different than the finite-element calculations of that ratio. Similarly, the buckling loads computed by the finite-element model for small and large CTE cylinders for the three eccentricity values are reported in Tab. 5.5. Both the absolute and the normalized values are given.

e_0	$\overline{\sigma}_{CTE}$, [MPa]		$\overline{\sigma}_{CTE}/\sigma_{CTC}$		
	small	large	small	large	Eq. (5.10)
0.50	352.59	140.21	0.8567	0.8404	0.8090
0.70	274.03	107.61	0.6659	0.6550	0.6163
0.85	186.58	72.65	0.4534	0.4355	0.4118

Table 5.4: Circumferentially-averaged axial stress for isotropic cylinders at the buckling condition

e_0	P_{CTE}, [N]		P_{CTE}/P_{CTC}		
	small	large	small	large	Eq.(5.10)
0.50	248121	986705	0.8567	0.8404	0.8090
0.70	192842	757300	0.6659	0.6550	0.6163
0.85	131298	511286	0.4534	0.4355	0.4118

Table 5.5: Axial load at the buckling condition of isotropic cylinders for three values of eccentricities

In Fig. 5.8 (a) and (b) the axial stress at the buckling condition as computed by *ABAQUS* for the CGC and CGE cylinders for all the eccentricity values under consideration for the small and the large cylinders, and normalized by the critical stress of the CGC, are plotted versus the normalized circumferential location $s/2\pi R_c$ (see Fig. 5.3) for

simply-supported boundary conditions. Comparing Fig. 5.8 and 5.7 it can be realized

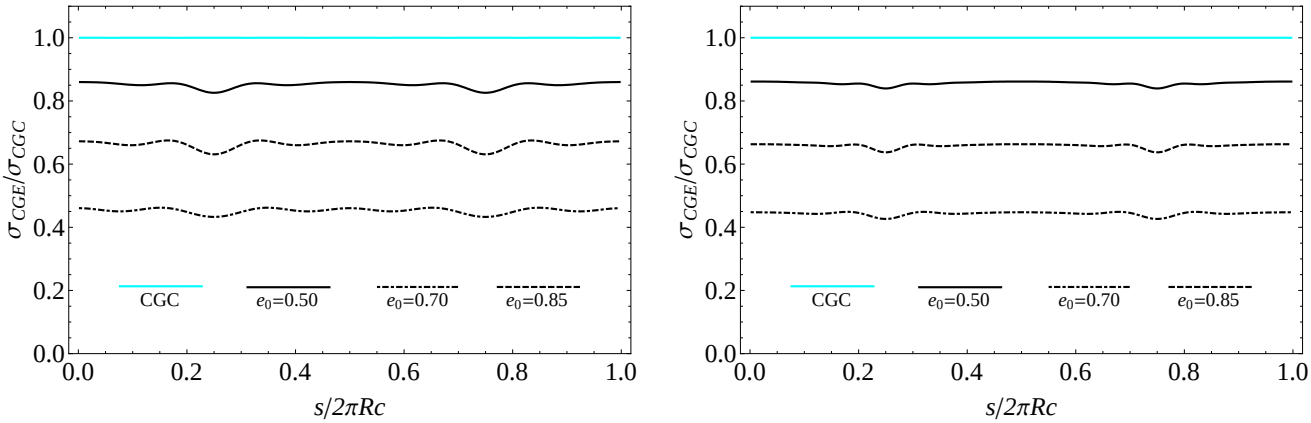

(a) small (b) large

Figure 5.8: Circumferential variation of axial stress at the buckling condition for small and large CGC and CGE cylinders and three values of eccentricity

that all the comments made regarding CTE and CTC cylinders apply as well as to CGE and CGC cylinders. In Tab. 5.6 both the circumferentially-averaged magnitude and the circumferentially-averaged normalized magnitude of the axial stress of the CGE cylinders at the buckling condition as computed from the finite element results of Fig. 5.8 are reported for all the eccentricity values of interest for both small and large cylinders. In the same table the ratio of buckling stress for the CGE cylinder relative to the CGC cylinder, $\sigma_{CGE}/\sigma_{CGC}$, predicted in the developed analysis by (5.10) and Fig. 5.6 is reported. Although the finite-element calculations show the axial stress in the CGE cylinders to vary somewhat with circumferential position, considering the average axial buckling stress from the finite-element calculations for the CTE cylinders in that ratio, i.e., $\overline{\sigma}_{CGE}/\sigma_{CGC}$, it is seen from the table that the analytic predictions of (5.10) are no more than 6% different than the finite-element calculations of that ratio. Similarly, the buckling loads computed by the finite-element model for small and large CGE cylinders for the three eccentricity values are reported in Tab. 5.7. Both the absolute and the normalized values are given. From Tabs.

e_0	$\overline{\sigma}_{CGE}$, [MPa]		$\overline{\sigma}_{CGE}/\sigma_{CGC}$		
	small	large	small	large	Eq. (5.10)
0.50	65.757	26.168	0.8508	0.8559	0.8090
0.70	51.213	20.124	0.6626	0.6583	0.6163
0.85	34.981	13.560	0.4526	0.4435	0.4118

Table 5.6: Circumferentially-averaged axial stress for isogrid cylinders at the buckling condition

e_0	P_{CGE}, [N]		P_{CGE}/P_{CGC}		
	small	large	small	large	Eq. (5.10)
0.50	46274	184148	0.8508	0.8559	0.8090
0.70	36039	141618	0.6626	0.6583	0.6163
0.85	24061	95425	0.4526	0.4435	0.4118

Table 5.7: Axial load at the buckling condition of isogrid cylinders for three values of eccentricities

5.5 and 5.7 it can be noted that the buckling load of a CTE and CGE cylinder decreases considerably with respect to the CTC and CGC cylinders, respectively, as the eccentricity increases. The ratios P_{CTE}/P_{CTC} and P_{CGE}/P_{CGC} are described quite accurately by (5.10). From the results reported in this section it can be concluded that the use of the maximum radius of curvature of an isotropic or isogrid elliptical cylinder in the equation for the critical stress of an isotropic circular cylinder (i.e., (3.44) with $g_{12} = 1$) results in a good estimation of the buckling load of the elliptical cylinders.

5.4 The factory analogy: Two improvement strategies

In this section two different techniques to improve the axial load capability of an elliptical cylindrical shell will be proposed. As mentioned in the previous section, while commenting on Fig. 5.4, for the circle all locations around the circumference equally resist deformations of the shell, while for an ellipse the more curved regions resist deformations more than the flatter regions. This behavior can be interpreted by saying that the load capability of an elliptical section is dependent on the circumferential location, due to the continuously changing curvature. When the cylinder is axially loaded, the flatter portions reach their critical stress before than any other locations around the circumference, and consequently control the bucking of the shell. It should be noted that all the remaining portions of the elliptical shell never reach their critical stress. Those arguments furnish an explanation of the reason why the elliptical shells deform at the flatter regions only. This interpretation agrees with the well-accepted results that the buckling is a local phenomenon governed by the local stiffness and stress level of the structure.

The deterioration of the buckling capacity of the original CTC (CGC) cylinder after a given eccentricity e_0 is assigned to its cross section provides motivation to improve the

buckling capacity of the elliptical cylinder and hopefully restore the capacity to that of the original CTC (CGC) cylinder. Two different strategies can be designed by using a striking analogy. Suppose that in a factory each employee has exactly the same skills as the other employees, so each can carry out the same amount of work before being too stressed to be productive. This would be a perfect factory. A circular section behaves exactly in this way. Unfortunately, real life is far from perfect and each employee is capable of carrying a different amount of work. Now if each task assigned to each different employee is crucial for the functioning of the factory, it should be quite easy to understand that the production of the factory is determined by the employee having the least skills. This is exactly what happens in an elliptical cylindrical shell, the flattest portion of the cross section having the least ability to resist buckling. At this point, in the factory, the human resources director has two options to make the factory more productive. The director can try to make the factory as perfect as possible by assigning a longer shift to the worst employees and a shorter one to the more productive workers, thereby trying to make the actual amount of work of each employee the same. This technique will be referred to in the following as the worst works more (WWM) approach. A different technique is to take cognizance of the imperfection of the world and try to distribute the work amount among the employees, taking into account the skills of each of them, i.e., giving a bigger charge to the more skilled employees and a lower charge to the less skilled ones. This technique will be referred to in the following as the best works more (BWM) approach. In the next two chapters the implementation of both the WWM and the BWM approaches will be investigated to improving the axial buckling capacity of an elliptical cylinder. In Chapter 6 it will be described how it is possible to tailor the thickness of an elliptical cylindrical shell constructed of a homogeneous isotropic material in order to force all the portions of the cylinder to reach their critical stress level at the same value of applied axial displacement, the result being the critical is stress independent of circumferential position (i.e., the WWM approach). In Chapter 7 it will be described how it is possible to tailor the material properties of an elliptical cylindrical shell, constructed of nonhomogeneous orthotropic material and having uniform thickness, in order to force all portions of the cylinder to reach their critical stress level at the same value of applied axial displacement, being the critical stress dependent on circumferential position (i.e., the BWM approach).

5.5 Nondimensionalization and notation

Based on the previous arguments, it is clear that when a variable thickness elliptical cylinder made of nonhomogeneous orthotropic material is taken into consideration, both the parameter η and the constitutive properties defining the critical stress (see (3.44)) become functions of the circumferential position and the assigned eccentricity of the elliptical cross section. This means that for each assigned eccentricity each different portion of the resulting elliptical cylinder becomes unstable for a different level of stress. Using the parameter t, previously introduced in (5.1), to parametrize the quantities of interest, the local critical stress for a nonhomogeneous orthotropic elliptical cylinder having variable thickness obtained by assigning an eccentricity e_0 to a circular cross section can be written using (3.44) as follows

$$\sigma_{cr}(t, e_0) = \eta_c \left(\frac{\zeta(t, e_0)\varphi(t, e_0)}{\rho(t, e_0)} \right) E_1(t, e_0) \tag{5.11}$$

where $\eta_c = h_c/R_c$ (see (3.7)) and $E_1(t, e_0)$ is the Young's modulus in the axial direction. The three functions in parenthesis are dimensionless. More precisely, $\varphi(t, e_0)$ depends only on constitutive properties and is defined by

$$\varphi(t, e_0) = \begin{cases} \sqrt{\dfrac{g_{12}(t, e_0)}{3e_{12}(t, e_0)(1 - \nu^2(t, e_0))}} & \forall\, t \in [0, 2\pi) : \, 0 < g_{12}(t, e_0) < 1 \\ \dfrac{1}{\sqrt{3e_{12}(t, e_0)(1 - \nu^2(t, e_0))}} & \forall\, t \in [0, 2\pi) : \, g_{12}(t, e_0) \geq 1 \end{cases} \tag{5.12}$$

whereas $\rho(t, e_0)$ depends only on the radius of curvature of ellipse and using (5.8) is defined by

$$\rho(t, e_0) = \frac{R(t, e_0)}{R_c} = \frac{1}{\mathcal{E}(e_0^2)} \sqrt{\frac{(1 - e_0^2 \cos^2(t))^3}{1 - e_0^2}} \qquad t \in [0, 2\pi) \tag{5.13}$$

and $\zeta(t, e_0)$ depends only on the thickness and is defined by

$$\zeta(t, e_0) = \frac{h(t, e_0)}{h_c} \qquad t \in [0, 2\pi) \tag{5.14}$$

From the definition (5.13) it is immediately seen that $\rho(t, 0) \equiv 1$. Similarly, from the definition (5.14) it is immediately seen that when the thickness of the elliptical cylinder is uniform with circumferential position and equal to the thickness of the original circular

cylinder h_c, then $\zeta(t,0) \equiv 1$.

Based on the previous arguments, it seems reasonable to assume that the critcal stress of a nonhomogeneous orthotropic elliptical cylinder, obtained by assigning an eccentricity e_0 to a circular cylinder and having the thickness varying with circumferential location, is determined by its weakest location around the circumference. Symbolically this concept can be expressed as

$$\sigma_{cr}(e_0) = \eta_c \left(\min_{0 \le t < 2\pi} \left\{ \left(\frac{\zeta(t,e_0)\varphi(t,e_0)}{\rho(t,e_0)} \right) E_1(t,e_0) \right\} \right) \tag{5.15}$$

As implied, in Chapter 6, to follow, (5.15) will be used to develop approaches to tailor, with circumferential position, the wall thickness of an elliptical cylinder constructed of an orthotropic material so as to improve its axial buckling capability. In Chapter 7 (5.15) will be used to tailor, with circumferential position, the orthotropic material properties of an elliptical cylinder with a constant wall thickness so as to improve its axial buckling capability.

Chapter 6

Variable thickness elliptical cylindrical shells: a WWM approach

6.1 Introduction

In Chapter 5 it was mentioned that the equation (3.44) for the buckling stress of a homogeneous orthotropic circular cylinder with a constant wall thickness provides a good approximation for the buckling stress of a constant-wall-thickness elliptical cross section when the radius of the circle is replaced with the radius of the maximum osculating circle. As seen, this techique is based on the idea of assuming the axial buckling behavior of an elliptical cylinder is identical to the axial buckling behavior of a circular cylinder having the radius equal to the maximum radius of curvature of the elliptical cross section. As shown in Tab. 5.4 the predictions based on this assumption are in good agreement with finite-element predictions. However, as shown in Fig. 5.4, elliptical cylinders deform mainly at the flatter regions, while circular cylinders deform in a axisymmetric fashion. As mentioned previously this behavior can be explained by recognizing that, due to the continuously varying curvature, each portion of the elliptical cross section reaches its critial level of stress for a different value of the applied axial displacement. When an axial displacement is applied to a homogeneous elliptical cylinder with constant wall thickness, the induced stress is roughly constant around the circumferential direction (see Fig. 5.7) and the flatter regions of the cross section reach

their critical level of stress before any other portions of the cross section, which are working at a lower stress level than their critical one. This behavior compromises the performance of the entire structure. The WWM approach, introduced at the end of Chapter 5, is based on the idea of forcing each location of the cross section to have the same critical stress. This approach can be implemented by tailoring the thickness of the elliptical cylinder in such a fashion so as to balance the effects of the continuously-varying curvature on the ability to resist buckling.

6.2 Three variable-thickness elliptical cylindrical shell designs

When a variable thickness elliptical cylinder made of a homogeneus orthotropic material is taken into consideration, both the Young's modulus in the axial direction $E_1(t, e_0)$ and the function $\varphi(t, e_0)$ become independent of the circumferential position and the assigned eccentricity (i.e., $E_1(t, e_0) = E_1$ and $\varphi(t, e_0) = \varphi$) and (5.15) assumes the following form:

$$\sigma_{cr}(e_0) = \eta_c E_1 \varphi \left(\min_{0 \le t < 2\pi} \left\{ \frac{\zeta(t, e_0)}{\rho(t, e_0)} \right\} \right) \tag{6.1}$$

To circumvent there being any location around the circumference of a noncircular cylinder where there is indeed a minimum, it will be further assumed that a variable-thickness homogeneous elliptical cylindrical shell can be designed with the condition

$$\frac{\zeta(t, e_0)}{\rho(t, e_0)} = constant \qquad 0 \le t < 2\pi \tag{6.2}$$

It would seem that the fulfillment of (6.2) should guarantee that the cylinder does not have a weaker (in the sense of local buckling) circumferential location that compromises the performance of the whole cylinder. Consequently, the entire elliptical cylinder should be involved in the deformation, increasing the axial load performance of the structure. The cross sectional shapes which result in the entire cylinder having the same buckling behavior are referred to as "shapes of uniform stability" that are discussed briefly in a book by Gajewski and Zyczkowski [64]. The choice of the constant in (6.2) will be addressed in different ways here, depending on the details of the specific objective to be achieved. In the following

section, three different designs of a variable-thickness elliptical cylindrical shell based on three different choices of the constant in (6.2) will be proposed. It is quite easy to realize that the only way to make $\zeta(t, e_0)/\rho(t, e_0) = constant$ all around the circumference is to choose

$$\zeta(t, e_0) = \alpha_\zeta \rho(t, e_0) \qquad \forall t \in [0, 2\pi) \tag{6.3}$$

where α_ζ is a positive scalar quantity. The design of the variable thickness elliptical (VTE) cylinder is complete once the value of the constant α_ζ in (6.3) is specified. In the present development the constant α_ζ will be chosen in three different ways, resulting in three different VTE cylinder designs:

1. to require the buckling stress σ_{VTE} of the VTE cylinder to be the same, point-by-point around the circumference, as the buckling stress σ_{CTC} of the original CTC cylinder
2. to require the buckling load P_{VTE} of the VTE cylinder to be the same as the buckling load P_{CTC} of the CTC cylinder
3. to require the cross-sectional area A_{VTE} of the VTE cylinder to be the same as the cross-sectional area A_{CTC} of the CTC cylinder

With the cylinders all the same length, requiring the cross-sectional areas to be identical guarantees that the volume, and consequently the weight, of the VTE cylinders is the same as the weight of the original CTC cylinder. Imposing conditions such as one of the three above is necessary because (6.2) is simply a statement regarding two geometric variables. The statement does not guarantee that the axial buckling stress in the VTE cylinder is the same as the axial buckling stress in the original CTC cylinder, nor does it guarantee that the cross-sectional area of the variable thickness wall is the same, or that the axial buckling load, which is directly related to both the axial buckling stress and the cross-sectional area, is the same. Conditions other than (6.2) are necessary to guarantee equality, in some sense, of the VTE and the original CTC cylinder. In order to design the VTE cylinders it is necessary to determine how the three ratios $\sigma_{VTE}/\sigma_{CTC}$, P_{VTE}/P_{CTC}, and A_{VTE}/A_{CTC} depend on the selection of the constant α_ζ. Based on the previous arguments (5.15) can be specialized for both CTC cylinder and VTE cylinder made of an homogeneous orthotropic material by

means of the following expressions:

$$\sigma_{CTC} = \eta_c E_1 \varphi \tag{6.4a}$$

$$\sigma_{VTE} = \eta_c E_1 \varphi \alpha_\zeta \tag{6.4b}$$

Dividing the two equations in (6.4) results in

$$\frac{\sigma_{VTE}}{\sigma_{CTC}} = \alpha_\zeta \tag{6.5}$$

Using (5.4) and (6.3) A_{VTE}/A_{CTC} can be analytically evaluated to give

$$\frac{A_{VTE}}{A_{CTC}} = \alpha_\zeta g^2(e_0) \tag{6.6}$$

where

$$g(e_0) = \frac{1}{\mathcal{E}(e_0^2)} \sqrt{\frac{8 - 8e_0^2 + 3e_0^4}{8\sqrt{1 - e_0^2}}} \tag{6.7}$$

Equation (6.7) is plotted in Fig. 6.1. It can be noted that $g(e_0)$ is always greater than one. More precisely, it is very close to the unity when $0 \leq e_0 < 0.6$, then increases very quickly and tends to infinity for e_0 approaching one. The ratio P_{VTE}/P_{CTC} can be evaluated

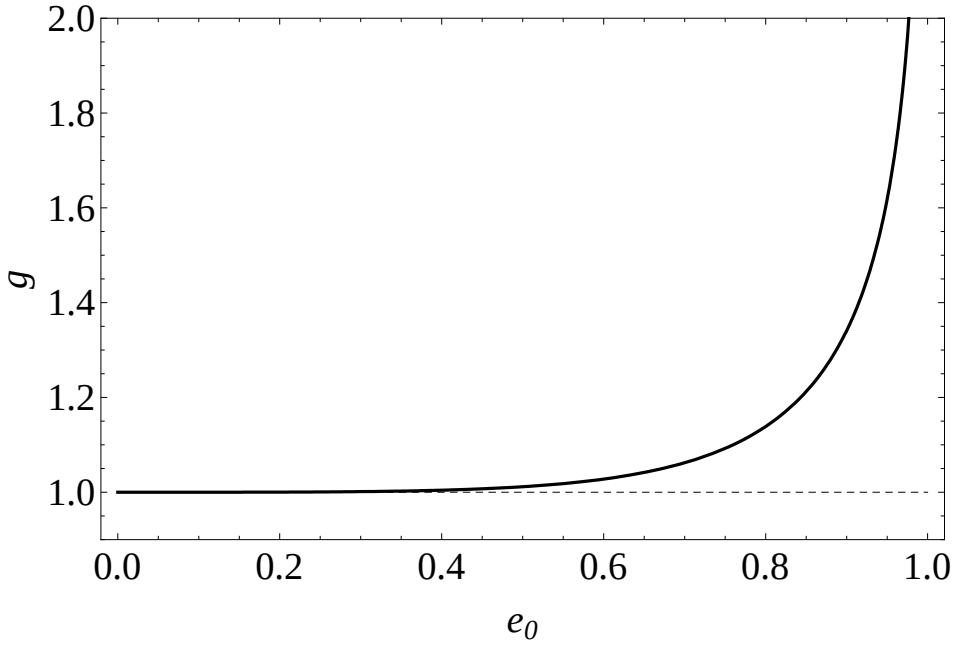

Figure 6.1: Variation of $g(e_0)$ with e_0

by simply multiplying (6.5) and (6.6) term by term, using the fact that each of the three designs requires the stress to be constant around the circumference. As a result,

$$\frac{P_{VTE}}{P_{CTC}} = \frac{\sigma_{VTE}}{\sigma_{CTC}} \frac{A_{VTE}}{A_{CTC}} = \alpha_\zeta^2 g^2(e_0) \tag{6.8}$$

Using (6.5), (6.8) and (6.6) the value of the constant α_ζ needed to design a VTE cylinder having the same buckling stress, the same buckling load, or the same cross-sectional area, hereafter known simply as same-stress, same-load, and same-area designs, of the original CTC cylinder can be determined. These values of α_ζ are listed in Tab.6.1 together with the normalized thickness $\zeta(t, e_0)$ for the three designs of interest. These dimensionless functions are plotted in Fig. 6.2 for $e_0 = 0.70$ together with the unit value representing the normalized thickness of the CTE cylinder, which has the same thickness as the CTC cylinder. Looking

design	α_ζ	$\zeta(t, e_0)$
same-stress	1	$\rho(t, e_0)$
same-load	$1/g(e_0)$	$\rho(t, e_0)/g(e_0)$
same-area	$1/g^2(e_0)$	$\rho(t, e_0)/g^2(e_0)$

Table 6.1: Values of α_ζ for the three designs of interest

at Fig. 6.2 it should be noted that all the VTE designs allocate a larger thickness to the most flat regions of the ellipse (see Fig. 5.3, $t = \pi/2$ and $t = 3\pi/2$). Moreover, it can be seen that the thickness profiles associated with the three different VTE designs never intersect each other. This means that for each value of the parameter t, the thickness of the same-stress design is larger than the thickness of the same-load design, which, in turn, is larger than the thickness of the same-area design. More precisely, it should be realized that the thickness of the same-load design is exactly the geometric mean between the thickness of the same-stress design and the same-area design.

For the sake of completeness it should be noted that once the parameter η_c associated with the original CTC cylinder is given, it is not possible to construct either a CTE cylinder or a VTE cylinder with an assigned eccentricity greater than a critical, or maximum, value without forcing the two opposite sides of the cross section to penetrate each other. This critical value of eccentricity is dependent on which of the three particular designs is being considered. More precisely, the critical eccentricity for each possible design can be defined

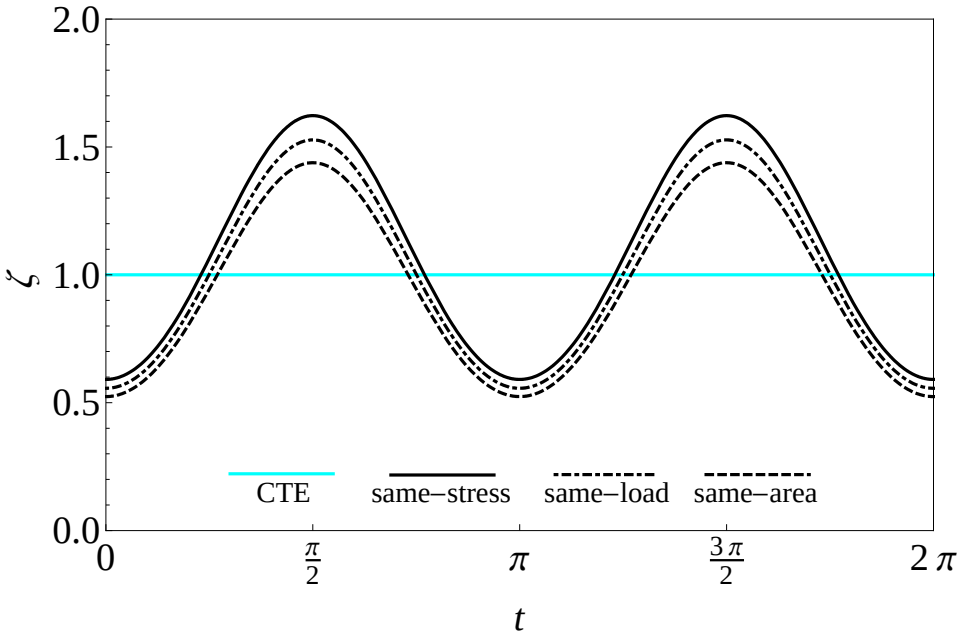

Figure 6.2: Variation of the normalized thickness with the circumferential location for $e_0 = 0.7$

by equating the parameter η_c with a dimensionless function depending only on the assigned eccentricity e_0. The value of the eccentricity fulfilling the equality is the maximum eccentricity that can be assigned to the original CTC cylinder cross section. This value will be referred to as the critical eccentricity and will be labeled by the symbol e_{cr}. The functions determining the critical eccentricity for each possible design are listed in Tab. 6.2 and are plotted in Fig. 6.3. Examination of Fig. 6.3 shows that when $\eta_c = 2$ it is impossible to

CTE	$2(1-e_0^2)/\mathcal{E}(e_0^2)$
VTE, same-stress	$2(1-e_0^2)$
VTE, same-load	$2(1-e_0^2)g(e_0)$
VTE, same-area	$2(1-e_0^2)g^2(e_0)$

Table 6.2: Dimensionless functions determining the critical eccentricity for the three designs

assign any eccentricity to the original circular cylindrical shell for any of the three designs. This geometric constraint can be explained referring to Fig. 5.3. From this figure it can be observed that when $\eta_c = 2$ the cylindrical shell becomes a solid cylinder of radius $2R_c$. Another relevant point to be noted in Fig. 6.3 is that when the ratio η_c approaches zero, the critical eccentricity approaches one for all the possible designs. This means that if the thickness of the original circular cylinder approaches zero, then it can be deformed until it becomes a flat plate. Based on these arguments, for the original CTC cylinder, the following

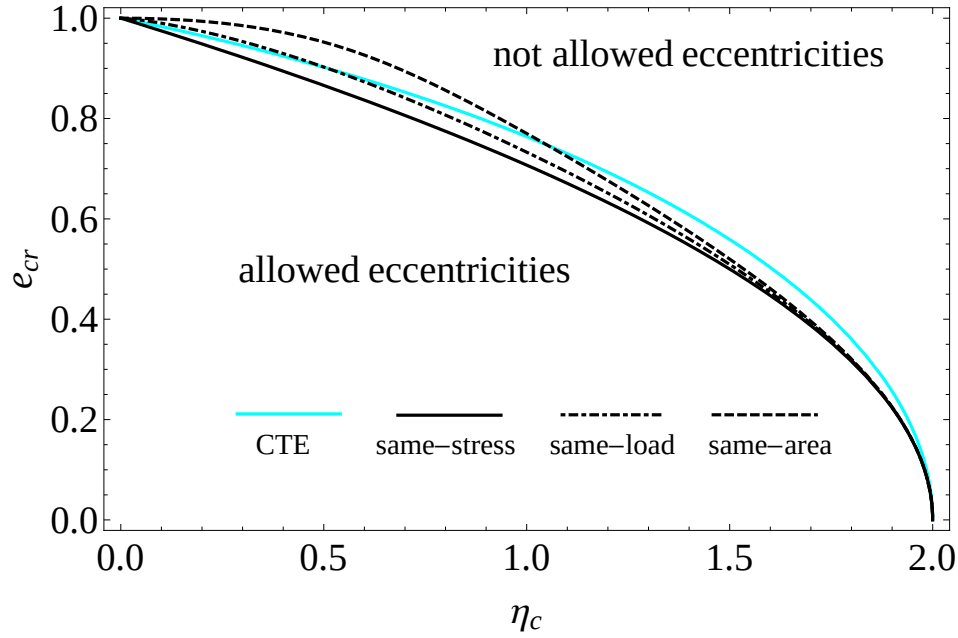

Figure 6.3: Critical eccentricity versus η_c

constraint must be fulfilled:

$$0 < \eta_c < 2 \tag{6.9}$$

For most cylindrical shells this condition is not a problem. It should also be noted from Fig. 6.3 that the relations for the three different VTE designs never intersect each other. This happens because the thicknesses of the three VTE cylinders are proportional to each other, as can be seen from Fig. 6.2 and Tab. 6.1. More precisely, the same-load design relation is bounded by the more restrictive same-stress design and the less restrictive same-area design. This means that if it is possible to construct the same-stress VTE cylinder for a given value of η_c and an assigned eccentricity e_0, then it is possible to construct the same-load and the same-area VTE cylinders for the same assigned eccentricity value. It should be finally noted that the relation for the CTE cylinder intersects both the same-load and the same-area relations, but does not intersect the same-stress relation. The physical interpretation of the critical eccentricity is illustrated in Fig. 6.4, where the cross sections for the critical eccentricity are plotted for $\eta_c = 0.15$ and the points of penetration are encircled. This ratio is quite large compared with the ones normally used in practical construction, but it has been chosen to emphasize the critical shape of the cross section. Looking at Fig. 6.4 it can be noted that while the singular penetration behavior for all three VTE cylinder designs

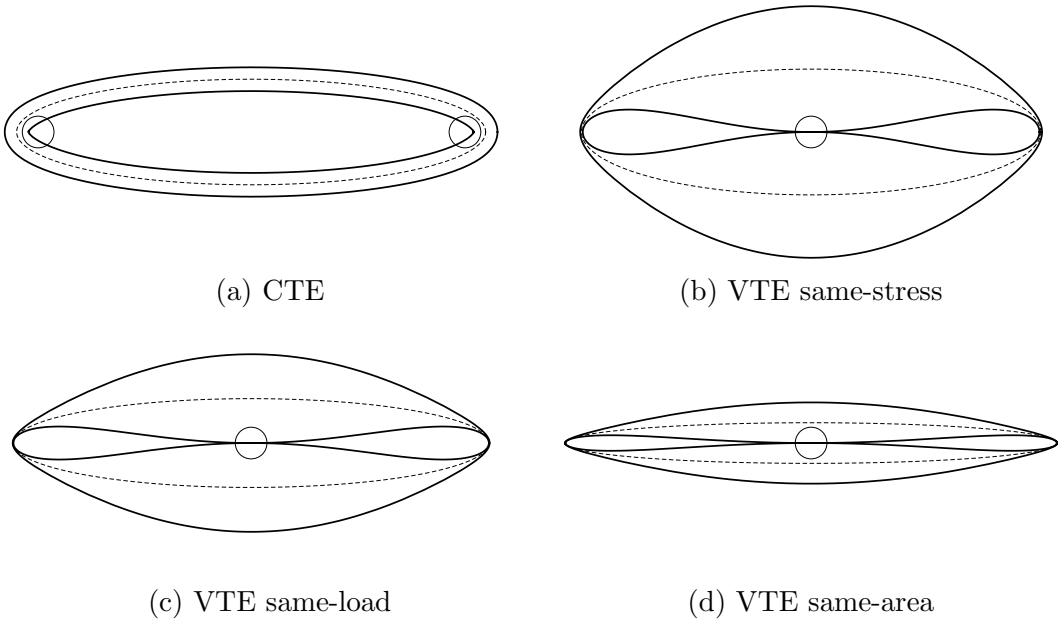

(a) CTE (b) VTE same-stress

(c) VTE same-load (d) VTE same-area

Figure 6.4: Cross sections for critical eccentricity, $\eta_c = 0.15$, points of penetrations encircled

occurs at the flatter portion of the cross section, for the CTE cylinder design penetration occurs at the more curved portion. The intersections in Fig. 6.3 of the relations for the same-load VTE cylinder and the CTE cylinder, and of the relations for the same-area VTE cylinder and the CTE cylinder simply mean that there exists particular values of η_c such that the singular behavior of the two cylinders corresponding to the two intersecting curves happens for the same value of the assigned eccentricity e_0. Referring to Fig. 6.3, it can be seen that when η_c is small, as happens for most of the cases of practical interest, the critical eccentricities are very close to unity. Moreover, when the eccentricity approaches the critical value, the walls of the VTE cylinder become so thick that some of the assumptions embedded in the shell theory (see Fig. 6.4) are no longer valid. Based on those arguments, it can be concluded that the critical eccentricity is a pure geometric limit, free of practical interest.

Before closing this section, it is interesting to make a comparison among the values that the three ratios $\sigma_{VTE}/\sigma_{CTC}$, P_{VTE}/P_{CTC}, and A_{VTE}/A_{CTC} assume in each of the three designs of interest. These comparisons are summarized in Tab. 6.3. Keeping in mind that $g(e_0)$ is always greater than the unity, it should be noted that:

1. the same-stress design produces for the VTE cylinder a buckling load and a cross-

design	$\sigma_{VTE}/\sigma_{CTC}$	P_{VTE}/P_{CTC}	A_{VTE}/A_{CTC}
same-stress	1	$g^2(e_0)$	$g^2(e_0)$
same-load	$1/g(e_0)$	1	$g(e_0)$
same-area	$1/g^2(e_0)$	$1/g^2(e_0)$	1

Table 6.3: Values of three key ratios for the three designs of interest

sectional area larger than for the original CTC cylinder

2. the same-load design produces for the VTE cylinder a lower buckling stress and a larger cross-sectional area than for the original CTC cylinder
3. the same-area design produces for the VTE cylinder a lower buckling stress and buckling load that for the original CTC cylinder

All the ratios in Tab. 6.3 vary monotonically with the eccentricity through the dimensionless function $g(e_0)$.

Finally, it is useful to explicitly derive analytical expressions for the axial stress resultant N. The axial stress resultant is defined as the integral of the axial stress through the thickness of the cylinder wall, and here is the product of the axial stress and the cylinder thickness. In Tab. 6.4 analytical expressions for the ratio N_{VTE}/N_{CTC} between the axial stress resultants of the VTE cylinder and the original CTC cylinder are given for all the three designs. These expressions are obtained multiplying member by member the last column of Tab. 6.1 and the first column of Tab. 6.3

design	N_{VTE}/N_{CTC}
same-stress	$\rho(t, e_0)$
same-load	$\rho(t, e_0)/g^2(e_0)$
same-area	$\rho(t, e_0)/g^4(e_0)$

Table 6.4: Analytical expressions for axial stress resultant ratios for the three designs of interest

6.3 Numerical validation of the proposed designs

In this section the three VTE cylinder designs proposed in the previous section will be further studied using numerical results computed with the general-purpose finite-element code *ABAQUS*. In particular, the results from *ABAQUS* will be compared with the results

from the developed analysis. Since the developed analysis was based on a rather simple premise, which did not consider prebuckling rotations or stresses other than the axial stress, such comparisons will be informative. Geometrically nonlinear prebuckling analysis will be employed, and the results for simply-supported boundary conditions will be considered. The buckling condition will be identified by applying to one end of each cylinder the smallest axial compressive displacement that causes the tangent stiffness matrix of the numerical analysis to become singular. The stress state for this condition, in particular, the axial stress level, will be considered as the buckling stress. The quantities of interest at this level of displacement will be compared with the respective analytical predictions for three values of assigned eccentricities ($e_0 = 0.50, 0.70, 0.85$) and for aluminum cylinders of two sizes (see Tab. 5.1) in order to check the generality of the findings of the previous section.

The thickness of each element will be assumed constant and equal to the thickness that the analytical function (6.3) assumes at the middle point of the element. In Fig. 6.5 a comparison between the actual area of a generic sector of the cross section associated with an element (black) and the area used in the numerical calculations (light grey) is shown. The superposition of the two different areas is filled in dark grey. As the number of nodes

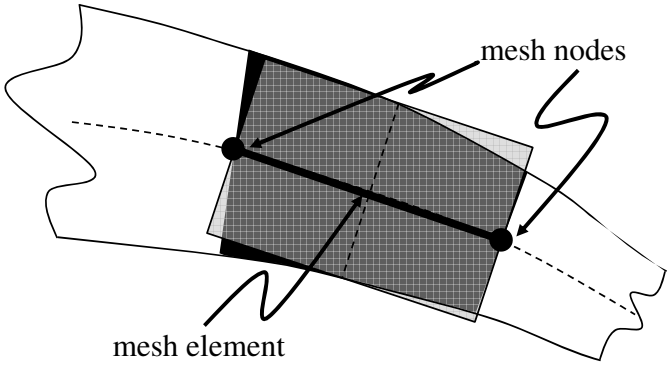

Figure 6.5: Comparison between the actual area and the numerical area of a sector of cross section

M in the circumferential direction increases, and consequently the circumferential length of each element decreases, the error in the representation of the cylinder cross-sectional area decreases. Specifically, the ratio between the cross-sectional area of the mesh for the VTE cylinder A_{VTE} and the cross-sectional area for the mesh for the original CTC cylinder A_{CTC}

can be expressed as follow

$$\frac{A_{VTE}}{A_{CTC}} = \frac{1}{Mh_c}\sum_{i=1}^{M} h(t_i) \tag{6.10}$$

where t_i is the solution of the transcendental equation

$$\int_0^{t_i} \left|\frac{d\mathbf{v}(t)}{dt}\right| dt = \left(i - \frac{1}{2}\right)\frac{2\pi R_c}{M} \quad i = 1...M \tag{6.11}$$

In Tab. 6.5, 6.6 and 6.7 the values that 6.10 assumes for $M = 12$, $M = 42$ and $M = 168$

e_0	$M = 12$		$M = 42$		$M = 168$		$g^2(e_0)$
	small	large	small	large	small	large	
0.50	1.02225	1.02225	1.02321	1.02321	1.02329	1.02329	1.02329
0.70	1.03096	1.12230	1.12758	1.12758	1.12803	1.12803	1.12806
0.85	1.04310	1.44769	1.46792	1.46792	1.46959	1.46959	1.46970

Table 6.5: Convergence of the area associated with the mesh for the same-stress design

e_0	$M = 12$		$M = 42$		$M = 168$		$g(e_0)$
	small	large	small	large	small	large	
0.50	1.01055	1.01055	1.01149	1.01149	1.01157	1.01157	1.01158
0.70	1.01916	1.05668	1.06165	1.06165	1.06207	1.06207	1.06210
0.85	1.03116	1.19416	1.21084	1.21084	1.21222	1.21222	1.21231

Table 6.6: Convergence of the area associated with the mesh for the same-load design

e_0	$M = 12$		$M = 42$		$M = 168$		1
	small	large	small	large	small	large	
0.50	0.99898	0.99898	0.99991	0.99992	0.99999	0.99999	1.00000
0.70	1.00749	0.99490	0.99957	0.99957	0.99997	0.99997	1.00000
0.85	1.01935	0.98503	0.99879	0.99879	0.99992	0.99992	1.00000

Table 6.7: Convergence of the area associated with the mesh for the same-area design

for the same-stress, -load , -area designs, respectively, and the three eccentricities of interest are shown. In the last column of the tables the theoretical value is given (see Tab. 6.3, last column). For the same-stress, -load, and -area designs, it can be seen that for $M = 168$ the ratio A_{VTE}/A_{CTC} converges to the theoretical value with less than 1‰ error. The accuracy slowly degenerates as the eccentricity increases.

6.3.1 Same-stress design

In Fig. 6.6 the circumferential variation of the axial stress at the buckling condition from the finite-element results for the simply-supported VTE cylinders for the same-stress

design are shown. Results for small and large cylinders with the three levels of eccentricity are illustrated. In each sub-figure the axial stresses, normalized by the critical stress of a CTC cylinder, as a function of normalized circumferential location are plotted. Each sub-figure includes the axial stress at the buckling condition for the VTE cylinder as predicted by the developed analysis (horizontal straight line), and the axial stress for the same VTE cylinder and the axial stress for the CTE cylinder at the buckling condition as computed by the finite-element model. The latter relations are repeated from Fig. 5.7. Looking at Fig. 6.6, it is first observed that the finite-element analysis predicts that axial stress for the VTE cylinders varies with circumferential position, as is the case for the CTE cylinder, but in contrast to the uniform stress state of the analytic calculation. The degree of variation depends again on the assigned eccentricity e_0 and the size of the cylinder. In general, the variation is less for the large cylinder and lower values of eccentricity. It appears that the developed analysis provides a reasonable estimate of the performance of the VTE cylinder. This is definitely the case for $e_0 = 0.50$ and in an average sense for $e_0 = 0.70$. For $e_0 = 0.85$ the developed analysis over-predicts average of the finite-element model by about 5% for small and 2% for large cylinders. Furthermore, a $\pm 5\%$ variation of axial stress around the circumference of the small cylinders is predicted by the finite-element model for $e_0 = 0.85$. For the large cylinders with $e_0 = 0.85$ the variation is less. Further quantitative comparisons regarding the stresses are made in Tab. 6.8 for simply-supported cylinders with the tabulation of key ratios of average axial stresses at the buckling condition. For all cases the ratio between $\overline{\sigma}_{VTE}$ and σ_{CTC} is very close to unit value, emphasizing the fact that the buckling stress of the original circular cylinder is, essentially, fully recovered. Recall from Tab. 6.3 that, according to the developed analysis, the ratio $\sigma_{VTE}/\sigma_{CTC}$ is of unit value for the same-stress design. Since with the developed analysis the stress does not vary with circumferential position, $\overline{\sigma}_{VTE}/\sigma_{CTC}$ is also of unit value. For comparison, this unit value is included in the last column of Tab. 6.8. The

e_0	$\overline{\sigma}_{VTE}/\overline{\sigma}_{CTE}$		$\overline{\sigma}_{VTE}/\sigma_{CTC}$		
	small	large	small	large	1
0.50	1.1715	1.1894	1.0036	0.9996	1.0000
0.70	1.5003	1.5504	0.9990	1.0001	1.0000
0.85	2.0903	2.2641	0.9489	0.9860	1.0000

Table 6.8: Comparison among key stress ratios of VTE and CTE cylinders at the buckling condition, same-stress design

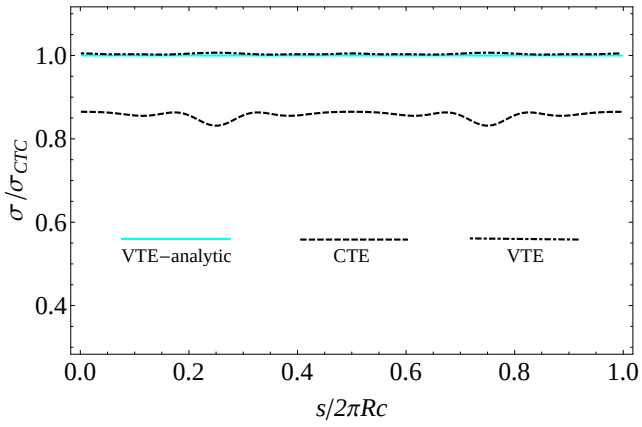

$e_0 = 0.50$ small

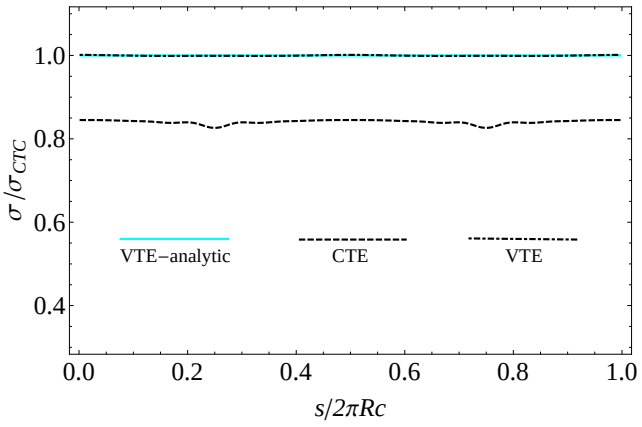

$e_0 = 0.50$ large

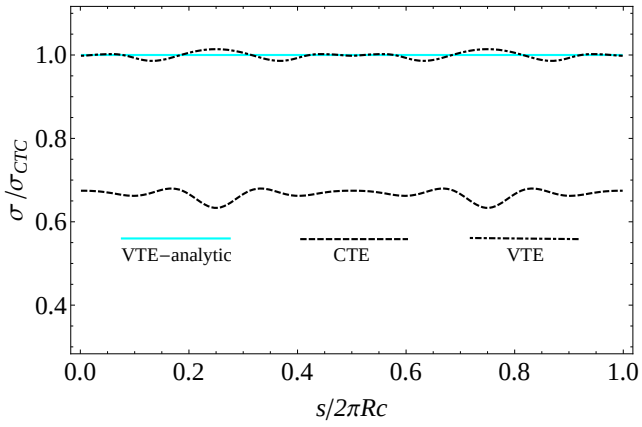

$e_0 = 0.70$ small

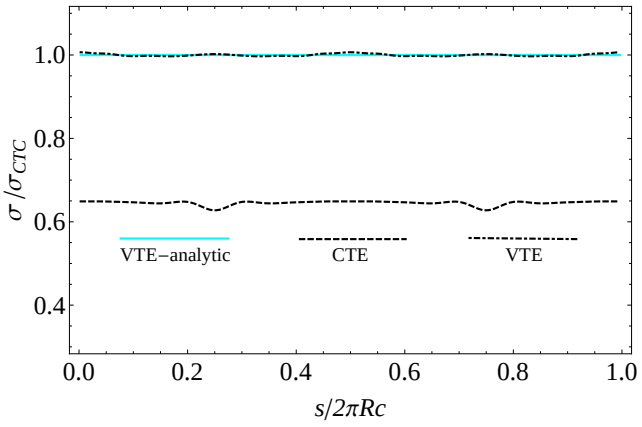

$e_0 = 0.70$ large

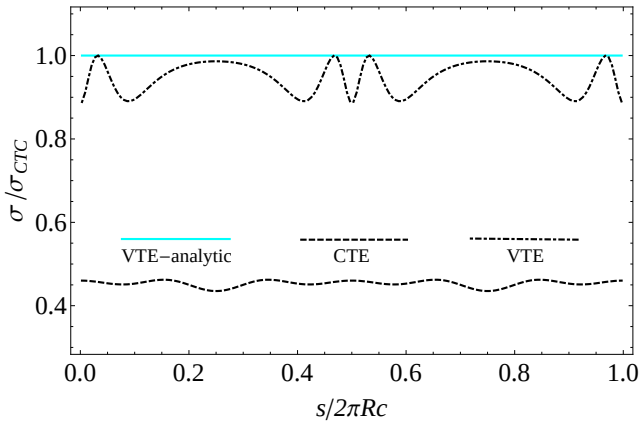

$e_0 = 0.85$ small

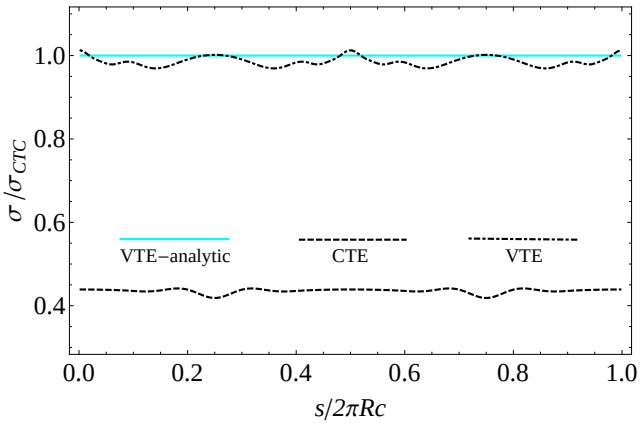

$e_0 = 0.85$ large

Figure 6.6: Comparison among the axial stresses at the buckling condition for small and large VTE and CTE cylinders for different eccentricities, same-stress design

ratio between $\overline{\sigma}_{VTE}$ and $\overline{\sigma}_{CTE}$ is a measure of the gain obtained by tailoring the thickness of the elliptical cylinder. As seen, this gain varies from about 17% for a small cylinder with $e_0 = 0.50$ to more that 100% for a large cylinder with $e_0 = 0.85$. A comparison of load ratios at the buckling condition is presented in Tab. 6.9 for the simply-supported cylinders. As

e_0	P_{VTE}/P_{CTE}		P_{VTE}/P_{CTC}		
	small	large	small	large	$g^2(e_0)$
0.50	1.1988	1.2170	1.0271	1.0228	1.0233
0.70	1.6935	1.7480	1.1277	1.1275	1.1281
0.85	3.0990	3.3261	1.4050	1.4485	1.4697

Table 6.9: Comparison among key buckling load ratios of VTE and CTE cylinders at the buckling condition, same-stress design

observed, the critical load of the VTE cylinder increases with respect to the CTC cylinder as the eccentricity increases. It is also seen that the ratio P_{VTE}/P_{CTC} is described quite accurately by $g^2(e_0)$, as predicted in Tab. 6.3. The ratio P_{VTE}/P_{CTC} is a measure of the gain in axial load capability of the elliptical cylinder relative to the original circular cylinder due to the tailoring of the thickness of the elliptical cylinder. As seen, the ratio is above one, so there is clearly a gain relative to the original circular cylinder. The ratio P_{VTE}/P_{CTE} is a measure of the gain obtained by tailoring the thickness of the elliptical cylinder relative to keeping the thickness of the elliptical cylinder uniform. This gain varies from about 20% for the small cylinder with $e_0 = 0.50$ to more than 200% for the large cylinder with $e_0 = 0.85$. It should be remarked that with the same-stress design the improvement in the buckling capacity of the VTE cylinder is due in part to an increment in cross-sectional area, also related to $g^2(e_0)$ (see Tabs. 6.3). However, the distribution of the area, i.e., varying the thickness with circumferential location, has a major role in the improvement in buckling capability. This is evident by realizing that while the ratio P_{VTE}/P_{CTE} shows over a 200% gain for both the small and the large cylinders with $e_0 = 0.85$ (i.e., $P_{VTE}/P_{CTE} = 3.3261$), the area has increased by only 47% (i.e., $A_{VTE}/A_{CTE} = 1.4697$, see Tabs. 6.3).

The variation of the axial stress resultant, N, with circumferential location at the buckling condition as predicted by the finite-element analysis is shown in Fig. 6.7. The resultants for small and large simply-supported VTE and CTE cylinders for the three values of eccentricity are shown. The analytical prediction from Tab. 6.4 for the VTE cylinder is also illustrated in the figures. The stress resultants are normalized by the stress resultant for

the CTC cylinder, N_{CTC}. For the purpose of discussion, the stress resultant for the CTC cylinder, N_{CTC}, is included and is the horizontal line at unity. At first glance, it is clear from Fig. 6.7 that, importantly, the prediction of the N vs. s relation by the developed analysis is almost indistinguishable from the finite-element calculations for all cases. Looking at more detail, it is observed that while the stress resultant for the CTE cylinder, N_{CTE}, is nearly uniform around the circumference, and always less than that for the CTC cylinder, the stress resultant for the VTE cylinder, N_{VTE}, has considerable amplitude modulation, being largest in the flatter regions of the elliptical cross section in all cases. This follows because the amplitude of N should be proportional to the thickness of the shell due to the proposed design that forces the stress to be uniform with circumferential location. It should be noted that N_{VTE} intersects N_{CTC} where the radius of curvature of the ellipse is equal to the radius of original circle, R_c. The area under the relationship for N vs. s is the total axial load. From a qualitative inspection of Fig. 6.7, it is quite evident that for each case the area under the N_{CTE} relation is less than the area under the other two. Moreover, the average value of N_{VTE} (not shown in the figure) seems to have a positive offset relative to N_{CTC}, particularly for large values of eccentricities and, for sure, relative to N_{CTE}. Consequently, as has been pointed out in previous tables, the axial buckling load of the VTE cylinder is greater than the axial buckling load of the CTE cylinder.

6.3.2 Same-load design

Comparing Fig. 6.8 with Fig. 6.6 and Fig. 6.9 with Fig. 6.7, it is seen that the overall characteristics of the stress and stress resultant variation with circumferential location for the same-load designs are similar to the characteristics of those responses for the same-stress designs. Additionally, the correlations between the stresses and stress resultants for the same-load design VTE cylinders as predicted by the developed analysis and the like response for the same-load design VTE cylinders as predicted by the finite-element model are generally good, but with less correlation in the stress levels for both small and large cylinders for the case of eccentricity $e_0 = 0.85$. There are, however, differences between the same-load designs and the same-stress designs. The most obvious difference between designs in the variations of stress with circumferential location, Figs. 6.8 and 6.6, is that the normalized stress levels

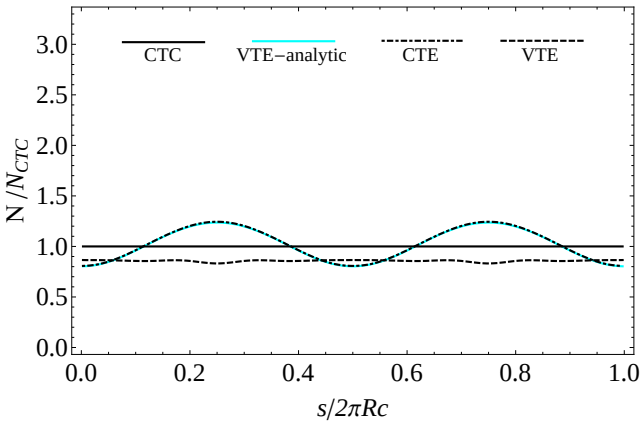

$e_0 = 0.50$ small

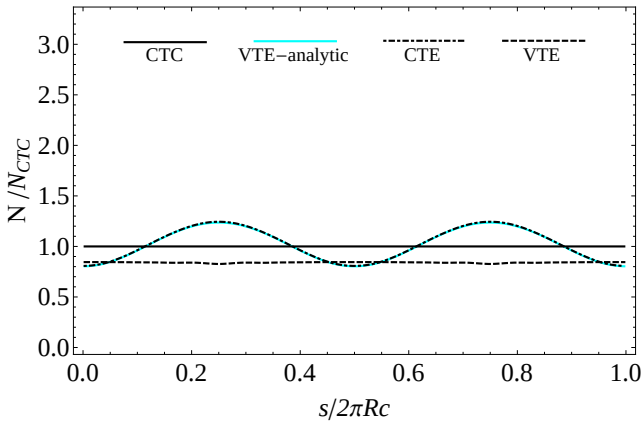

$e_0 = 0.50$ large

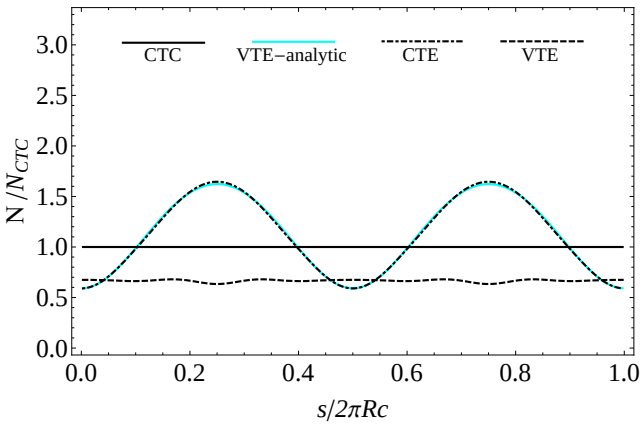

$e_0 = 0.70$ small

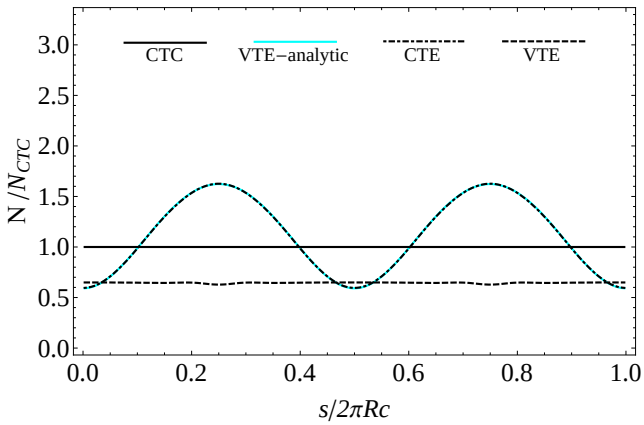

$e_0 = 0.70$ large

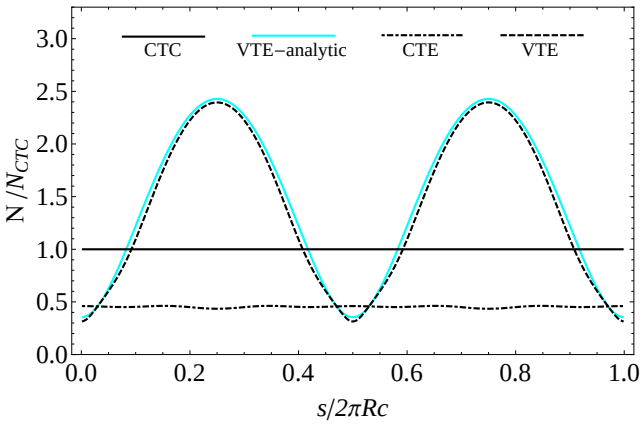

$e_0 = 0.85$ small

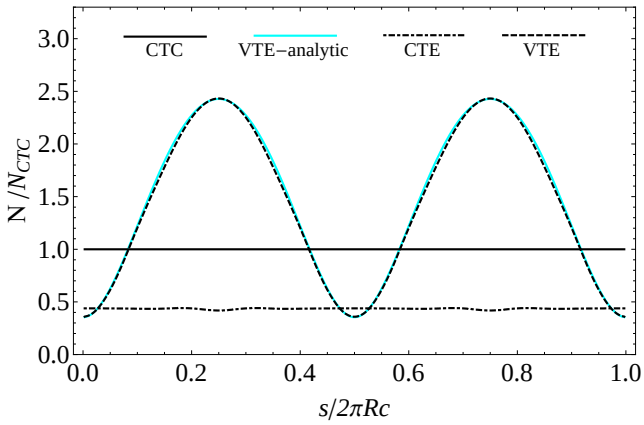

$e_0 = 0.85$ large

Figure 6.7: Comparison among the stress resultants at the buckling condition for small and large VTE and CTE cylinders for different eccentricities, same-stress design

for the same-load design VTE cylinders, as predicted by both the developed analysis and the finite-element model, are lower than those for the same-stress design. The same is true of the stress resultant levels of the same-load design, Fig. 6.9, as compared with those of the same-stress design, Fig. 6.7. This trend is particularly evident for the case of large eccentricities, where in Fig. 6.8 for both small and large same-load design VTE cylinders with $e_0 = 0.85$ the normalized stress level is near 0.8, as opposed to a value near unity for both small and large same-stress design VTE cylinders with eccentricity $e_0 = 0.85$ in Fig. 6.6. Likewise, for both small and large cylinders with eccentricity $e_0 = 0.85$, the peak loads of the normalized stress resultants for the same-stress designs in Fig. 6.7 are close 2.5 for both small and large cylinders, while for the same-load designs in Fig. 6.9, the peak levels are about 1.7. A review of Tab. 6.9 reveals that for the same-stress design the ratio of P_{VTE}/P_{CTC} is greater than unity, and increases with increasing eccentricity, meaning that the buckling load of the VTE cylinder is greater than the buckling load of the original CTC cylinder. For this ratio to be unity, as is required for the same-load design, meaning that the buckling loads are the same, does not require as high a stress level for the VTE cylinders. Hence the lower levels of stress and stress resultants for the same-load design. The lower stress levels for the same-load design are reflected in all the stress ratios of Tab. 6.10 as compared to those of Tab. 6.8, and the load ratios of Tab. 6.11 as compared to those of Tab. 6.9.

Regarding the lower level of stress for the same-load design, it is seen from Tab. 6.3 that the ratio $\sigma_{VTE}/\sigma_{CTC}$ is given by $1/g(e_0)$ in the developed analysis. Since $g(e_0)$ is greater than one, the lower value of $\sigma_{VTE}/\sigma_{CTC}$ for the same-load design must be expected. The value of $1/g(e_0)$ is given in Tab. 6.10 and it is observed that it correlates well with the value of $\overline{\sigma}_{VTE}/\sigma_{CTC}$ as computed by the finite-element analysis.

e_0	$\overline{\sigma}_{VTE}/\overline{\sigma}_{CTE}$		$\overline{\sigma}_{VTE}/\sigma_{CTC}$		
	small	large	small	large	$1/g(e_0)$
0.50	1.1591	1.1770	0.9930	0.9891	0.9886
0.70	1.4143	1.4622	0.9417	0.9432	0.9415
0.85	1.7472	1.8773	0.7921	0.8175	0.8249

Table 6.10: Comparison among key stress ratios of VTE and CTE cylinders at the buckling condition, same-load design

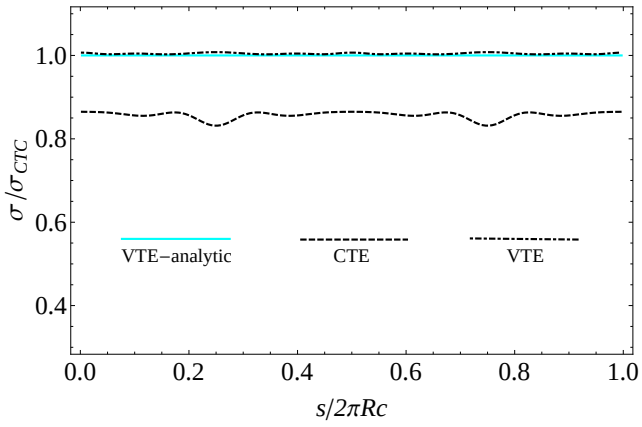

$e_0 = 0.50$ small

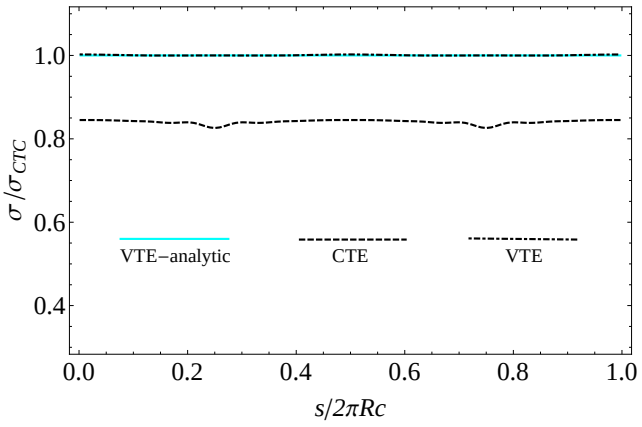

$e_0 = 0.50$ large

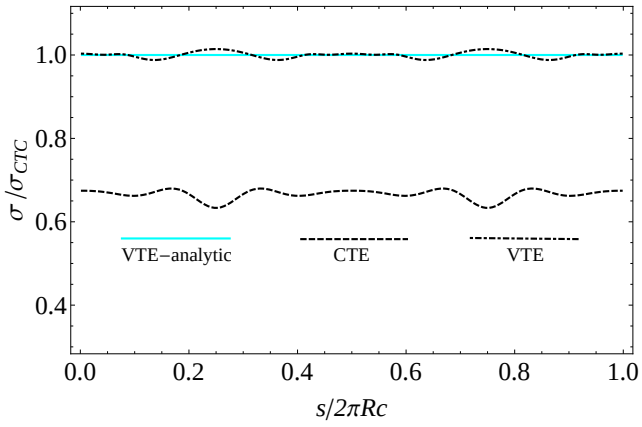

$e_0 = 0.70$ small

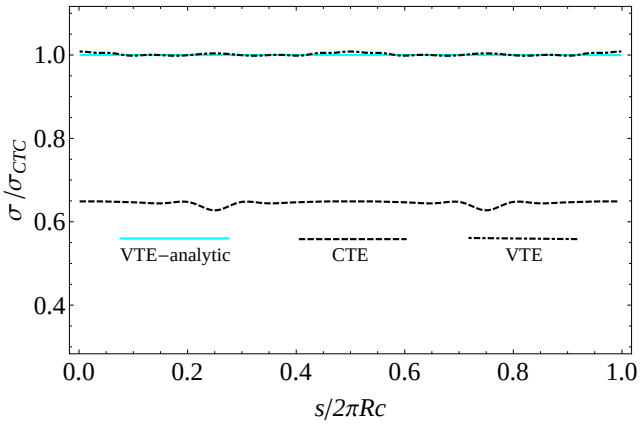

$e_0 = 0.70$ large

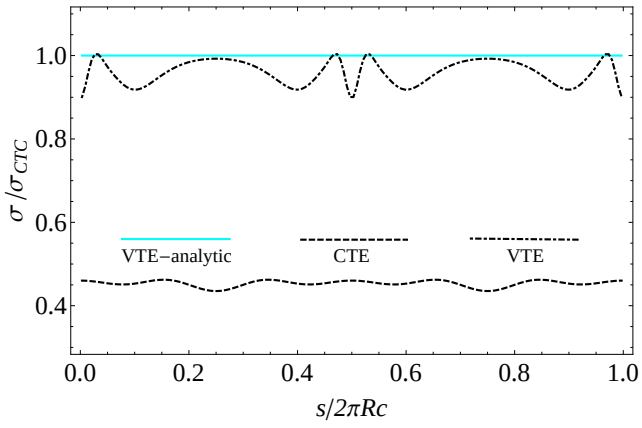

$e_0 = 0.85$ small

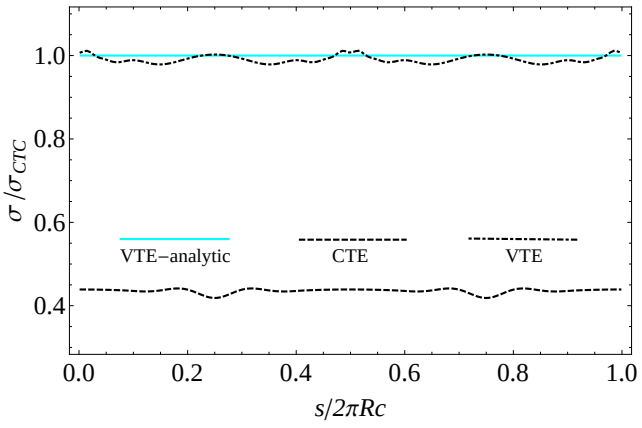

$e_0 = 0.85$ large

Figure 6.8: Comparison among the axial stresses at the buckling condition for small and large VTE and CTE cylinders for different eccentricities, same-load design

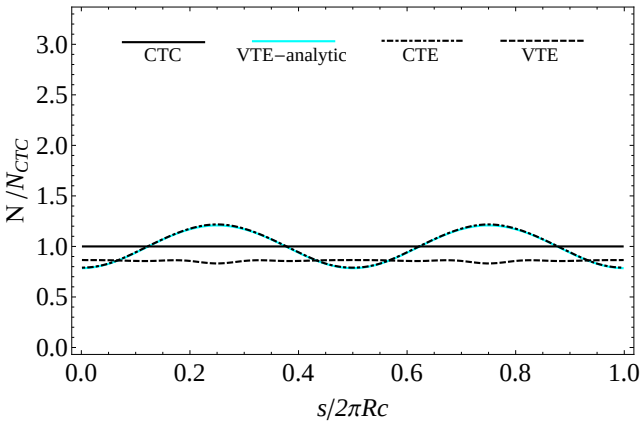

$e_0 = 0.50$ small

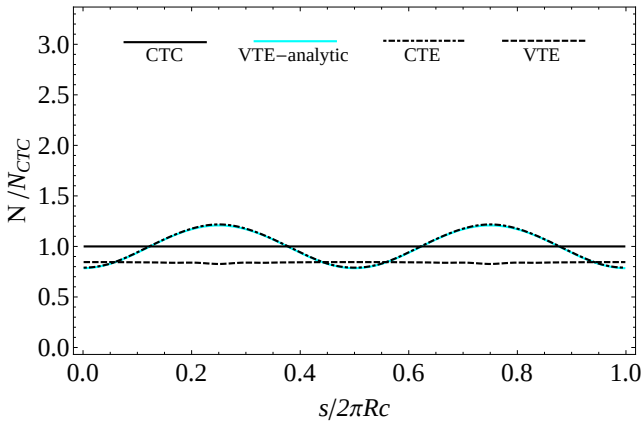

$e_0 = 0.50$ large

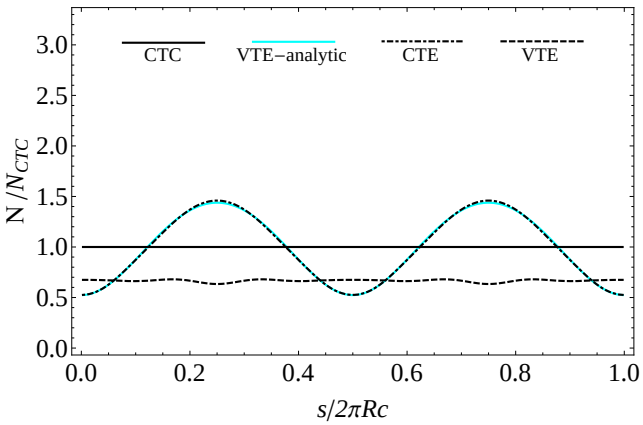

$e_0 = 0.70$ small

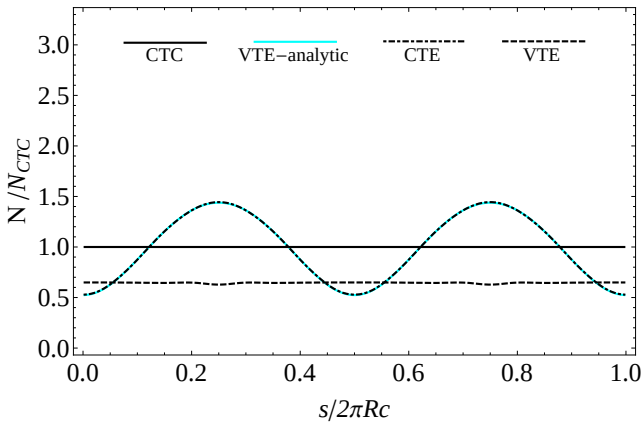

$e_0 = 0.70$ large

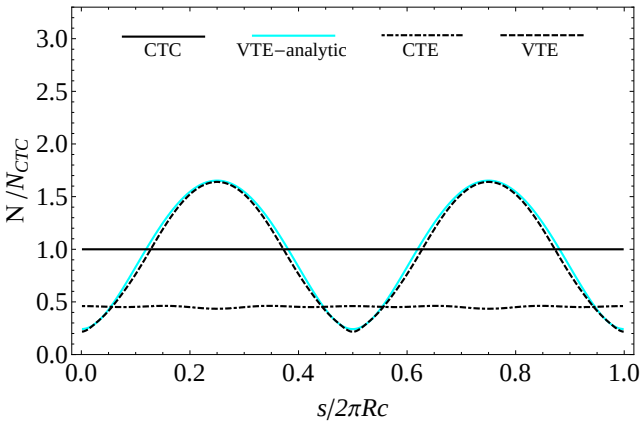

$e_0 = 0.85$ small

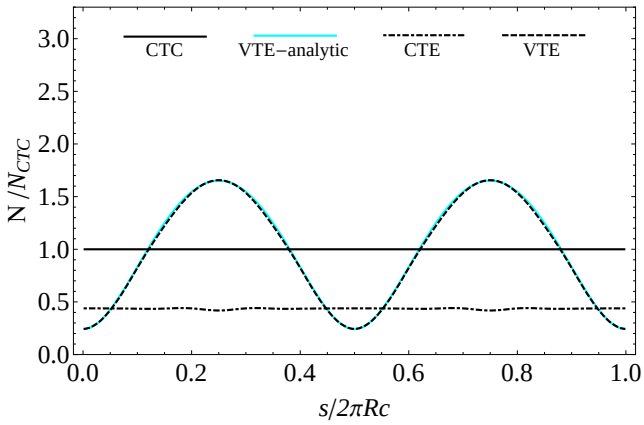

$e_0 = 0.85$ large

Figure 6.9: Comparison among the axial stress resultants at the buckling condition for small and large VTE and CTE cylinders for different eccentricities, same-load design

e_0	P_{VTE}/P_{CTE}		P_{VTE}/P_{CTC}		
	small	large	small	large	1
0.50	1.1726	1.1904	1.0046	1.0005	1.0000
0.70	1.5029	1.5521	1.0007	1.0012	1.0000
0.85	2.1285	2.2736	0.9650	0.9901	1.0000

Table 6.11: Comparison among key load ratios of VTE and CTE cylinders at the buckling condition, same-load design

The ratios $\overline{\sigma}_{VTE}/\overline{\sigma}_{CTE}$ and P_{VTE}/P_{CTE} in Tabs. 6.10 and 6.11, respectively, again reflect the gain in varying the thickness of the cylinder wall with circumferential position in the elliptical cylinders. Some of this gain is due to an increment of area, as given by the values of $g(e_0)$ (see Tabs. 6.3), but again, most of the gain must be attributed to the redistribution of material by varying the thickness with circumferential location. For example, for $e_0 = 0.85$ the buckling load for the large VTE cylinder is over 100% greater then the buckling load for the large CTE cylinder, (i.e. $P_{VTE}/P_{CTE} = 2.2736$), while the area increase is only 21%.

6.3.3 Same-area design

The variations of the normalized stresses and stress resultants as a function of circumferential location for the same-area design VTE cylinders are illustrated in Figs. 6.10 and 6.11, respectively. Tables 6.12 and 6.13 provide information similar to Tables 6.8 and 6.10, and 6.9 and 6.11 for the same-stress and same-load designs, respectively. By comparing Fig. 6.10 with Figs. 6.6 and 6.8, it is observed that for both small and large cylinders with $e_0 = 0.85$, for example, the normalized stress level around the circumference for the VTE cylinders has decreased from about unity for the same-stress designs, to about 0.8 for the same-load designs, to just below 0.7 for the same-area designs. Likewise, by comparing Fig. 6.11 with Figs. 6.7, and 6.9, it is observed that the peak value of the stress resultant for both small and large VTE cylinders with $e_0 = 0.85$ has decreased from about 2.5 for the same-stress designs, to about 1.7 for the same-load designs, to about 1.2 for the same-area designs. The correlation between the predictions of the developed analysis and the finite-element model are again quite good for eccentricities $e_0 = 0.50$ and $e_0 = 0.70$, with less agreement for the case of $e_0 = 0.85$. The lower overall stress level for the same-area designs, compared to the other two designs, is reflected in data of Tabs. 6.12 and 6.13 as compared

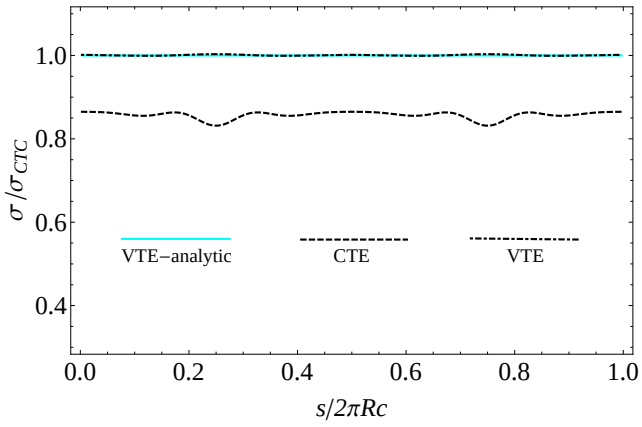

$e_0 = 0.50$ small

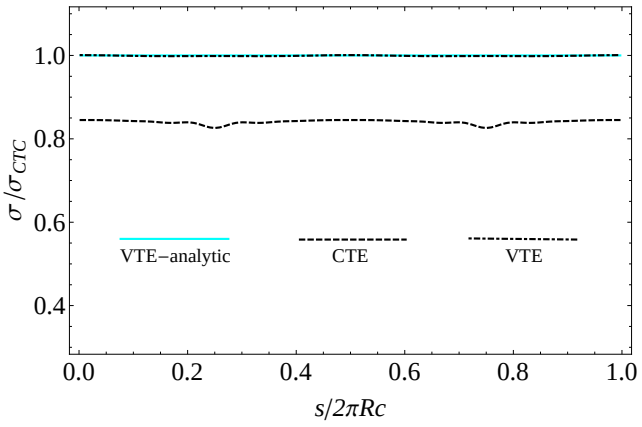

$e_0 = 0.50$ large

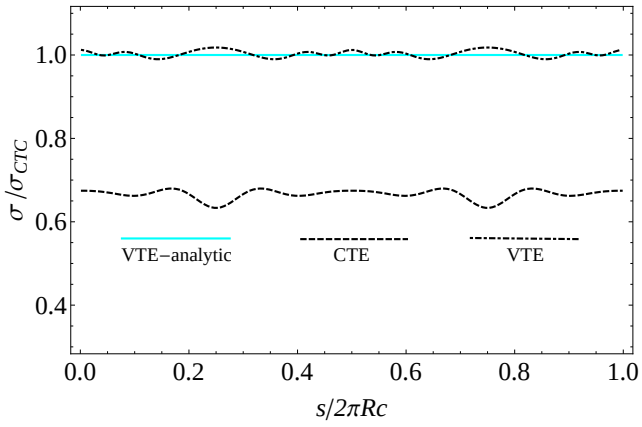

$e_0 = 0.70$ small

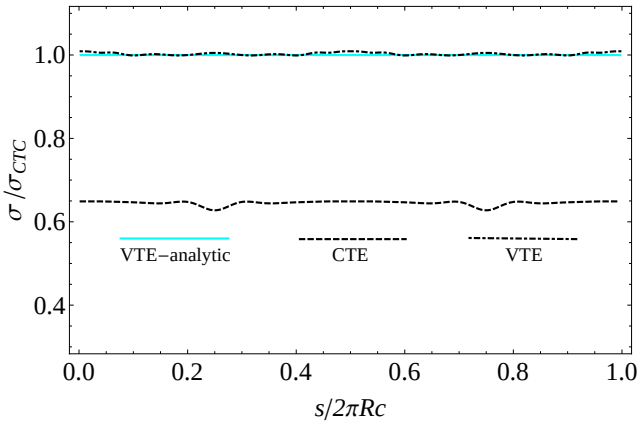

$e_0 = 0.70$ large

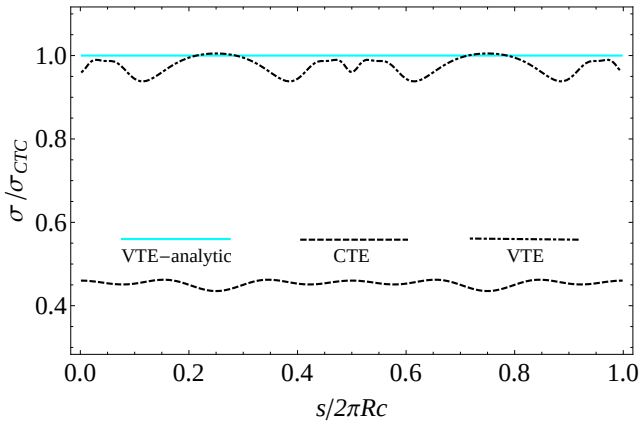

$e_0 = 0.85$ small

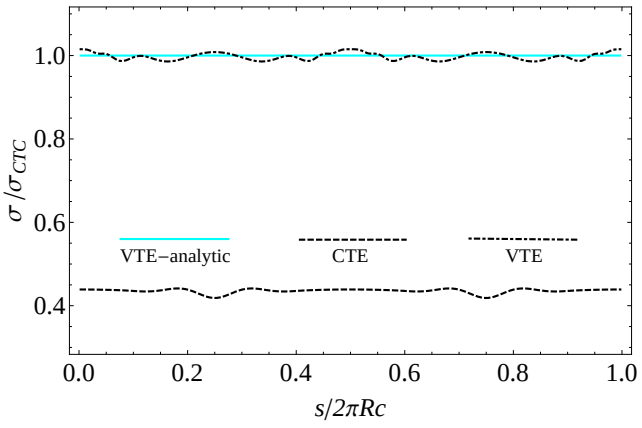

$e_0 = 0.85$ large

Figure 6.10: Comparison among the stresses at the buckling condition for small and large VTE and CTE cylinders for different eccentricities, same-area design

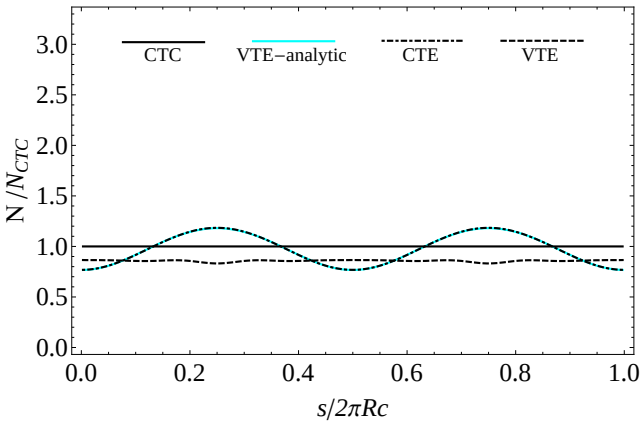

$e_0 = 0.50$ small

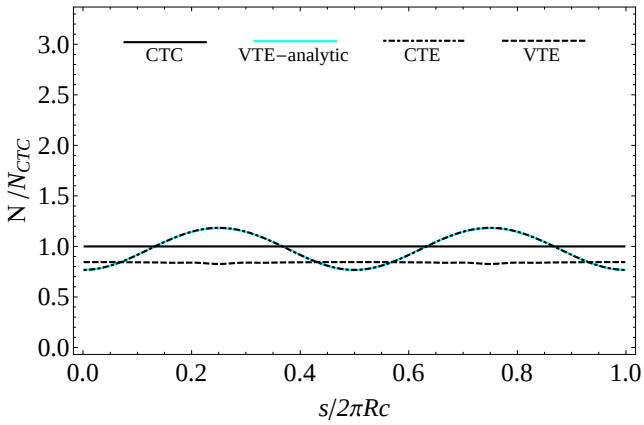

$e_0 = 0.50$ large

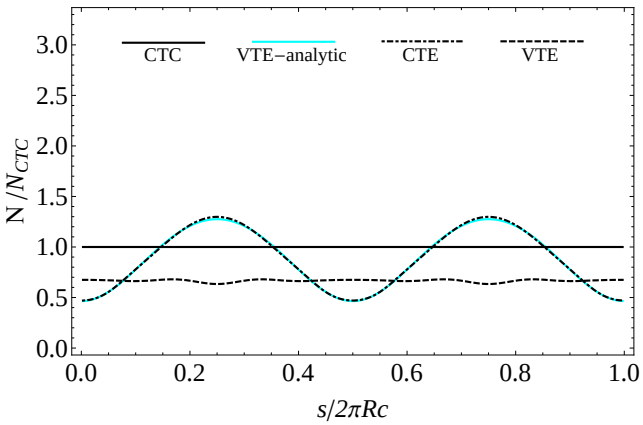

$e_0 = 0.70$ small

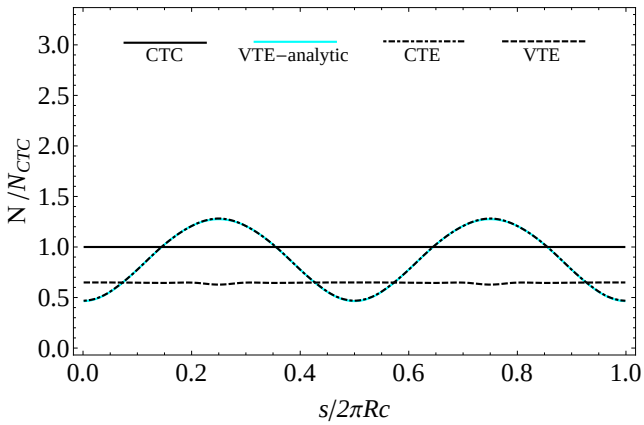

$e_0 = 0.70$ large

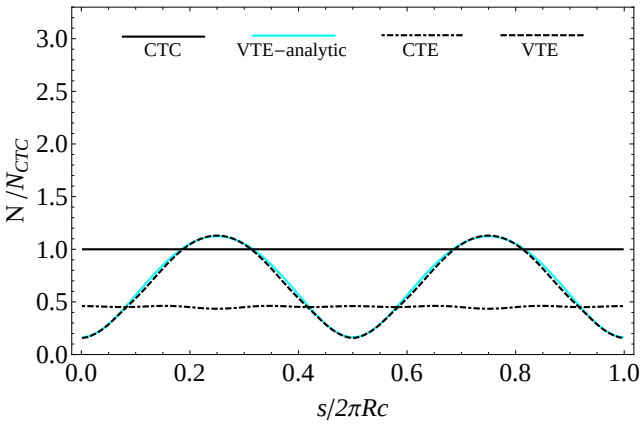

$e_0 = 0.85$ small

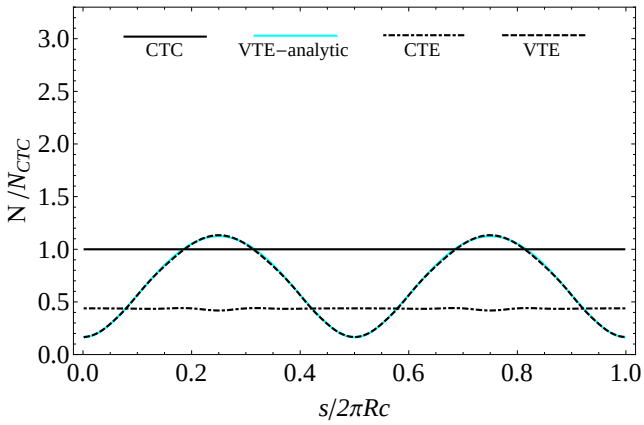

$e_0 = 0.85$ large

Figure 6.11: Comparison among the axial stress resultants at the buckling condition for small and large VTE and CTE cylinders for different eccentricities, same-area design

to entries of Tabs. 6.8 and 6.9 and Tabs. 6.10 and 6.11 for all three values of eccentricity. From Tab. 6.3 the ratios $\sigma_{VTE}/\sigma_{CTC}$ are given by $1/g^2(e_0)$. The values of $1/g^2(e_0)$ are given in Tab. 6.12 and 6.13 and it is seen that the ratios $\overline{\sigma}_{VTE}/\sigma_{CTC}$ and P_{VTE}/P_{CTC} from the finite-element calculations and the value of $1/g^2(e_0)$ correlate well. Furthermore, the fact that the ratio P_{VTE}/P_{CTE} is greater than unity for all three values of eccentricity and both small and large cylinders for the same-area VTE designs unequivocally verifies the gain in redistributing the area in the elliptical cylinders. Specifically, from Tab. 6.13, for the large same-area design VTE cylinders, there is an increment of about 56% in the buckling load compared to the CTE cylinder for $e_0 = 0.85$. However, unlike the same-stress design VTE cylinders where the ratio P_{VTE}/P_{CTC} is greater than unity for all cases, meaning the same-stress design VTE cylinders have buckling loads greater than original CTC cylinders, and unlike the same-load design VTE cylinders where the ratio P_{VTE}/P_{CTC} is forced to be unity, meaning the same-load design VTE cylinders have buckling load equal to CTC cylinders, for the same-area design VTE cylinders the ratio P_{VTE}/P_{CTC} is less than unity, meaning that the same-area design VTE cylinders have buckling loads less than those of the original CTC cylinders.

e_0	$\overline{\sigma}_{VTE}/\overline{\sigma}_{CTE}$		$\overline{\sigma}_{VTE}/\sigma_{CTC}$		
	small	large	small	large	$1/g^2(e_0)$
0.50	1.1414	1.1618	0.9779	0.9764	0.9772
0.70	1.3356	1.3781	0.8893	0.8889	0.8865
0.85	1.4644	1.5593	0.6639	0.6790	0.6804

Table 6.12: Comparison among key stress ratios of VTE and CTE cylinders at the buckling condition, same-area design

e_0	P_{VTE}/P_{CTE}		P_{VTE}/P_{CTC}		
	small	large	small	large	$1/g^2(e_0)$
0.50	1.1415	1.1616	0.9779	0.9762	0.9772
0.70	1.3361	1.3773	0.8896	0.8884	0.8865
0.85	1.4685	1.5570	0.6658	0.6781	0.6804

Table 6.13: Comparison among key load ratios of VTE and CTE cylinders at the buckling condition, same-area design

This completes the discussion of the WWM approach to improving the axial buckling capability of elliptical cylinders. By a number of measures, gains in capability were demonstrated and attention now turns to consideration of the BWM approach.

Chapter 7

Variable geometry elliptical anisogrid cylindrical shells: a BWM approach

7.1 Introduction

In Chapter 5 it was mentioned that the equation (3.44) for the buckling stress of a homogeneous orthotropic circular cylinder with a uniform wall thickness provides a good approximation for the buckling stress of an elliptical cylinder when the radius of the circle is replaced with the radius of the maximum osculating circle. As seen, this techique is based on the idea of assuming the axial buckling behavior of an elliptical cylinder is identical to the axial buckling behavior of a circular cylinder having the radius equal to the maximum radius of curvature af the elliptical cross section. As shown in Tab. 5.4 the predictions based on this assumption are in good agreement with finite-element predictions, which included prebuckling rotation effects. However, as shown in Fig. 5.4, elliptical cylinders deform mainly at the flatter regions, while circular cylinders deform in an axisymmetric fashion. As mentioned, this behavior can be explained by recognizing that, due to the continuously varying curvature, each portion of the elliptical cylinder reaches the critial level of stress for a different value of applied axial displacement. When an axial displacement is applied to a constant thickness homogeneous elliptical cylinder, the induced stress is roughly constant around the circunferential direction (see Fig. 5.7). The flatter regions reach their critical

level of stress before any other portions of the cylinder, which are working at a lower stress level than the their critical level. This behavior compromises the performance of the entire structure. The BWM approach, introduced at the end of Chapter 5, is based on the idea of forcing each part of the cylinder cross section to work at its best. This approach can be implemented by tailoring the material properties of the orthotropic material in such a fashion as to force the actual stress, produced by an assigned axial displacement, to be equal to the critical level of stress point by point for all circumferential locations.

7.2 Variable-material property elliptical cylindrical shell design

When a constant thickness elliptical cylinder made of a nonhomogeneus orthotropic material is taken into consideration, the function $\zeta(t, e_0)$ becomes independent of both the circumferential position and the assigned eccenticity, and is equal in value to unity (i.e., $\zeta(t, e_0) = \zeta \equiv 1$) and (5.15) assumes the following form

$$\sigma_{cr}(e_0) = \eta_c \left(\min_{0 \le t < 2\pi} \left\{ \left(\frac{\varphi(t, e_0)}{\rho(t, e_0)} \right) E_1(t, e_0) \right\} \right) \tag{7.1}$$

To circumvent there being any location around the circumference of a noncircular cylinder where the actual level of stress, produced by a uniform axial srain ϵ_0, is different from the critical level of stress for that location, it will be further assumed that a variable material property elliptical cylindrical shell can be designed with the condition

$$\sigma_{cr}(t, e_0) = \sigma(t, e_0) = E_1(t, e_0)\epsilon_0 \qquad \forall t \in [0, 2\pi) \tag{7.2}$$

Equation (7.2) stipulates that the actual stress distribution $\sigma(t, e_0)$ produced in the cylinder by the application of a uniform axial strain ϵ_0 is required to be equal, point-by-point around the circumference, to the critical stress level that each point can support. An alternative way to describe this approach is by stating that, point-by-point, each location around the circumference of the variable material property elliptical cylinder is required to behave as a circular cylinder having radius equal to the local radius of curvature of the ellipse and with the local material properties of the ellipse. The latter interpretation is visualized in Fig. 7.1,

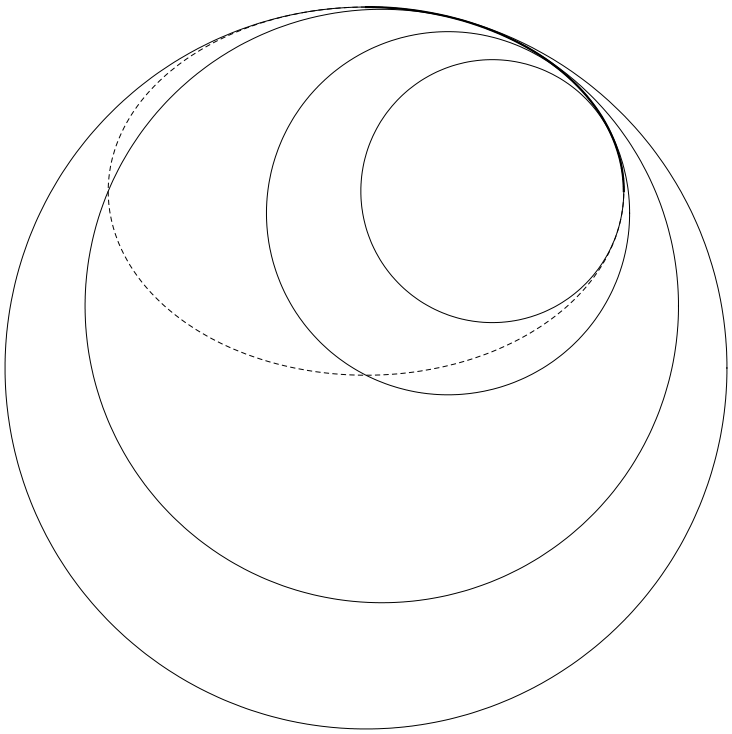

Figure 7.1: Local approximation of the ellipse with its osculating circles

where the profile of an ellipse having $e_0 = 0.70$ is dashed, the four osculating circles obtained for $t = 0$, $t = \pi/6$, $t = \pi/3$, and $t = \pi/2$, are shown, and the first quadrant of the ellipse obtained by joining the proper portions of those circles is shown as a bold line. It should be remarked that although both the WWM aproach and the BWM approach require the stress to be equal to the critical stress point by point, with the first approach the cylinder is designed with the purpose of making its critical stress independent of the circumferential location, while with the second approach the cylinder is designed with the purpose of having the actual stress distribution equal point by point to the critical stress that is a function of the circumferential location. Substituting (7.1) in (7.2) and eliminating $E_1(t, e_0)$ from both sides, the design condition can be written in the following form:

$$\eta_c \frac{\varphi(t, e_0)}{\rho(t, e_o)} = \epsilon_0 \quad \Rightarrow \quad \varphi(t, e_0) = \alpha_\varphi \rho(t, e_o) \qquad \forall t \in [0, 2\pi) \tag{7.3}$$

where $\alpha_\varphi = \epsilon_0/\eta_c$ is a positive scalar quantity. The design of the variable material property elliptical cylinder is complete once the value of the constant α_φ in (7.3) is specified. Here the constant α_φ will be selected so the value of axial strain that produces the buckling in

the variable material property elliptical cylinder will be the same value that produces the buckling in the original circular cylinder. Only this choice of α_φ will be addressed in this Chapter, though other choices can be made.

7.3 Variable-geometry elliptical anisogrid cylindrical shell design

Theoretically speaking, once the function $\zeta(t, e_0)$ is known, it is obvious how the variable thickness design, proposed in the previous Chapter, can be implemented. Conversely, for the variable material property design, although the function $\varphi(t, e_0)$ is known, it is not obvious how to implement material property tailoring. In Chapter 4 in Fig. 4.3 it was shown how the buckling behavior of a constant geometry circular (CGC) anisogrid cylinder depends on the rib angle ϕ [1]. In the present section this knowledge will be used to specialize (7.3) in order to design a variable geometry elliptical (VGE) anisogrid cylinder for implementing the BWM approach.

In order to proceed, the terms appearing in (7.3) (i.e., α_φ, $\varphi(t, e_0)$) must be specified. First of all, it is necessary to establish the rib angle for the original CGC anisogrid cylinder that will be assigned an eccentricity e_0 and with which the buckling load of the VGE cylinder can be compared. The most reasonable choice seems to be $\phi = 30°$ (i.e., an isogrid cylinder), the behavior of which has been already investigated in Chapter 5. The applied strain ϵ_0 that produces the axial buckling of the original CGC isogrid cylinder can be estimated using (4.12), namely,

$$\epsilon_0 = \eta_c \frac{1}{2}\sqrt{\frac{3}{2}} \quad \Rightarrow \quad \alpha_\varphi = \frac{\epsilon_0}{\eta_c} = \frac{1}{2}\sqrt{\frac{3}{2}} \tag{7.4}$$

Second, the function $\varphi(t, e_0)$ can be specialized for an anisogrid structure by substituting (4.8) and (4.9) into (5.12). The following expression is obtained:

$$\varphi(\phi(t, e_0))) = \begin{cases} \dfrac{1+\sin^3(\phi)}{\cos^2(\phi)}\sqrt{\dfrac{2}{3}\left(\sin^4(\phi) + \sqrt{\sin^5(\phi)+\sin^8(\phi)}\right)} & 0 < \phi < \frac{\pi}{6} \\ \dfrac{1+\sin^3(\phi)}{\cos^2(\phi)}\sqrt{\dfrac{1}{3}\sin(\phi)} & \frac{\pi}{6} \leq \phi < \frac{\pi}{2} \end{cases} \tag{7.5}$$

where, for brevity of notation, the dependence of the function on the circumferential location

[1] As stated, in the notation CGC, the G standing for geometry refers to rib angle.

and the assigned eccentricity through the rib angle (i.e., $\phi(t, e_0)$) is highlighted on the left side of the equation only. The function (7.5) is plotted in Fig. 7.2. Based on Fig. 7.2, a few

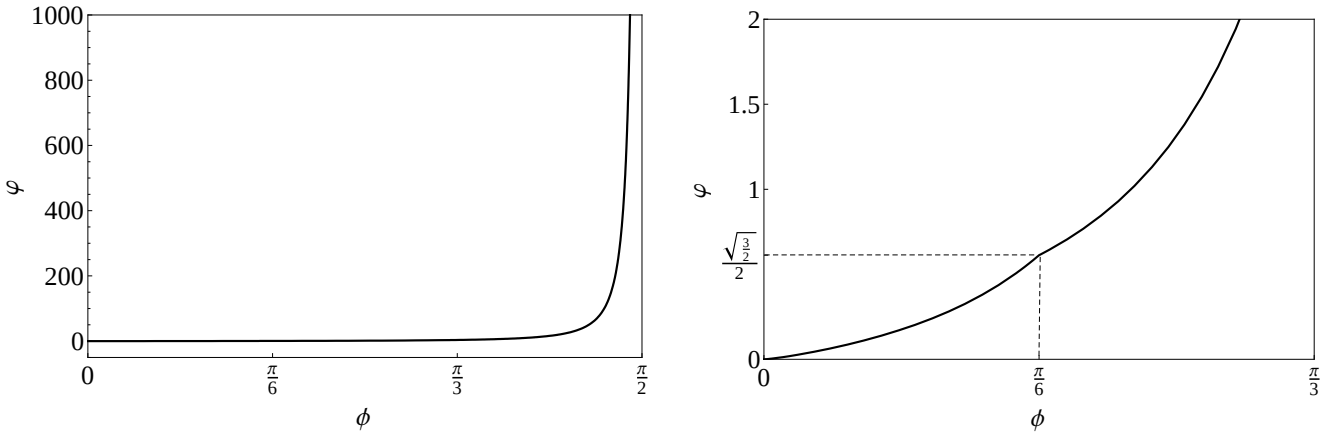

(a) (b)

Figure 7.2: φ vs. ϕ: (a) $0 < \phi < \pi/2$, (b) $0 < \phi < \pi/3$

comments can be made regarding (7.5). First, as expected, the function exibits an inflection point at $\phi = \pi/6$ due to the junction of the axisymmetric and the nonaxisymmetric branches at this value of ϕ (see part (b) of the figure). Second, the function monotonically increases from zero to infinity (see part (a) of the figure) when the rib angle ϕ is varied between zero, i.e., axial ribs, and $\pi/2$, i.e., circumferential ribs. Based on this argument, keeping in mind that when the assigned eccentricity is varied in its admissible range (i.e., $0 \leq e_0 < 1$), the function $\rho(t, e_0)$ assumes only positive values and it is realized that (7.3) is solvable. Substituting (7.4), (7.5), and (5.8) in (7.3) the rib angle as a function of the circumferential position for each assigned eccentricity can be found. It is given by

$$\phi(t, e_0) = \varphi^{-1}\left(\frac{1}{2\mathcal{E}(e_0^2)}\sqrt{\frac{3(1 - e_0^2\cos^2(t))^3}{2(1 - e_0^2)}}\right) \qquad \forall t \in [0, 2\pi) \tag{7.6}$$

Unfortunately, due to the transcendental nature of (7.5) the inverse function $\varphi^{-1}(.)$ cannot be analytically evaluated, except for the two limit cases (i.e., $e_0 = 0$ and $e_0 = 1$). More precisely, setting $e_0 = 0$ in (7.6) the following relation is obtained

$$\phi(t, 0) = \varphi^{-1}\left(\frac{1}{2}\sqrt{\frac{3}{2}}\right) = \frac{\pi}{6} \qquad t \in [0, 2\pi) \tag{7.7}$$

Looking at Fig. 7.2 part (b) it is immediately seen that the solution of (7.7) is $\phi = \pi/6$. Equation (7.7) simply means that (7.3) correctly predicts that if no eccentricity is assigned to the original CGC isogrid cylinder, then no adjustment to the rib angle is necessary. The second analytically solvable case can be studied taking the limit of (7.6) for e_0 approaching unity. The result is

$$\phi(t,1) = \lim_{e_0 \to 1} \phi(t, e_0) = \lim_{e_0 \to 1} \varphi^{-1} \left(\frac{1}{2\mathcal{E}(e_0^2)} \sqrt{\frac{3(1 - e_0^2 \cos^2(t))^3}{2(1 - e_0^2)}} \right) = \begin{cases} 0 & t = 0, \pi \\ \frac{\pi}{2} & otherwise \end{cases} \tag{7.8}$$

Equation (7.8) means that when the original cylinder is squeezed into a flat panel, the ribs should be made circumferential at each point except the two edges, where the ribs should be axial. Of course these limiting cases have only a purely theoretical interest and should not be taken into consideration for practical implementaton. Other than these two limiting cases, a numerical solution must be employed. For convenience of notation (7.6) will be solved on a grid of 168 points corresponding to equispaced locations around the cylinder circumference. (See the discussion in Sec. 5.3 regarding the finite-element model employed and (6.11)). The numerical solution of (7.6) is shown in Fig. 7.3, as a function of normalized arc length, for different values of assigned eccentricity.

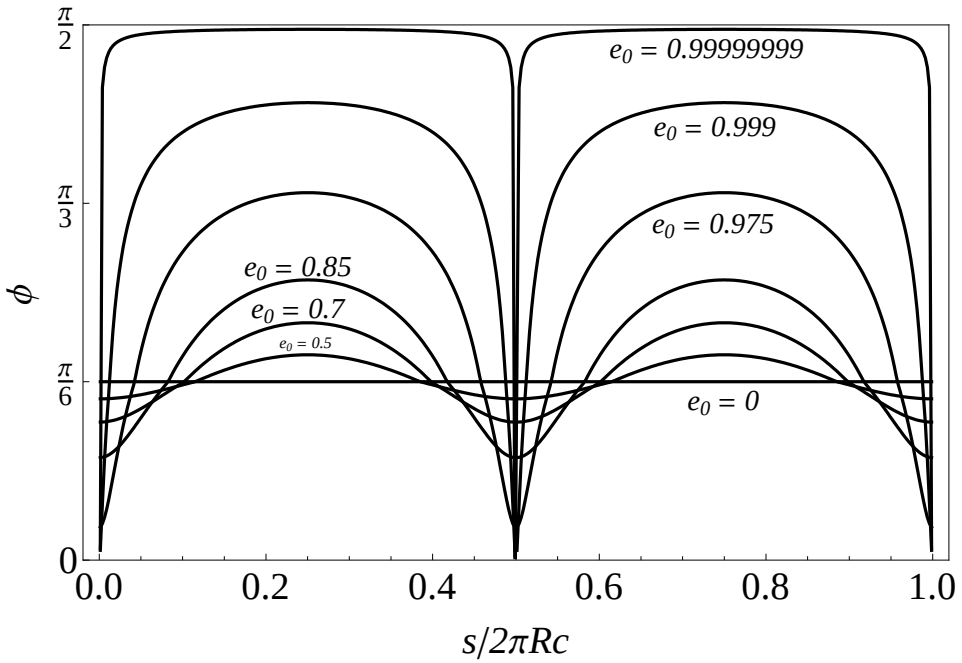

Figure 7.3: Rib angle vs. normalized circumferential position for different eccentricities

A few comments can be made regarding Fig. 7.3. First, it can be noted that, as expected, the function $\phi(t, e_0)$ gradually varies between the two limiting functions $\phi(t, 0)$ (see (7.7)) and $\phi(t, 1)$ (see (7.8)). More precisely, the variation is quite smooth when the assigned eccentricity is lower than about $e_0 = 0.9$ and changes very fast when $0.9 < e_0 < 1$. Second, the flatter regions of the ellipse, i.e., the regions around $s/2\pi R_c = 0.25$ and $s/2\pi R_c = 0.75$, are associated with rib angle values greater than $\phi = \pi/6$, which correspond to a softer axial modulus than in the original CGC isogrid cylinder. Moreover, as seen in Chapter 4, rib angles greater than $\phi = \pi/6$ correspond to an over shear-GMI material and an axisymmetric buckled shape. Conversely, the more curved regions of the ellipse, i.e., the regions around $s/2\pi R_c = 0$ and $s/2\pi R_c = 0.5$, are associated with rib angles lower than $\phi = \pi/6$. This corresponds to a stiffer axial modulus than in the original CGC isogrid cylinder. Moreover, as seen in Chapter 4, rib angles lower than $\phi = \pi/6$ correspond to under shear-GMI material and a nonaxisymmetric buckled shape. Finally, it is seen from the figure that the more the eccentricity increases the more the over shear-GMI regions enlarge, bordering the under shear-GMI regions at the more curved locations. According with the previous arguments, the present theory predicts the VGE anisogrid cylinder to buckle with an axisymmetric pattern in the flatter regions, which tend to enlarge as eccentricity approaches unity, and a nonaxisymmetric pattern in the curved regions, which tend to shrink the more the eccentricity approaches unity. More precisely, the border between the over shear-GMI region and the under shear-GMI region is located where the radius of curvature of the VGE anisogrid cylinder is equal to the radius of the original CGC isogrid cylinder. For this location the material is shear-GMI.

Once the function $\phi(t, e_0)$ is known, the axial stress, as a function of the circumferential location, can be easily determined. In fact, it can be noted that when the rib angle is tailored using $\phi(t, e_0)$, by definition the strain level at the buckling condition is constant all around the cylinder circumference and consequently the following expression can be written for a VGE anisogrid cylinder:

$$\sigma_{VGE} = E_1(\phi(t, e_0))\epsilon_0 \qquad t \in [0, 2\pi) \tag{7.9}$$

Similarly, using (7.7) and (4.7) the axial buckling stress of the original CGC isogrid cylinder

can be determined to be

$$\sigma_{CGC} = E_1(\phi(t,0))\epsilon_0 = E_1(\pi/6)\epsilon_0 = E_r\delta\epsilon_0 \qquad t \in [0, 2\pi) \tag{7.10}$$

Dividing (7.9) by (7.10), the following expression is obtained:

$$\frac{\sigma_{VGE}}{\sigma_{CGC}} = \frac{E_1(\phi(t,e_0))\epsilon_0}{E_r\delta\epsilon_0} = \frac{\cos^4(\phi(t,e_0))}{\sin(\phi(t,e_0)) + \sin^4(\phi(t,e_0))} \qquad t \in [0, 2\pi) \tag{7.11}$$

Equation (7.11) states that the ratio $\sigma_{VGE}/\sigma_{CGC}$ can be estimated by means of the ratio between the axial Young's modulus of the VGE anisogrid cylinder and the axial Young's modulus of the original CGC isogrid cylinder. This ratio is independent of the constitutive and geometric properties of the cylinder other than the rib angle as a function of the circumferential position (i.e., $\phi(t, e_0)$). Moreover, the ratio is coincident with the function $e_{12}(\phi)$ defined in (4.9). Since the material is homogeneous through the thickness, which is constant around circumference, (7.11) can be also used to predict the ratio between the axial stress resultants of the VGE anisogrid cylinder and the CGC isogrid cylinder. Symbolically that ratio is

$$\frac{N_{VGE}}{N_{CGC}} = \frac{\sigma_{VGE}}{\sigma_{CGC}} = e_{12}(\phi(t,e_0)) \qquad t \in [0, 2\pi) \tag{7.12}$$

The ratio between the load capacity of the VGE anisogrid cylinder and the load capacity of the CGC isogrid cylinder can be estimated by integrating (7.12) around the cylinder circumference to give

$$\frac{P_{VGE}}{P_{CGC}} = \int_0^{2\pi} \frac{N_{VGE}}{N_{CGC}} dt = \int_0^{2\pi} e_{12}(\phi(t,e_0))dt \qquad t \in [0, 2\pi) \tag{7.13}$$

It should be noted that (7.13) depends only on the assigned eccentricity e_0. Equation (7.13) is plotted in Fig. 7.4. Looking at Fig. 7.4 it is seen that the VGE anisogrid cylinder is not able to completely recover the the axial buckling load of the original CGC isogrid cylinder. Despite that, it can be seen that the VGE anisogrid cylinder is able to recover more than 90% of the original axial buckling load when the assigned eccentricity is less that about 0.75, and more than 80% of the original axial buckling load when the assigned eccentricity is less that about 0.95. When the assigned eccentricity is more than 0.95, the axial buckling load performance of the VGE anigogrid cylinder decays quickly and reaches zero for $e_0 = 1$. As

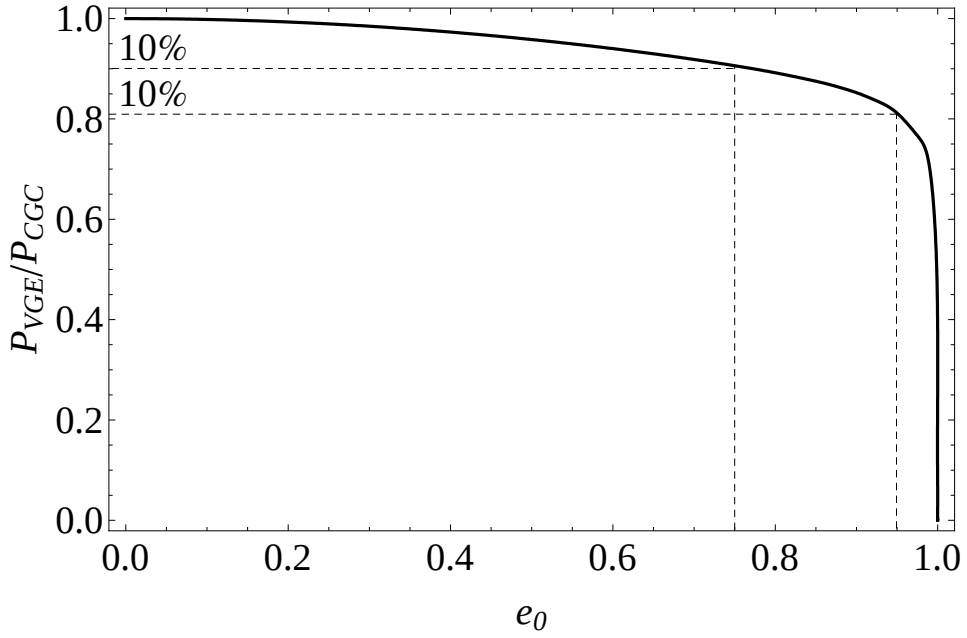

Figure 7.4: Ratio P_{VGE}/P_{CGC} versus assigned eccentricity

seen in Chapter 5 (see Fig. 5.6), for a VGE isogrid cylinder about 20% of the original axial buckling load is lost when an eccentricity of approximatly 0.5 is assigned to the circular cross section.

The volume of the lattice construction can be estimated multiplying the total length of the ribs in the cylinder by the cross-sectional area of one rib. It can be easily realized that for an assigned eccentricity of e_0 all the helical ribs have equal length l_h. Moreover, the length of circumferential ribs l_c is independent of the eccentricity and is equal to the cylinder circumference, namely $2\pi R_c$. Consequently, considering n_h to be the total number of helical ribs and n_c the total number of circumferential ribs, the total length l_{total} of all the ribs is

$$l_{total} = n_h l_h + n_c l_c \tag{7.14}$$

Due to the constraint equation (4.4) that produces the grid structure shown in Fig. 4.1, the total number of helical ribs must be equal to the total number of circumferential ribs, i.e., $n_h = n_c$. Moreover, n_c must be an even number. Denoting by $x(s, e_0)$ the axial position of a point along a helical rib, measured from the one end of the cylinder, as a function of the

circumferential position, for an assigned eccentricity, the following relation can be written:

$$\frac{\partial x(s,e_0)}{\partial s} = \cot(\phi(s,e_0)) \tag{7.15}$$

Using (7.15), the infinitesimal length of each helical rib can be written as

$$dl_h = \sqrt{1+\left(\frac{\partial x(s,e_0)}{\partial s}\right)^2}\,ds = \frac{ds}{\sin(\phi(s,e_0))} \tag{7.16}$$

The total length of each helical rib can be obtained integrating (7.16) around the circumference as

$$l_h = \int_0^{2\pi R_c} \frac{ds}{\sin(\phi(s,e_0))} \tag{7.17}$$

Keeping in mind that $n_c = n_h$, the ratio between the volume of the VGE anisogrid cylinder and the volume of the original CGC isogrid cylinder can be estimated using (7.14) as

$$\frac{V_{VGE}}{V_{CGC}} = \frac{l_c + (l_h)_{VGE}}{l_c + (l_h)_{CGC}} = \frac{2\pi R_c + \displaystyle\int_0^{2\pi R_c} \frac{ds}{\sin(\phi(s,e_0))}}{2\pi R_c + \displaystyle\int_0^{2\pi R_c} \frac{ds}{\sin(\pi/6)}} = \frac{1}{3}\left(1 + \frac{1}{2\pi R_c}\int_0^{2\pi R_c} \frac{ds}{\sin(\phi(s,e_0))}\right) \tag{7.18}$$

Equation (7.18) is plotted in Fig. 7.5. Looking at Fig. 7.5 it is seen that the volume of the

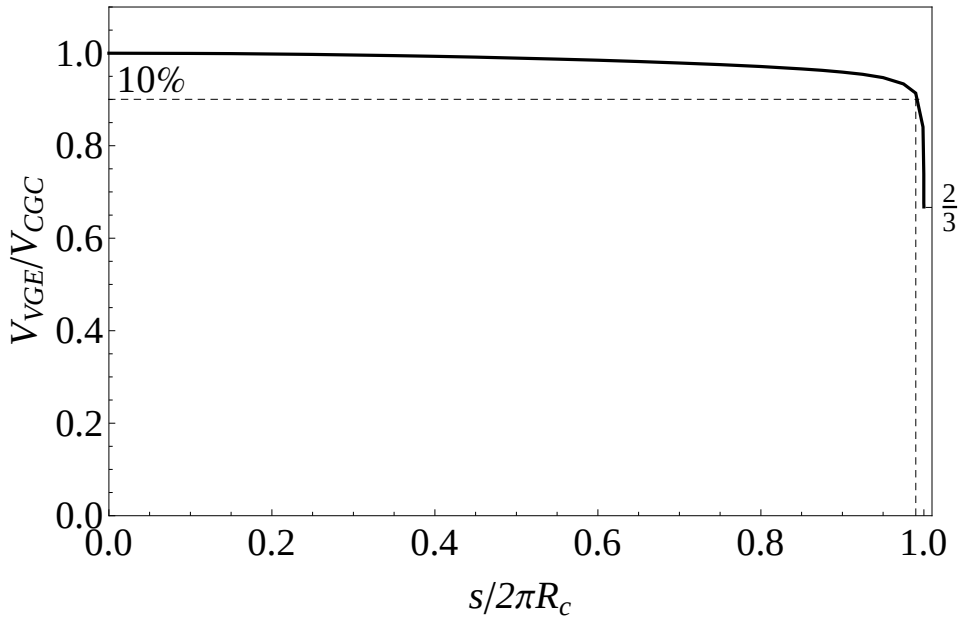

Figure 7.5: Ratio V_{VGE}/V_{CGC} vs. assigned eccentricity

VGE anisogrid cylinder is less than the volume of the original CGC cylinder for all values of eccentricity. For practical values of eccentricity, the volume is about 5% less, an interesting finding. When the assigned eccentricity approaches unity, the ratio (7.18) approaches 2/3. This behavior can be understood by realizing that in the CGC isogrid cylinder each helical rib is two times longer than a circumferential rib, while in the VGE anisogrid cylinder with $e_0 = 1$ the helical ribs becomes horizontal and coincident in length with circumferential ribs. Consequently, when the assigned eccentricity is varied from zero to unity, one-third of the total length is lost.

The previous arguments highlight that the tailoring of the rib angle with circumferential location based on (7.3) does not produce significative chances in the volume of the material in the cylinder. Moreover, these slight changes are always negative. Of course, considering a lattice construction made of homogeneus material, (7.18) also gives an estimation of the weight ratio between the CGC cylinder and the CGE cylinder.

7.4 Design of the grid of the variable-geometry anisogrid cylinder

The tailoring of the rib angle with circumferential location has been achieved in the previous section by treating the lattice as a nonhomogeneous orthotropic material. In this section it will be shown how the actual grid geometry of the lattice structure can be obtained by the knowledge of the function $\phi(s, e_0)$. This operation is not obvious because it involves many geometric compatibility issues. To avoid unnecessary complications, the cylinder will be unrolled onto the plane $(x/2\pi R_c, s/2\pi R_c)$, where, consistent with notation of the previous section, $x/2\pi R_c$ represents the axial position on a helical rib measured from one end of the cylinder and normalized by the cylinder circumference, while $s/2\pi R_c$ represents the circumferential arc length on a helical rib measured as shown in Fig. 5.3 and normalized by the circumference. The function $x(s, e_0)$ can be obtained by integrating (7.15) in s. Denoting by $X(e_0)$ for a given eccentricity e_0 the axial position of the point on a generic helical rib reached by moving along the rib while making one revolution around the circumference, i.e.,

$X(e_0) = x(2\pi R_c, e_0)$, the following relation can be written:

$$X(e_0) = \int_0^{2\pi R_c} \frac{\partial x(s, e_0)}{\partial s} ds = \int_0^{2\pi R_c} \cot(\phi(s, e_0)) ds \tag{7.19}$$

Stated differently, (7.19) is the furthest axial position from one end of the cylinder reached by moving along a generic rib while make one revolution around the circumference. In Fig. 7.6 part (a) are shown the helical ribs unrolled in the plane $(s/2\pi R_C, x/2\pi R_c)$ for different eccentricities. As seen from Fig. 7.6 part (a) the axial position furthest from one end of the cylinder, $X(e_0)/2\pi R_c$, has a maximum for $e_0 = 0$ equal to $\sqrt{3}$ and decreases the more the eccentricity increases until it becomes zero for $e_0 = 1$. The understanding of Fig. 7.6 part (a) makes clear why the length of the helical ribs varies from two times the circumferential length to one time the circumferential length, as stated in the previous section. The maximum axial

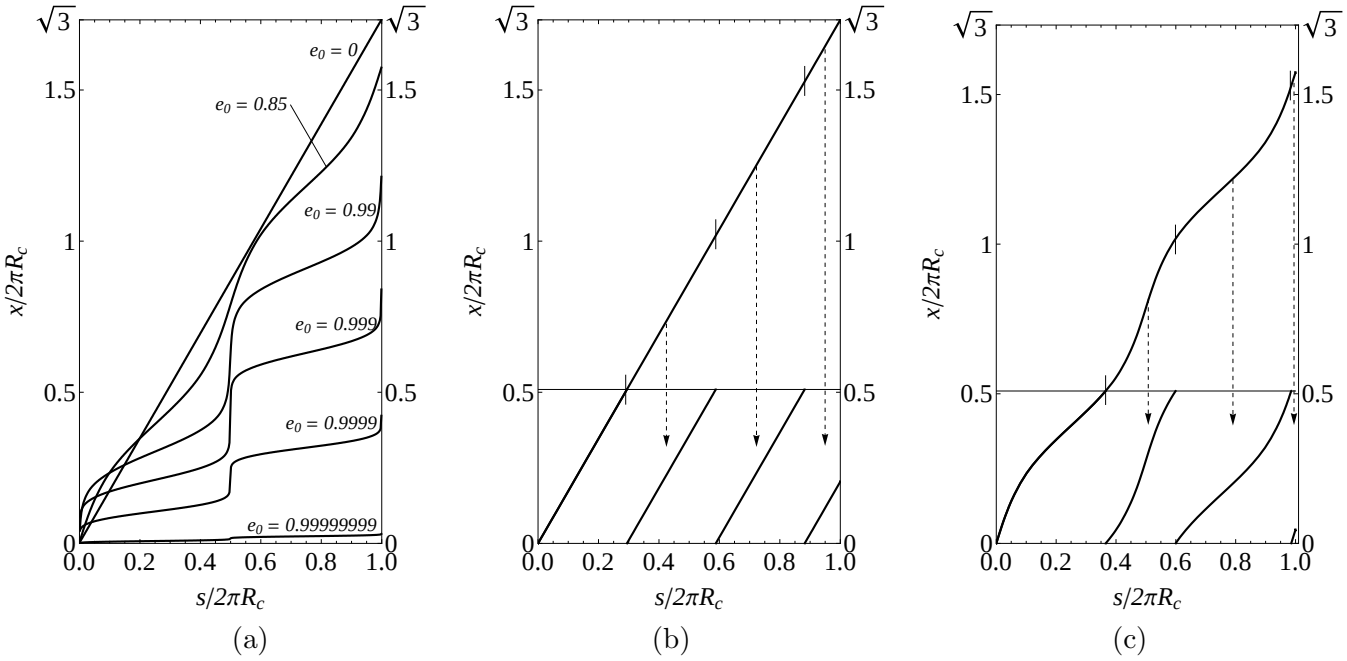

Figure 7.6: (a) Unrolled rib for different eccentricities, (b) sectioned rib for $e_0 = 0$, (b) sectioned rib for $e_0 = 0.85$

position $X(e_0)$ for one revolution of the circumference is fixed once the function $\phi(s, e_0)$ has been determined. The maxiumum axial position cannot be changed. Unfortunately, $X(e_0)$ may not coincide with the required length of cylinder for a particular application, meaning that once the full length of helical rib has been rolled into a cylindrical shape, it reaches the axial position $X(e_0)$ that could likely be different than any specific required length of

cylinder. Stated differently, only very specific lengths of cylinders can be constructed with lattice construction. This inconvenience can, however, be easily resolved by realizing that the function $\phi(s, e_0)$ allocates a specific rib angle to each circumferential location, independently from the axial position of the ribs in the cylinder. This means that the helical ribs can be shifted axially without compromising the homogenized model of the lattice used to estimate the function $\phi(s, e_0)$. Based on these arguments, the helical ribs can be cut and shifted axially each time a rib reaches the required length. This procedure is illustrated in Fig. 7.6 parts (b) and (c) for $e_0 = 0$ and $e_0 = 0.85$, respectively. In the following this technique will be referred to as the "cut and shift" procedure. Unfortunately, this procedure is not enough to guarantee geometric compatibility within the lattice. In fact, in order to form the grid structure shown in Fig. 4.1 into a cylinder, it is necessary that the maximum axial position of the last section of rib on the left of Fig. 7.6 parts (b) and (c) be equal to an integer multiple of the quantity $2a_c$ (where a_c is the spacing between two adjacent circumferential ribs). Otherwise, when the grid is rolled to form a cylinder the grid will be not continuous at the junction points. This requirement makes it generally impossible to construct a lattice cylinder of any particular required length. What is necessary is a slight adjustment that depends on the eccenticity and the number of ribs included in the structure. Once the number of circumferential ribs n_c to include in the lattice construction is known, the length L closest to the desired value L_c and capable of guaranteeing geometrical compatibility of the left side with the right side of the cut and shift construction in Fig. 7.6 can be evaluated by means of the following expression:

$$L(e_0, n_c) = \frac{1}{2} \frac{n_c X(e_0)}{\left\lceil \dfrac{n_c X(e_0)}{2L_c} - \dfrac{1}{2} \right\rceil} \tag{7.20}$$

Subtituting (7.19) in (7.20) and performing the needed calculations, it can be observed that the length adjustment needed to guarantee geometric compatibility is quite moderate for all eccentricity values. The latter statement is proven in Fig. 7.7, where the length $L(e_0, n_c)$ normalized by the desired length L_c is plotted vs. the assigned eccenticity e_0 for $n_c = 30$. As seen, the magnitude of the adjustment is about $\pm 1\%$.

According with the grid structure shown in Fig. 4.1, the entire grid can be obtained by

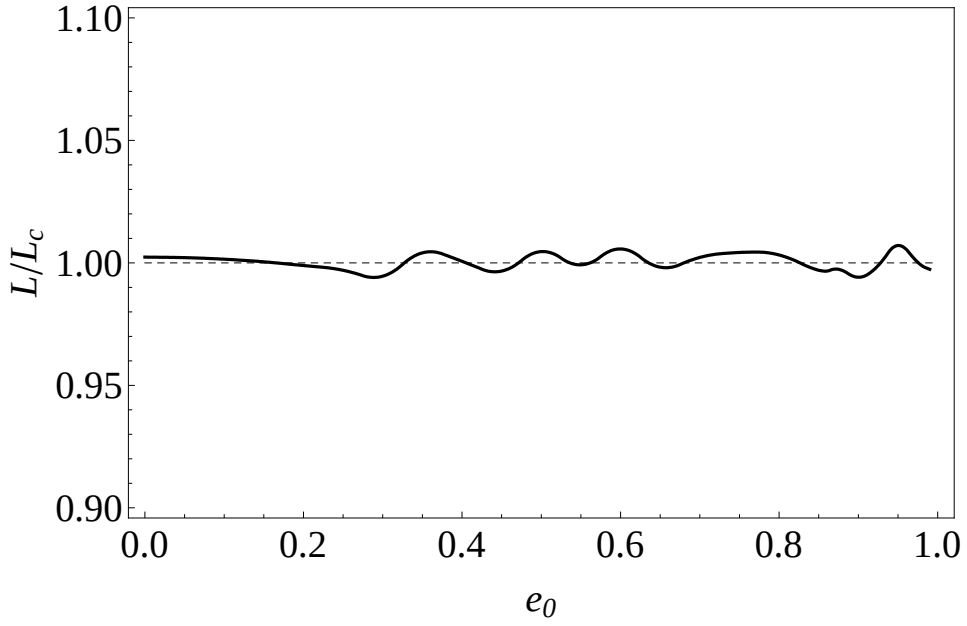

Figure 7.7: Ratio L/L_c versus assigned eccentricity for $n_c = 30$

attaching $n_c/2$ (since n_c must be even, $n_c/2$ is always an integer) basic strips of axial length $2a_c$ one to another, where a_c is the spacing between circumferential ribs defined as

$$a_c(e_0, n_c) = \frac{L(e_0, n_c)}{n_c}. \tag{7.21}$$

The fundamental strip can be obtained with the four steps listed below and illustrated in Fig. 7.8 for $e_0 = 0.85$ and $n_c = 30$, where different colors are used to highlight the construction procedure:

1. Consider a strip of circumferential dimension $2\pi R_c$ and axial dimension $2a_c$ as shown in Fig. 7.8 part (a);

2. Consider one helical rib which has one end attached to the lower left corner of the strip and apply the cut and shift procedure (see Fig. 7.6) to the rib, moving up and to the right along the rib, as shown in Fig. 7.8 part (b);

3. Consider a second helical rib, which has one end attached to the lower right of the strip and apply the cut and shift procedure (see Fig. 7.6) to the rib, moving up and to the left along the rib in Fig. 7.8 part (c);

4. Add two circumferential ribs (i.e., two horizontal lines) having axial position $a_c/2$ and $3a_c/2$, respectively, as shown in Fig. 7.8 part(d)

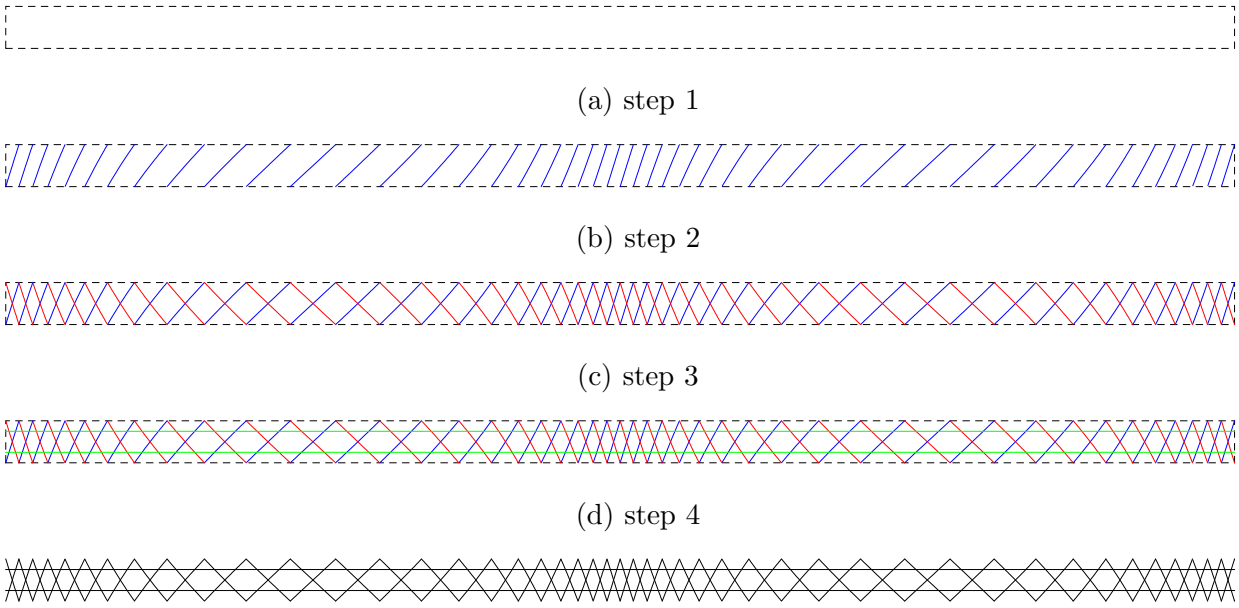

(a) step 1

(b) step 2

(c) step 3

(d) step 4

(e) complete fundamental strip

Figure 7.8: Constructive procedure to build a fundamental strip $e_0 = 0.85$, $n_c = 30$

Looking at Fig. 7.8 part (e) it is seen that a fundamental strip contains two entire circumferential ribs and two entire helical ribs. The latter statement is true because, due to the adjustment of the cylinder length (7.20), the cut and shift procedure applied to a strip having axial dimension $2a_c$ results in the maximum axial position of the last section of helical rib to be exacly $2a_c$. This fact makes even clearer the reason why the volume estimation given in (7.18) is meaningful. As previously mentioned, the entire grid can be obtained by adding $n_c/2$ fundamental strips, one adjacent to another. The grids obtained for $e_0 = 0$, $e_0 = 0.50$, $e_0 = 0.70$, and $e_0 = 0.85$ are shown in Figs. 7.9, 7.10, 7.11, and 7.12, respectively. As seen from these figures, the variable geometry of the grid becomes more evident as the eccentricity increases. The variable geometry produces an increased density of the helical ribs in the more curved regions of the ellipse. The distance between the ribs becomes narrow and narrow as the eccentricity increases. Conversely, the density of the ribs is decreased in the flatter regions of the ellipse and the distance between ribs becomes wider and wider as the eccentricity increases. This variable geometry leads to a circumferentially-uniform

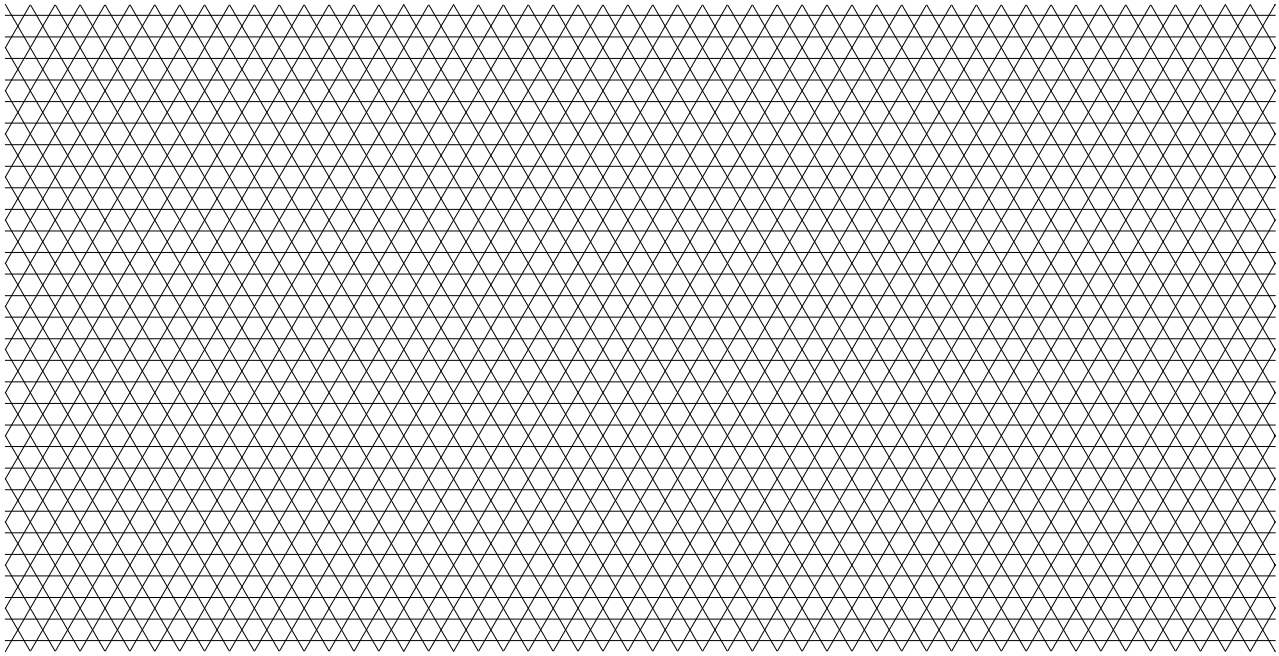

Figure 7.9: Unrolled grid for $e_0 = 0$

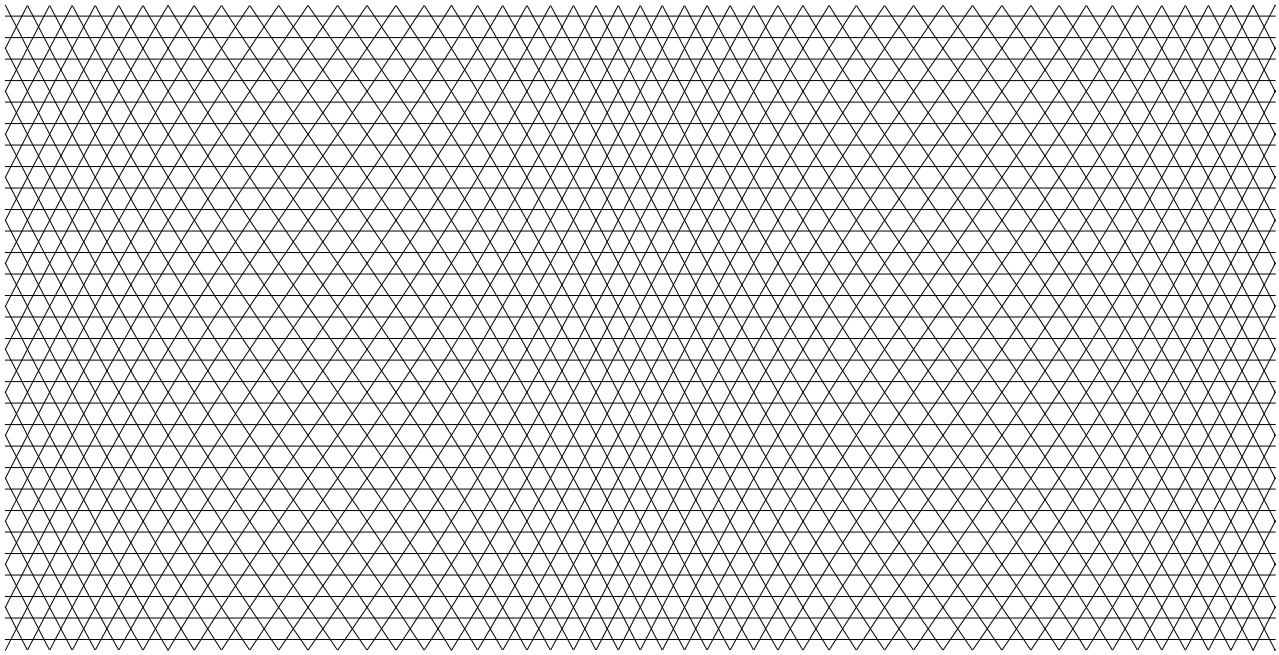

Figure 7.10: Unrolled grid for $e_0 = 0.50$

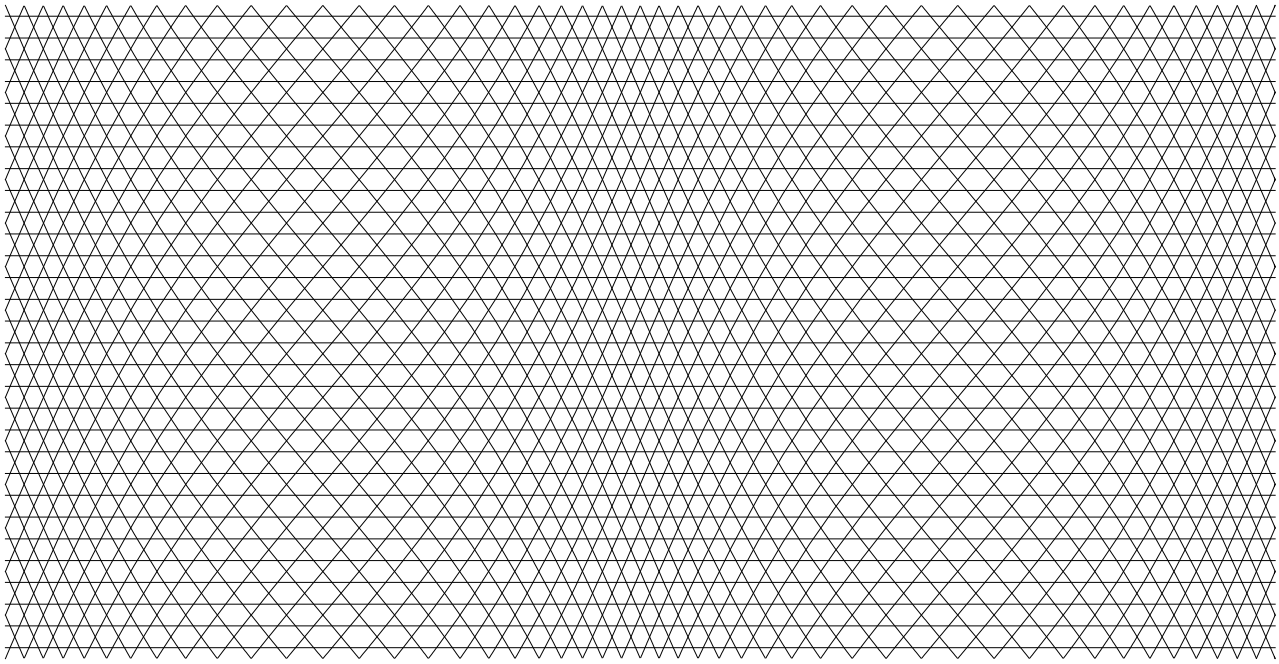

Figure 7.11: Unrolled grid for $e_0 = 0.70$

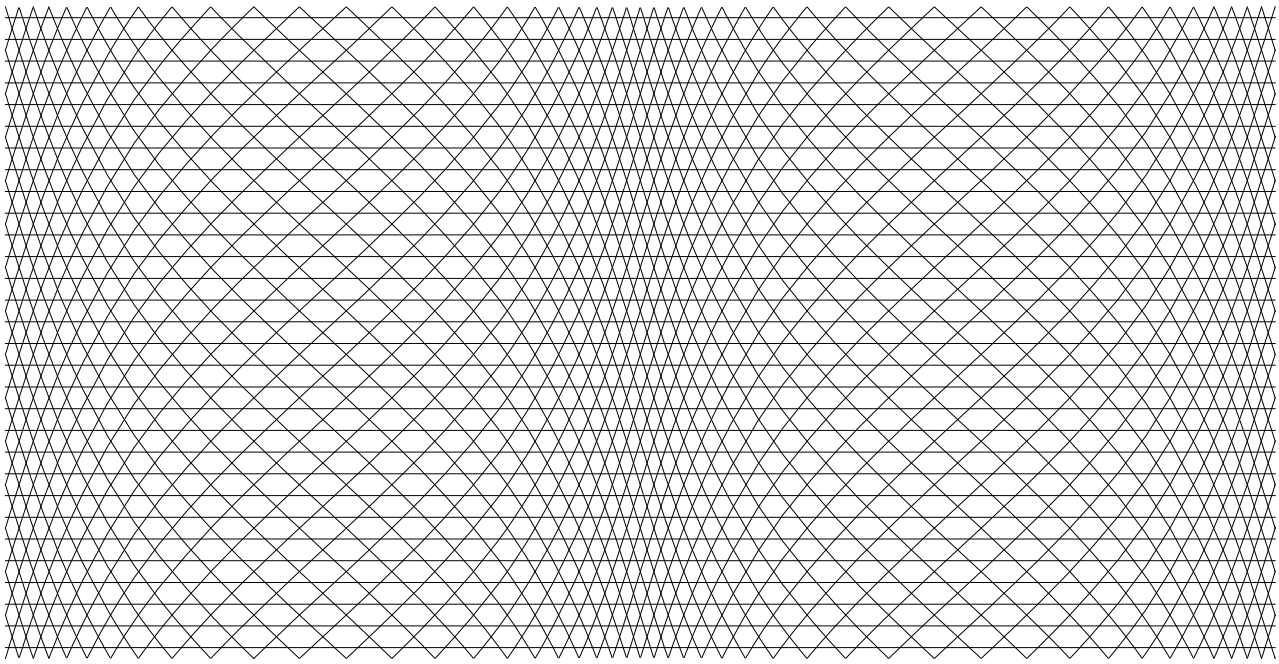

Figure 7.12: Unrolled grid for $e_0 = 0.85$

critical strain level, but the axial modulus of the cylinder is modulated so as to produce a higher stress level in the more curved regions.

7.5 Numerical validation of the proposed design

In this section the VGE cylinder design proposed in section 7.2 will be further studied using numerical results computed with the general-purpose finite-element code *ABAQUS*. In particular, the results from *ABAQUS* will be compared with the results from the developed analysis. Since the developed analysis was based on a rather simple premise, which did not consider prebuckling rotations or stresses other than the axial stress, such comparisons will be informative. Geometrically nonlinear prebuckling analysis will be employed, and the results for simply-supported boundary conditions will be considered. The buckling condition will be identified by applying to one end of each cylinder the smallest axial compressive displacement that causes the tangent stiffness matrix of the numerical analysis to become singular. The stress state for this condition, in particular, the axial stress level, will be considered the buckling stress. The quantities of interest at this level of displacement will be compared with the respective analytical predictions for three values of assigned eccentricities ($e_0 = 0.50,\ 0.70,\ 0.85$) and for anisogrid cylinders of two sizes (see Tab. 5.1) in order to check the generality of the findings of section 7.2.

In Fig. 7.13 the circumferential variation of the axial stress at the buckling condition from the finite-element results for the simply-supported VGE anisogrid cylinders and CGE anisogrid cylinders are shown. Results for small and large cylinders with the three levels of eccentricity are illustrated. In each sub-figure the axial stresses, normalized by the critical stress of a CGC isogrid cylinder, as a function of normalized circumferential location, are plotted. Since the material is homogeneous through the thickness, which is uniform with circumferential location, the axial stress ratio is also the axial stress resultant ratio. The analytical prediction (7.11) ((7.12)) for the ratio $\sigma_{VGE}/\sigma_{CGC}$ (N_{VGE}/N_{CGC}) is also illustrated in the figures. For the purpose of discussion, the stress (stress resultant) for the CGC isogrid cylinder, σ_{CGC} (N_{CGC}), is included and is the horizontal line at unity. At first glance it is clear from Fig. 7.13 that, importantly, the prediction of the σ (N) vs. s relation by

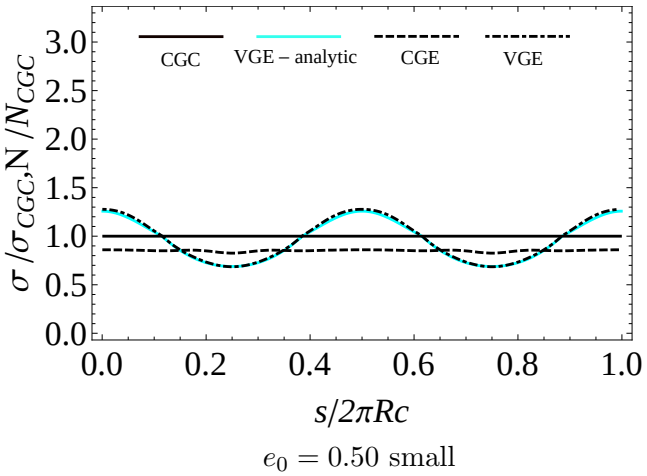

$e_0 = 0.50$ small

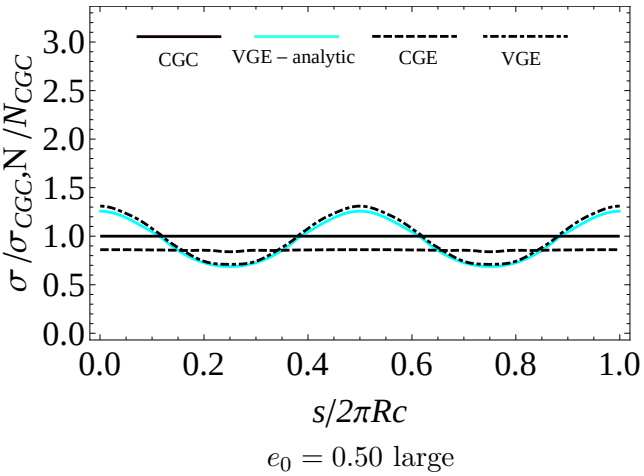

$e_0 = 0.50$ large

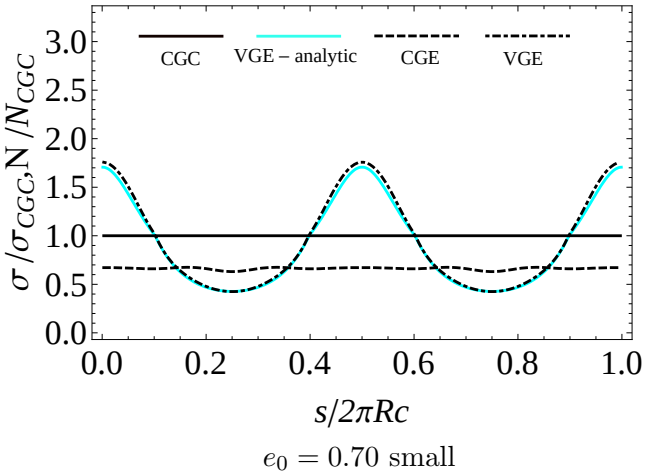

$e_0 = 0.70$ small

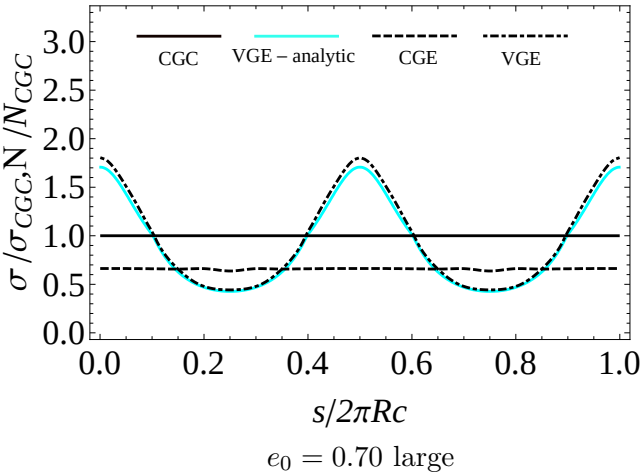

$e_0 = 0.70$ large

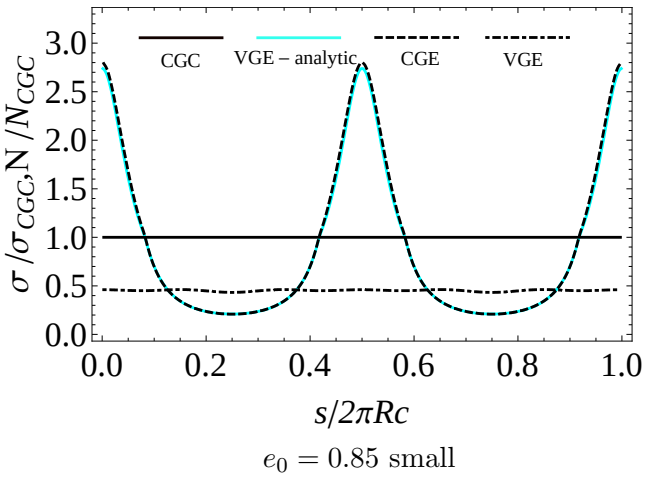

$e_0 = 0.85$ small

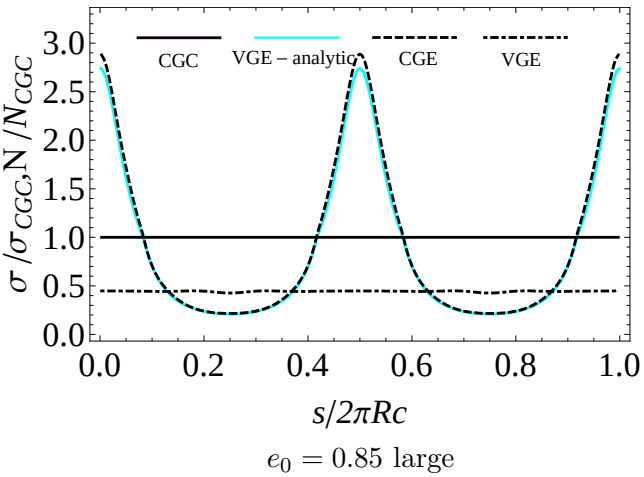

$e_0 = 0.85$ large

Figure 7.13: Comparison among the axial stresses and axial stress resultants at the buckling condition for small and large VGE and CGE cylinders for different eccentricities

the developed analysis is very close to the finite-element calculations for all cases. Looking at more detail, it is observed that while the stress (stress resultant) for the CGE isogrid cylinder, σ_{CGE} (N_{CGE}), is nearly uniform around the circumference, and always less than the CGC isogrid cylinder, the stress (stress resultant) for the VGE cylinder, σ_{VGE} (N_{VGE}), has considerable amplitude modulation, being largest in the more curved regions of the elliptical cross section in all cases ($s/2\pi R_c = 0, 0.5$). This follows because the amplitude of σ (N) should be proportional to the Young's modulus in the axial direction due to the proposed design that forces the stress to be equal to the critical stress for each circumferential location. It should be noted that σ_{VGE} (N_{VGE}) intersects σ_{CGC} (N_{CGC}) where the radius of curvature of the ellipse is equal to the radius of original circle, R_c. The area under the relationship for N vs. s is the total axial load.

From a qualitative inspection of Fig. 7.13, it is quite evident that for each case the area under the N_{CGE} relation is less than the area under the other two, meaning that the tailoring of the rib angle with circumferential position results in an increase of the axial buckling capability of a VGE anisogrid cylinder with respect to a CGE isogrid cylinder. A quantitative comparison among key buckling load ratios of VGE, CGE, and CGC cylinder at the buckling condition, as computed from finite-element analyses and as predicted is given in Tab. 7.1. Looking at Tab. 7.1, a few comments can be made. First, it is seen that (7.13)

e_0	P_{VGE}/P_{CGE}		P_{VGE}/P_{CGC}		
	small	large	small	large	Eq. 7.13
0.50	1.1403	1.1562	0.9702	0.9900	0.9582
0.70	1.4275	1.4583	0.9459	0.9599	0.9185
0.85	1.9738	2.0638	0.8934	0.9154	0.8751

Table 7.1: Comparison among key load ratios of VGE, CGE, and CGC cylinders at the buckling condition

slightly underestimates the load gain obtained by tailoring the rib angle in the VGE design. The underestimation is in the range of about $1-3\%$ for the small cylinders and about $3-5\%$ for the large cylinders. Second, even if rib angle tailoring is unable to completly restore the axial buckling load of a CGE isogrid cylinder to the axial buckling load of a *CGC* isogrid cylinder, tailoring results in a relevant increase in the buckling performace, the increase being dependent on the assigned eccentricity. More precisely, the finite-element analyses predict the load increment to vary from about 15% for $e_0 = 0.50$ to about 100% for $e_0 = 0.85$. Based

on Fig. 7.5 it can be seen that the load increase is accompanied by a decrease of the weight of the lattice cylinder.

This completes the discussion of the BWM approach to improving the axial buckling capability of elliptical cylinders. Gains relative to an isogrid elliptical cylinder were demonstrated and a near-restoration of the performance of an isogrid circular cylinder were illustrated. The next chapter summarizes the analytical developments and findings of the entire study.

Chapter 8

WWM versus BWM: Comparison and conclusions

8.1 Introduction

In Chapters 6 and 7 the WWM and the BWM approaches have been, respectively, implemented. The goal of the two approaches has been to mitigate the disadvantages of having the radius of curvature of a noncircular cylinder vary with circumferential position. The WWM approach has been implemented by tailoring the thickness of the elliptical cylinder with the circumferential position, whereas the BWM approach has been implemented by tailoring the material properties of an orthotropic material with circumferential position. As seen, both approaches result in the actual level of stress produced by an uniform assigned axial strain to be equal point by point to the critical level of stress of each specific circumferential location. The main difference between the two approaches is that while for the WWM approach the critical stress distribution is made independent of the circumferential position, for the BWM approach the critical stress distribution is a function of the circumferential position.

In the first part of this chapter the WWM and BWM approaches, independently studied in Chapters 6 and 7, respectively, will be compared. The similarities in the two approaches will be discussed through a parallel step-by-step derivation of the two designs. In the last

part of this chapter the important conclusions from the dissertation will be summarized and a few interesting opportunities for future investigation will be highlighted.

8.2 WWM approach versus BWM approach

In order to highlight the similarities and the differences with respect to the implementation of WWM and BWM approaches, a step-by-step parallel derivation of the two complementary approaches will be presented. As seen in Chapters 6 and 7, both the WWM and BWM approaches are based on (5.15). In Tab. 8.1 a step-by-step parallel comparison of the special-

Step	$WWM\ (VTE)$	$BWM\ (VGE)$
1	$\varphi(t,e_0)=\varphi,\ E_1(t,e_0)=E_1$	$\zeta(t,e_0)=\zeta\equiv 1$
2	$\sigma_{cr}(t,e_0)=\eta_c\varphi E_1\left(\dfrac{\zeta(t,e_0)}{\rho(t,e_0)}\right)$	$\sigma_{cr}(t,e_0)=\eta_c\zeta E_1(t,e_0)\left(\dfrac{\varphi(t,e_0)}{\rho(t,e_0)}\right)$
3	$\sigma_{cr}(t,e_0)=E_1\epsilon_0=constant$	$\sigma_{cr}(t,e_0)=E_1(t,e_0)\epsilon_0$
4	$\eta_c\varphi\left(\dfrac{\zeta(t,e_0)}{\rho(t,e_0)}\right)=\epsilon_0$	$\eta_c\zeta\left(\dfrac{\varphi(t,e_0)}{\rho(t,e_0)}\right)=\epsilon_0$
5	$\zeta(t,e_0)=\alpha_\zeta\rho(t,e_0)$	$\varphi(t,e_0)=\alpha_\varphi\rho(t,e_0)$
6	$\alpha_\zeta=\dfrac{\epsilon_0}{\eta_c\varphi}=\dfrac{\epsilon_0}{\epsilon_c}$	$\alpha_\varphi=\dfrac{\epsilon_0}{\eta_c\zeta}=\dfrac{\epsilon_0}{\eta_c}$

Table 8.1: Parallel step-by-step derivation of WWM and BWM designs

ization of (5.15) for the WWM and BWM approaches, starting from the basic assumption of the two derivations, is outlined. A few comments can be made for each step:

step 1 For the VTE designs the orthotropic material used to design the cylinder is considered homogeneous and the thickness is assumed variable. This assumption affects two terms of (5.15), namely, the axial modulus $E_1(t,e_0)$ and the dimensionless function $\varphi(t,e_0)$. Both of these quantities become independent of circumferential position and assigned eccentricity. Conversely, for the VGE design the orthotropic material used to design the cylinder is considered nonhomogeneous and the thickness is assumed constant. This

assumption affects only one term of (5.15), namely, the dimensionless function $\zeta(t, e_0)$ that becomes identical to unity.

step 2 Including the symbol ζ, even if it is identical to unity, the critical stress function expression obtained by enforcing the assumptions of step 1 in (5.15) can be made exactly complementary.

step 3 When the critical stress is made equal to the actual stress produced by an assigned strain ϵ_0, the main difference between WWM and BWM is revealed automatically. In fact, due to the assumptions made in step 1 for the VTE designs, the actual stress, and consequently the critical stress, must be uniform with circumferential position due the the homogeneity of the material. Conversely, the equivalence between the actual stress and the critical stress is weaker in the VGE design i.e., the equivalence is realized point by point but different points can have different stress levels, and consequently different critical stress levels. A more physical way to understand the difference between the two approaches is to say that the tailoring of the thickness with circumferential position affects the critical stress but does not affect the actual level of stress (it affects the stress resultant only), whereas the tailoring of the material properties affects simultaneously both the critical stress and the actual level of stress.

step 4 Again, including the symbol ζ, even if it is identical to the unity, the critical stress function expression obtained enforcing step 2 condition can be made exactly complementary. Moreover, the structure of the equation indicates that the terms in bracket must be constant.

step 5 The design conditions for VTE and VGE can be made again exactly complementary. More precisely, for the VTE designs the thickness is tailored by means of the function $\zeta(t, e_0)$ in order to compensate for the continuously changing curvature of the ellipse, whereas for the VGE design the material properties are tailored by means of the function $\varphi(t, e_0)$ in order to compensate for the continuously changing curvature of the ellipse. The tailoring of the function $\varphi(t, e_0)$ produces a modulation of the axial modulus $E_1(t, e_0)$, which, in turn, produces a modulation of the actual level of stress.

step 6 The meaning of the proportionality constant is different in the two approaches. In

fact, for the VTE designs the constant α_ζ can be interpreted as the ratio between the assigned axial strain ϵ_0 and the axial strain ϵ_c that causes buckling in the original circular cylinder. Instead, for the VGE design the constant α_φ can be interpreted as the ratio between the assigned axial strain ϵ_0 and the parameter η_c defining the original circular cylinder geometry. This asymmetry can be motivated by realizing that while the function $\zeta(t, e_0) \equiv 1$ for constant thickness cylinder, the function $\varphi(t, e_0) \neq 1$ for homogeneous material, meaning that for a homogeneous material the axial strain which produces the critical stress is dependent on material properties. This difference apart, it should be noted that neither the VTE nor the VGE designs are completely specified by the design condition given at step 2. Each design is complete only when the constants of proportionality α_ζ or α_φ are specified. Based on the previous interpretation, specifying the proportionality constant is the same as choosing the assigned axial strain ϵ_0 for which the cylinder will reach the crucial level of stress simultaneously at each point around the circumference.

Based on the previous arguments it is clear that both VTE and VGE designs can be seen as complementary implementations of a unique design philosophy. What seems to be really important is that the term in brackets in (5.15) needs to be constant in order to force the stress produced by an uniform axial strain to be equal point by point to the critical level of stress at each specific location of the cylinder. The latter concept can be expressed symbolically through the following expression

$$\left(\frac{\zeta(t, e_0)\varphi(t, e_0)}{\rho(t, e_0)} \right) = constant \tag{8.1}$$

The complete understanding of (8.1) makes clear that a mixed approach can be implemented by choosing the function $\zeta(t, e_0)$ and $\varphi(t, e_0)$ with the following rule

$$\zeta(t, e_0) = \alpha_\zeta \rho_1(t, e_0) \qquad \varphi(t, e_0) = \alpha_\varphi \rho_2(t, e_0) \tag{8.2}$$

where the following constraint must be fulfilled

$$\rho_1(t, e_0)\rho_2(t, e_0) = \rho(t, e_0) \tag{8.3}$$

and α_ζ and α_φ are arbitrary positive constants that can be physically interpreted as

$$\alpha_\zeta \alpha_\varphi = \frac{\epsilon_0}{\eta_c} \tag{8.4}$$

In Tab. 8.2 are reported the values assumed by α_ζ, α_φ, $\rho_1(t, e_0)$, and $\rho_2(t, e_0)$ for the three VTE designs and for the VGE design. An understanding of Tab. 8.2 makes evident that

	VTE same-stress	VTE same-load	VTE same-area	VGE
α_ζ	1	$\frac{1}{g(e_0)}$	$\frac{1}{g^2(e_0)}$	1
α_φ	1	1	1	$\frac{1}{2}\sqrt{\frac{3}{2}}$
$\rho_1(t, e_0)$	$\rho(t, e_0)$	$\rho(t, e_0)$	$\rho(t, e_0)$	1
$\rho_2(t, e_0)$	1	1	1	$\rho(t, e_0)$

Table 8.2: Specification of the α_ζ, α_φ, $\rho_1(t, e_0)$, and $\rho_2(t, e_0)$ for the three VTE designs and the VGE design

the four designs proposed in this dissertation are but a few possible choices among infinitely many possibilities. All the choices are made here with the spirit of restoring one of the relevant measures of performance of the original circular structure, namely the critical stress with the VTE same-stress design, the critical load with the VTE same-load design, the weight with the VTE same-area design, and the critical strain with the VGE design, but other choices can be made.

The value assumed by relevant measures of performance in the four proposed designs, normalized by corresponding quantities for the original circular cylinder, will be summarized and compared in Tab. 8.3. In order to specify measures for both VTE and VGE designs together, the labels CXC and VXE will be adopted where the character 'X' stands for 'T' or 'G' depending on the particular design philosophy. In Tab. 8.3 are reported the values assumed for the measures of interest for the three VTE designs and the VGE design. More precisely, the critical axial strain, the critical axial stress, the critical axial stress resultant, the critical axial load, the volume, and the critical axial load per unit of volume are tabulated. The latter quantity will be referred to as the specific critical axial load and will be used in

the following to make an objective comparison among different designs.

	VTE same-stress	VTE same-load	VTE same-area	VGE
$\frac{\epsilon_0}{\epsilon_c}$	1	$\frac{1}{g(e_0)}$	$\frac{1}{g^2(e_0)}$	1
$\frac{\sigma_{VXE}}{\sigma_{CXC}}$	1	$\frac{1}{g(e_0)}$	$\frac{1}{g^2(e_0)}$	$e_{12}(\phi(s,e_0))$
$\frac{N_{VXE}}{N_{CXC}}$	$\rho(t,e_0)$	$\frac{\rho(t,e_0)}{g^2(e_0)}$	$\frac{\rho(t,e_0)}{g^4(e_0)}$	$e_{12}(\phi(s,e_0))$
$\frac{P_{VXE}}{P_{CXC}}$	$g^2(e_0)$	1	$\frac{1}{g^2(e_0)}$	$\int_0^{2\pi R_c} e_{12}(\phi(s,e_0))ds$
$\frac{V_{VXE}}{V_{CXC}}$	$g^2(e_0)$	$g(e_0)$	1	$\frac{1}{3}\left(1+\frac{1}{2\pi R_c}\int_0^{2\pi R_c}\frac{ds}{\sin(\phi(s,e_0))}\right)$
$\frac{\frac{P_{VXE}}{P_{CXC}}}{\frac{V_{VXE}}{V_{CXC}}}$	1	$\frac{1}{g(e_0)}$	$\frac{1}{g^2(e_0)}$	$\frac{\int_0^{2\pi R_c} e_{12}(\phi(s,e_0))ds}{\frac{1}{3}\left(1+\frac{1}{2\pi R_c}\int_0^{2\pi R_c}\frac{ds}{\sin(\phi(s,e_0))}\right)}$

Table 8.3: Comparison among relevant normalized quantities for four different designs

In Fig. 8.1 is shown a comparison among the normalized axial stress resultants at the buckling level as predicted by the developed analysis (see Tab. 8.3) for the four different designs and for two different eccentricities, namely $e_0 = 0.70$ and $e_0 = 0.85$. Looking at Fig. 8.1 a few comments can be made. First, all the VTE designs allocate a greater portion of the load to the flatter regions of the elliptical cylinder, whereas the VGE design allocates a greater portion of the load to the more curved regions. This is the consequence of the complementary nature of the WWM and the BWM approaches, where in this contest the ability to 'work' is identified with the curvature of the shell. Second, the VTE same-stress design and the VGE design intersect unity (i.e., CXC) at the same axial location. As mentioned earlier, these locations correspond exactly to those circumferential locations which have the same curvature as the original CXC cylinder. This fact is not true for the other two VTE designs, namely, same-load and same-stress designs. Based on these arguments it can be stated that VTE same-stress and VGE designs are exactly complementary to each other. In fact, for each circumferential location if the normalized axial stress resultant associated with the VTE

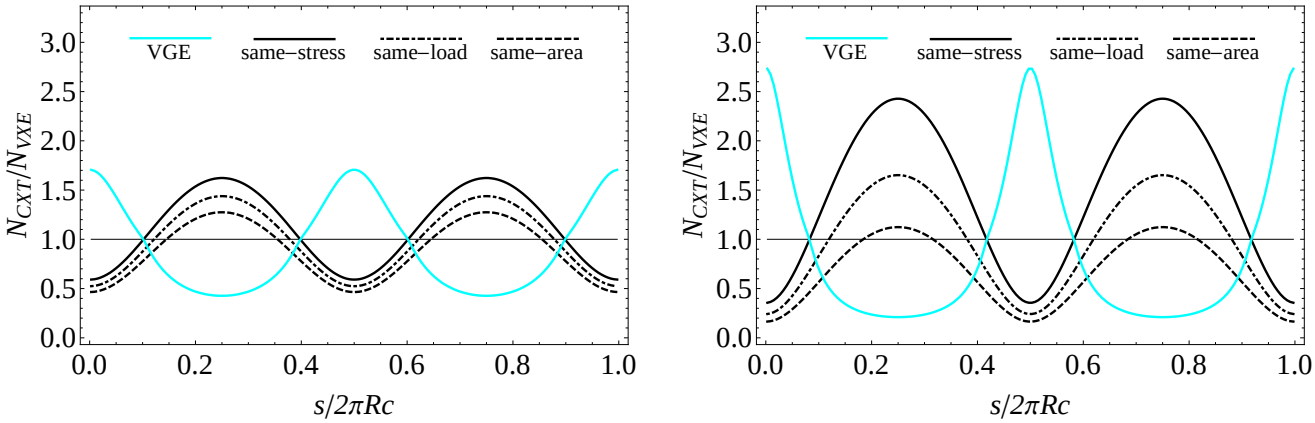

(a) $e_0 = 0.70$ (b) $e_0 = 0.85$

Figure 8.1: Comparison among normalized stress resultants for different designs

same-stress design is greater than unity, then the normalized axial stress resultant associated with the VGE design is lower than unity. Stated differently, the circumferential locations supporting the majority of the load are exactly complementary in the two designs. This behaviour is due to the fact that both the VTE same-stress and VGE designs reach their own level of critical stress for the same value of assigned strain (see first row of Tab. 8.3). Finally, it can be noted that for all the three VTE designs the curvatures of the positive and negative peaks are similar, whereas in the VGE design the positive peaks are sharper than the negative peaks.

Another objective comparison among different designs can be made using the critical load per unit of weight as defined in the last row of Tab. 8.3. The relations corresponding to the four designs are plotted in Fig. 8.2 vs. assigned eccentricity. As seen from Fig. 8.2, only the VTE same-stress design has the same specific load capability as the original circular cylinder. All the remaining designs experience a deterioration of the specific load capability as the assigned eccentricity increases. It is interesting to note that for eccentricity values lower than about 0.70 the specific load capability of a VTE same-load design is greater than the VGE design. Conversely, when $0.70 < e_0 < 1$ the VGE design has a better specific load capability than VTE same-load design. Similar comments can be made for the comparison between VTE same-area and VGE designs, where the breaking point is at $e_0 \simeq 0.55$ instead of at $e_0 \simeq 0.70$.

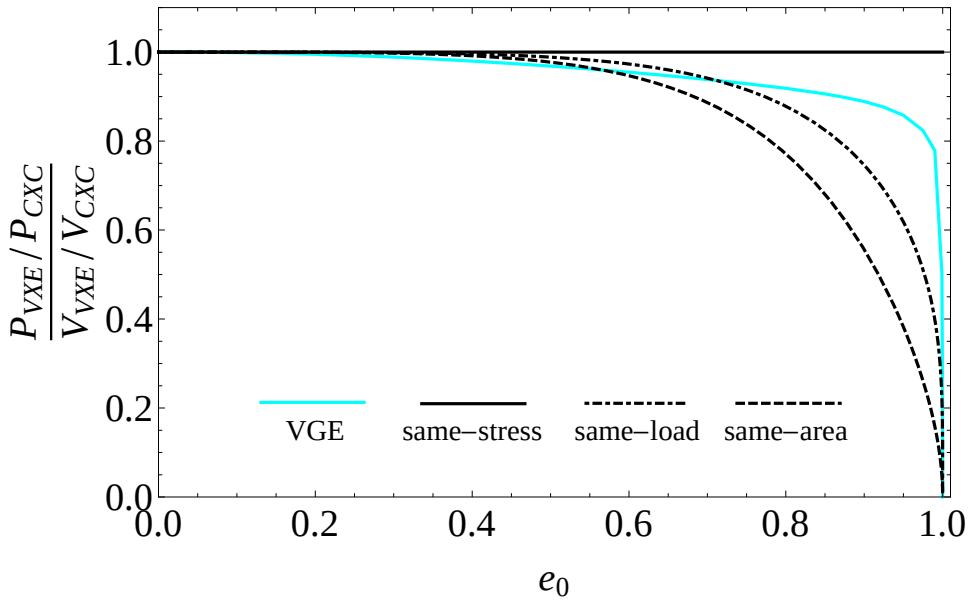

Figure 8.2: Comparison among critical load per unit of weight for different designs

Before closing this section the prebuckling deformations of small simply-supported VTE same-stress and VGE design cylinders will be compared among themselves and with the prebuckling deformations of CXE cylinders. These deformations are illustrated in Figs. 8.3, 8.4, and 8.5 and a few comments can be made by comparing figures. First, it is seen that while for the CXE cylinders shown in Fig. 5.4 the deformations are mainly localized within the flatter regions, for the both the VTE and the VGE cylinders the deformations involve the entire circumference. Moreover, as happens for the CXC cylinders, the prebuckling rotations are confined to boundary layers localized at the two ends of the shell. More precisely, the prebuckling rotation boundary layer in the VTE same-stress design cylinders have a modulated length proportional to the local radius of curvature of the ellipse (i.e., the boundary layer width is wider in the flatter regions where the radius of curvature is larger, and more narrow in the more curved regions where the radius of curvature is smaller). The prebuckling rotation boundary layer in the VGE design cylinders seems to have a uniform width around the circumference. Another remarkable difference among VTE same-stress and VGE designs prebuckling deformed shapes is the deformation in the more curved regions. As seen from the figures in the VTE design the deformation of the more curved region increases as the assigned eccentricity increases due to the decreasing thickness at those locations. Conversely, for the VGE design the deformation of the more curved region decreases as the

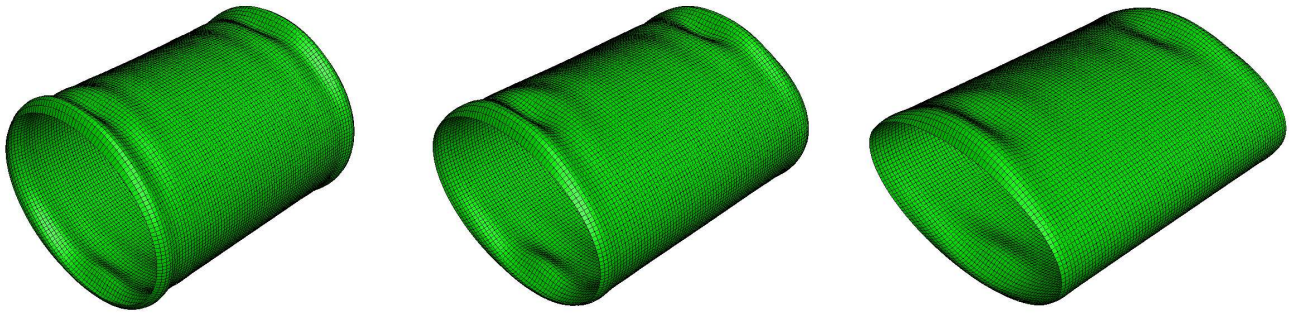

(a) $e_0 = 0.50$ (b) $e_0 = 0.70$ (c) $e_0 = 0.85$

Figure 8.3: Deformed prebuckling shape of axially-loaded simply-supported small CXE cylinders.

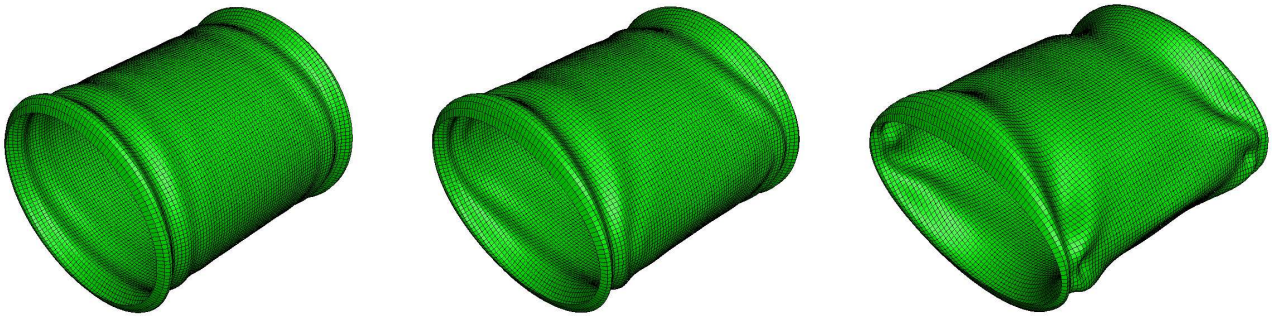

(a) $e_0 = 0.50$ (b) $e_0 = 0.70$ (c) $e_0 = 0.85$

Figure 8.4: Deformed prebuckling shape of an axially-loaded simply-supported small VTE cylinders for same-stress design.

(a) $e_0 = 0.50$ (b) $e_0 = 0.70$ (c) $e_0 = 0.85$

Figure 8.5: Deformed prebuckling shape of an axially-loaded simply-supported small VGE cylinder.

assigned eccentricity increases due to the increasing of the material's axial stiffness at those locations. The prebuckling deformed shapes associated with the same-load and -area designs (not shown here) are qualitatively similar to those of the same-stress design shown in Fig. 8.4. The only difference that can be found is in the amplitude of the deformation that results because the same-stress design allows a larger displacement before reaching the critical stress at the buckling condition as compared to the same-load and -area designs.

8.3 Concluding remarks

The buckling load analysis of a circular cylinder made of orthotropic material is studied here in depth. The analyses is based on quasi-shallow shell theory and prebuckling rotations are ignored in the stability equations. The concept of geometric mean isotropic (GMI) material associated with an orthotropic material is introduced and fruitfully used in order to give an novel mechanical interpretation to the axial buckling behaviour of an orthotropic circular cylinder. The dimensionless parameter g_{12} defined as a combination of the engineering properties of the orthotropic material is introduced. It is shown that the estimation of this parameter is sufficient to predict the qualitative axial buckling deformation behavior of the cylinder. No other calculations are needed. Closed-form expressions for a lower bound of the buckling load of an orthotropic circular cylinder are given. A mathematical explanation of the apparently random pattern of deformation of an isotropic circular cylinder is given and a procedure to obtain a chart to allow prediction of the deformation pattern of the cylinder once its geometry is known. This chart is general and needs to be constructed only one time. In Fig. 3.10 is shown a small portion of this chart.

The general notions developed for orthotropic circular cylinder are used to investigate the axial buckling behavior of an anisogrid lattice structure as a function of rib angles, assuming the lattice grid is dense enough to be modelled as a smeared orthotropic material. The closed-forms for the estimation of the buckling load as a function of the rib angle are given. It is shown that there exists an optimal rib angle for which the buckling load of an anisogrid cylinder is a maximum. This rib angle is independent of the material properties, rib density, and cylinder geometry.

Elliptical cylinders are introduced as the continuous deformation of a circular cylinder. The deformation is assumed to preserve the circumferential length. The deterioration of the axial buckling capability is analytically estimated as a function of the eccentricity assigned to the original circle, which is chosen as a comparison basis. The analytical expression is based on a rather simple assumption. More precisely, the elliptical cylinder is considered as a circular cylinder having radius equal to the maximum radius of curvature of the ellipse. The developed theory is validated using a finite-element model that includes a more accurate consideration of the cylindrical shell, i.e., the actual elliptical geometry is used and prebuckling rotations are included. Even if the absolute values of buckling load predicted by finite-element model are slightly smaller than the ones predicted with the developed analysis, normalized quantities are estimated with a error no larger than 6%.

Based on an analogy two philosophical approaches to the improvement of the buckling performance of an elliptical cylinder are proposed. In the first approach the axial buckling capability of the elliptical cylinder, made of homogeneous orthotropic material, is improved by tailoring the thickness with circumferential position. Three different designs are proposed. The first design is devoted to restoring the axial buckling stress to the level of the original circle. The second design is devoted to restoring the axial buckling load to the value of the original circle. The third design is devoted to maintaining the cylinder volume equal to the that of the original circle. A purely analytical treatment is given and the analytical expressions for relevant load-related quantities are derived and compared for all three designs. Since the theory is based on a rather simple assumption, a finite-element model, including more accurate consideration of the variable thickness elliptical shell, is produced. The predictions based on the developed analysis are found to be in good agreement with the finite element analysis.

In the second approach the axial buckling capability of the elliptical cylinders having constant thickness is improved by tailoring the material properties with circumferential position. The actual implementation of the material tailoring is performed by changing the rib angle of an anisogrid cylinder with circumferential position. Semi-analytical expressions for all the relevant load-related quantities are derived. Since the theory is also based on rather simple assumption, a finite-element model including a more accurate consideration of the

variable geometry elliptical anisogrid cylindrical shell is produced. The predictions based on the developed analysis are found to be in good agreement with the finite-element analysis. The problem of designing the actual grid structure of a variable geometry elliptical anisogrid cylinder, once the variation of the rib angle with circumferential position is known, is studied and completely solved. Finally, it is shown that both approaches can be viewed as two specific complementary designs of a much more general design philosophy. More precisely, the main assumption at the base of the design philosophy is that the closed-forms (3.44) derived for a circular orthotropic cylinder can be still used for a noncircular cross section, obtained by a continuous deformation of a circular cross section, which has material properties and local thickness varying with the circumferential position if the minimum value the stress assumes all around the circumference is kept as the critical stress of the whole cylinder. This assumption has been formalized in (5.15), which is a simple relation derived from (3.44), by assuming both the thickness and material properties to be function of the circumferential position. This equation is applicable to noncircular cylinders and predicts a loss of load capability for an elliptical cylinder with the same circumference and wall thickness as the circular cylinder (see (5.10)).

Equation (5.15) has been used as to develop three designs to increase the axial load capability of elliptical cylinder by considering a variable wall thickness. In fact, (5.15) has been used to specify the variation of wall thickness with circumferential position for the elliptical cylinder. Numerical results for the same-stress, same-load, and same-area designs developed with (5.15) as a guideline have been computed and compared to results obtained for a finite-element model considering prebuckling rotations of these three designs. There are some differences between the finite-element results and the predictions based on (5.15). However, designing the variation of the wall thickness using finite elements is a cumbersome and time-consuming approach. In that context, (5.15) does well. Moreover, the results obtained using (5.15) are good enough that conclusions can be drawn regarding trade-offs in the designs. For example, and continuing with an earlier example, according to Fig. 5.6, which is based on (5.10) of the developed analysis, a simply-supported CTE cylinder with $e_0 = 0.70$ retains only 62% of the buckling load of the original CTC cylinder. This is verified by the finite-element calculations in Tab.5.5, where a buckling load retention of 66% rather than 62% is computed by the finite-element analysis for the small cylinders. Both the

developed analysis, i.e., $1/g^2(e_0)$, and the finite element calculations for the small cylinder illustrate that the same-area VTE design for the case of $e_0 = 0.70$ in Tab. 6.13 retains 89% of the buckling load of the CTC cylinder. This translates into better than a 30% increase in buckling load of the VTE cylinder compared to the CTE cylinder, i.e., P_{VTE}/P_{CTE}. Since the developed analysis correlates so well with the finite element calculations, the developed analysis can then be used to quickly conclude that the buckling load of the small VTE cylinder can be made to retain 100% of the buckling load of the CTC cylinder by using the same-load design (see Tab. 6.11, $P_{VTE}/P_{CTC} = 1.0007$) if a 6% increase in weight (i.e., $g(0.70) = 1.0621$) can be tolerated. If even more weight can be tolerated, Tab. 6.9 can be used to show that significant increases in buckling loads can be realized for the case of $e_0 = 0.70$ with only slightly more than a 12% increase in weight (i.e., $g^2(0.70) = 1.181$).

Finally (5.15) has been used to develop a design to increase the axial load capability of elliptical cylinder by considering a nonhomogeneous material properties. In fact, (5.15) has been used to specify the variation of rib angle with circumferential position for the elliptical lattice cylinder. Numerical results for the developed design with (5.15) as a guideline have been computed and compared to results obtained for a finite-element model considering prebuckling rotations of this design. There are some differences between the finite-element results and the predictions based on (5.15). However, designing the variation of rib angle using finite elements would be quite a chore. In that context, (5.15) does well. Moreover, the results obtained using (5.15) are good enough that conclusions can be drawn regarding trade-offs in the designs. For example, and continuing with an earlier example, according to Fig. 5.6, which is based on (5.10) of the developed analysis, a simply-supported CGE cylinder with $e_0 = 0.70$ retains only 62% of the buckling load of the original CGC cylinder. This is verified by the finite element calculations in Tab.5.7, where a buckling load retention of 66% rather than 62% is computed by the finite-element model for the small cylinders. Both the developed analysis, i.e., (7.13), and the finite-element calculations for the small cylinder illustrate that the VGE design for the case of $e_0 = 0.70$ in Tab. 7.1 retains 94% of the buckling load of the CTC cylinder. This translates into better than a 40% increase in buckling load of the VGE cylinder compared to the CGE cylinder, i.e., P_{VGE}/P_{CGE}. Since the developed analysis correlates well with the finite-element calculations, the developed analysis can then be used to quickly estimate the axial buckling load improvement of a VGE

anisogrid cylinder with respect to the axial buckling load of the CGC isogrid cylinder.

8.4 Future prespective

There are a number of issues to consider for future investigations of the variable wall thickness designs. The role of imperfections is always an important issue with cylindrical structures. That is no less the case here, particularly imperfections at circumferential locations were the walls are thinner. A study of the postbuckling behavior would also be important. For all cases considered here the stresses at buckling were less than the compressive yield of many aluminum alloys, particularly for the large cylinder. Therefore, snap-through and other large elastic deformations associated with postbuckling would be of interest.

Another relevant aspect to be explored in future investigations is the study of a variable geometry elliptical lattice cylinder joined with a skin layer or sandwiched in the between two skin layers. The skin layers could be made of composite material where the fiber angle is, in turn, also tailored with circumferential position.

As previously mentioned the four designs presented in this dissertation can be seen as special cases of a more general design philosophy. In the framework of this general theory many other different designs can be investigated and even noncircular cross sections different from an an ellipse can be taken into consideration.

Bibliography

[1] R.M. Jones. *Buckling of Bars, Plates, and Shells*. Bull Ridge Publishing, Blacksburg, Virginia, USA, 2006. ISBN 0-9787223-0-2, chap. 4.

[2] W. Fairbairn. On the resistence of tubes to collapse. *Phil. Trans. Roy. Soc.*, 148:389–414, 1858.

[3] J. A. Bresse. *Cours de mecanique applique*, volume 1. 1866.

[4] S. Timoshenko. Einige stabilitats probeme der elastizitats theorie. *Z. angew. Math. Phys.*, 58(4):337–385, 1910.

[5] R. Southwell. On the collapse of tube by external pressure. *Phil. Maz. se.*, 25(149):687–697, 1913.

[6] R. Mises. Der kritische aussendruck zylindrischer rohre. *VDI- Zeitschrift*, 58:750–755, 1914.

[7] W. Flugge. Die stabilitat der kreiskzylindershale. *Ing.-Archiv*, 3:463–506, 1932.

[8] L. H. Donnell. A new theory for the buckling of thin cylinders under axial compression and bending. *Trans. ASME*, 56:795–806, 1934.

[9] K. Marguerre. Zur theorie der gekrümmten platte grosser formänderung. *Proceeding of 5-th Intenational Congres of Applied Mechenics*, pages 93–101, 1938.

[10] Kh. M. Mushtari. Some generalizations of thin shells theory with applications to elastic stability problems. *Prikl. Mat. Mekh.*, 2(6):439–456, 1939. (in Russian).

[11] T. Karman and H. S. Tsien. The buckling of thin cylindrical shells under axial compression. *Journal of Aero. Sci.*, 8:303–312, 1941.

[12] H.S. Tsien. Lower buckling load in the nonlinear buckling theory of thin shells. *Quart. Appl. Math.*, 5(2):236–237, 1947.

[13] W. T. Koiter. Elastic stability and postbuckling behavior. *Proc. Symp. Nonlinear Problems*, pages 257–275, 1963.

[14] B. Budiansky and J. W. Hutchinson. Dynamic buckling of imperfections-sensitive structures. *Proc. XI-th Int. Congr. Appl. Mech.*, pages 636–651, 1964.

[15] L. H. Donnell and C. C. Wan. Effect of imperfections on buckling of thin cylinders and columns under axial compression. *Journal Appl. Mech.*, 17(1):73,83, 1950.

[16] Kh. M. Mushtari. On elastic equilibrium of thin shells with initial imperfections in middle surface. *Prikl. Mat. Mekh.*, 15(6):743–750, 1951. (in Russian).

[17] R. C. Tennyson. A note on the classical buckling load of circular cylindrical shell under axial compression. *AIAA Journal*, 1(2):475–476, 1963.

[18] R. C. Tennyson. Buckling of circular cilindrical shells in axial compression. *AIAA Journal*, 2(7):1351–1353, 1964.

[19] R. C. Tennyson. An experimental investigation of the buckling of circular cylindrical shells in axial compression using the photoelastic technique. Technical Report Rept. 102, University of Toronto, 1964.

[20] K. Marguerre. Stability of cylindrical shell of variable curvature. Technical Report TM 1032, NACA, 1951.

[21] C. A. Meyers and M.W. Hyer. Response of elliptical composite cylinders to internal pressure loading. *Mechanics of Composite Material and Structures*, 4:317–343, 1997.

[22] C. A. Meyers and M.W. Hyer. Response of elliptical composite cylinders to axial compression loading. *Mechanics of Composite Materials and Structures*, 6(2):169–194, 1999.

[23] F. Romano and J. Kempner. Stress and displacement analysis of simply supported noncircular cylindrical shells under lateral pressure. *PIBAL Report No. 415*, 1958.

[24] F. Romano and J. Kempner. Stress in short noncircular cylindrical shells under lateral pressure. *Journal of Appl. Mech.*, 12:69–77, 1962.

[25] J. M. Klosner and F. V. Pohle. Natural frequencies of an ininitely long noncircular cylindrical shell. *PIBAL Report No 476*, 1958.

[26] J. Kempner and Y. N. Chen. Large deflections of an axially compressed oval cylindrical shell. PIBAL Report 694, Polytechnic Institute of Booklyn, Brooklyn, NY, May 1964. Also in Prooceedings of the XI International Congress of Appleed Mechanics, Munich, Germany,1964, ed. Henry Görtler, Springer-Verlag, Berlin/Heidelberg, 1966, pp. 299-305.

[27] G. Sun. Buckling and initial post-buckling behavior of laminated oval cylindrical shells under axial compression. *Journal of Applied Mechanics*, 58(1):848–851, 1991.

[28] K. P. Soldados. Nonlinear analysis of transverse shear deformable laminated composite cylindrical shells part I: Derivation of governing equations. *ASME Journal of Pressure Vessel Technology*, 114(1):105–109, 1992.

[29] K. P. Soldados. Nonlinear analysis of transverse shear deformable laminated composite cylindrical shells part II: Buckling of axially compressed cross-ply circular and oval cylinders. *ASME Journal of Pressure Vessel Technology*, 114(1):110–114, 1992.

[30] C. T. Sambandam, B. P. Patel, S. S. Gupta, C. S. Munot, and M. Ganapathi. Buckling characteristics of cross-ply elliptical cylinders under axial compresion. *Composite Structures*, 62(1):7–17, 2003.

[31] B. P. Patel, C. S. Munot, S. S. Gupta, C. T. Sambandam, and M. Ganapati. Application of higher-order finite element for elastic stability analysis of laminated cross-ply oval cylindrical shells. *Finite Element in Analysis and Design*, 40(9-10):1083–1104, 2004.

[32] Y. N. Nemish. Solution of three-dimensional boundary-value problems for laminated noncircular cylinders. *Int. Appl. Mech.*, 29:738–744, 1993.

[33] O. S. Heck. The stability of orthotropic elliptical cylnders in pure bending. Technical Report TM 834, NACA, 1937.

[34] J. Kempner and Y. N. Chen. Buckling and postbuckling of an axially compressed oval cylindrical shell. In D. Muster-Univ. Houston, editor, *Proceedings - Symposium*

On theory of shells to honor Lloyd Hamilton Donnell, pages 141–175, Houston, 1967. McCutchaw Publishing Corporation.

[35] J. W. Hutchinson. Buckling and initial postbuckling behavior of oval cylindrical shells under axial compression. *Journal of Appl. Mech.*, 35(1):66–72, 1968.

[36] J. Kempner and Y. N. Chen. Postbuckling of an axially compressed oval cylindrical shell. In M. Hetényi and W.G. Vincenti, editors, *Proceedings of the XII International Congress of Applied Mechanics*, pages 246–256, Stanford, CA, 1968. Springer-Verlag, Berlin/Heidelberg, 1969.

[37] B. O. Almroth. Collapse analysis for elliptical cones. *AIAA Journal*, 9(1):32–37, 1971.

[38] Y. N. Chen, G. Feinstein, and J. Kempner. Buckling of clamped oval cylindrical shells under axial compresion. *AIAA Journal*, 9(9):1733–1738, 1971.

[39] G. Feinstein, B. Erickson, and J. Kempner. Stability of oval cylindrical shells. *Exper. Mech.*, 11(11):514–520, 1971.

[40] K. P. Soldados and G. J. Tzivanidis. Buckling and vibrations of cross-ply laminated non-circular cylindrical shells. *Journal of Sound and Vibration*, 82(3):425–434, 1982.

[41] I. Sheinman and M. Firer. Buckling analysis of laminated cylindrical shell with arbitrary cross-section. *AIAA Journal*, 32(3):648–654, 1994.

[42] M. Firer and I. Sheinman. Nonlinear analysis of laminated noncircular cylindrical shells. *International Journal of Solids and Structures*, 32(10):1405–1416, 1995.

[43] M. Sun. *Use of material tailoring to improve the axial load capacity of ellipical composite cylinders*. PhD thesis, Virginia Polytechnic Institute and State University, 2006. also in *AIAA Journal*, 46 (3): 770-782, 2008.

[44] F. R. Shanley. Simplified analysis of general instability of stiffened shells in pure bending. *Journal of Aereo Science*, 16(10):590–592, 1949.

[45] W. R. Micks. Minimum weight of stiffened cylindrical shells in pure bending. *Journal of Aero Science*, 17(4):211–216, 1950.

[46] J. M. Hedgepeth. Design of stiffened cylinders in axial compression. Technical Report D-1510, NASA, 1962.

[47] A. B. Burns. Structural optimization of axially compressed cylinders considering ring-stringer eccentricity effects. *Journal of Spacecraft and Rockets*, 3(8):1263–1268, 1966.

[48] A. B. Burns. Optimum cylinders with contrasting materials and various ring/stringer configurations. *Journal of Spacecraft and Rockets*, 4(3):375–385, 1967.

[49] C. Cvetkov. Determination of most convenient shapes of stiffeners of cylindrical shells. *Tekhn. Mysl*, 3(4):511–515, 1966. (in Bulgarian).

[50] C. Lakshmikantham and H. Becker. Minimum weigth aspects of stiffened cylinders under compression. Technical Report TR-CR-81693, NASA, 1967.

[51] D. L. Block. Minimum weight design of axially compressed ring and stringer stiffened cylindrical shells. Technical Report CR-1766, NASA, 1971.

[52] G. J. Simitses and I. Sheinman. Optimization of geometrically imperfect stiffend cylindrical shells under axial compresion. *Computers and Structures*, 9(4):377–381, 1978.

[53] K. Kunoo and T. Y. Yang. Minimum weight design of cylindrical shell with multiple stiffener sizes. *AIAA Journal*, 16(1):35–40, 1978.

[54] J. Singer and A. Rosen. The influence of boundary conditions on the buckling of stiffened cylindrical shells. Technical report, DTIC, 1974.

[55] G. Sun and R. Mao. Optimization of stiffened laminated-composite circular-cylindrical shells for buckling. *Composite Structures*, 23(1):53–60, 1993.

[56] M. Ruzzene. Non-axisymmetric buckling of stiffened shells: static and dynamic analysis. *Comput. Struct.*, 82:257–269, 2004.

[57] S. S. Wang, K. B. Su, and M. G. Dunham. A structural efficiency study of isogrid-stiffened fiber composite laminate shells: buckling postpuckling analyses and experiments. In A. Poursartip and K. Street, editors, *Proceedings of ICCM/10:* 10^{th}

Int. Conf. on Composite Materials, volume V, pages 59–68, Whistler, Canada, August 1995. Woodhead Publishing Limited, Cambridge, UK. ISBN 1 85573 226 2, www.woodheadpublishing.com.

[58] V. V. Vasiliev, V. A. Barynin, and A. F. Rasin. Anisogrid lattice structures - survey of development and applications. *Composite Structures*, 54:361–370, 2001.

[59] S. M. Huybrechts, S. E. Hahn, and T. E. Meink. Grid stiffened structures: survey of fabbrication, analysis and design methods. In T. Massard and A. Vautrin, editors, *Proceeding of ICCM/12:* 12^{th} *Int. Conf. on Composite Materials CDROM*, Paris, France, 5-9 July 1999. Woodhead Publishing Limited, Cambridge, UK. ISBN-13: 9781855734760, www.woodheadpublishing.com.

[60] S. M. Huybrechts, T. E. Meink, P. M. Wegner, and Ganley J. M. Manufactoring theory for advanced grid stiffened structures. *Composites Part A*, 33:155–166, 2002.

[61] V. Vasiliev. *Mechanics of composite structures.* Taylor & Francis, 1993.

[62] D.O. Brush and B.O. Almroth. *Buckling of Bars, Plates, and Shells.* McGraw-Hill, New York, NY, 1975. pp. 168.

[63] *ABAQUS Version 6.6, Hibbit, Karlsson & Sorensen, Inc.* 1080 Main Street Pawtucket, RI 02860-4847. www.abaqus.com.

[64] A. Gajewski and M. Zyczkowski. *Optimal structure design under stability contraints.* Kluwer Academic Publishers, Netherlands, 1988. ISBN 90-247-3612-9.